THE UNIVERSITY
of EDINBURGH

Non-Standard Neutrino Interaction Analysis with Atmospheric Neutrino Data in Super-Kamiokande I-IV and the Design of the Hyper-Kamiokande Outer Detector

Mahdi Taani

Doctor of Philosophy
The University of Edinburgh
June 2020

Dedicated to my mother

Abstract

Neutrino oscillation is a well-established phenomenon and oscillation parameters are being measured with great accuracy. This unprecedented accuracy allows sensitivity to sub dominant effects which could indicate new physics. Non-standard interactions (NSI) is a general term for interactions not described by the Standard Model. In this thesis NSIs are studied using 5326 days of Super-Kamiokande atmospheric neutrino data. This work focuses on NSIs which allow neutral current induced flavour transitions and interactions which allow different neutral current interaction amplitudes for different neutrino flavours. The strength of the NSI between neautrino flavours α and β is characterised by the parameter $\varepsilon_{\alpha\beta}$. A limit is obtained for the NSI strength, $-0.046 < \varepsilon_{\mu\tau} < 0.019$ at 90% C.L., which is a slight improvement over the previous Super-K measurement and is consistent with recent IceCube measurements. Additional constraints on $\varepsilon_{e\tau}$ and $\varepsilon_{\tau\tau}$ are obtained for different values of ε_{ee}; the constraints in the $e-\tau$ sector are somewhat looser than previous Super-K measurements.

Further improvements are expected with the next generation neutrino oscillation experiment Hyper-Kamiokande (Hyper-K). Hyper-K is a water Cherenkov detector which will make use of an outer detector to veto incoming charged particles and reduce backgrounds. This work details the design of the outer detector for Hyper-K, in particular research and development work carried out to enhance the light collection. Wavelength shifting plates are modelled and their efficiencies are studied. Reflective materials and their impact in the outer detector are also discussed.

Lay Summary

Neutrinos are the most abundant massive particle in the universe and they very rarely interact with anything, travelling the universe largely undisturbed. Due to their low interaction rates, neutrinos created in stars or in different galaxies can still reach us without being stopped. This makes them an excellent source to look far out into the universe and understand star formation and supernovae as well as back in time to understand the early universe.

As they rarely interact, large detectors are required in order to increase the chance of detecting a neutrino. One such large detector is called Super-Kamiokande or Super-K; it is a 50 kton tank filled with ultrapure water and 13,000 highly sensitive light detectors which are used to observe neutrino interactions. Super-K has been taking data since 1996 and has detected many neutrinos from various sources. Examining the energy, direction and flavour of the detected neutrinos allows us to determine their fundamental properties.

All known fundamental particles and the interactions between them are described by a theory known as the Standard Model of particle physics. The theory is very successful and experiments have consistently verified its predictions. However, the Standard Model does not correctly describe the neutrino. For many years these particles were thought to be massless but experimental evidence shows that the particles do have mass. These particles come in three flavours and experiments have proven that a neutrino of one flavour can change into a neutrino of a different flavour. This property of neutrinos is exciting as it indicates new physics beyond the Standard Model.

Extensions to the Standard Model which account for the neutrino mass have been proposed; naturally, these extended models allow exotic interactions which are not allowed by the Standard Model. These interactions are known as non-standard interactions (NSIs) and have not yet been observed. Observation of neutrino NSIs could indicate the existence of new particles or other exotic physics scenarios. In this thesis, 15 years of Super-K data has been analysed in order to look for possible non-standard interactions. No evidence of NSI was found and tight limits have been set on the possible strength of neutrino NSIs.

While the understanding of neutrino properties has advanced significantly in the last two decades, some questions remain open. Possibly the most important ques-

tion is whether or not neutrinos and antineutrinos, their antimatter counterpart, behave in the same way. If they do not, then neutrinos could be the reason that the universe is dominated by matter while there is hardly any antimatter. To answer this question a much larger number of neutrinos must be detected which requires a larger detector.

In 2028 a new large detector Hyper-Kamiokande (Hyper-K), eight times larger than Super-K, will begin taking data. This thesis details the work carried out to design and eventually build Hyper-K. The detector will observe many neutrino events and will make use of a veto system to reject non-neutrino events. The work shown in this thesis is the design and optimisation of the Hyper-K veto detector.

Acknowledgements

Firstly, I would like to sincerely thank my supervisor Matthew Needham for his excellent guidance and advice. I am very grateful for the constant support and the freedom you allowed me in exploring new ideas. Without your counsel over the last four years, this work could not have been completed.

I am hugely indebted to my second supervisor Stephen Playfer who was extremely generous in sharing his expertise and knowledge. Thank you for always being available to discuss ideas and for being great fun.

I spent a lot of time in Nagoya and would like to express my deepest appreciation towards my third supervisor Yoshitaka Itow. Thank you for sharing your intimate knowledge of Super-K and for welcoming me to Nagoya. Thank you for all the help in physics and day-to-day life in Japan.

The NSI analysis in this thesis would most definitely not have been possible without Roger Wendell. I am extremely grateful to you for sharing your wisdom and for being patient with me.

It has been fantastic working on Super-K and I am grateful for the discussions with all of the collaborators, especially the ATMPD group. Thank you Ed Kearns for your advise throughout my analysis.

I have really enjoyed being a part of Hyper-K and I am thankful to the whole collaboration, particularly the OD group. I have been fortunate enough to work with Lilia Drakopoulou, Stephane Zsoldos and Federico Nova; it has been a pleasure working with you, striving for perfect plates!

Outside of physics I would like to thank my brothers: Bruno, Daniele, Farhang, Jerry, Junzy, Louis and Nadeem for helping me to stay sane, and giving me a little perspective in life.

Contents

List of Figures

List of Tables

Chapter 1

Thesis Overview

The discovery of neutrino oscillations has proven that neutrinos have a non-zero mass which is unaccounted for in the Standard Model of particle physics. Many models of neutrino mass naturally include some form of phenomenologically allowed interactions which are not included in the Standard Model; such interactions are called non-standard interactions. If present, non-standard interactions can affect the production, detection and propagation of neutrinos through matter. The analyses carried out in this thesis aim to search for sub dominant effects in neutrino oscillations which may be due to non-standard interactions with matter in the Earth.

This thesis begins with an introduction to neutrino masses and oscillation theory, as well as an overview of the current experimental status, in Chapter 2. The theories of standard oscillations as well as standard and non-standard matter effects are presented. The neutrino data used in this thesis comes from the Super-Kamiokande experiment.

Super-Kamiokande (Super-K) is an underground water Cherenkov detector which has been running since 1996. Data has been collected in four distinct phases SK-I, SK-II, SK-III and SK-IV. A detailed description of the Super-Kamiokande detector and its four phases are given in Chapter 3. The detector's calibration is outlined in Chapter 4. The analyses in this thesis compare the expected atmospheric neutrino flux to the observed flux, where the expected flux is given by a Monte Carlo (MC) simulation described in Chapter 5.

Super-Kamiokande is built under ~ 1 km of rock in order to reduce backgrounds

from cosmic rays. The level of cosmic rays reaching the detector are reduced by five orders of magnitude compared to a detector located on the surface. While backgrounds are significantly reduced, they still make up the overwhelming majority of triggered events. Efforts must be taken to reduce the large amount of background events keeping only the neutrino events. This data reduction is carried out regularly with occasional changes in the data reduction steps depending on the detector's configuration. In SK-IV it was found that some high energy events were being misclassified because they left a crosstalk signal in the veto region. I was a member of a data reduction taskforce which implemented the most recent changes to the data reduction, in particular I was in charge of implementing a crosstalk selection cut. The details of the data reduction as well as the implementation of the crosstalk cut are found in Chapter 6.

Chapter 7 details the event selection and binning of the events as well as the formulation of the χ^2. Searches are then carried out for non-standard interactions in the $\nu_\mu - \nu_\tau$ and $\nu_e - \nu_\tau$ sectors which are explained in Chapter 8. I performed the analysis and extended the existing Super-K oscillation analysis framework to allow for the calculation of non-standard oscillation probabilities.

In order to increase the physics sensitivity, Super-Kamiokande have decided to add Gadolinium to the ultrapure water in the tank. Gadolinium loaded water improves the ability to detect neutrons which can reduce backgrounds as well as increase the detector's ability to separate neutrinos events from antineutrino events. Super-K shut down in the middle of 2018 ending the run of SK-IV. I had the amazing opportunity to enter the tank and take part in the refurbishment of the detector in preparation for Gadolinium doping. Getting to see the inside of the detector was a valuable experience which gave me a good understanding of the detector setup. The knowledge was useful for the development of Super-Kamiokande's successor Hyper-Kamiokande.

Hyper-Kamiokande is a large underground water Cherenkov detector with roughly eight times the fiducial mass of Super-Kamiokande. While both tanks are water Cherenkov detectors, which use similar technologies, complications arise when designing the larger detector. Hyper-Kamiokande will have an improved sensitivity to neutrino oscillation parameters and nucleon decays in addition to the increased capability of supernovae observation. The improved sensitivity requires backgrounds to remain low, many of which are removed by an outer detector. The design of the Hyper-Kamiokande detector is described in Chapter 9. Chapter 10 describes the study and design of the Hyper-Kamiokande detector,

and in particular the outer detector. I developed the analytic simulation of the WLS plates and carried out significant development of the outer detector in WCSim. The hardware measurements and R&D were carried out by me and other members of the Edinburgh Hyper-K group. This thesis ends with a summary chapter, detailing the conclusions from the various studies and outlook to future studies.

Chapter 2

Introduction

The neutrino is the most abundant massive particle in the universe. There are many sources of neutrinos, both natural and manmade: the Sun, cosmic ray interactions in the Earth's atmosphere, supernovae, nuclear reactors and accelerators. Each source of neutrinos has their own characteristic flavour and energy spectrum, allowing the study of various physics phenomena. Neutrinos interact only via the weak force and their very small cross section makes them difficult to detect. For this reason, detectors with large target volumes and low levels of background must be used.

In the late 1960s the Homestake experiment [64] measured the solar neutrino flux and observed a solar neutrino flux which was much lower than that predicted by the Standard Solar Model. Kamiokande [84], SAGE [7] and Super-Kamiokande [81] later confirmed the deficit. This problem became known as the solar neutrino anomaly. Another anomaly was later found in the flux of atmospheric neutrinos. The atmospheric neutrino flux is expected to have a (ν_μ/ν_e) ratio of 2 for neutrino energies below 1 GeV (see Section 5.1) while the Kamiokande [83], IMB [49] and Soudan [39] experiments measured a value roughly two thirds of this, indicating an excess in ν_e or a deficit in ν_μ (or both). This was known as the atmospheric neutrino anomaly and was solved by Super-Kamiokande [85] when they found that the measured neutrino flux had a zenith angle dependence for ν_μ which was consistent with $\nu_\mu \rightarrow \nu_\tau$ oscillation. In 2002 the solar neutrino problem was solved when SNO [30] measured the total solar neutrino flux with a detector which was sensitive to ν_e, ν_μ and ν_τ. The total solar neutrino flux measured by SNO was consistent with the Standard Solar Model

prediction and solar neutrino oscillation $\nu_e \rightarrow \nu_\mu/\nu_\tau$ was confirmed.

Since the first evidence of neutrino oscillations, much progress has been made in determining the precise values of neutrino oscillation parameters. The precision of neutrino oscillation experiments now allows us to look for sub-leading effects, such as non-standard neutrino interactions, and to achieve a better understanding of this mysterious particle.

2.1 Standard Model

The Standard Model of particle physics is a mathematical framework which describes the behaviour of subatomic particles. The model incorporates all known elementary particles and three of the four known fundamental forces. The model includes fermions, matter particles with half integer spin, and bosons, force-carrying particles with integer spin. There are 12 fermions which are made up of six quarks and six leptons; the fermions are grouped together into three generations of increasing mass. The three fundamental forces in the Standard Model are the electromagnetic, weak and strong forces. The electromagnetic force is mediated by the massless photon and the weak nuclear force is mediated by massive W^+, W^- and Z^0 bosons; the photon and W/Z bosons collectively mediate the electroweak interaction. The strong interaction is mediated by massless gluons. A schematic diagram of the Standard Model is shown in Figure 2.1.

The interactions in the Standard Model are defined by gauge symmetries. The gauge group of the Standard Model is $SU(3)\times SU(2)\times U(1)$ where $SU(2)\times U(1)$ is the electroweak group and $SU(3)$ is the strong gauge group. The Higgs field [100] interacts with the gauge fields which results in spontaneous symmetry breaking causing the weak bosons and charged fermions to gain mass. The Higgs field also gives rise to a massive, spin-0 boson, the Higgs boson.

Neutrinos do not interact via the electromagnetic or strong interactions which means they rarely interact with matter, making them difficult to detect. Weak interactions are called charged current (CC) if they are mediated by a $W^\pm$ boson, and neutral current (NC) if they are mediated by the Z^0 boson. The three generations of neutrino are ν_e, ν_μ and ν_τ which are defined by the flavour of the charged lepton associated with their charged current interactions. While the SM is a very successful theory, with many successful experimental predictions, it does

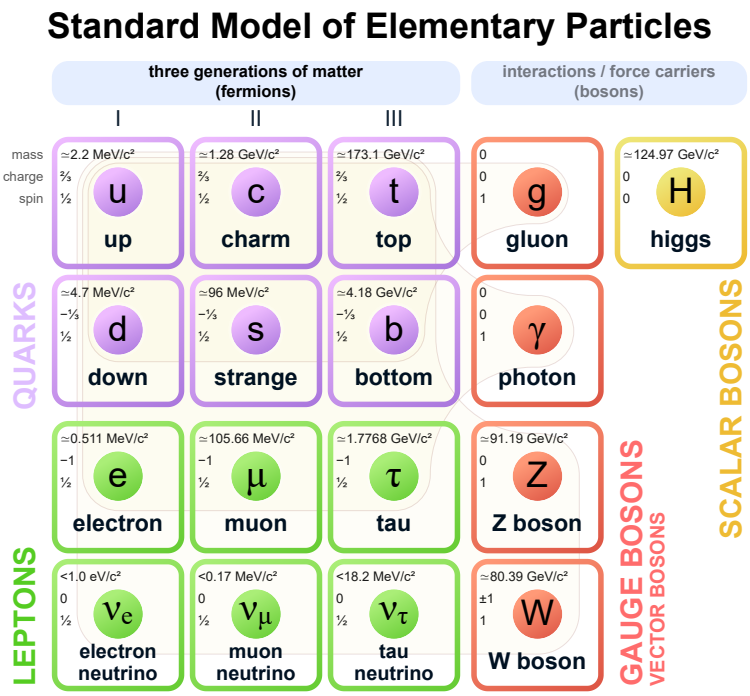

Figure 2.1 *A summary showing the fermions and bosons in the Standard Model. Taken from [1].*

not yet include a way to generate neutrino mass or allow neutrino oscillations.

2.2 Neutrino Oscillations

Neutrinos are produced in various charged-current (CC) weak interaction processes, associated with a charged lepton. The three charged leptons means there are three neutrino flavours: electron neutrino (ν_e), muon neutrino (ν_μ) and tau neutrino (ν_τ). The type of neutrino is determined either by the charged lepton associated with a neutrino's creation or the detected charged lepton resulting from a neutrino CC interaction. In the late 1950s Pontecorvo [144] predicted a phenomenon that would cause neutrinos to change flavour in a process known as neutrino oscillation. The oscillation is caused by the interference of different massive neutrinos. In 1962 Maki, Nakagawa and Sakata [126] first introduced a model with the mixing of different neutrino flavours. Neutrino oscillation has been observed by atmospheric [85], solar [29] and reactor [21, 41] neutrino experiments. The discovery of neutrino oscillation proves that neutrinos have a non-zero mass, directly contradicting the assumption made in the Standard Model.

2.2.1 Neutrino Oscillation Theory

Neutrinos are in one of three flavour eigenstates at production and detection: $|\nu_e\rangle$, $|\nu_\mu\rangle$ or $|\nu_\tau\rangle$. During propagation however, the neutrino is made up of a superposition of three mass eigenstates: $|\nu_1\rangle$, $|\nu_2\rangle$ or $|\nu_3\rangle$. The transformation between flavour and mass bases is described by the Pontecorvo-Maki-Nakagawa-Sakata (PMNS) unitary mixing matrix:

$$\begin{pmatrix} \nu_e \\ \nu_\mu \\ \nu_\tau \end{pmatrix} = \begin{pmatrix} U_{e1} & U_{e2} & U_{e3} \\ U_{\mu 1} & U_{\mu 2} & U_{\mu 3} \\ U_{\tau 1} & U_{\tau 2} & U_{\tau 3} \end{pmatrix} \begin{pmatrix} \nu_1 \\ \nu_2 \\ \nu_3 \end{pmatrix}. \tag{2.1}$$

Equation 2.1 shows that a neutrino flavour eigenstate is a superposition of mass eigenstates which can be written in the form:

$$|\nu_\alpha\rangle = \sum_{i=1}^{3} U^*_{\alpha i} |\nu_i\rangle , \tag{2.2}$$

where ν_α represents a neutrino of flavour $\alpha = e$, μ or τ. U is the PMNS matrix and ν_i represents the neutrino mass eigenstate where $i = 1$, 2 or 3. The PMNS matrix is the product of three independent rotation matrices with rotation angles θ_{12}, θ_{13} and θ_{23} and a complex phase δ_{cp}:

$$U = \begin{pmatrix} 1 & 0 & 0 \\ 0 & \cos\theta_{23} & \sin\theta_{23} \\ 0 & -\sin\theta_{23} & \cos\theta_{23} \end{pmatrix} \begin{pmatrix} \cos\theta_{13} & 0 & \sin\theta_{13} e^{-i\delta_{cp}} \\ 0 & 1 & 0 \\ -\sin\theta_{13} e^{i\delta_{cp}} & 0 & \cos\theta_{13} \end{pmatrix} \begin{pmatrix} \cos\theta_{12} & \sin\theta_{12} & 0 \\ -\sin\theta_{12} & \cos\theta_{12} & 0 \\ 0 & 0 & 1 \end{pmatrix}. \tag{2.3}$$

2.2.2 Neutrino Oscillations in a Vacuum

Let us now consider the propagation of neutrinos. The massive neutrino states are eigenstates of the Hamiltonian and their time evolution is governed by the Schrödinger equation:

$$i\frac{d}{dt} |V_i(t)\rangle = \mathcal{H} |V_i(t)\rangle . \tag{2.4}$$

Equation 2.4 suggests that the neutrino mass states evolve in time as plane waves:

$$|V_j(t)\rangle = e^{-iE_j t}\,|V_j\rangle\,, \tag{2.5}$$

where E_j are the energy eigenvalues.

When a neutrino is created, with a definite flavour state α, at time $t = 0$ equations 2.2 and 2.5 give us the time evolution of the neutrino:

$$|V_\alpha(t)\rangle = \sum_j U^*_{\alpha j} e^{-iE_j t}\,|V_j\rangle\,. \tag{2.6}$$

The mass states can be written in terms of flavour states by using the unitarity of the mixing matrix. The time evolution equation (Equation 2.6) then can be rewritten in terms of flavour states:

$$|V_\alpha(t)\rangle = \sum_{\beta=e,\mu,\tau} (\sum_j U^*_{\alpha j} U_{\beta j} e^{-iE_j t})\,|V_\beta\rangle\,. \tag{2.7}$$

Equation 2.7 shows that, assuming a non-diagonal mixing matrix, a neutrino created with a definite flavour then propagates as a superposition of flavour states. The amplitude of the transition from neutrino flavour α to β is given by:

$$A_{\nu_\alpha \to \nu_\beta} \equiv \langle \nu_\beta | \nu_\alpha(t)\rangle = \sum_j U^*_{\alpha j} U_{\beta j} e^{-iE_j t}. \tag{2.8}$$

The transition probability is then given by:

$$P_{\nu_\alpha \to \nu_\beta} = |A_{\nu_\alpha \to \nu_\beta}|^2 = \sum_{j,k} U^*_{\alpha j} U_{\beta j} U_{\alpha k} U^*_{\beta k} e^{-i(E_j - E_k)t}. \tag{2.9}$$

At ultrarelativistic energies, the energy eigenvalue, E_j, can be approximated by ignoring higher order terms of the Taylor expansion:

$$E = \sqrt{(\vec{p^2} + m^2)} \tag{2.10}$$

$$= \vec{p}\sqrt{1 + \frac{m^2}{\vec{p^2}}} \tag{2.11}$$

$$= \vec{p}(1 + \frac{m^2}{2\vec{p^2}} + \frac{m^4}{8\vec{p^4}} + ...) \tag{2.12}$$

$$\simeq \vec{p} + \frac{m^2}{2\vec{p^2}}. \tag{2.13}$$

The $E_j - E_k$ term that appears in the transition probability then becomes:

$$E_j - E_k = (\vec{p} + \frac{m_j^2}{2\vec{p^2}}) - (\vec{p} + \frac{m_k^2}{2\vec{p^2}}) = \frac{\Delta m_{jk}^2}{2E_\nu}, \tag{2.14}$$

where $E_\nu \approx |\vec{p}|$, neglecting the neutrino mass contribution, and $\Delta m_{jk}^2 = m_j^2 - m_k^2$. Neutrino experiments do not typically measure the neutrino propagation time, but rather the distance between the source and detector. Neutrinos travel close to the speed of light so substituting t with propagation distance L and setting $c = 1$, Equation 2.9 becomes:

$$P_{\nu_\alpha \to \nu_\beta} = |A_{\nu_\alpha \to \nu_\beta}|^2 = \sum_{j,k} U_{\alpha j}^* U_{\beta j} U_{\alpha k} U_{\beta k}^* exp(-i \frac{\Delta m_{jk}^2}{2E} L). \tag{2.15}$$

This shows that neutrinos can change flavour as they propagate through space, with an oscillation phase determined by the energy of the neutrino, the propagation length and the mass squared differences. The amplitude of oscillations is governed by the mixing matrix. The mixing parameters and mass squared differences are physical constants so in order to probe neutrino oscillations experiments must vary the neutrino energy or travel distance.

The antineutrino oscillation probability is derived in the same way except that the complex conjugate of the mixing matrix is used instead. If the mixing matrix is real ($\delta_{cp} = 0$) then the transition probabilities are the same for neutrinos and antineutrinos, otherwise they differ.

Two Flavour Approximation

Neutrino experiments are not always sensitive to three flavour neutrino mixing, in this case a two flavour model can be used. The two flavour model is simpler and has fewer parameters. In the two flavour case the mixing matrix U reduces

to a 2×2 unitary mixing matrix:

$$U = \begin{pmatrix} \cos\theta & \sin\theta \\ -\sin\theta & \cos\theta \end{pmatrix}, \tag{2.16}$$

where θ is the mixing angle. Since two flavours are considered there is only one mass squared difference $\Delta m^2 = m_2^2 - m_1^2$. Here the flavour states can be written as:

$$\begin{pmatrix} \nu_\alpha \\ \nu_\beta \end{pmatrix} = \begin{pmatrix} \cos\theta & \sin\theta \\ -\sin\theta & \cos\theta \end{pmatrix} \begin{pmatrix} \nu_1 \\ \nu_2 \end{pmatrix}. \tag{2.17}$$

In this case, Equation 2.15 becomes:

$$P_{\nu_\alpha \to \nu_\beta} = \sin^2(2\theta)\sin^2(\frac{\Delta m^2 L}{4E}), \tag{2.18}$$

when $\alpha \neq \beta$, and the survival probability becomes

$$P_{\nu_\alpha \to \nu_\alpha} = 1 - \sin^2(2\theta)\sin^2(\frac{\Delta m^2 L}{4E}). \tag{2.19}$$

In this discussion, and throughout this thesis, natural units $\hbar = c = 1$ are used. Numerically, for Δm^2 in eV^2, L in km and E in GeV, a factor of 1.267 is used in the oscillation frequency. We can see from Equation 2.19 that the oscillation maximum occurs when $\frac{\Delta m^2 L}{2E} = \pi$ so oscillation experiments can choose a baseline and neutrino energy range to be sensitive to different values of Δm^2. Figure 2.2 shows the two flavour neutrino survival probability as function of flight length.

2.2.3 Neutrino Oscillations in Matter

The previous section described neutrino oscillations in a vacuum, however when neutrinos propagate through matter the oscillation behaviour changes. L. Wolfenstein [160] proposed that neutrinos propagating in matter are subject to a potential due to coherent forward elastic scattering with electrons, protons and neutrons. The Feynman diagrams for charged current (CC) and neutral current (NC) scattering in matter are shown in Figures 2.3a and 2.3b. The NC and CC introduce new potentials V_{NC} and V_{CC} into the Hamiltonian respectively. Neutrino oscillations arise due to the phase difference between the

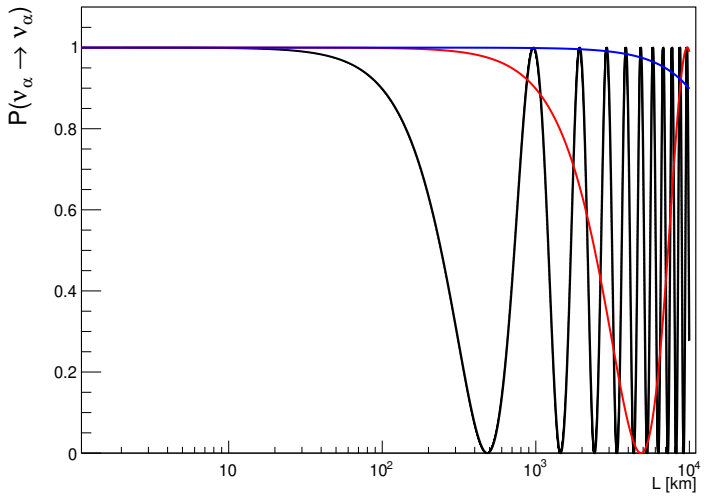

Figure 2.2 *Two flavour survival probability of ν_α as a function of propagation length. The black curve represents $E_\nu = 1$ GeV, the red curve is $E_\nu = 10$ GeV and the blue curve for $E_\nu = 100$ GeV. This is for maximal mixing $\theta = \pi/4$ and $\Delta m^2 = 2.56 \times 10^{-3}$ eV^2.*

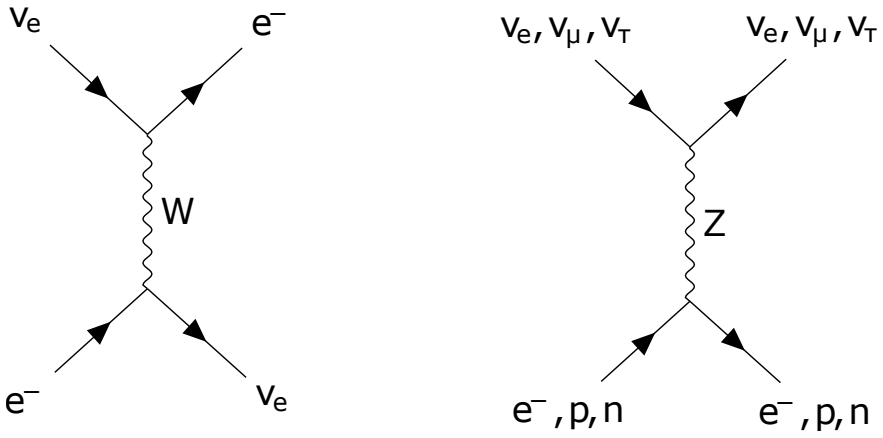

(a) *Charged current* **(b)** *Neutral current*

Figure 2.3 *Feynman diagrams of the elastic coherent forward scattering interactions that neutrinos undergo through propagation in a medium. The flow of time is left to right.*

mass eigenstates, in matter the phase difference can be affected by the total energy of the mass eigenstate.

Neutral current scattering is the same for all of the neutrino flavours, Section 2.2.4 describes the scenario where this may not be the case. The neutral current

interactions add the same phase to all neutrino flavours so the phase difference is unaffected, however electron neutrinos (and antineutrinos) undergo additional charged current interactions on the electrons in matter. These interactions add a flavour dependent phase to electron neutrinos. The additional potential V_{CC} is given by:

$$V_{CC} = \pm\sqrt{2}G_F N_e, \tag{2.20}$$

where G_F is the Fermi coupling constant and N_e is the number density of electrons in the matter, the plus (minus) sign is for neutrinos (antineutrinos). In 1985 Mikheev and Smirnov introduced resonant flavour transitions which can occur when neutrinos propagate through a medium of varying density. This resonant transition was used to explain the flavour transition of neutrinos leaving the sun and is known as the MSW effect [129].

In order to see the effect we can consider the simple case of two flavour oscillations where one of the neutrinos is an electron neutrino, a constant mass density is assumed.

The Hamiltonian in a vacuum in the mass basis is

$$H_{vac} = \begin{pmatrix} \frac{m_1^2}{2E} & 0 \\ 0 & \frac{m_2^2}{2E} \end{pmatrix} \tag{2.21}$$

and the mixing matrix is defined as

$$\begin{pmatrix} \nu_e \\ \nu_\beta \end{pmatrix} = \begin{pmatrix} \cos\theta & \sin\theta \\ -\sin\theta & \cos\theta \end{pmatrix} \begin{pmatrix} \nu_1 \\ \nu_2 \end{pmatrix}. \tag{2.22}$$

The Hamiltonian then is transformed to the flavour basis using the mixing matrix such that the vacuum Hamiltonian becomes

$$H_{vac} \rightarrow U H_{vac} U^\dagger \tag{2.23}$$

and the Schrödinger equation in the flavour basis becomes

$$i\frac{d}{dt}=\begin{pmatrix}\nu_e\\ \nu_\beta\end{pmatrix}=UH_{vac}U^\dagger\begin{pmatrix}\nu_e\\ \nu_\beta\end{pmatrix}=\frac{\Delta m^2}{4E}\begin{pmatrix}-\cos 2\theta & \sin 2\theta\\ \sin 2\theta & \cos 2\theta\end{pmatrix}\begin{pmatrix}\nu_e\\ \nu_\beta\end{pmatrix}. \tag{2.24}$$

Following the arguments from the previous section, the transition probability would be:

$$P_{(\nu_e\to\nu_\beta)}=\sin^2 2\theta\sin^2(\frac{\Delta m^2 L}{4E}) \tag{2.25}$$

Now we add the potential from the matter, affecting only ν_e:

$$H_{mat}=\begin{pmatrix}V_{CC} & 0\\ 0 & 0\end{pmatrix} \tag{2.26}$$

When adding this potential we can shift the matrix by a multiple of the identity and the Schrödinger becomes

$$i\frac{d}{dt}=\begin{pmatrix}\nu_e\\ \nu_\beta\end{pmatrix}=[UH_{vac}U^\dagger+H_{mat}]\begin{pmatrix}\nu_e\\ \nu_\beta\end{pmatrix}=\frac{\Delta m^2}{4E}\begin{pmatrix}-\cos 2\theta+A & \sin 2\theta\\ \sin 2\theta & \cos 2\theta-A\end{pmatrix}\begin{pmatrix}\nu_e\\ \nu_\beta\end{pmatrix}, \tag{2.27}$$

where

$$A\equiv\frac{2EV_{CC}}{\Delta m^2}. \tag{2.28}$$

It is convenient to write Equation 2.27 in this form as the traceless matrix can be easily diagonalised to get the effective mixing angle θ_m and mass splitting Δm^2_m. The effective parameters are

$$\sin 2\theta_m\equiv\frac{\sin 2\theta}{\sin^2 2\theta+(\cos 2\theta-A)^2} \tag{2.29}$$

and

$$\Delta m^2_m\equiv\Delta m^2\sqrt{\sin^2 2\theta+(\cos 2\theta-A)^2}. \tag{2.30}$$

Equation 2.24 then becomes

$$i\frac{d}{dt} = \begin{pmatrix} \nu_e \\ \nu_\beta \end{pmatrix} = \frac{\Delta m^2_m}{2E} \begin{pmatrix} -\cos 2\theta_m & \sin 2\theta_m \\ \sin 2\theta_m & \cos 2\theta_m \end{pmatrix} \begin{pmatrix} \nu_e \\ \nu_\beta \end{pmatrix}. \tag{2.31}$$

It can be seen that in the case of a vanishing matter potential the effective parameters reduce to their vacuum values. In the case when $A = \cos 2\theta$ the effective mixing angle is maximal ($\pi/4$) and the effective mass squared splitting is minimised, this condition is called the MSW resonance condition.

It should also be noted that while vacuum neutrino oscillations are not sensitive to the sign of the mass squared splitting Δm^2, Equation 2.30 shows that the effective mass splitting in matter does have a term $(\cos 2\theta - A)^2$ which is dependent on the sign of the mass splitting. For this reason matter effects can be used to resolve the sign of the mass splitting.

2.2.4 Non-Standard Neutrino Interactions

Non-standard neutrino interactions (NSI) were first considered by Wolfenstein [160, 161] and are now a natural part of most neutrino mass models [130, 137]. In order to study NSIs in a model independent way, phenomenologically they can be described with an effective four fermion Lagrangian

$$\mathcal{L}_{NSI} = -2\sqrt{2}G_F\varepsilon^{ff'C}_{\alpha\beta}(\overline{\nu}_\alpha\gamma^\mu P_L\nu_\beta)(\overline{f}\gamma_\mu P_C f'), \tag{2.32}$$

where G_F is the fermi constant, $\varepsilon^{ff'C}_{\alpha\beta}$ are the NSI strength parameters, $\alpha, \beta = e, \mu, \tau$, P is the chiral projector and $C = L, R$. Neutrino NSIs can be CC-like or NC-like, if $f \neq f'$ in Equation 2.32 then the interaction is CC-like, whereas if $f = f'$ then the interaction is NC-like and the NSI parameters are then defined as $\varepsilon^{fC}_{\alpha\beta} \equiv \varepsilon^{ffC}_{\alpha\beta}$. Figure 2.4 shows a diagram of an NC-like NSI interaction.

Charged current NSIs affect the production and detection of neutrinos whereas neutral current NSIs affect the propagation of neutrinos through matter. The CC NSI parameters are constrained by at least an order of magnitude better than the NC parameters and will not be discussed further in this thesis.

To describe neutrino propagation with NSIs the matter potential in Section 2.2.3

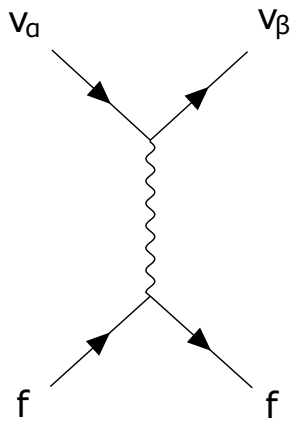

Figure 2.4 *A pseudo-Feynman diagram of a neutral-current non-standard neutrino interaction. α is the initial neutrino flavour, β is the final neutrino flavour and f is a first generation fermion (e, u or d). The flow of time is left to right.*

is modified to:

$$\mathcal{A} \equiv \sqrt{2} G_F N_e \begin{pmatrix} 1+\varepsilon_{ee} & \varepsilon_{e\mu} & \varepsilon_{e\tau} \\ \varepsilon_{\mu e} & \varepsilon_{\mu\mu} & \varepsilon_{\mu\tau} \\ \varepsilon_{\tau e} & \varepsilon_{\tau\mu} & \varepsilon_{\tau\tau} \end{pmatrix}. \tag{2.33}$$

As neutrinos propagate through the Earth we cannot distinguish between NSI interactions on left and right handed fermions so the effective NSI parameters are defined as $\varepsilon^f_{\alpha\beta} = \varepsilon^{fL}_{\alpha\beta} + \varepsilon^{fR}_{\alpha\beta}$. As the Earth contains electrons, up and down quarks, the effective NSI parameters in Equation 2.33 are defined as

$$\varepsilon_{\alpha\beta} \equiv \sum_{f=e,u,d} \frac{N_f}{N_e} \varepsilon^f_{\alpha\beta}, \tag{2.34}$$

where N_f is the number density of the fermion f.

Including the NSIs, the effective Hamiltonian for neutrino propagation through matter becomes:

$$H_{eff} = \frac{1}{2E} U \begin{pmatrix} 0 & 0 & 0 \\ 0 & \Delta m^2_{21} & 0 \\ 0 & 0 & \Delta m^2_{31} \end{pmatrix} U^\dagger \pm \sqrt{2} G_F N_e \begin{pmatrix} 1+\varepsilon_{ee} & \varepsilon_{e\mu} & \varepsilon_{e\tau} \\ \varepsilon_{\mu e} & \varepsilon_{\mu\mu} & \varepsilon_{\mu\tau} \\ \varepsilon_{\tau e} & \varepsilon_{\tau\mu} & \varepsilon_{\tau\tau} \end{pmatrix}, \tag{2.35}$$

where the first term is the vacuum component and the second term is the matter component. The 1 in the matter matrix corresponds to the standard matter effect on electron neutrinos and the plus (minus) sign corresponds to neutrinos (antineutrinos).

If the diagonal components of the NSI matrix ($\varepsilon_{\alpha\alpha}$) are different from each other, then the NC scattering amplitude is different for the different neutrino flavours, this is known as lepton non-universality. If the off diagonal elements ($\varepsilon_{\alpha\beta}$ where $\alpha \neq \beta$) are non-zero then we get flavour-changing neutral currents (FCNC). In general the off-diagonal elements are complex with $\varepsilon_{\alpha\beta} = \varepsilon^*_{\beta\alpha}$ but for the work in this thesis the complex phase was not considered. The diagonal parameters can cause a matter induced mass squared difference which could create additional resonances even if neutrinos had zero mass, while the off-diagonal parameters play a role similar to the mixing angles where even in the absence of vacuum mixing there could be matter induced mixing. Lastly the complex phases of the off-diagonal NSI elements could introduce a new source of CP violation. These cause some non-trivial degeneracies in neutrino oscillation parameter measurements.

2.3 Experimental Status

Many experiments have observed neutrino oscillations and their complimentary measurements give us a clearer picture of the overall mechanism. This section summarises the latest values of the neutrino oscillation parameters.

2.3.1 Standard Oscillations

The parameters θ_{23} and Δm^2_{32} are referred to as the atmospheric mixing parameters, which are measured by looking for ν_μ disappearance (by oscillation to ν_τ). These parameters are measured by atmospheric neutrino experiments such as Super-K [18] and IceCube [5] as well as accelerator neutrino experiments such as T2K [90], NOvA [23] and MINOS [24]. Figure 2.5 shows contours for the 68% and 90% confidence region of these parameters. The mixing angle has been measured to be near maximal and one of the remaining questions is whether the mixing angle is less than or greater than $\pi/4$. Another open question is the sign of the mass splitting Δm^2_{32}. The sign of the mass-squared splitting is resolved by matter effects (see Section 2.2.3) which are a sub-leading effect in

atmospheric neutrino oscillations. In principle, atmospheric neutrinos travelling upwards traverse the diameter of the Earth and can be used to resolve the mass hierarchy. Super-K's atmospheric neutrino data shows a preference for the normal hierarchy ($\nu_3 > \nu_2$) [113].

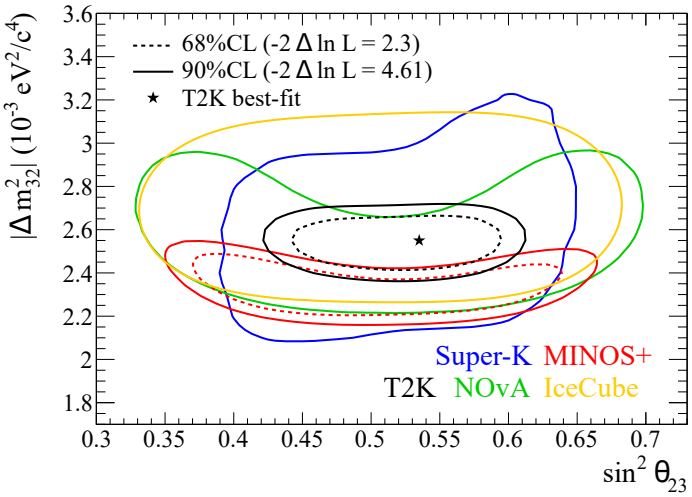

Figure 2.5 *The 68% and 90% confidence regions for the* $\sin^2\theta_{23}$-$|\Delta m^2_{32}|$ *plane, assuming normal mass hierarchy. Contours from NOvA [26], MINOS [24], SK [158] and IceCube [3] are included. Taken from [16].*

The parameters θ_{12} and Δm^2_{21} are measured by solar and reactor neutrino experiments. In 2002 the SNO solar neutrino experiment measured the flux of solar neutrinos via NC interactions and found a non e-like component to the neutrino flux [31] due to oscillations to ν_μ and ν_τ. Since then, measurements from Super-K [15] and KamLAND [20] as well as global analyses [10] have greatly constrained these parameters. The electron density in the sun is very large so unlike with atmospheric neutrinos, solar neutrinos are subject to large matter effects and the sign of Δm^2_{21} is known.

Figure 2.6 shows the allowed region for the $\nu_1 - \nu_2$ neutrino oscillation parameter space. As solar neutrinos propagate through the earth, a regeneration of ν_e is expected due to the matter effect. In 2014 Super-K measured a day-night asymmetry in solar neutrino events [148], this affects the solar experiment's measured mass splitting, preferring a lower value. The mass splitting measured in this way does not agree well with KamLAND.

The mixing angle θ_{13} was the last to be measured. While accelerator ν_e appearance can give limits on this parameter, the best measurements come from reactor $\overline{\nu}_e$ disappearance measurements. In 2003 the CHOOZ reactor experiment

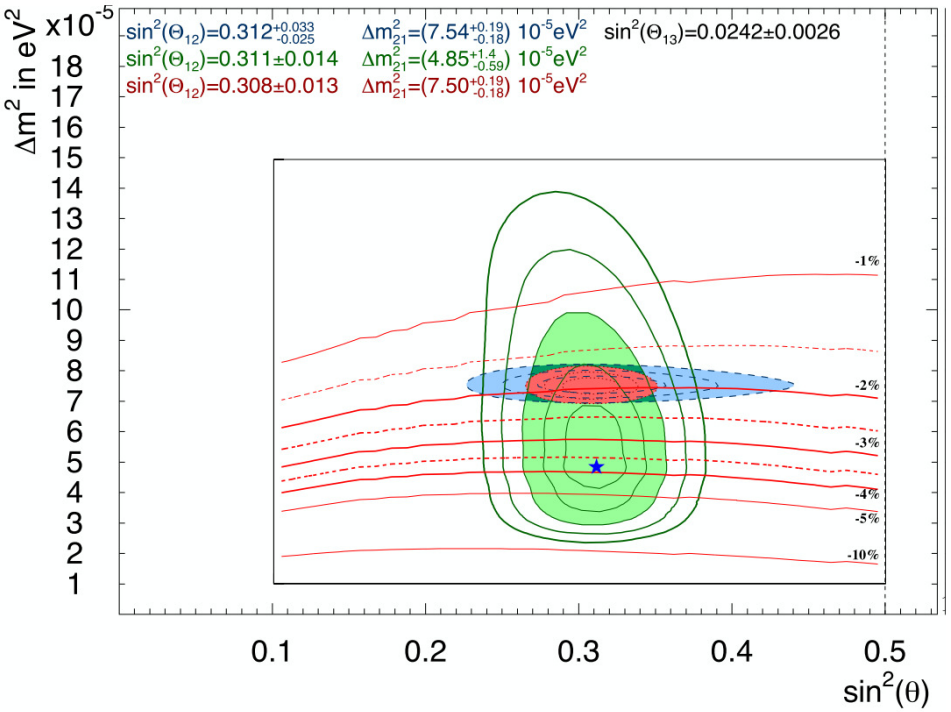

Figure 2.6 *A plot of the allowed $\nu_1 - \nu_2$ neutrino oscillation parameter region. Solar experiments are shown in green with contours showing 1-5σ, KamLAND (reactor) is shown in blue and the red shows the combined analysis results. The filled regions indicate the 3σ region. The overlaid red lines show the contours for day-night asymmetry. Taken from [17].*

found no evidence of $\overline{\nu}_e$ oscillation and set an upper limit $\sin^2\theta_{13} < 0.15$ at 90% CL [42]. A decade later, short baseline reactor experiments Daya Bay [41], Double CHOOZ [21] and RENO [32] independently reported values of $\sin^2 2\theta_{13} \approx 0.1$ and T2K observed electron neutrino appearance in their muon beam [14], giving a best fit value of $\sin^2 2\theta_{13} \approx 0.14$.

The remaining unknowns in the standard neutrino oscillation parameters, in particular δ_{CP}, will be tackled by the Hyper-K experiment and are discussed further in Chapter 9.

2.3.2 NSI Parameters

Solar and atmospheric neutrino oscillations are described very well by the standard oscillation framework so the NSI are at most a sub leading effect. It is important to note that NSI parameters are usually measured by setting all NSI to zero except for the parameters of interest. NSI parameters can be highly

Table 2.1 *Three flavour oscillation parameters from a 2019 global analysis [71]. For normal ordering $\Delta m^2_{3l} \equiv \Delta m^2_{31} > 0$ and for inverted ordering $\Delta m^2_{3l} \equiv \Delta m^2_{32} < 0$. The best fit point was with normal hierarchy.*

Parameter	Best Fit $\pm 1\sigma$	
	Normal Hierarchy	Inverted Hierarchy
$\sin^2\theta_{12}$	$0.310^{+0.013}_{-0.012}$	$0.310^{+0.013}_{-0.012}$
$\sin^2\theta_{23}$	$0.582^{+0.015}_{-0.019}$	$0.582^{+0.015}_{-0.019}$
$\sin^2\theta_{13}$	$0.02240^{+0.00065}_{-0.00066}$	$0.02263^{+0.00065}_{-0.00066}$
$\frac{\Delta m^2_{21}}{10^{-5}eV^2}$	$7.39^{+0.21}_{-0.20}$	$7.39^{+0.21}_{-0.20}$
$\frac{\Delta m^2_{3l}}{10^{-3}eV^2}$	$+2.525^{+0.033}_{-0.031}$	$-2.512^{+0.034}_{-0.031}$

correlated so this must be taken into consideration when interpreting results.

The solar neutrino survival probability is expected to increase with decreasing energy, this is because of the transition from matter dominated oscillations at higher energies to vacuum oscillations at lower energies. Figure 2.7 shows the expected survival probabilities for various different scenarios. While both sides of the spectrum have been measured, the spectrum up-turn has yet to be measured. Various analyses have found a slightly better agreement with small NSI than the standard oscillation scenario [77, 142]. This is due to the lack of observed spectrum upturn in solar neutrino survival probability [131] as well as the tension in the mass splitting, which is eased with the addition of NSI.

When looking at NSI in solar neutrinos it is common to reduce the Hamiltonian to an effective 2×2 matrix. This is done by rotating to a specific basis and using the one mass scale dominance approximation $\Delta m^2_{31} \to \infty$ resulting in a system where the third eigenstate decouples from the system [33, 123, 130].

The ν_e survival probability then becomes:

$$P(\nu_e \to \nu_e) = c^4_{13} P_{eff} + s^4_{13}, \tag{2.36}$$

where $s_{ij} = \sin(\theta_{ij})$, $c_{ij} = \cos(\theta_{ij})$. P_{eff} can be calculated using the effective 2×2

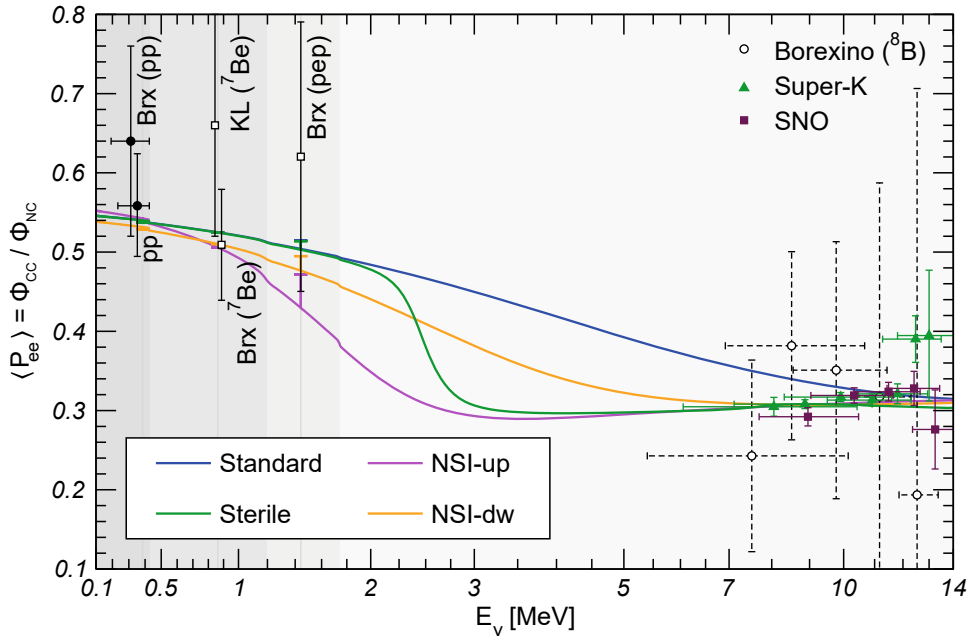

Figure 2.7 *The expected survival probability of solar neutrinos for various physics scenarios, including data from solar neutrino experiments. All scenarios use* $sin^2\theta_{13} = 0.022$. *The standard oscillations use* $(\sin^2\theta_{12}, \Delta m^2_{21}) = (0.31, 7.5 \times 10^{-5} eV^2)$. *The single additional sterile neutrino uses* $(\sin^2\theta_{12}, \Delta m^2_{21}, \sin^2 2\alpha, \Delta m^2_{01}) = (0.31, 7.5 \times 10^{-5} eV^2, 0.005, 1.2 \times 10^{-5} eV^2)$. *NSI on up quarks scenario uses* $(\sin^2\theta_{12}, \Delta m^2_{21}, \varepsilon^u_D, \varepsilon^u_N) = (0.30, 7.25 \times 10^{-5} eV^2, -0.22, -0.30)$ *and the NSI on down quarks scenario uses* $(\sin^2\theta_{12}, \Delta m^2_{21}, \varepsilon^d_D, \varepsilon^d_N) = (0.32, 7.35 \times 10^{-5} eV^2, -0.12, -0.16)$. *Taken from [127].*

Hamiltonian:

$$H_{eff} = \frac{\Delta m^2_{21}}{4E} \begin{pmatrix} -\cos 2\theta_{12} & sin2\theta_{12} \\ sin2\theta_{12} & \cos 2\theta_{12} \end{pmatrix} + \begin{pmatrix} \cos^2\theta_{13} A & 0 \\ 0 & 0 \end{pmatrix} + A \sum_{f=e,u,d} \frac{N_f}{N_e} \begin{pmatrix} -\varepsilon^f_D & \varepsilon^f_N \\ \varepsilon^{f*}_N & \varepsilon^f_D \end{pmatrix}, \tag{2.37}$$

where $A = \sqrt{2} G_F N_e$ and the diagonal, ε_D and off-diagonal, ε_N, parameters are related to the NSI parameters, $\varepsilon_{\alpha\beta}$ by [130]:

$$\begin{aligned} \varepsilon_D = c_{13} s_{13} \Re[e^{i\delta_{CP}} (s_{23}\varepsilon_{e\mu} + c_{23}\varepsilon_{e\tau})] - (1 + s^2_{13}) c_{23} s_{23} \Re(\varepsilon_{\mu\tau}) \\ - \frac{c^2_{13}}{2}(\varepsilon_{ee} - \varepsilon_{\mu\mu}) + \frac{s^2_{23} - s^2_{13} c^2_{23}}{2}(\varepsilon_{\tau\tau} - \varepsilon_{\mu\mu}) \end{aligned} \tag{2.38}$$

and

$$\varepsilon_N = c_{13}(c_{23}\varepsilon_{e\mu} - s_{23}\varepsilon_{e\tau}) + s_{13}e^{-i\delta_{CP}}[s_{21}^2\varepsilon_{\mu\tau} - c_{23}^2\varepsilon_{\mu\tau}^* + c_{23}s_{23}(\varepsilon_{\tau\tau} - \varepsilon_{\mu\mu})]. \quad (2.39)$$

An analysis of solar neutrino and KamLAND experiments [127] obtained found the best fit points on the diagonal and off-diagonal NSI parameters $(\varepsilon_D^u, \varepsilon_N^u) = (-0.22, -0.3)$ and $(\varepsilon_D^d, \varepsilon_N^d) = (-0.12, -0.16)$ for up quarks and down quarks respectively. A global oscillation analysis [88] found that large negative values of $\varepsilon_{ee} \approx$ -4 are compatible with the oscillation data.

The standard oscillation framework describes the ν_μ disappearance of atmospheric neutrinos quite well, and large NSI in the $\nu_\mu - \nu_\tau$ sector would be incompatible with high energy atmospheric neutrino data. For this reason, atmospheric neutrinos can provide tight constraints on the $\mu - \tau$ parameters. In 2011 a Super-K [133] two flavour analysis resulted in the following constraints at the 90% C.L.

$$|\varepsilon_{\mu\tau}^{dV}| < 0.011\,, \qquad |\varepsilon_{\mu\mu}^{dV} - \varepsilon_{\tau\tau}^{dV}| < 0.049. \quad (2.40)$$

Recently, IceCube carried out a three flavour analysis using their most recent DeepCore data and obtained the constraint [6]:

$$-0.0067 < \varepsilon_{\mu\tau}^{dV} < 0.0081 \quad (2.41)$$

at 90% C.L.

A generalised NSI potential involves different parameters for different charged fermions in matter (e,u and d). The Earth has a reasonably consistent matter profile with the neutron to electron ratio $Y_n = 1.012$ in the mantle and 1.137 in the core and an average of 1.051 all over the Earth. Earth's matter is neutral which means that the proton to electron ratio $Y_p = 1$. For this reason atmospheric neutrinos which traverse the Earth can be parameterised with a single $\varepsilon_{\alpha\beta}$ as seen in Equation 2.34. In the sun, the chemical composition varies significantly and Y_n varies from 1/2 in the centre to 1/6 at border of solar core [130] so it is not possible to have a common parameter accounting for all of the different fermions so only one fermion is considered at a time.

Bounds from accelerator neutrinos come from $\nu_\mu \to \nu_\mu$ and $\bar{\nu}_\mu \to \bar{\nu}_\mu$ channels. To first approximation $\varepsilon_{\mu\tau}$, $\varepsilon_{\mu\mu}$ and $\varepsilon_{\tau\tau}$ are the relevant NSI parameters. The MINOS experiment, with a long baseline of 730 km obtained the bound [25] at

the 90% C.L.:

$$-0.067 < \varepsilon_{\mu\tau}^{dV} < 0.023. \tag{2.42}$$

In addition to reactor and accelerator neutrino experiments, measurements of NSI parameters are made by various neutrino scattering experiments in which neutrino interactions with matter could be significantly affected. Bounds for NSI parameters are usually for specific fermions and the handedness of the fermions, so comparison of various bounds involve some assumptions. For example, although neutrino oscillation experiments measure an overall NSI strength, this number is often converted to assume all NSI only occurs on down quarks for the purpose of comparison. For a recent review of neutrino NSI status, the reader is referred to [72].

Chapter 3

The Super-Kamiokande Detector

Super-Kamiokande (SK) is a 50 kton underground water Cherenkov detector located in Kamioka mine under Mt Ikeno, Gifu Prefecture, Japan [82]. The experiment began taking data in April, 1996 with four distinct running periods SK-I (1996-2001), SK-II (2003-2005), SK-III (2006-2008) and SK-IV (2008-2018). The location within Kamioka mine results in an overburden of 1 km which reduces the backgrounds from cosmic ray interactions in the atmosphere by five orders of magnitude. A sketch of the detector site is shown in Figure 3.1.

The physics program of SK consists of searches for nucleon decay and dark matter, as well as observation of neutrinos from different sources: the sun, cosmic ray interactions in the atmosphere, supernovae and accelerator neutrinos produced at the J-PARC [108] facility in Tokai, Japan [9].

3.1 Cherenkov Radiation

Cherenkov radiation [56] is emitted when a relativistic charged particle passes through an optically transparent medium with a velocity greater than the local phase velocity of light. The particle polarises the medium along its trajectory forming wavelets which are in phase with one another (see Figure 3.2). As the particle passes, the displaced electrons return to their normal positions emitting coherent radiation [112]. The emission is cylindrically symmetrical along the particle track, resulting in a cone of light.

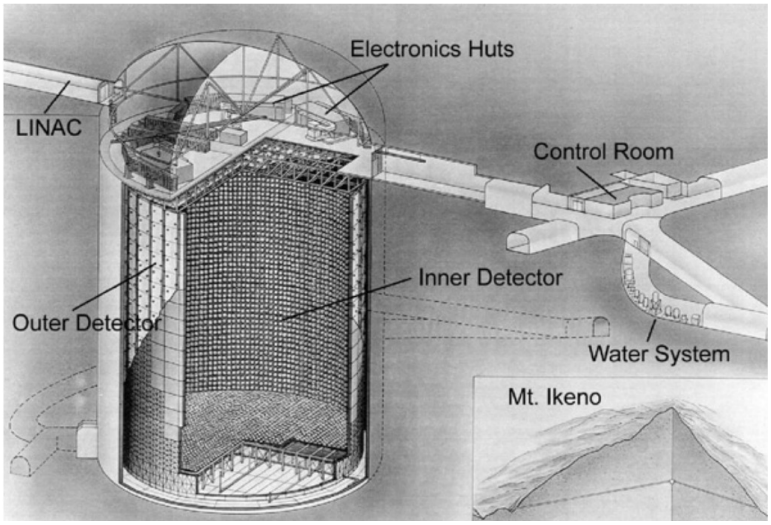

Figure 3.1 *A sketch of the Super-Kamiokande detector site under Mt Ikeno. Taken from [82].*

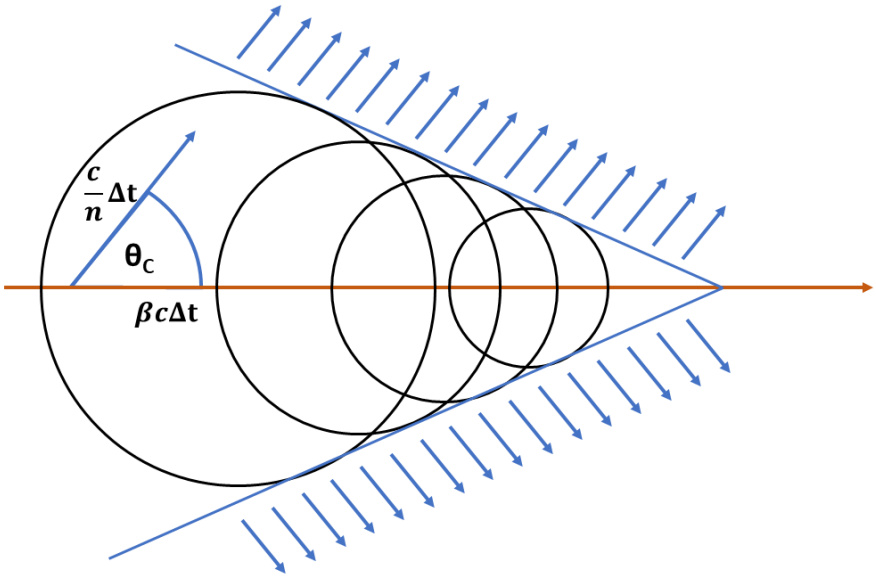

Figure 3.2 *A diagram showing Cherenkov light production by a charged particle.*

The angle of emission relative to the particle track is given by

$$\cos\theta_c = \frac{1}{\beta n}, \tag{3.1}$$

where θ_c is the Cherenkov angle, n is the refractive index of the medium and $\beta = v/c$ is the speed of the charged particle relative to the speed of light in vacuum. For water, $n = 1.33$ giving $\theta_c = 41^\circ$ for ultra-relativistic particles. Table 3.1 shows the minimum energy required by different particles in order to

emit Cherenkov radiation, when $\beta = 1/n$.

Table 3.1 *The Cherenkov threshold energy in water, for common charged particles.*

Particle	Cherenkov Energy Threshold (MeV)
electron	0.77
muon	160
pion	211
proton	1420

When the Cherenkov cone is projected onto the surface of the detector, the light of the cone appears as a ring. Electrons undergo electromagnetic showering, via Bremsstrahlung radiation and pair production, giving a fuzzy ring. The thickness of the ring depends on the length of the track where the charged particle was able to produce Cherenkov radiation. If a particle emits Cherenkov radiation while leaving the detector, then the ring is completely filled in. The energy of electron-like events is reconstructed by counting the overall number of photo-electrons. Muons generally do not cause electromagnetic showers and so they produce sharper rings. Such events are referred to as muon-like. Figure 3.3 shows example event displays for e-like and μ-like events.

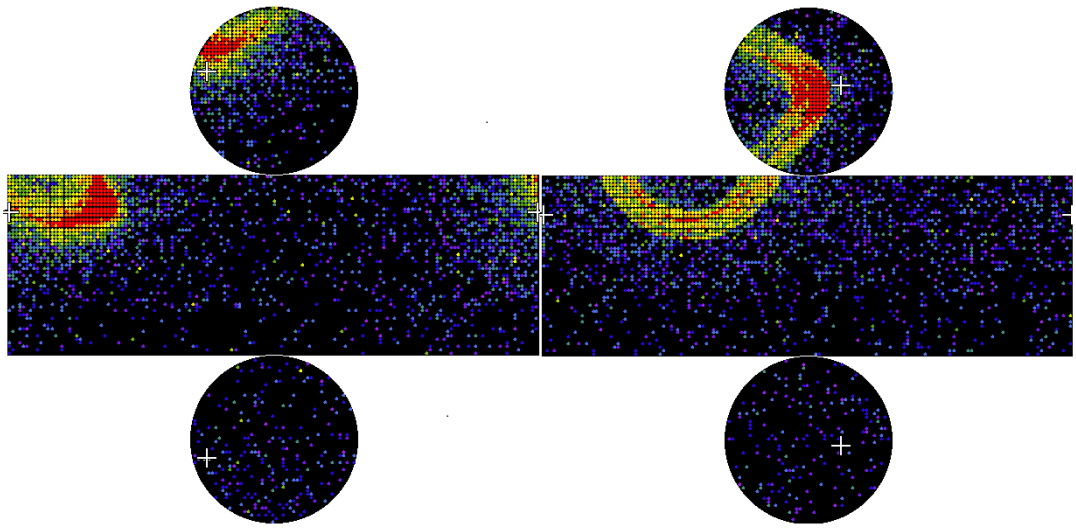

(a) *e-like event* **(b)** *μ-like event*

Figure 3.3 *A typical event display for an electron-like event [left] and muon-like event [right]. The blue dots represent a low number of photons and the red dots represent a larger number of photons.*

The number of Cherenkov photons per unit wavelength (λ) per unit path length

is expressed by

$$\frac{d^2N}{d\lambda dx} = \frac{2\pi z^2\alpha}{\lambda^2}(1 - \frac{1}{\beta^2 n^2(\lambda)}) = \frac{2\pi z^2\alpha}{\lambda^2}\sin^2\theta_c \tag{3.2}$$

where z is the particle's charge in units of the electron charge and α is the fine structure constant. It can be seen from Equation 3.2 that Cherenkov radiation is typically produced at blue/UV wavelengths. Though the $1/\lambda^2$ dependence continues to shorter wavelengths the emitted light is absorbed by the water. For electrons and muons, roughly 340 photons are emitted per centimetre in a wavelength range of 300-600 nm.

3.2 Detector Design

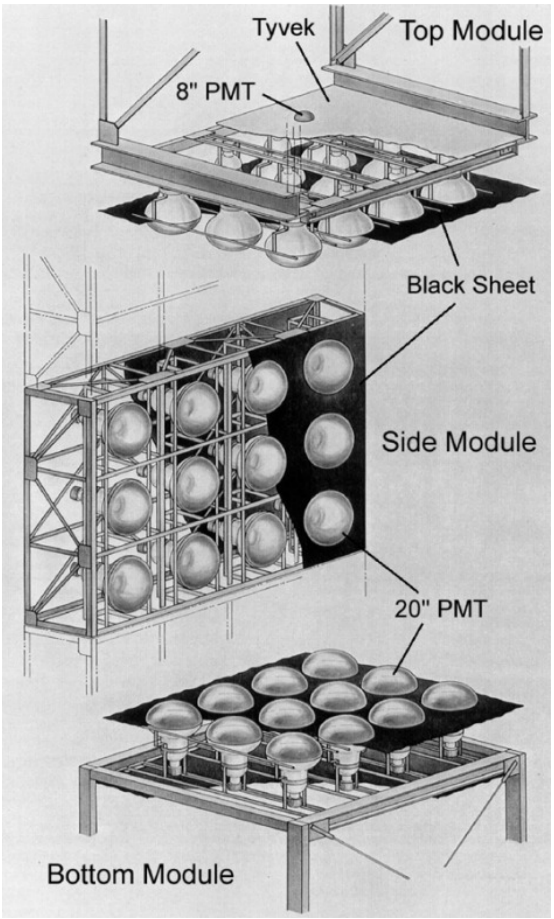

Figure 3.4 *A schematic view of the Super-Kamiokande support structure for the inner detector. Taken from [82].*

The SK detector [82] consists of a large stainless-steel tank with a height of 41.4 m

and a diameter of 39.3 m. SK is filled with 50 ktons of ultra pure water and is split up into two optically separated regions referred to as the inner detector (ID) and the outer detector (OD). A 36.2 m tall, 33.8 m diameter cylindrical support structure splits the tank into ID and OD volumes. Both sides of the support structure hold photomultiplier tubes (PMTs) and are lined with a lightproof material to ensure optical separation between the two regions.

The inside of the structure, the ID, contains 32 ktons of water and this serves as the target volume for neutrino interactions. Roughly 40% of the ID's surface area is covered by inward-facing photocathodes each with a diameter of 50 cm, in the form of 11,129 Hamamatsu R3600 PMTs [95]. The remaining surface area is covered with opaque black polyethylene terephthalate sheets to stop light getting through. Figure 3.5 shows a picture of the ID.

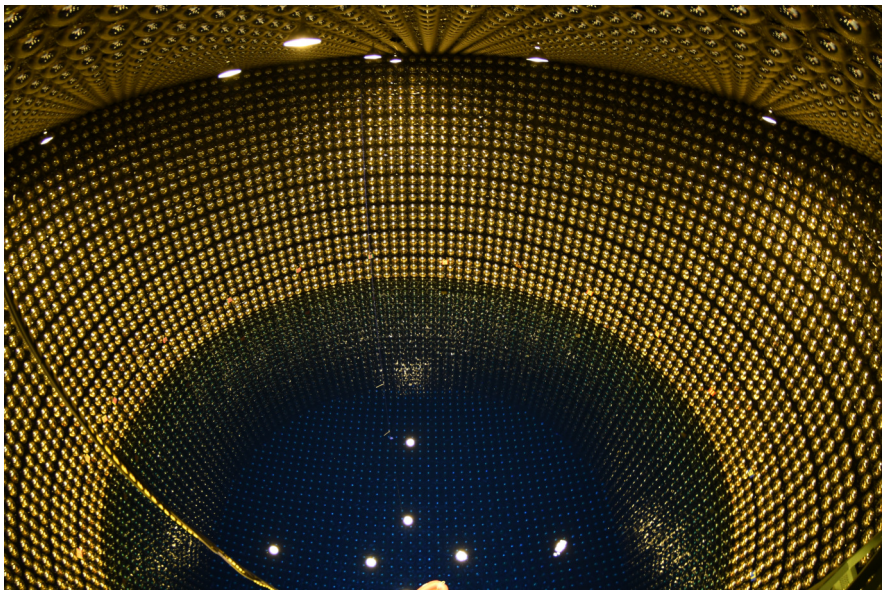

Figure 3.5 *A picture of the Super-K inner detector taken in July 2018. The detector was being drained and refurbished. Photo taken by Nakahata-san.*

The outer region, the OD, serves as a shield for γ-rays and neutrons from the surrounding rock as well as a veto for incoming charged particles. The OD side of the support structure is instrumented with 1,885 outward-facing 20 cm Hamamatsu R1408 PMTs [94]. Each PMT was preassembled with a 60 cm x 60 cm x 1.3 cm wavelength shifting plate (WLS) [50]. The WLS plates are square acrylic plates doped with 50 mg/L of bis-MSB. Each plate has a machined hole in the centre for the PMT to be mounted and the edge of the hole is angled such that a good optical coupling can be achieved by physical contact. The WLS plates, together with the PMTs, were originally used in the IMB experiment [50, 58].

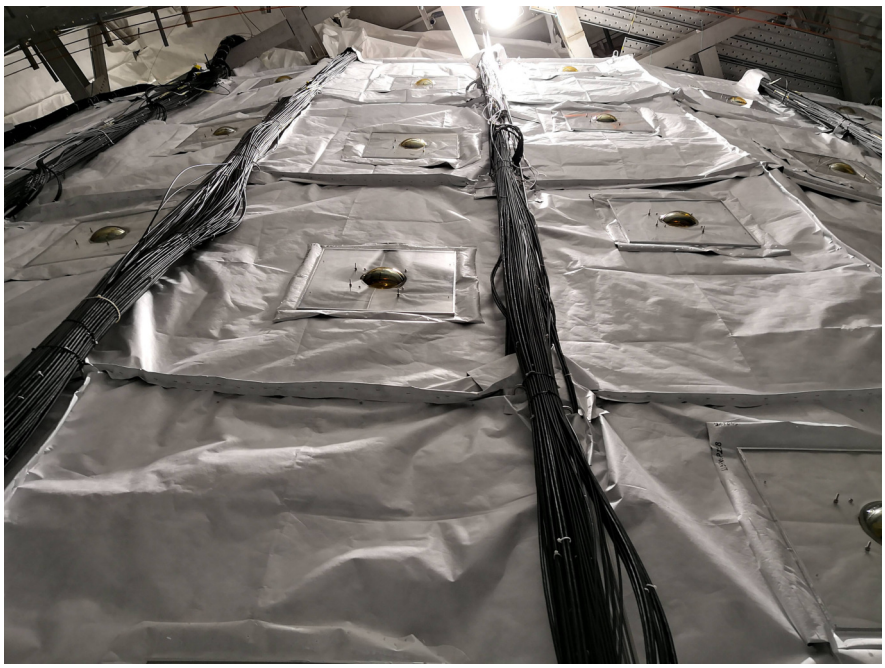

Figure 3.6 *A picture of the Super-K outer detector taken in July 2018. The detector was being drained and refurbished.*

The OD (see Figure 3.6) was designed to be used as a veto and the design was chosen such that light collection is maximised. The time resolution requirements of the OD are relatively modest since only the total number of hits in a window of $\mathcal{O}(100)$ ns needs to be known to act as a veto. The inner surface of the OD is lined with a custom material made up of Tyvek® [68] which faces the OD volume, a 25 μm thick central layer of low-density polyethylene (LDPE) and a 25 μm thick layer of black LDPE. This custom lining material reflects light coming from the OD volume side while absorbing any light coming from the dead space between the ID and OD. The outer surface of the OD volume is lined with Tyvek® 1073B. This material has a measured reflectivity value around 80% for λ =340 nm rising to about 90% above 400 nm [82]. The reflective material on either side of the OD allows Cherenkov light to reflect multiple times enhancing the light collection and the overall detection efficiency.

In 2006 new sheets of Tyvek® were added in order to optically separate the end caps of the OD and the barrel region of the OD. The OD segmentation, shown in Figure 3.7, greatly increases the ability to recognize a partially contained event instead of mistaking it for an incoming charged particle.

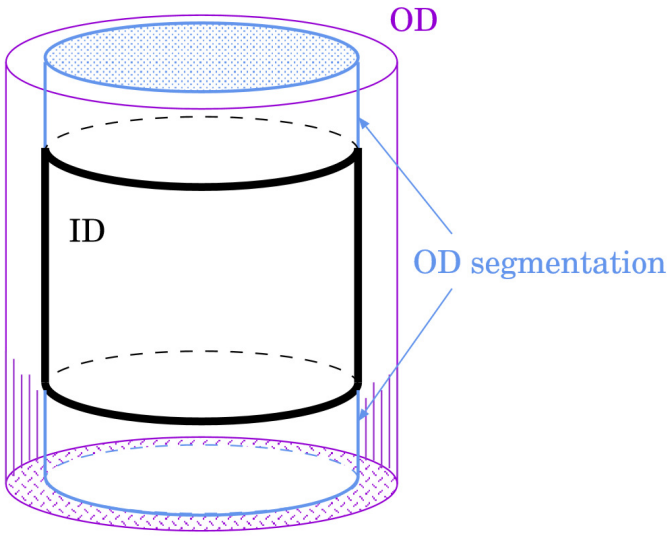

Figure 3.7 *Schematic diagram showing the optical separation of the end caps and barrel regions of the OD.*

3.3 Photomultiplier Tubes

The ID PMTs were designed by Hamamatsu in collaboration with KamiokaNDE collaborators and further improved for use in SK [154]. The R3600 PMT consists of a bialkali (Sb-K-Cs) photocathode, chosen due to its spectral sensitivity to blue light and its low thermionic emission. The PMT is sensitive to the predominant wavelengths in the Cherenkov spectrum and has a peak quantum efficiency of 22 % at 390 nm. Figure 3.9 shows the Cherenkov spectrum in water, the sharp cut-off is due to the reduced transparency of water below 300 nm.

The ID PMTs have a uniform gain of 10^7 at a high voltage ranging from 1500 V to 2000 V; Table 3.2 lists the main characteristics of the ID PMTs. The large ID PMTs are sensitive to the earth's magnetic field as it affects the propagation of the electrons within the tube. Hence, SK has 26 Helmholtz coils surrounding the detector to counteract the earth's magnetic field, reducing the typical value from 450 mG to 50 mG.

Intrinsically the OD PMTs have a worse timing resolution (13 ns). Factoring in the fluorescence decay constant (4 ns) and the propagation time in the plate, the effective time resolution is around 15 ns.

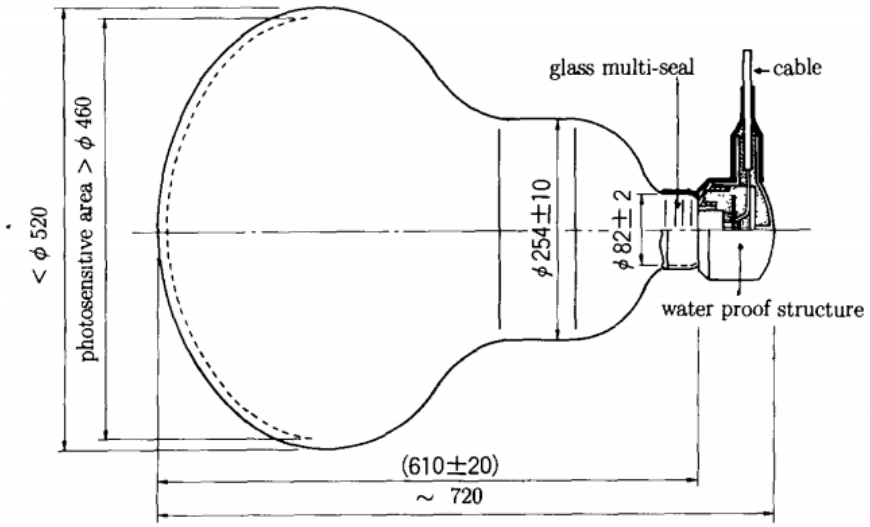

Figure 3.8 *A schematic diagram of the 50 cm SK ID PMT, taken from [82]. All measurements are in mm.*

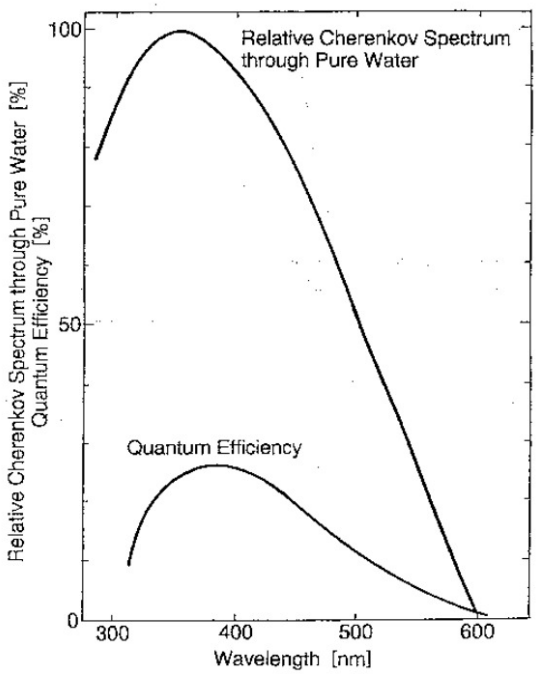

Figure 3.9 *Plot showing the relative Cherenkov spectrum through pure water in addition to the quantum efficiency of the R3600 PMT. Taken from [136].*

3.4 Electronics and Data Acquisition

From 1996-2009 the ID PMT signals were processed by custom electronics modules called analogue timing modules (ATM) which contained charge-to-

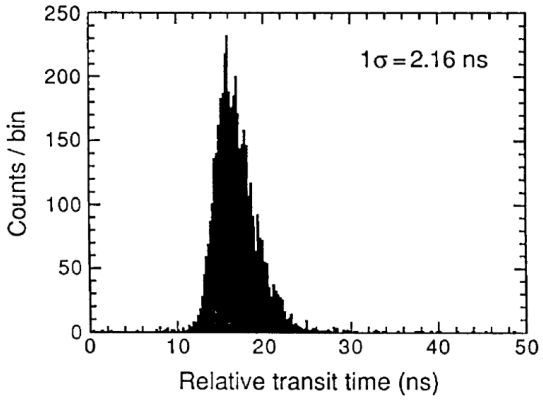

Figure 3.10 *Relative transit time distribution for the SK ID PMT tested with 410 nm light source at single photon level. Taken from [82].*

Table 3.2 *SK inner detector PMT specification [73].*

Shape	Hemispherical
Photocathode diameter	50 cm
Window material	Bialkali (Sb-K-Cs)
Quantum efficiency	22% at λ=390 nm
Dynode structure	11 stage Venetian blind
Gain	10^7 at $\sim$2000 V
Dark current	200 nA at 10^7 gain
Dark pulse rate	3 kHz at 10^7 gain
Transit time	90 ns at 10^7 gain
Transit time spread	2.2 ns (1σ) at single photoelectron level
Weight	13 kg
Pressure tolerance	6 kg/cm^2

analogue (QAC) and time-to-analogue (TAC) converters [107]. In August 2008, the electronics and data acquisition (DAQ) systems were upgraded. The threshold for a PMT hit was set to 0.25 photoelectrons. The dynamic range was from 0$\sim$450 pC (0.2 pC resolution) for charge and -300$\sim$1000 ns (0.4 ns resolution) for time. The OD PMTs were connected to a system consisting of charge-to-time converters which output a timing signal with a width proportional to the overall charge.

Figure 3.11 shows a diagram of the upgraded DAQ. The upgrade included replacing the old front-end electronics modules with new ones called QTC-based electronics with ethernet (QBEE) [163]. The signals from ID and OD PMTs go through a QTC which has three dynamic ranges which are summarized in Table 3.3. The analogue to digital conversion is carried out for each range separately but the one used is the highest resolution range that is unsaturated.

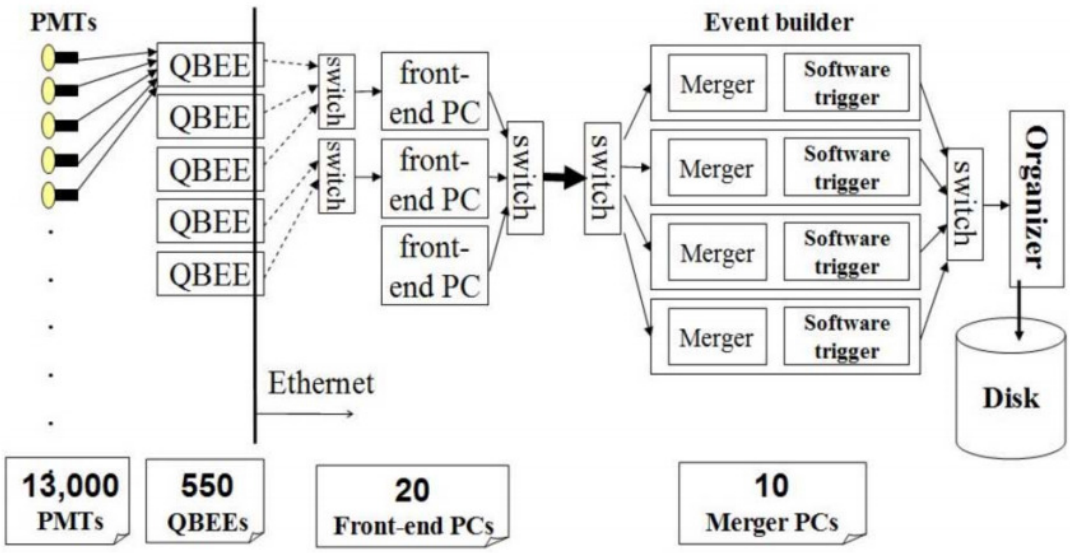

Figure 3.11 *Schematic view of the new data acquisition system [163].*

Table 3.3 *Summary of QTC ranges in the new DAQ system [12].*

Range	Measuring Region [pC]	Resolution [pC]
Small	0∼51	0.1
Medium	0∼357	0.7
Large	0∼2500	4.9

The output of the QTC is fed into a time-to-digital (TDC) converter which measures the width of the pulse. The digitized time and width are then sent to a field-programmable gate array (FPGA) for processing. The time resolution of the QBEE board, for signal heights similar to that expected for single photons, is 0.3 ns. This is better than the 2.2 ns intrinsic time resolution of the SK ID PMTs.

Another big improvement comes from the ability to quickly process the PMT signals. The processed information is sent to merger PCs for sorting and merging, and the data is then scanned by a customizable software trigger. Prior to the upgrade a hardware trigger was used; the deadtime after the hardware trigger was initiated made the detection of decay electrons, from stopping muons, less efficient. SK has several different trigger configurations:

- **OD** : OD trigger detects charged particles in the OD.
- **SLE** : Super low energy for lower energy solar neutrinos.

Table 3.4 *Summary of trigger types used in the SK software trigger.*

Trigger	Threshold [Hits/200 ns]	Event Time Window [μs]
OD	22	–
SLE	34	-0.5→1.0
LE	47	-5→35
HE	50	-5→35
SHE	58	-5→35
AFT	SHE and no OD	35→535

- **LE** : Low energy trigger for solar and supernova neutrino events.
- **HE** : High energy trigger for atmospheric neutrino events.
- **SHE** : Special high energy with a slightly higher threshold.
- **AFT** : If the SHE trigger is unaccompanied by an OD trigger then the after trigger records an additional 500 μs of data, to look for possible neutron captures.

When the number of hits in a sliding 200 ns time window reaches a preset threshold, a trigger is issued and the hits in the event time window are recorded. The OD trigger counts only the PMT hits in the OD while other triggers count the hits in the ID. The current trigger types used in SK are summarized in Table 3.4.

3.5 Water System

The 50 ktons of water used in the detector is sourced from the mountain it sits in, and is constantly circulated through a water purification system. The water must be cleared of small particles in order to ensure a high attenuation length for the Cherenkov light; the measured attenuation length is 120 m at a wavelength of 400 nm. The water purification system also removes radioactive materials from the water which would otherwise introduce a low energy ($\sim$ MeV) background. The system, shown in Figure 3.12, is made up of the following components

- **1 μm Mesh Filters** : Removes dust and particles which would affect the transparency of water and possibly be a source of radon.
- **Heat Exchanger** : Cools down the water, to roughly 13° C, to suppress the growth of bacteria. The lower temperature also results in lower PMT

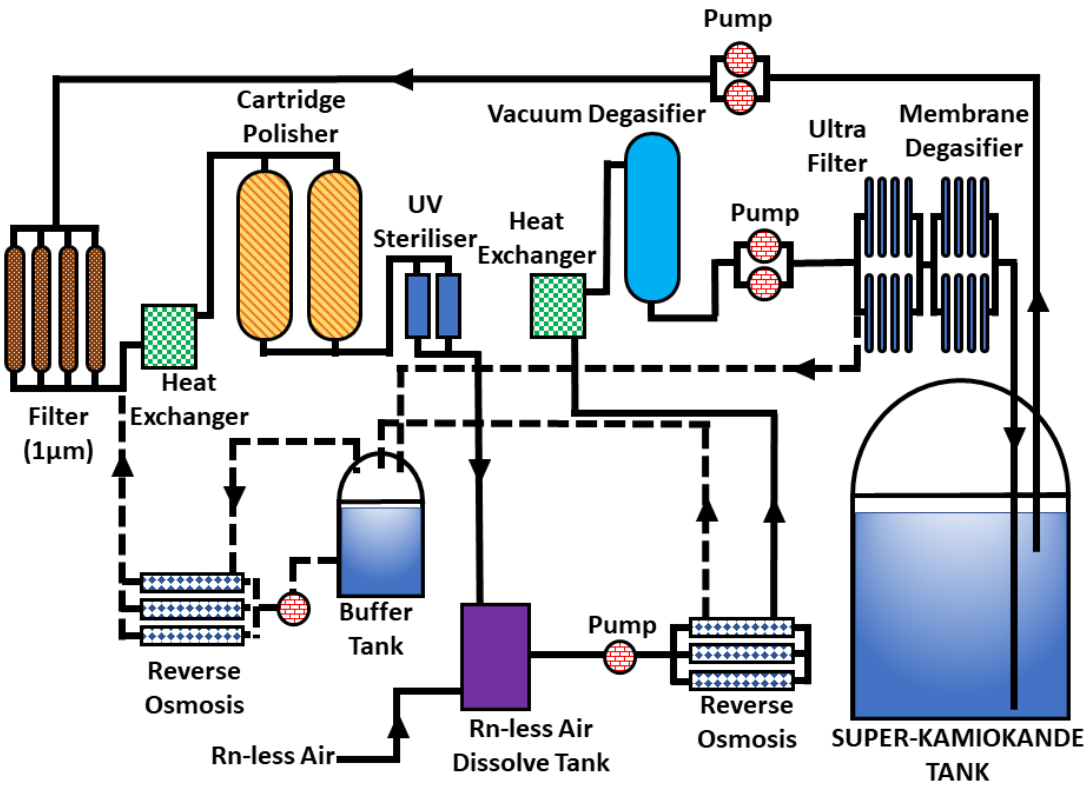

Figure 3.12 *A schematic diagram of the water purification system used in SK [82].*

dark noise levels. This also removes heat which is generated by the PMTs and reduces the convection and turbulence in the tank.

- **Cartridge Polisher** : Removes heavy ions which would otherwise affect the water transparency, some of these ions are also radioactive. Originally an ion exchanger was included in the water purification system but the resin was found to be a significant radon source and was removed. The resistivity of the water, after it passes through the cartridge polisher, increases from around 8 MΩcm to 18 MΩcm.

- **UV Steriliser** : Any bacteria which survive the heat exchanger are then killed by the UV light.

- **Radon Reduced Air Dissolving System** : This tank dissolves radon-reduced air into the water which increases the radon removal efficiency of the vacuum degasifier.

- **Reverse Osmosis** : Removes particulates.

- **Vacuum Degasifier** : Removes dissolved gasses from he water. Dissolved radon gas introduces a low energy background and dissolved oxygen

encourages bacteria growth. The removal efficiency of radon gas, after passing through the vacuum degasifier, is estimated to be around 96%.

- **Ultra Filter** : The ultra filter is made up of hollow membrane filters which remove very small particles. The typical number of particles above 0.2 μm in diameter in the water is reduced from 1000 particles/cc to 6 particles/cc.

- **Membrane Degasifier** : The membrane degasifier is made up of 30 hollow fibre membrane modules and a vacuum pump. Radon-reduced air is supplied as a purge gas. The membrane degasifier removes radon with an efficiency of 83%.

The water is circulated at a rate of roughly 50 ton/hour in a closed cycle system. After passing through the water purification system, the attenuation length [1] for light with a wavelength of 420 nm is approximately 100 m which is roughly twice as large as the longest particle track length in the detector. The purified water has a typical radon concentration of 0.4 $\pm$ 0.2 mBq m^{-3}.

3.6 Air Purification

The air in the mine has a high concentration of radon which is emitted by the surrounding rock. Mine air typically has radon concentrations of 2000-3000 Bq m^{-3} in the warmer months and 100-300 Bq m^{-3} in the cooler months [2]. In order to reduce the radon levels, air from outside the mine is passed through a purification system and then pumped into the mine. The air purification system, shown in Figure 3.13, is made up of compressors, filters, driers and 8 m^3 of activated charcoal. The final set of charcoal filters are cooled to -40° C to increase the radon removal efficiency. The air purified by this system is referred to as radon-reduced air and has a radon concentration of $\sim$3 mBq m^{-3}.

The radon-reduced air is pumped into the gap between the top of the water surface and the top of the tank and kept at a slight overpressure in an attempt

[1] The attenuation length is dependent on the wavelength of light and is not constant. Changes in the water transparency result in a varying attenuation length over time.

[2] The annual variation in radon concentrations in the air is due to the flow of air through the mine. From May to October, wind tends to flow out of the mine carrying the radon-rich air from deep within the mine past the experimental area. From November to April, wind tends to flow into the mine and has a relatively short path length in the mine before reaching the experimental area [82].

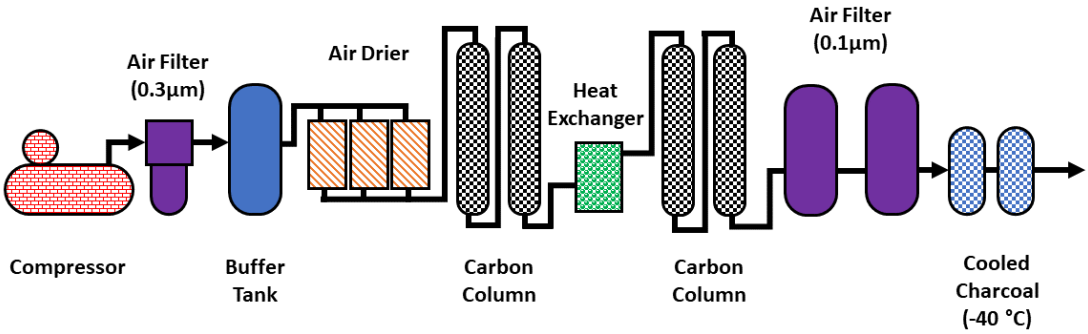

Figure 3.13 *A schematic diagram of the air purification system used in SK [82].*

Table 3.5 *Summary of SK run periods. "Implosion Covers" refers to the protective plastic covers used to prevent an implosion incident. OD-SEG refers to the segmentation of the OD with Tyvek®.*

Phase	SK-I	SK-II	SK-III	SK-IV	SK-V
Start	Apr 1996	Jan 2003	Jun 2006	Aug 2008	Jan 2019
End	Jul 2001	Oct 2005	Aug 2008	Jun 2018	–
Live days	1489.2	798.6	518.1	3235.3	–
ID PMTs	11,146	5,182	11,129	11,129	11,129
OD PMTs	1,885	1,885	1,885	1,885	1,885
Implosion Covers	No	Yes	Yes	Yes	Yes
OD-SEG	No	No	Yes	Yes	Yes
Photo-coverage	40%	19%	40%	40%	40%
DAQ	ATM	ATM	ATM	QBEE	QBEE
Trigger	Hardware	Hardware	Hardware	Software	Software

to reduce radon-rich air from entering the detector. The SK dome, having air pumped in from outside the mine, typically has radon concentrations of $\sim$40 mBq m^{-3}.

3.7 Run Periods

SK started data-taking in 1996 and, since then, there have been five distinct detector phases which are summarized in Table 3.5.

SK-I The first data-taking period started in April 1996, with an ID photocoverage of 40%. After a run comprising of 1489.2 live days of data, the detector was stopped for maintenance in July 2001. During the refilling of the detector, an ID PMT imploded causing a chain implosion which destroyed roughly half of the PMTs in the inner and outer detectors.

SK-II After the implosion disaster, the PMTs were redistributed evenly throughout the detector. The photocoverage in this run period was 19%. The ID PMTs were each covered with an acrylic cover at the front and a fibreglass reinforced plastic (FRP) cover in the back, to prevent another chain implosion incident. The second SK run period started in January 2003 and ran until October 2005. During this run period 798.6 live days of data was collected.

SK-III During the second run period, more PMTs were manufactured and after SK-II the photocoverage was restored to 40%. At this point additional Tyvek® sheets were put in place to optically separate the endcaps and barrel region of the OD. The SK-III phase began in June 2006 and ended in August 2008, collecting 518.1 live days of data.

SK-IV In August 2008, the electronics and data acquisition (DAQ) system were upgraded allowing for continuous data recording and better reconstruction and detection of decay electrons. The SK-IV period ended in June 2018, with a total of 3235.3 live days of data.

SK-V In June 2018, the SK tank was opened up for refurbishment and upgrades to enable it to be loaded with Gadolinium (Gd). Water systems to appropriately deal with Gd have been installed. Works were also carried out in order to stop the tank from leaking. SK started taking data again in January 2019. Gd is expected to be dissolved into the detector in June 2020 with an initial concentration of 0.02% $Gd_2(SO_4)_3$, increasing to 0.2% by October 2020.

Chapter 4

Detector Calibration

The SK detector is continuously calibrated and monitored so as to understand its performance and ensure consistency when there are changes in hardware or water quality. The calibration procedures also prevent systematic errors from arising due to a particle's position and direction in the tank. Three calibration procedures are carried out related to: PMT response, water transparency and energy scale. These are described in this chapter.

4.1 PMT Calibration

The two main characteristics that determine a PMT's ability to detect photons are the quantum efficiency and the collection efficiency of photoelectrons. The combination of these two properties is referred to as the QE of a PMT. The purpose of the PMT calibration is to understand the QE, gain and timing response of each PMT.

Understanding the QE is crucial for low energy events, such as solar neutrinos, which mainly leave single photoelectron hits in the detector. The gain of a PMT is the conversion between the number of photoelectrons and the output charge (in pC). High energy events, for example upward going muons, give multiple photoelectrons in the same PMT. Consequently, good knowledge of the gain is important.Calibrations are carried out in order to know the QE and the gain for each individual PMT.

4.1.1 High Voltage Setting

The high voltage (HV) applied to each PMT needs to be adjusted such that the charge output for a single photoelectron is the same for all PMTs. To achieve this, an isotropic light source is placed in the centre of the ID. There are several factors affecting how much light makes it to each PMT. Since the SK tank is not spherically symmetric, twice as many photons reach the closest PMTs compared to those furthest away. In addition, the way in which photons propagate in the water together with water quality and reflections in the ID need to be considered. This further complicates the calculation of expected intensities.

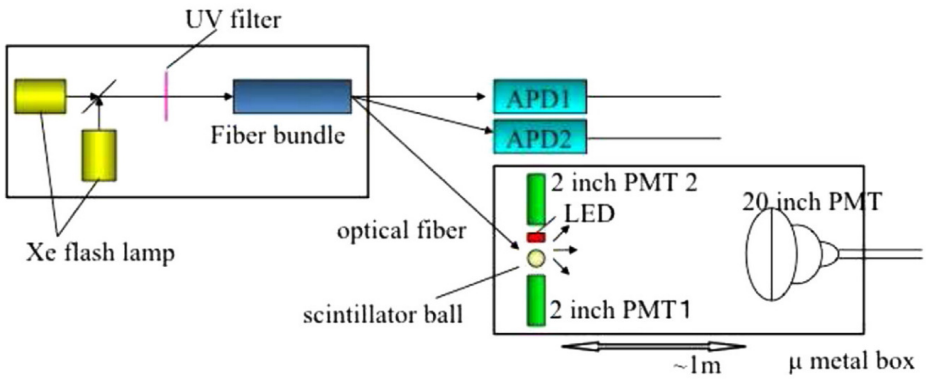

Figure 4.1 *A schematic view of the pre-calibration setup. Taken from [12].*

To simplify the HV calibration, the HV values for 420 PMTs were individually determined, prior to installation, in the system shown in Figure 4.1. Light from a Xe lamp was passed through a UV filter which then fed into three optical fibres. Two of the optical fibres led to avalanche photodiode (APD) modules, which monitored the intensity of the light, and the third optical fibre went into a scintillator ball. The scintillator ball is an acrylic ball, 5 cm in diameter, containing 15 ppm of POPOP[1] as a wavelength shifter and 2000 ppm of MgO as a diffuser. Two 5 cm PMTs were mounted in the pre-calibration system to measure the light intensity of the scintillator ball. The PMT was placed in a μ-metal box to shield it from the Earth's magnetic field. The HV value for each PMT was then adjusted so that the observed ADC counts for all of the PMTs matched.

The 420 PMTs were then placed in the detector to serve as references for other PMTs. The HV of each PMT is set so that the observed charge matches the average of the reference PMTs matching its geometric relationship

[1]POPOP is a wavelength shifter alternatively called 1,4-bis(5-phenyloxazol-2-yl) benzene.

to the scintillator ball. An example of PMT groups with identical geometric relationships to the light source can be seen in Figure 4.2.

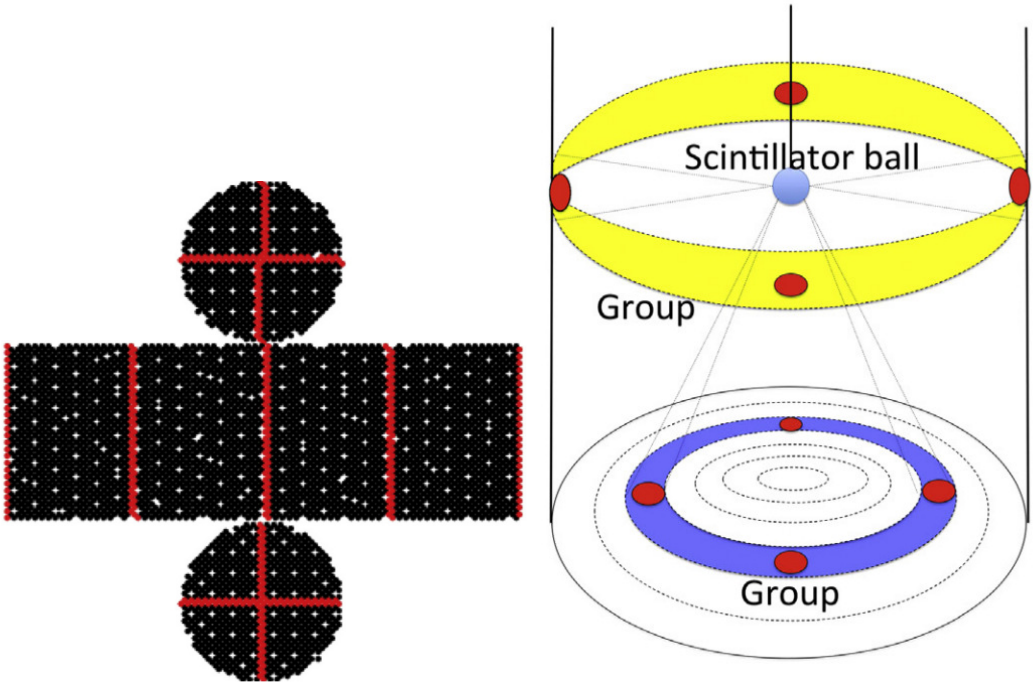

(a) *Position of reference PMTs* **(b)** *Example of grouped PMTs*

Figure 4.2 *The position of the reference ID PMTs in red [left] and examples of how PMTs with a similar geometric relationship are grouped [right]. Taken from. Taken from [12].*

The scintillator ball is a permanent fixture in the ID and is used for constant monitoring of the ID PMT gain.

4.1.2 Relative Gain

The relative gain calibration is carried out in order to understand the differences in the response of individual PMTs. This calibration is performed with a nitrogen-laser-driven dye laser fed into an optical fibre attached to a diffuser ball. The overall intensity of the light is controlled by a filter wheel, consisting of neutral density filters, placed between the dye laser and the optical fibre. The diffuser ball is then used at various positions in the ID.

The first part of this calibration uses high intensity flashes where each PMT receives multiple photons, producing an average charge, $Q_{obs}(i)$ in the i^{th} PMT.

The value of $Q_{obs}(i)$ is estimated by the equation:

$$Q_{obs}(i) \propto I_S \times a(i) \times \epsilon_{qe}(i) \times G(i) \tag{4.1}$$

where I_S is the average intensity of the light flash, $a(i)$ is the acceptance angle of the i^{th} PMT, $\epsilon_{qe}(i)$ is its QE and $G(i)$ is its gain. The second part of this calibration uses low intensity flashes where a small number of PMTs are hit in each event, such hits are likely to be single-pe hits. The quantity measured here is the number of times the i^{th} PMT records a hit (above a threshold) $N_{obs}(i)$. The value of $N_{obs}(i)$ is estimated from:

$$N_{obs}(i) \propto I_W \times a(i) \times \epsilon_{qe}(i) \times G(i), \tag{4.2}$$

where I_W is the average intensity of the light flash.

The ratio of Equation 4.1 and Equation 4.2 yields the gain of each individual PMT:

$$G(i) \propto \frac{Q_{obs}(i)}{N_{obs}(i)}. \tag{4.3}$$

The gain of each PMT is normalised to the average gain over the detector to give the relative gain. The light source is not moved between the two measurements so the acceptance and the QE of each PMT cancel each other out. The normalisation also cancels out the intensity ratio I_S/I_W. The relative gain is used as a fine correction factor, in the conversion between the observed charge and the number of photoelectrons, for each individual PMT. The high voltage calibration ensures that $Q_{obs}(i)$ for each PMT was the same, so we deduce that the differences in gain are due to the differences in QE for each PMT.

4.1.3 Absolute Gain

The absolute gain calibration uses the charge distribution of single photoelectron signals to convert the observed charge into the number of photoelectrons. This calibration is carried out by placing a ^{252}Cf source into a ball made of NiO and polyethylene. This source has a half-life of 2.654 years and 3.09% of its decays

are via spontaneous fission [116]. The emitted neutrons thermalize and capture on the nickel, resulting in gamma emissions from 2 to 9 MeV [109]. The Cf-Ni ball is placed in the centre of the tank where the stable, isotropic, low intensity light results in an average of $\sim$50 PMT hits per event, 99% of which are single photoelectron hits. Figure 4.3 shows the total single photoelectron response of the detector. The effect of dark noise was reduced by taking data when no signal was expected (off-time) and subtracting it from the data taken when a signal was expected (on-time).

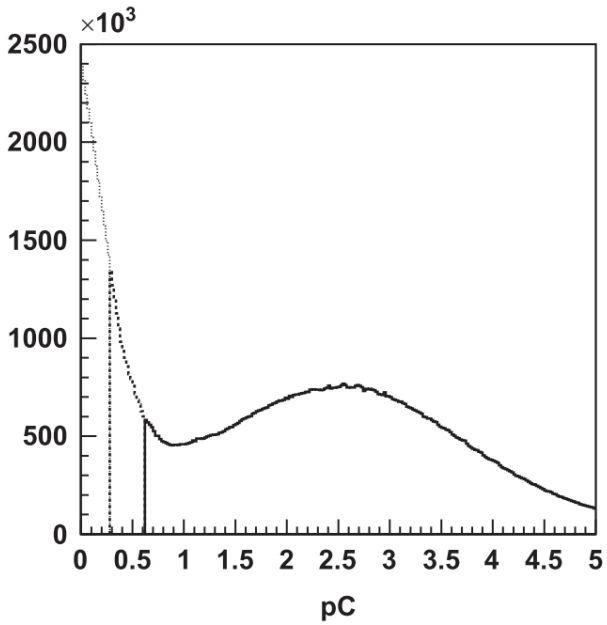

Figure 4.3 *The single photoelectron charge distribution for the Cf-Ni source in SK-III, taken from [12]. The solid line shows the data with normal PMT gain and a 0.25 photoelectron threshold, the dashed line shows the data with double the gain and half the threshold. The dotted line shows a linear extrapolation.*

The charge of the single photoelectron peak is averaged and the value is set as the pC per photoelectron conversion factor. The conversion factors for the different SK run periods are shown in Table 4.1. A long-term increase in PMT gain causes the conversion factor to change over time, the reason for this increase is currently unknown but is accounted for in the various physics analyses.

4.1.4 Timing Calibration

There are several factors which affect the timing response of the readout channels: differences in the transit time of PMTs, the length of PMT signal cables as well as

Table 4.1 *The absolute gain conversion from the single photoelectron to observed output PMT charge (pC).*

Run Period	Absolute Gain (pC / pe)
SK-I	2.055
SK-II	2.297
SK-III	2.243
SK-IV	2.645

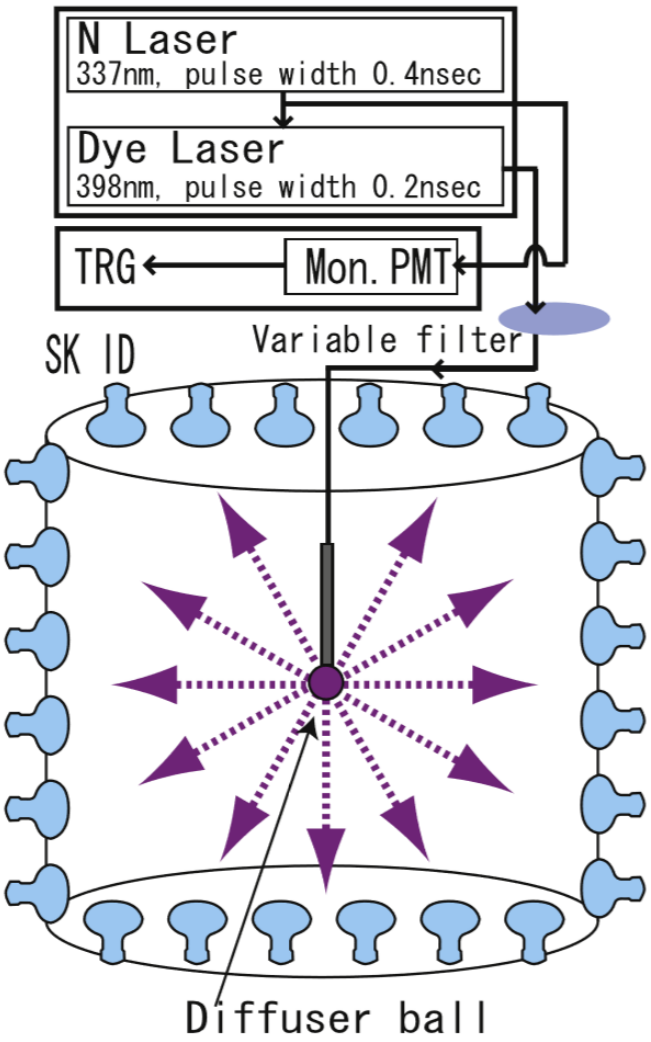

Figure 4.4 *A schematic diagram showing the time calibration system. Taken from [12].*

the signal processing. Time-walk refers to an effect where the signal pulse height varies the time response even when PMTs receive light at the same time. Time-walk occurs because the rise time of a larger signal is faster than that of a smaller one, as a result larger signals appear sooner (see Figure 4.5). Understanding the timing response of each readout channel allows for the precise reconstruction of

event vertices and particle directions.

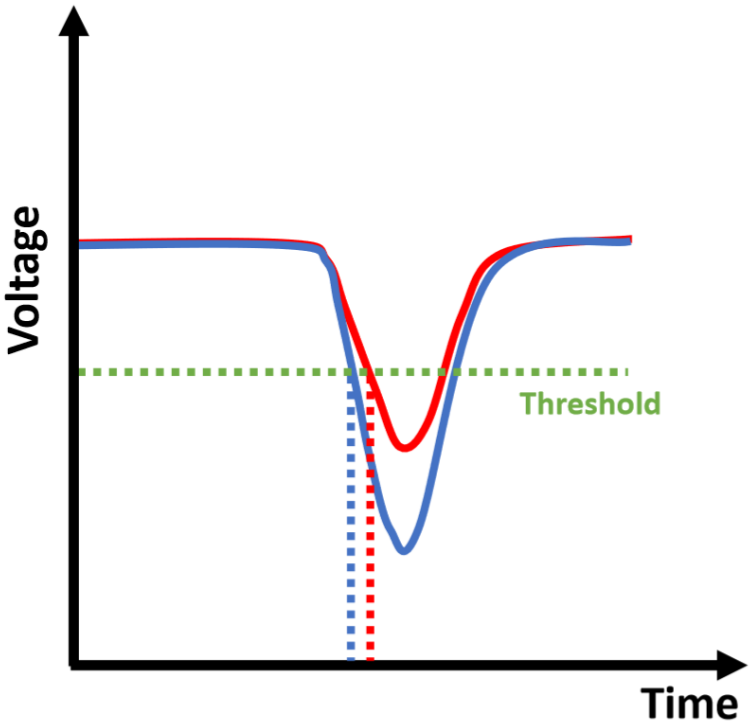

Figure 4.5 *A diagram showing the time-walk effect. A larger signal has a faster rise time, thus reaching the threshold sooner than a smaller signal starting at the same time.*

The time calibration system, shown in Figure 4.4, uses a nitrogen laser as the initial light source. The nitrogen laser emits 0.4 ns (FWHM) pulses of light with a wavelength of 337 nm through to a dye which shifts the wavelength to 398 nm and shortens the pulse to 0.2 ns. An optical filter varies the intensity of the light before an optical fibre injects the light into a MgO diffuser ball (see Figure 4.6) in the centre of the tank. The nitrogen laser's light is monitored by a Hamamatsu H2431-50 PMT [93], which has a 0.37 ns TTS, to define the injection time of the light.

The time response for each channel is measured as a function of the output charge. After correcting for the time of flight (TOF) between the diffuser ball and the hit PMTs, a 2D time versus charge (TQ) plot is created for each readout channel. A polynomial function is then fit to the data to create a lookup table referred to as the TQ-map. Figure 4.7 shows an example TQ distribution.

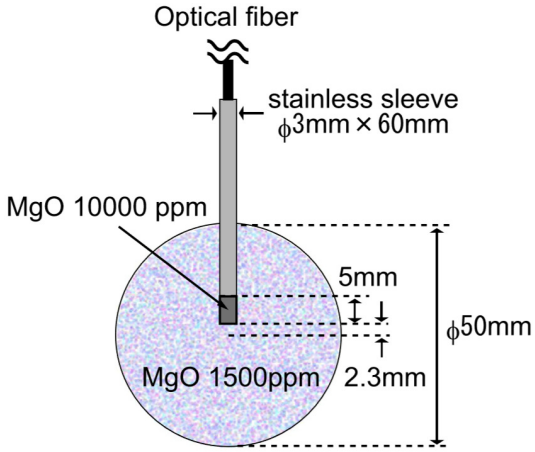

Figure 4.6 *Cross-section of the MgO diffuser ball. Taken from [12].*

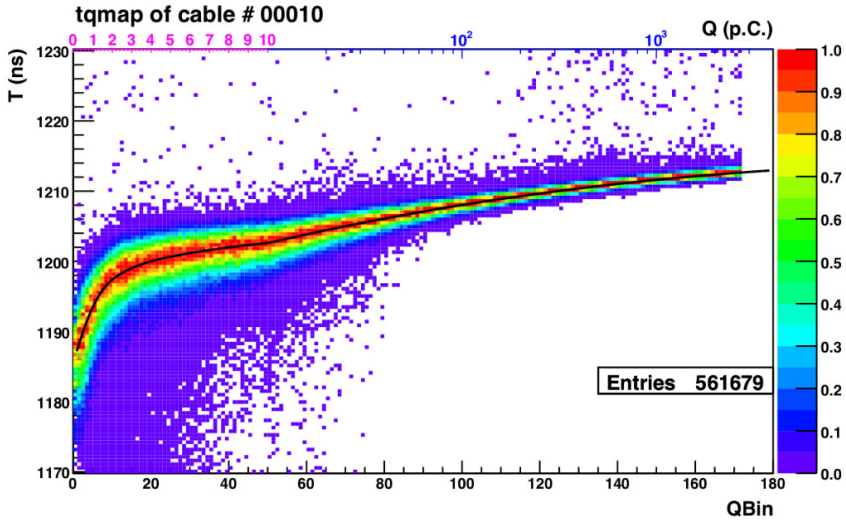

Figure 4.7 *Time vs charge for readout channel 00010. Qbin refers to the amount of charge (pC) of each hit, which are binned in a linear scale (0.2 pC/Qbin) from 0 to 10 pC and a log scale (50log(pC)/Qbin) from 10 to 3981 pC. The timing (T) has been corrected for TOF, the larger T corresponds to earlier hits. The plot is referred to as a TQ distribution and the fitted polynomial (black line) is known as the TQ-map. Taken from [12].*

4.2 Water Calibration

The propagation of photons in the ID must be well understood in order to accurately simulate the detector. The water calibration system measures the absorption and scattering in the water (water quality) as well as the reflection of light at the ID wall.

4.2.1 Absorption and Scattering

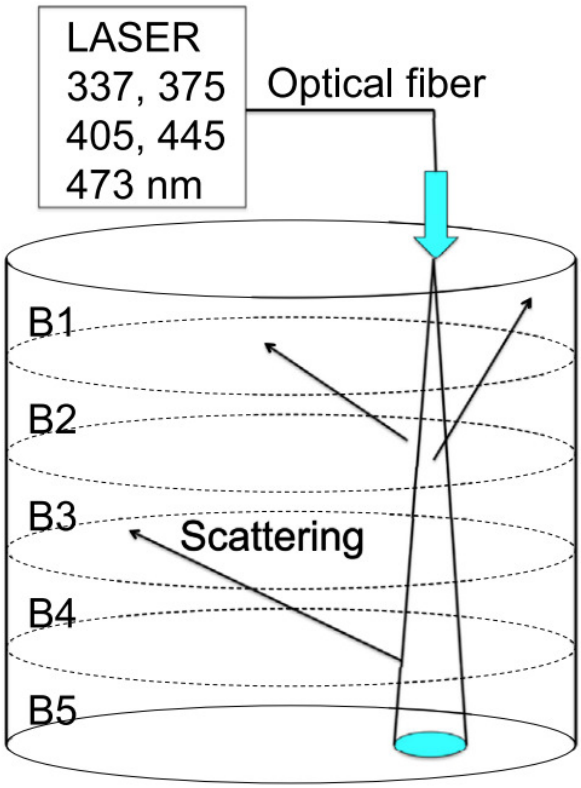

Figure 4.8 *A diagram showing the real-time water quality calibration system. The analysis splits up the PMTs into 5 barrel regions and the top. The blue circle indicates the laser target used for the TOF calculations. Taken from [12].*

The water transparency measurement represents the combined effect from absorption, Rayleigh scattering and Mie scattering [128]. Rayleigh scattering occurs when the dimensions of the target are smaller than wavelength of incident light; when the dimensions of the target are larger than the wavelength of incident light, Mie scattering occurs. For the purposes of this calibration, the scattering will be split up into symmetric and asymmetric components. The symmetric component consists of Rayleigh and symmetric Mie scattering, described by a scattering angle distribution intensity of $1 + \cos^2\theta$. The asymmetric component consists of forward Mie scattering where the probability of scattering increases linearly from $\cos\theta = 0$ to $\cos\theta = 1$, for $\cos < 0$ there is no scattering.

The intensity of light, of wavelength λ, in water decreases according to

$$I(\lambda) = I_0(\lambda)e^{-\frac{l}{L(\lambda)}}, \tag{4.4}$$

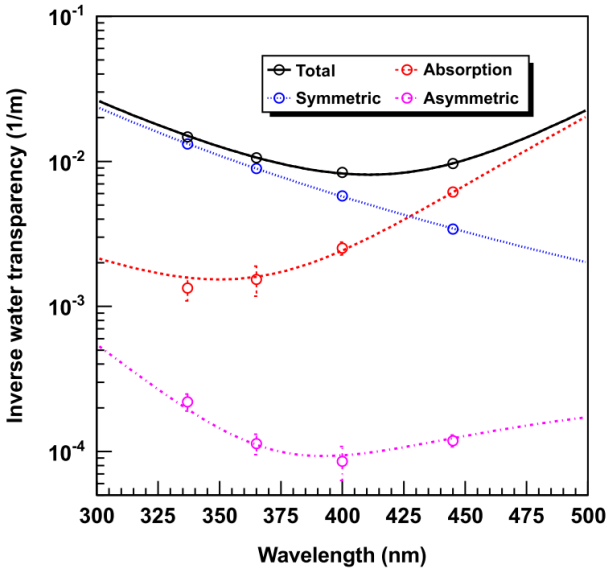

Figure 4.9 *SK-MC typical fitted functions for the absorption and scattering coefficients. The circles are data points obtained in April 2009 and the lines show the fitted functions. The solid black line shows the total sum of the dotted lines. Taken from [12].*

where $I_0(\lambda)$ is the initial light intensity, $I(\lambda)$ is the intensity at a distance l and $L(\lambda)$ is the attenuation length.

The attenuation length in the SK simulation (SK-MC) is defined as:

$$L(\lambda) = \frac{1}{\alpha_{abs}(\lambda) + \alpha_{sym}(\lambda) + \alpha_{asym}(\lambda)}, \tag{4.5}$$

where $\alpha_{abs}(\lambda)$, $\alpha_{sym}(\lambda)$ and $\alpha_{asym}(\lambda)$ are the coefficients for absorption, symmetric and asymmetric scattering respectively.

A nitrogen laser is fed through an optical fibre which injects light into the ID (see Figure 4.8). The absorption and scattering coefficients are adjusted in the SK-MC until there is agreement with the laser data (see Figure 4.9). Laser data is taken at several wavelengths ranging from 337 to 473 nm every 6 seconds during normal data-taking in order to continuously measure the water transparency which varies with time and wavelength.

4.3 Energy Calibration

The calibrations detailed in the previous sections convert the observed PMT charge to the number of photoelectrons, but we still need to understand how many photoelectrons to expect for a particle of a given energy. The various neutrino analyses require an accurate energy determination so it is important to understand the absolute energy scale. To calibrate this, four methods covering a wide range of particle momenta are used:

- Track length of high energy stopping muons ($1 \sim 10$ GeV/c).
- Cherenkov angle of low energy stopping muons ($200 \sim 500$ MeV/c).
- Invariant mass of π^0 produced by neutrino interactions (~ 130 MeV/c).
- The endpoint of the decay spectrum for Michel electrons from stopped muons (momentum of decay electron) (50 MeV/c).

The accuracy of the absolute energy scale is determined by comparing the observed data with the Monte Carlo (MC) simulation for each calibration source. The difference between the data and MC is combined with the time variation of the energy scale and considered as a systematic uncertainty.

4.3.1 Range of Stopping Muons

The kinetic energy of stopping muons can be determined from the muon track length: $L(m) \sim 4.5 \times E_{\mu}(GeV)$. The track length of stopping muons is reconstructed from the distance between the entry point at the ID boundary and the decay electron vertex. The vertex resolution for stopping muons and decay electrons is better than 50 cm.

For this calibration, muons which fit the following criteria are selected:

- Muon's entry point must be on the top cap of the ID.
- Muon's direction must be downwards ($\cos\theta > 0.94$).
- One decay electron event must be detected after the muon has stopped.

- Reconstructed muon track must be between 7 and 30 m (1.5 to 7 GeV).

The muon momentum loss per cm is ~ 2.3 MeV/c. Comparisons between the MC and data show agreement in the absolute energy scale within 0.7%, 1.1%, 2.0% and 2.2% for SK-I to SK-IV respectively.

4.3.2 Cherenkov Angles of Stopping Muons

The momentum of low energy muons (< 400 MeV/c) can be calculated using the equation:

$$\cos\theta_C = \frac{1}{n\beta} = \frac{1}{n}\sqrt{1 + \frac{m^2}{p^2}}, \tag{4.6}$$

where θ_C is the Cherenkov angle, n is the refractive index of water, m is the known muon mass and p is the estimated particle momenta. As the momentum increases the Cherenkov angle converges to a single value which is why this method of calibration can only be used at low momenta. Figure 4.10 shows the relationship between muon momentum and Cherenkov angle.

For this calibration, muons which fit the following criteria are used:

- Muon's entry point must be on the top cap of the ID.
- Muon's direction must be downwards ($\cos\theta > 0.9$).
- One decay electron event must be detected after the muon has stopped.
- Total number of photoelectrons in the ID must be less than 1500 (750 for SK-II).

Comparisons between the MC and data show agreement in the absolute energy scale within 0.7%, 1.3%, 2.1% and 2.1% for SK-I to SK-IV respectively.

4.3.3 Invariant Mass of Neutral Pions

The neutral pions used in this calibration are produced by neutral current atmospheric neutrino interactions in the detector. The neutral pions then decay

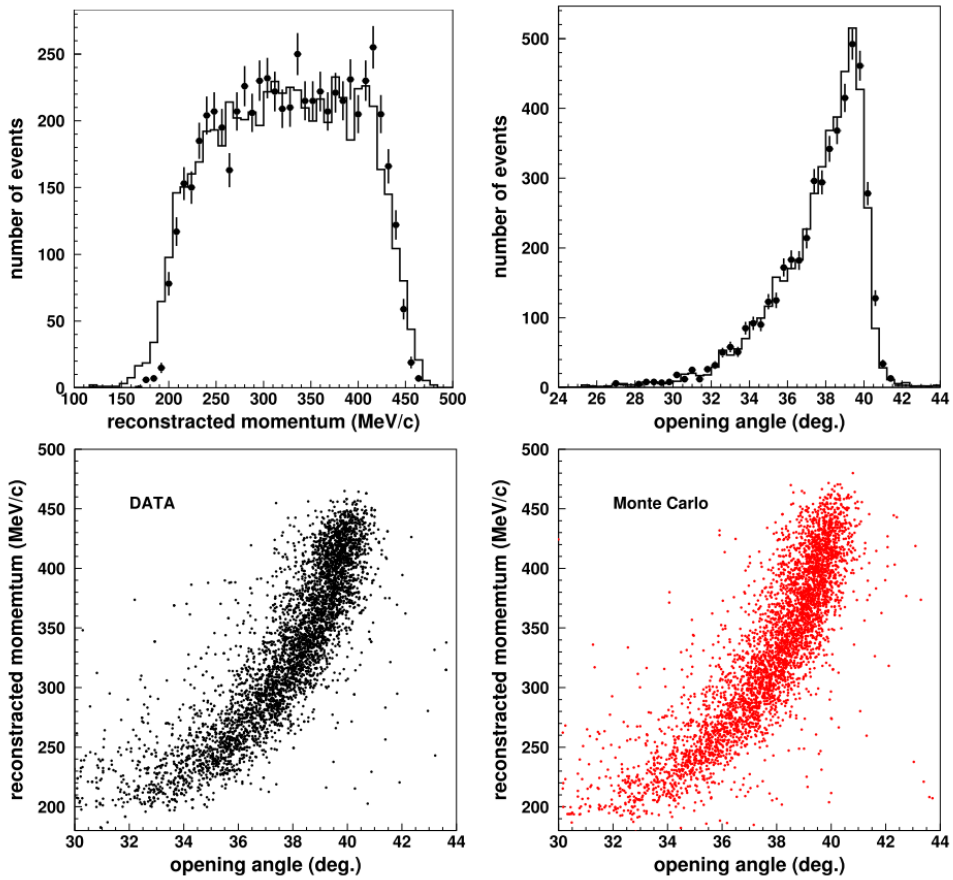

Figure 4.10 *The energy calibration using low-energy stopping muons with reconstructed Cherenkov opening angles. The upper plots show the reconstructed momentum (left) and reconstructed opening angle (right) for data (black circles) and MC (black lines). The lower plots show the reconstructed momentum versus opening angle for data (left) and MC (right). All plots are made using SK-II data and MC. Taken from [143].*

into two γ-rays. The invariant mass of the neutral pion can be reconstructed in events with two showering-type Cherenkov rings using the following equation:

$$M_{\pi^0}^2 = 2P_{\gamma 1}P_{\gamma 2}(1 - \cos\theta) \tag{4.7}$$

where the $P_{\gamma 1}$ and $P_{\gamma 2}$ are the momenta of the two γ-rays and θ is the opening angle. The π^0 events must satisfy this following criteria:

- Event must have two electron-like Cherenkov rings
- Decay electron, from a stopping muon, must not be detected (rejects charged current backgrounds)

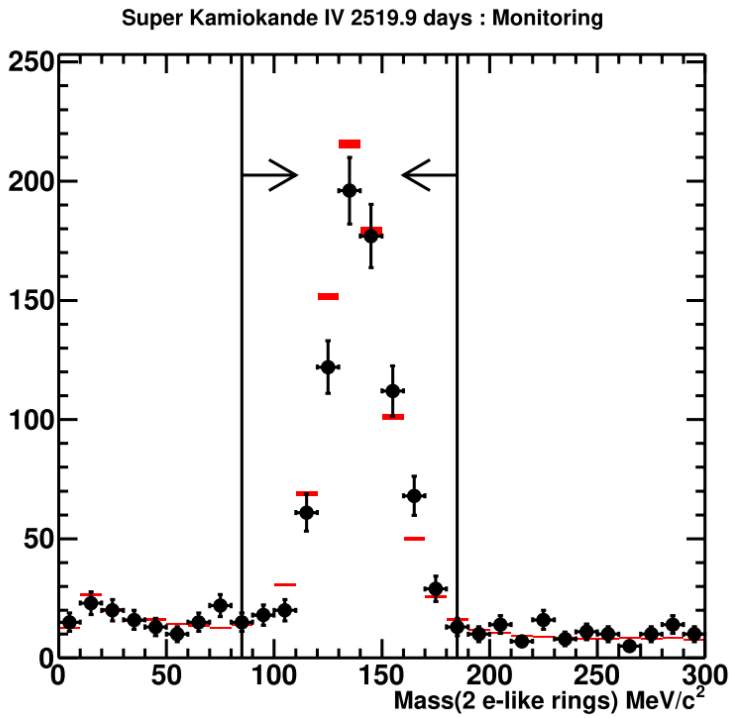

Figure 4.11 *The invariant mass distribution of reconstructed neutral pions for 2520 days of SK-IV live time. The black circles represent data and the red lines represent the MC. The MC has been normalised to the live time of the data.*

- Reconstructed vertex must be within the fiducial volume ($>$ 2 m away from the ID wall)

Although π^0 events are easily identified, the detection efficiency decreases with increasing momentum. A π^0 with a higher momentum would result in a smaller opening angle between the decay γ-rays which results in overlapping rings. The second reason for the decrease in efficiency is that an asymmetric decay may result in one of the γ-rays not having enough energy to be properly reconstructed. A Gaussian function is used to fit the invariant mass distribution (see Figure 4.11) for the data and MC. Comparisons between the MC and data show agreement in the π^0 mass within 0.7%, 1.3%, 0.3% and 1.7% for SK-I to SK-IV respectively.

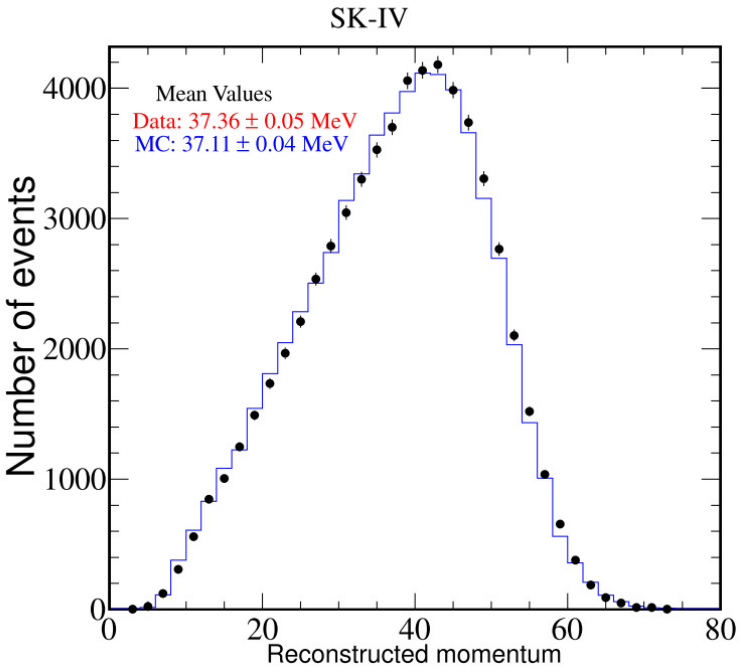

Figure 4.12 *Momentum of decay electrons for data (black dots) and MC (blue histogram). The MC has been normalised to the live time of the data.*

4.3.4 Decay Electrons

Decaying cosmic muons produce an electron, also called a Michel electron, which is visible in the detector in the majority of events[2]. The expected spectrum of these Michel electrons is well understood and the endpoint can be used for calibrations for energies around 50 MeV.

Decay electron events are selected using the following criteria:

- The event must occur between 2 to 8 μs after a stopping cosmic muon.
- Must have more than 60 (30 for SK-II) PMT hits in a 50 ns window. This rejects muon capture events.
- The vertex fit goodness must be larger than 0.5.
- Reconstructed vertex must be within the fiducial volume (> 2 m away from the ID wall).

[2]Sometimes μ^- capture on a proton and there is no decay electron, this process does not occur for μ^+. Roughly 20% of μ^- capture on ^{16}O in Super-K [149].

In Figure 4.12, the observed decay electron momentum spectrum is compared to the expected spectrum (MC) which show agreement in the absolute energy scale within 0.6%, 1.6%, 0.8% and 1.6% for SK-I to SK-IV respectively.

4.3.5 Energy Scale Summary

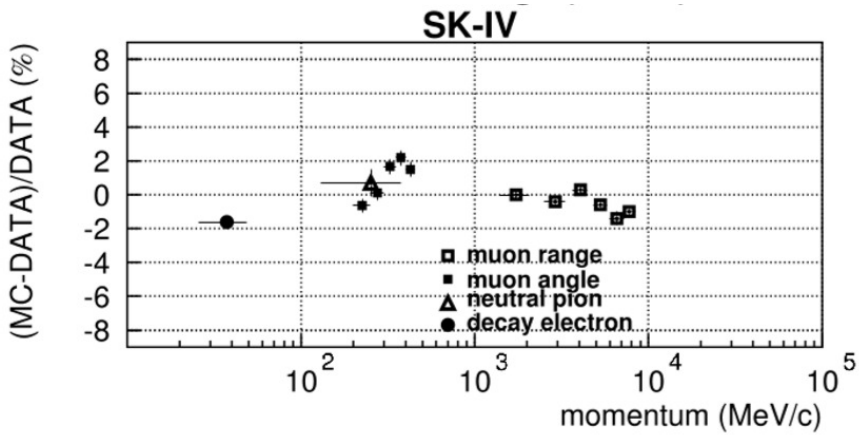

Figure 4.13 *The energy scale deviation at various momenta for SK-IV. Taken from [110].*

The several different sources of calibration yielded uncertainties at different energy ranges; the combined overall uncertainty is estimated to be 0.88%, 0.55%, 1.79% and 2.19% for SK-I to IV respectively. Figure 4.13 shows a summary of the absolute energy scale calibration for SK-IV. The energy scale is monitored over time using stopping muons and decay electrons, the fluctuation of absolute energy scale is estimated to be 0.74%, 1.60%, 2.08% and 0.39% for SK-I to SK-IV respectively.

Decay electrons and stopping muons are used to monitor the variation of the energy scale over time due to changes in water quality. Figure 4.14 shows the variation in reconstructed momenta over time. The uncertainty in energy scale added in quadrature with the uncertainty over time results in an overall estimated uncertainty of 1.1%, 1.7%, 2.7% and 2.3% for SK-I to SK-IV respectively.

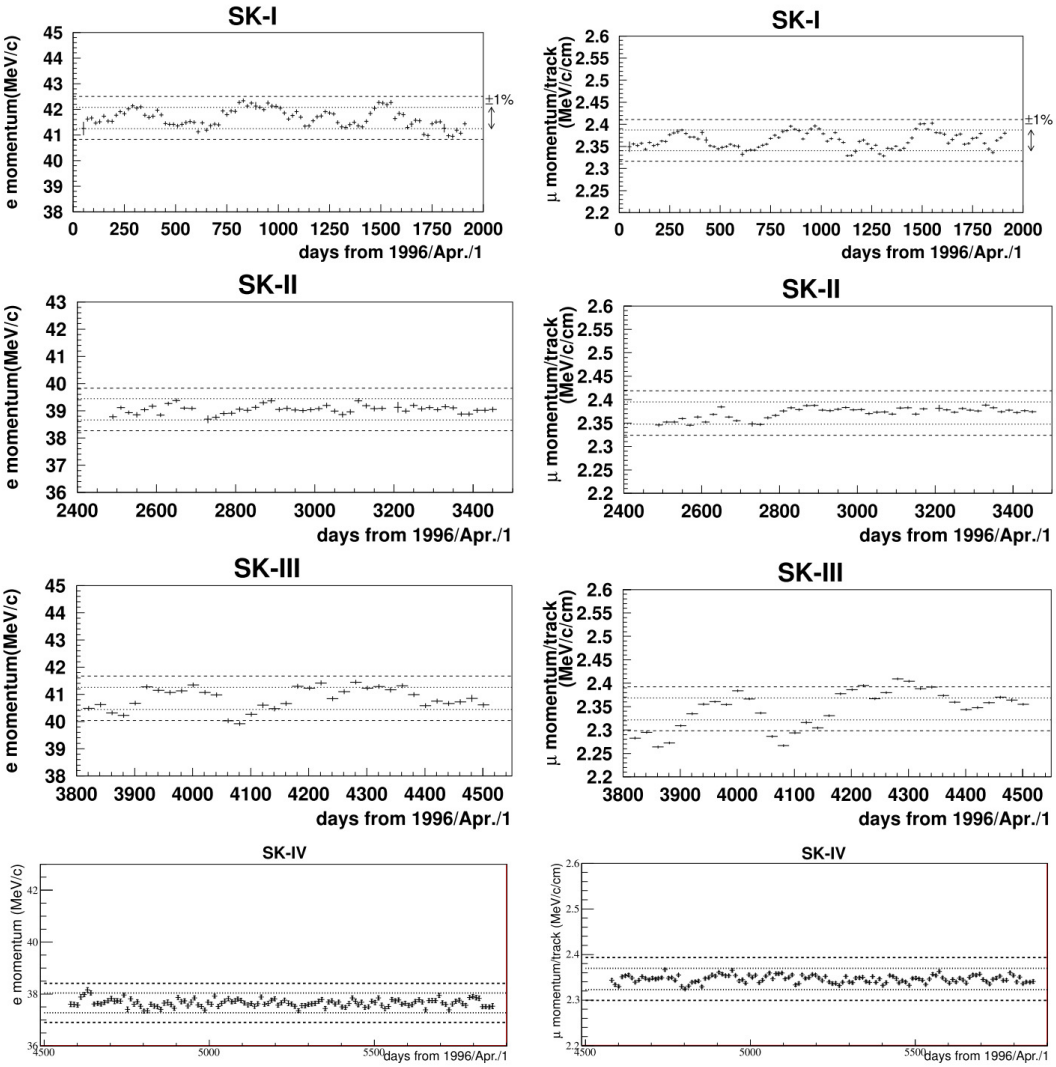

Figure 4.14 *The Super-K average reconstructed particle momentum since 1st April 2006. The plots on the left show the reconstructed momentum for decay electrons and the plots on the right show the reconstructed muon momentum per unit track length. From top to bottom the plots are shown for SK-I, SK-II, SK-III and SK-IV respectively. The dotted and dashed lines represent a 1% and 2% variation respectively. Taken from [143].*

Chapter 5

Atmospheric Neutrino Monte Carlo Simulation

The physical properties of atmospheric neutrinos are studied by comparing the observed data to the predictions made using Monte Carlo (MC) simulations. To be confident that the differences between the data and MC are due to real physics effects, it is important that the simulation is realistic.

There are three main parts to the SK atmospheric neutrino MC simulation: the atmospheric neutrino flux reaching the SK detector, the neutrino interactions in the detector target volume (water) and the response of the detector to the final state particles produced in the neutrino interaction.

5.1 Atmospheric Neutrinos

The analysis performed in this thesis was carried out on atmospheric neutrinos. Primary cosmic rays, mainly made up of protons, constantly bombard the Earth interacting with nuclei in the atmosphere. The interactions result in the production of secondary cosmic rays such as pions and kaons in hadronic showers. Mainly pions are produced, which then decay into muons:

$$\pi^+ \rightarrow \mu^+ + \nu_\mu \,, \qquad \pi^- \rightarrow \mu^- + \overline{\nu}_\mu . \tag{5.1}$$

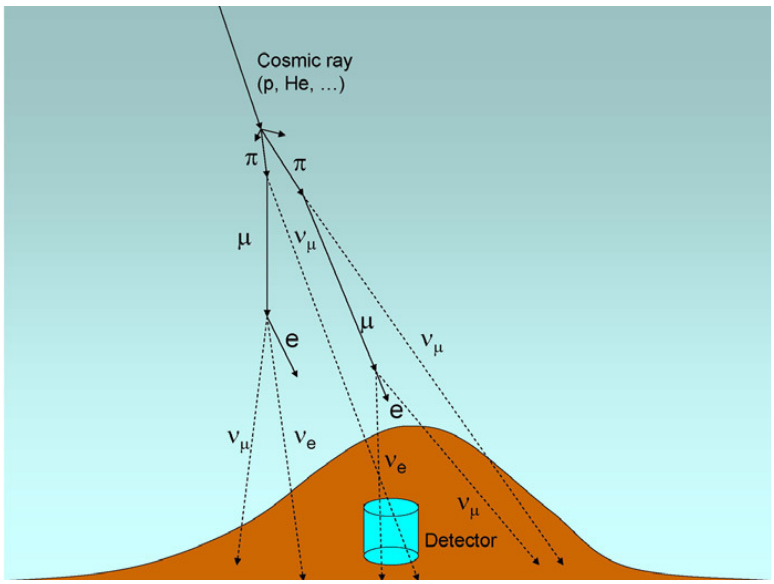

Figure 5.1 *Diagram of neutrino production in the Earth's atmosphere. The typical height of neutrino production is 15 km above the ground. Taken from [115].*

Electrons are then produced from the decay of muons which do not reach the ground:

$$\mu^+ \rightarrow e^+ + \nu_e + \overline{\nu}_\mu \,, \qquad \mu^- \rightarrow e^- + \overline{\nu}_e + \nu_\mu. \tag{5.2}$$

The neutrinos resulting from the pion and muon decays make up the majority of atmospheric neutrinos. From the decays in Equations 5.1 and 5.2 it can be seen that the decay of a pion results in two muon neutrinos for every electron neutrino. This holds true for lower energy neutrinos around 1 GeV as most of the parent muons decay before reaching the ground. Above 1 GeV the fraction of cosmic muons reaching the ground before decaying starts to increase, leading to an increase in the muon neutrino to electron neutrino ratio, this can be seen in Figure 5.2.

Atmospheric neutrinos are constantly created around the earth so the flight length of the neutrino, before being detected, ranges from $10 \sim 10^4$ km. The energy range of the atmospheric neutrinos detected, spans $10^{-1} \sim 10^3$ GeV.

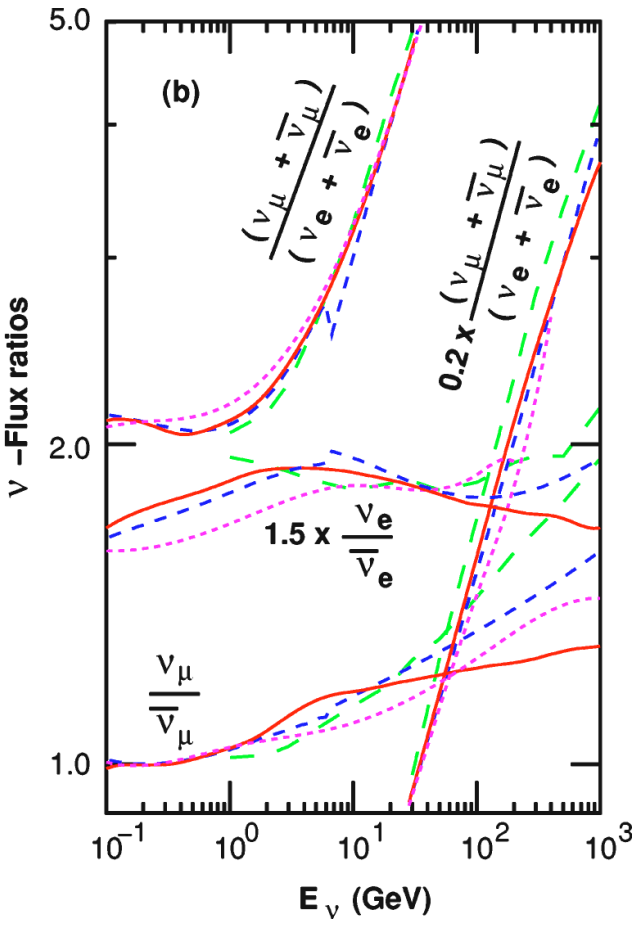

Figure 5.2 *Neutrino flux ratios from various atmospheric neutrino calculations. Taken from [104].*

5.2 Atmospheric Neutrino Flux

Since neutrino analyses at SK compare the observed to the expected neutrino flux it is important to accurately predict the expected flux of atmospheric neutrinos. In order to understand the flux, the initial cosmic ray flux and the hadronic showers that they produce must be understood.

Several models which predict the neutrino flux from the primary cosmic ray flux exist. The models will be referred to as the Honda flux [103–106], the Fluka flux [47] and the Bartol flux [45]. The SK atmospheric neutrino analysis uses the Honda flux as the primary flux model; the Fluka and Bartol fluxes are used to estimate the systematic uncertainties on the Honda calculation. An additional model, the Volkova flux [157], is used for energies above 10 TeV which is the

cut-off energy for the Honda calculation.

The neutrino flux calculation uses a primary cosmic ray flux model based on measurements taken by the Alpha Magnetic Spectrometer (AMS) [34, 35] and the Balloon-borne Experiment with a Superconducting Spectrometer (BESS) [92, 150]. A factor is applied to the primary cosmic ray flux above 10 TeV such that the model agrees with emulsion chamber data. Figure 5.3 shows the primary cosmic ray model used in the Honda calculation.

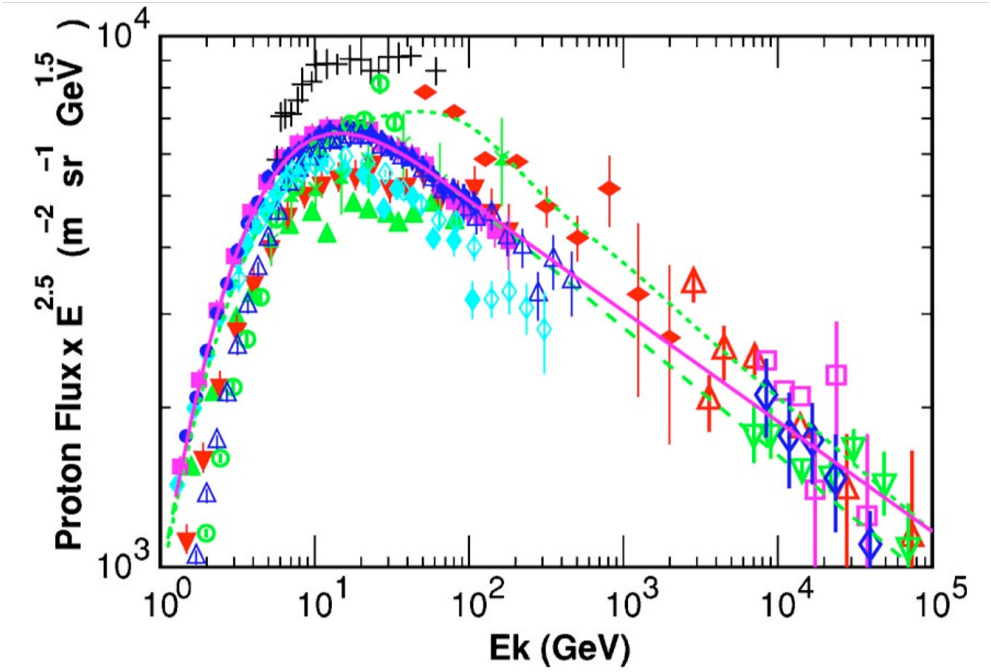

Figure 5.3 *A compilation of primary cosmic ray observations from various experiments. The green dashed line shows an initial calculated flux, the green dotted line includes corrections to bring the model into agreement with data above 10 TeV. The solid pink line is the Honda flux model [102]. The various points represent data taken by different experiments at solar minimum. See Ref [104] for further details.*

Variations in solar wind have noticeable effects on the flux of low energy cosmic rays. There is more than a factor of two difference in the flux of primary cosmic rays around 1 GeV between solar maximum (periods with high solar activity) and solar minimum (periods with low solar activity); This effect reduces to ∼10% at ∼10 GeV.

The primary cosmic ray flux is also affected by the Earth's geomagnetic field (east-west effect [124]). Lower energy cosmic rays are deflected away from Earth resulting in a low energy cut-off in the flux. The majority of primary cosmic rays are protons, the geomagnetic field deflects the positively charged particles

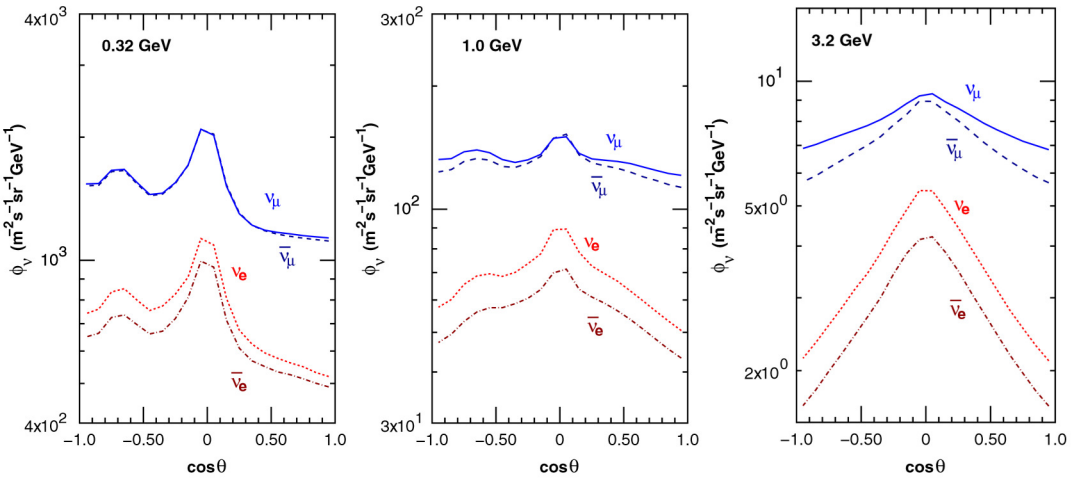

Figure 5.4 *The (calculated) zenith angle dependence of the atmospheric neutrino flux of neutrinos reaching Kamioka. θ is the incoming neutrino direction, where* $\cos\theta$ *= 1 for vertically downward-going neutrinos and* $\cos\theta$ *= -1 for vertically upward-going neutrinos. Taken from Ref [106].*

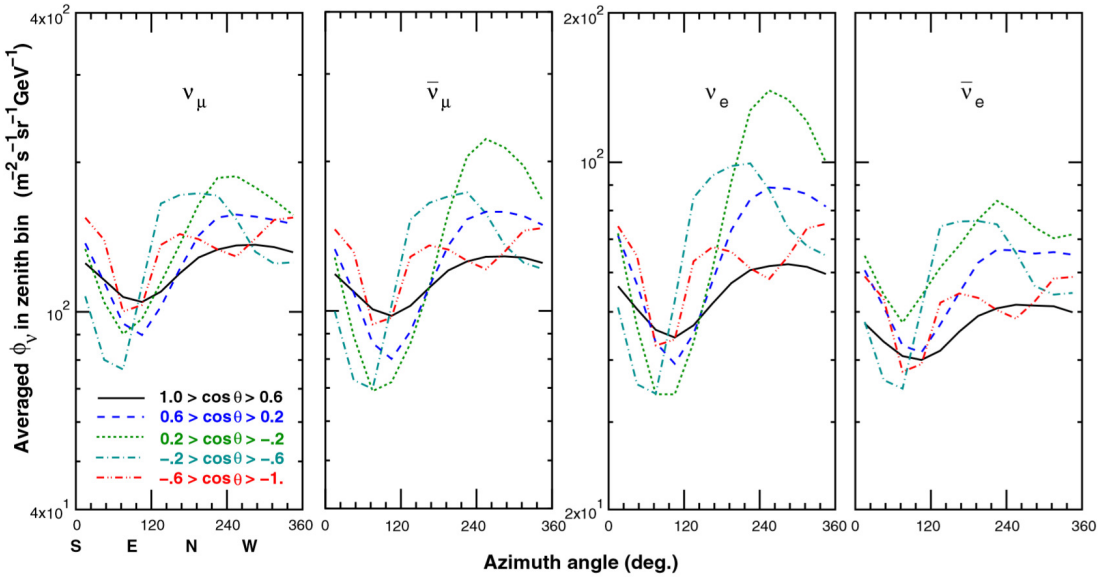

Figure 5.5 *The (calculated) azimuthal angle dependence of the atmospheric neutrino flux of 1 GeV neutrinos reaching Kamioka. Taken from Ref [106].*

towards the east resulting in an excess of observed cosmic rays arriving from the west. Similar to the east-west asymmetry, the slightly higher than average magnetic field around Kamioka results in a slight up-down asymmetry in the neutrino flux, the effects of the geomagnetic field become negligible for cosmic rays above 10 GeV. Figure 5.5 shows the east-west asymmetry and Figure 5.4 shows the up-down asymmetry of the neutrino flux at Kamioka.

Primary cosmic rays interact with nuclei in the atmosphere producing secondary particles. The secondary particles consist mainly of pions and kaons which then decay into muons and neutrinos. Muons approaching from the horizon have a longer path length to decay into neutrinos resulting in a peak in the neutrino flux near the horizon (see Figure 5.4). The density of Earth's atmosphere is given by the US Standard Atmosphere 1976 model [44] and the geomagnetic field is based on the International Geomagnetic Reference Field [2].

Figure 5.6 shows the total atmospheric neutrino flux reaching Kamioka. This part of the MC simulation ignores neutrino oscillation.

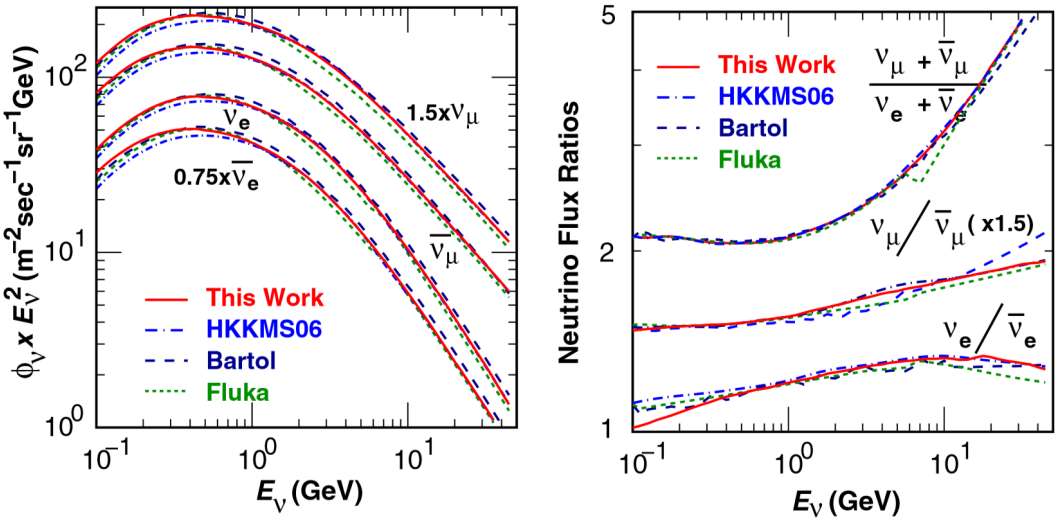

Figure 5.6 *The atmospheric neutrino flux reaching Kamioka [left] and the flux ratios [right] calculated using various models. "This Work" refers to the Honda 2011 calculation. Taken from Ref [106].*

5.3 Neutrino Interactions

Knowledge of the energy and direction of the neutrino are crucial to the SK physics program. Neutrinos are not observed directly, rather the products of the neutrino's interaction in water are observed. Therefore, it is important to simulate the neutrino interactions with nuclei in water and the surrounding rock. To simulate such interactions SK uses a neutrino event generator called NEUT [96]. Interactions with atomic electrons are neglected as the interaction cross section is three orders of magnitude smaller than that of atomic nuclei.

NEUT first simulates the initial interaction between the neutrino and the target

nucleon. Any produced hadrons are then propagated through the nucleus where additional interactions are simulated. If a neutrino interacts with a particle by exchanging a $W^{\pm}$ boson then the interaction is classified as charged current (CC). CC interactions produce a charged lepton with the same flavour as the incoming neutrino. These interactions produce a signal of the neutrino flavour making them important in the oscillation analyses. Alternatively, a neutrino can interact with a particle by exchanging a Z^0 boson, such events are referred to as neutral current (NC) events. NC events are considered a background as the incoming neutrino flavour can not be determined.

The five main types of interaction simulated in NEUT are:

- Quasi-elastic scattering: $\nu + N \rightarrow l + N'$
- Meson exchange current: $\nu + NN^* \rightarrow l + N'N'^*$
- Single meson production: $\nu + N \rightarrow l + N' + meson$
- Coherent pion production: $\nu + ^{16}O \rightarrow l + ^{16}O + \pi$
- Deep inelastic scattering: $\nu + N \rightarrow l + N' + hadrons$

where ν is neutrino or antineutrino, N and N^* are initial nucleons, N' and N'^* are outgoing nucleons and l is the outgoing lepton. Contributions to the total neutrino cross section with nucleons can be seen in Figure 5.7.

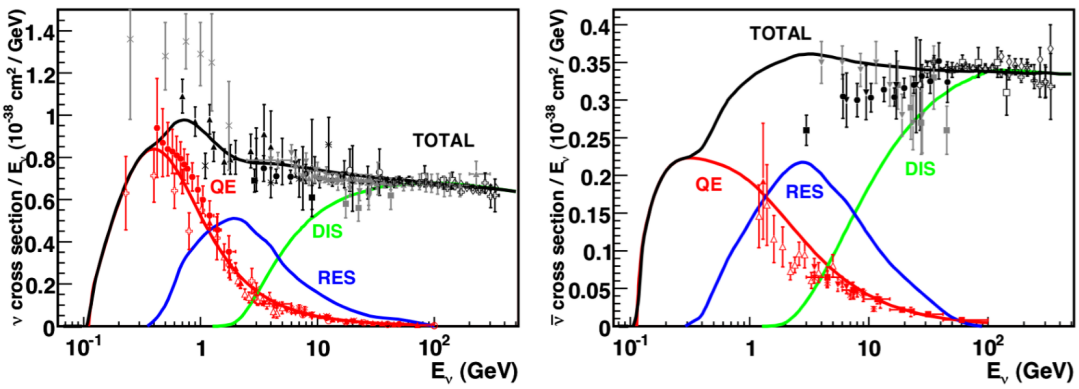

Figure 5.7 *NEUT simulation cross sections for neutrinos [left] and antineutrinos [right] compared to experiment data [75]. Contributions from different interaction modes shown. Taken from Ref [111].*

5.3.1 Elastic Scattering

Neutrinos can undergo a NC interaction with nucleons elastically scattering off of them with no change in the system except momentum transfer. A similar CC version of this interaction converts the incoming neutrino into a charged lepton and the incoming nucleon changes in order to conserve charge, this is referred to as charged current quasi-elastic (CCQE) scattering.

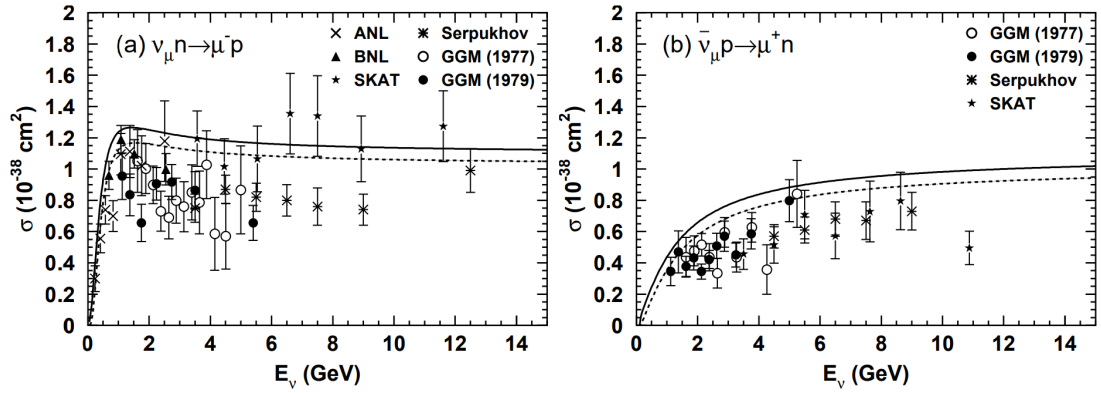

Figure 5.8 *The charged current quasi-elastic cross sections for muon neutrinos [left] and muon antineutrinos [right]. Solid lines show the calculated cross sections for free target nucleons and the dotted line shows the calculated cross sections for bound target nucleons (protons in oxygen). The points represent data from several experiments. Taken from Ref [96].*

The quasi-elastic scattering simulation is based on the Llewellyn-Smith model [125] for free nucleons and the relativistic Fermi gas model [152] is used for bound nucleons. Figure 5.8 shows the calculated cross sections compared to data from several experiments.

5.3.2 Meson Exchange Current

The quasi-elastic scattering interaction described in Section 5.3.1 ignores any correlations between nucleons in the nucleus so that the neutrino interacts with a single nucleon only. However, including such correlation effects would mean that a neutrino can interact with multiple nucleons in a meson exchange current (MEC) process. This is supported by the tension between existing models and data from experiments such as MiniBooNE [28]. NEUT simulates the MEC process using a model by Nieves et al. [135]. Although effects between bound nucleons should be

present in all types of interactions, NEUT only simulates the effect for this CC process.

5.3.3 Single Meson Production

The dominant hadron production mechanism below a hadronic invariant mass of 2.0 GeV/c^2 is single meson production. This process produces a meson via the decay of an intermediate baryon resonance as shown in Equation 5.3

$$\begin{aligned} \nu + N &\rightarrow l + N^* \\ N^* &\rightarrow N' + meson, \end{aligned} \tag{5.3}$$

where N is the initial nucleon, N^* is the baryon resonance and N' is the outgoing nucleon. NEUT assumes one meson is generated by the decay of the resonance. The simulation of this process is based on Rein and Sehgal's model [146].

5.3.4 Coherent Pion Production

Coherent pion production occurs when a neutrino interacts with a nucleus as a whole, the nucleus remains the same with a very small momentum transfer from the neutrino and a pion is produced with the same charge as the exchanged boson. As there is a small momentum transfer to the nucleus, the outgoing lepton and pion will be very forward-going with respect to the initial neutrino direction. Coherent pion production is simulated in NEUT using a modified version of the Rein and Sehgal model [147].

5.3.5 Deep Inelastic Scattering

At high neutrino energies where the energy of a neutrino is much larger than the mass of a nucleon ($E_\nu >> m_N$) the dominant scattering process is deep inelastic scattering (DIS). In this process the particle interacts with the quarks inside a nucleon, breaking it up, resulting in a number of final state hadrons. NEUT simulates this interaction for hadronic systems with an invariant mass higher than 1.3 GeV/c^2. The nucleon structure used for this interaction is taken from the parton distribution function GRV98 [87] with corrections by Bodek and

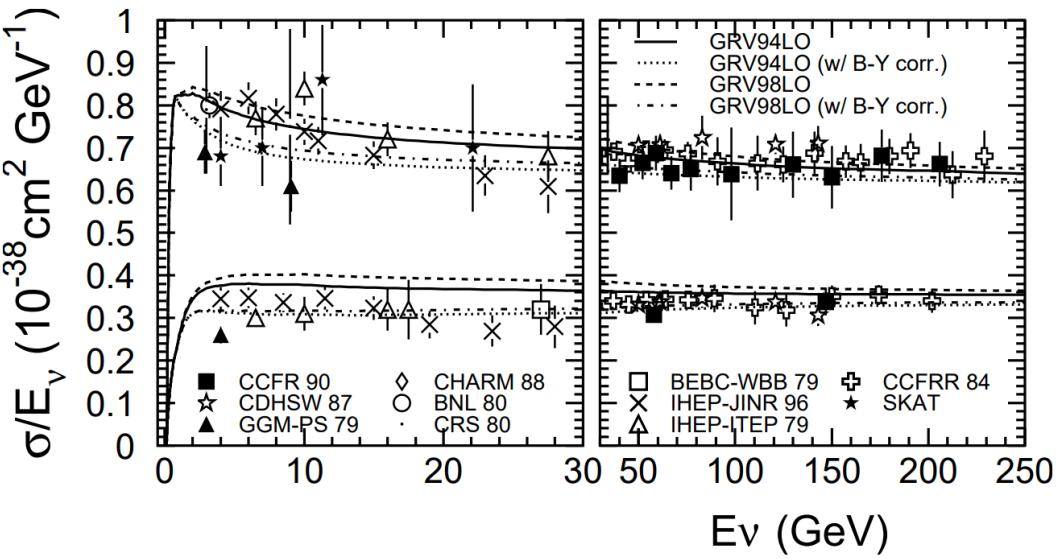

Figure 5.9 *The total charged current neutrino (upper) and antineutrino (lower) cross sections. Lines show the models used and the points represent data from several experiments. Taken from Ref [96].*

Yang [51] which give better agreement with experimental data in the low q^2 region.

As there is an overlap in the invariant mass (W) ranges used for single pion production ($W \leq 2$ GeV/c ^{2}) and DIS ($W > 1.3$ GeV/c^2) a precaution is taken in order to avoid double counting. NEUT calculates the probability of generating more than one pion when $W < 2$ GeV/c^2. Figure 5.9 shows the total CC cross sections including quasi-elastic scattering, single meson production and DIS processes.

5.3.6 Nuclear Effects

Once NEUT has simulated the neutrino interaction with bound nucleons the resulting hadrons may interact within the nucleus (^{16}O in SK). NEUT simulates the propagation of pions, kaons, η-mesons and nucleons using cascade models until the hadrons are either absorbed or leave the nucleus.

For neutrino energies larger than 1 GeV the pion production cross section is large, as is the pion-nucleon interaction cross section. The pion's interaction within the nucleus must be understood in order to relate the observed final state particles in the detector to the initial neutrino interaction.

Pions in the NEUT simulation can interact in several different ways; NEUT considers the interaction of pions, elastic scattering, charge exchange, absorption and multiplication in the nuclear medium. The probabilities for each type of interaction have been tuned using measurements from scattering experiments. Figure 5.10 shows the results of a NEUT simulation compared to experiment data. Similar cascade models and tuning is carried out in order to simulate kaons, η-mesons and nucleons leaving the nucleus (see Reference [96] for more details).

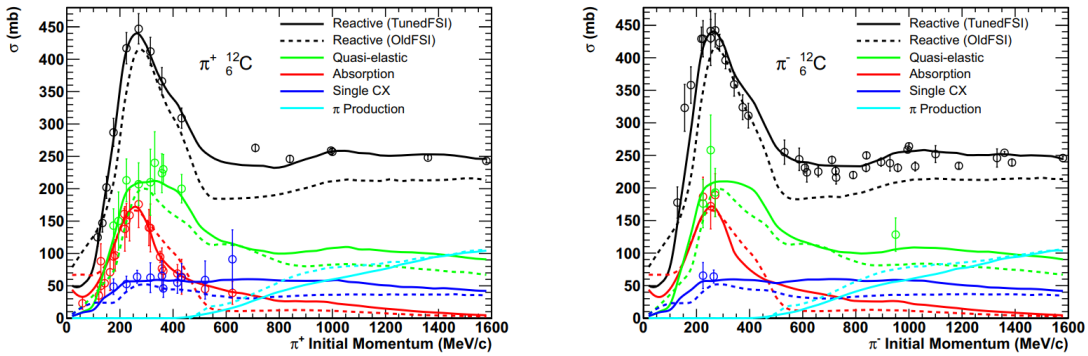

Figure 5.10 *NEUT simulation of π-^{12}C scattering compared to experiment data [38, 43, 80, 114, 122] for π^+ [left] and π^- [right]. Taken from Ref [65].*

5.4 Detector Simulation: SKDETSIM

The final stage of the MC simulation is to simulate the final state particles' interaction in the detector volume and the detector response. The particles resulting from the neutrino and nuclear interactions from NEUT are propagated into a custom GEANT3-based [53] detector simulation called SKDETSIM.

The particles' interaction with water, their decays, Cherenkov photon production and propagation are all simulated by GEANT. The hadronic interactions are simulated by GCALOR [86] except for pions below 500 MeV/c where the NEUT cascade model is used instead.

The propagation of Cherenkov photons is dependent on the transparency of the water. The photons can either be absorbed or undergo Rayleigh or Mie scattering. The calibration described in Section 4.2 is used to model the photon propagation in the simulation. Absorption and reflection in detector surfaces is modelled using

calibration measurements [12]. The response of the PMTs is simulated using the calibration measurements described in Chapter 4.

Chapter 6

Event Selection

The trigger system of SK fires 10^6 times per day. Approximately 10 atmospheric neutrinos, 20 solar neutrinos and 10 beam neutrinos are expected to be detected each day. Figure 6.1 shows an atmospheric neutrino event on the SK event display. The majority of triggers are due to cosmic muons passing through the tank and low energy radioactive decays. In order to filter out candidate neutrino interactions, the data undergoes several reduction steps.

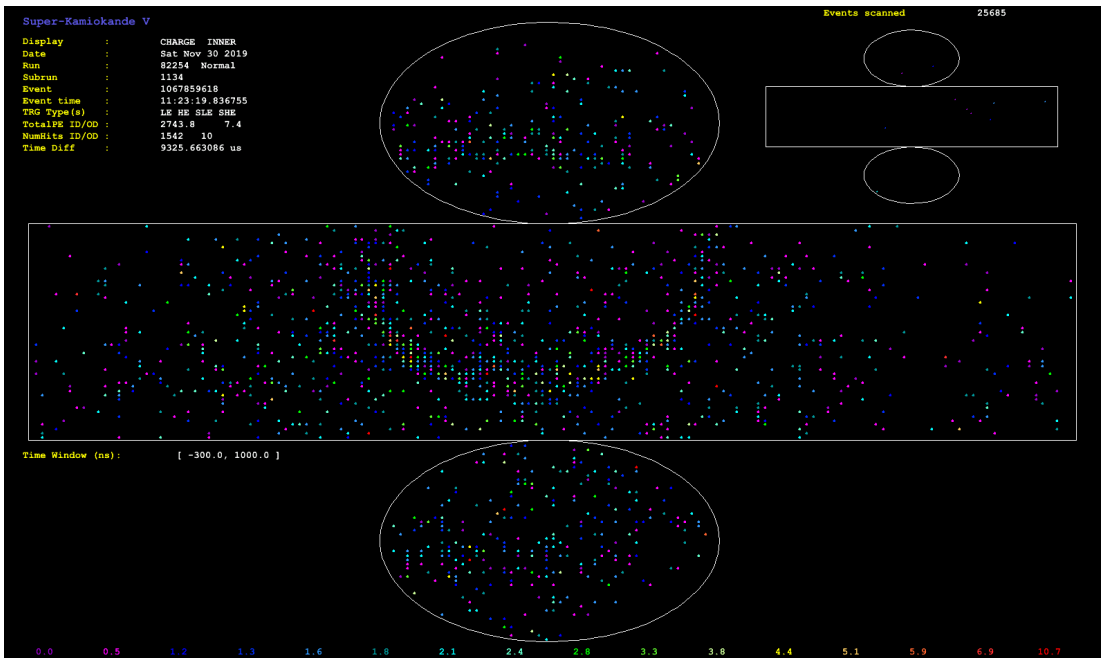

Figure 6.1 *An atmospheric neutrino event, detected in SK-V, shown on an event display*[1].

[1]As the Super-K event display shows events at a rate of 0.3 Hz, observing a neutrino event on screen is unlikely. The author of this thesis was fortunate enough to observe this event "live"

There are four main event classifications which can be seen in Figure 6.2: fully-contained (FC), partially-contained (PC) and upward-going muons (UPMU), which are separated into stopping and through-going events. FC events have a neutrino interaction vertex inside the fiducial volume of the detector and all secondary particles remain in the ID. PC events also have an event vertex inside the fiducial volume but secondary particles exit the ID and enter the OD. UPMU events are muons produced by neutrino interactions in the surrounding rock which then enter the tank. Rock muons are also produced above the detector but are indistinguishable from cosmic muons so this sample is restricted to upwards-going muons.

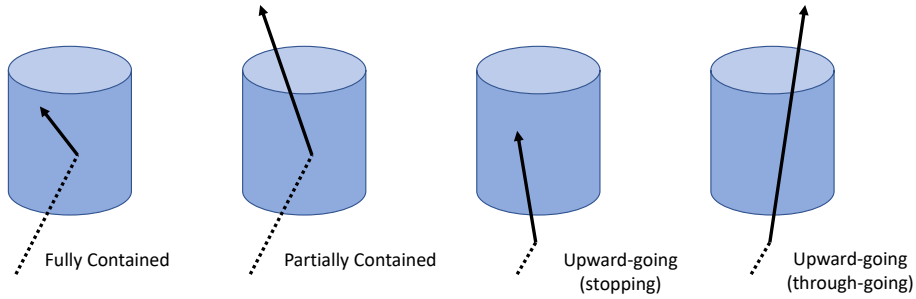

Figure 6.2 *Different event classifications in Super-K. The dashed lines show the neutrino path whereas the solid lines show the path of secondary particles.*

The process of removing background events from the data is referred to as data reduction. Each class of events has its own reduction process which will be explained in this chapter. The reduction process is applied to the full SK dataset with many of the cuts being applied to all of the SK periods, however some of the cuts are tuned such that the rejection power is similar between running periods. The main differences arise in reduction steps involving the ID during SK-II. During this period the photocoverage was roughly half of that in other periods so the cuts are half of their typical values.

The cuts stated in this chapter indicate the requirements for an event to remain in the data sample. Events not satisfying the cuts shown are rejected. For each step of the data reduction, an efficiency calculation is carried out. The reduction efficiency is estimated by applying the reduction to simulated atmospheric neutrino events and determining the percentage which survive the cuts. The values for the reduction efficiency quoted in this chapter apply to SK-IV. However,

as it showed up in real-time.

similar values were found the other SK periods.

6.1 Fully-Contained Reduction

The FC reduction is divided into five stages, FC1 to FC5. If an event passes the criteria for a reduction stage it then moves on to the next reduction stage. This staged approach optimises the processing time.

6.1.1 FC1

This reduction step is used to filter out obvious high energy backgrounds such as cosmic muons as well as the low energy backgrounds such as radioactivity or solar neutrinos.

The first step in this stage of the reduction removes low energy events and ensures that there is enough activity in the ID, the criteria for this is:

1. Total number of photoelectrons in the inner detector in a sliding 300 ns time window must be larger than 200 (100 for SK-II).

The next step is to use OD information to remove events consistent with an incoming cosmic muon or an exiting particle. The following cuts are applied:

2. The number of OD PMTs hit must be larger than 0.
3. The number of OD hits in a time window -500 ns to +300 ns must be ≤ 50 (55 for SK-IV).

Cut 2 ensures that the OD is functioning correctly. At the start of SK-IV the OD electronics boards had been changed and the gains of the PMTs had also changed. This cut was tuned to reject similar muon energies as previous SK periods.

This reduction step reduces the event rate from 10^6 events per day to 2,500 events per day. The reduction efficiency for this step is estimated to be 100%.

6.1.2 FC2

This reduction step is designed to remove electrical noise as well remaining high energy backgrounds. Events due to electrical noise typically have the majority of charge deposited in one PMT. To remove these events the following cut is applied:

4. The number of photoelectrons from any single PMT should be less than half of the total number of photoelectrons in the ID in that event.

Some fully contained events with a high enough energy can cause hits in the OD through ID-OD crosstalk, this is discussed further in Section 6.4. The following cuts are applied to tighten cut 3, removing cosmic muon events while allowing very high energy events which may leak current into the OD.

5. One of the following conditions must be satisfied
   (a) The number of photoelectrons in the ID is larger than 100,000 (50,000 for SK-II).
   (b) The number of OD hits in a time window -500 ns to +300 ns must be ≤ 25 (30 for SK-IV).

This reduction step reduces the event rate to 500 events per day. The efficiency for this step is estimated to be 100%.

6.1.3 FC3

The third stage of reduction is designed to target specific types of background events and so the cuts are more complicated than the first two reduction stages. The first step in this stage of the reduction is to remove very high energy cosmic muons with energies $E_\mu \geq 1$ TeV. At this energy the muons undergo Bremsstrahlung [117]. The photon produced in this process may then undergo pair conversion. The resulting shower of particles will give a large number of hits in a short time. The following cut removes these "hard" muon events:

6. The number of OD PMTs hit within a 500 ns sliding time window must be less than 40.

If the ID contains more than 231 photoelectrons spread out over at least 1000 tubes a fitter is used to look for a through-going muon. The fitter finds two clusters in the OD, corresponding to the entry and exit points, separated by a reasonable travel time. After the fitter has been applied the following cut is used to remove through-going muons:

7. One of the following conditions must be satisfied
   (a) The goodness of fit must be less than 0.75.
   (b) Less than 10 hit OD PMTs in each PMT cluster (< 8 m radius from entry/exit point) in the 800 ns time window.

Similar cuts are used to remove stopping-muons which have an entry point but no exit point. The cuts used are:

8. One of the following conditions must be satisfied
   (a) The fitter must not find an entry point (goodness of fit < 0.0).
   (b) Less than 10 hit OD PMTs in the PMT cluster (< 8 m radius from entry point) in the 800 ns time window.

The next cut removes remaining low energy backgrounds by applying a time-of-flight (TOF) fitter to obtain an event vertex. All hits are TOF corrected and the event must then satisfy the criterion:

9. The number of hits in the ID in a sliding 50 ns time window must be larger than 50 (25, for SK-II).

The following cuts are used to remove PMT flasher events [165]. These are events where electrical discharge inside the PMT causes light to be emitted into the tank. The time distribution of the hits is typically longer in flasher events so the following criteria are used to reject them:

10. For (SK-I) one of the two conditions must be satisfied
    (a) The minimum number of hits in the ID in a 100 ns sliding time window between +200 ns→+700 ns must be less than 10.

(b) The above cut is relaxed to 15 if the total number of hits in the ID is larger than 800.

11. For (SK-II to SK-IV)

    (a) The minimum number of hits in the ID in a 100 ns sliding time window between +200 ns→+700 ns must be less than 20.

The final cut used to remove flasher events is to require the goodness of the TOF vertex fitter to be larger than 0.4. This cut removes low-energy flasher events which may pass the other criteria. The wide time distribution of flasher events would be difficult to fit to a single vertex position often resulting in a poor goodness of fit.

As the rate of low-energy triggers is high, the coincidence rate of cosmic muons with these is significant. Such coincidence muons allow these events to pass the low energy cuts as there is light deposited into the ID by the muon. Additionally, these events are not removed by the high energy cuts as the low energy trigger occurred before the OD activity. Such events are removed using the following criteria:

12. One of the following conditions must be satisfied

    (a) The number of hits in the OD between +300 ns and +800 ns must be less than 20.

    (b) The number of photoelectrons in the ID between +300 ns and +800 ns must be less than 5,000 (2,500 for SK-II)

The final cut applied in this reduction stage is used to reject a type of cosmic muon background. The Super-K PMT cables go up the sides of the Super-K tank in bundles and are fed through 12 (4 large and 8 small) cable holes at the top. Due to the size of the cable bundles it is possible for muons to pass through some dead regions in the OD where they would not be detected and could appear as fully contained events. Such muons are referred to as cable muons. In an effort to remove this kind of background large scintillators were placed above each of the four large cable holes (the smaller holes are dealt with in FC5). The following cuts are then applied:

13. One of the following conditions must be satisfied

(a) The veto counter (scintillator) must not register any hits

(b) The entry point given by the stopping muon fitter must be more than 4 m away from the large cable holes.

14. For SK-IV additional tighter cuts are applied. One of the following conditions must be satisfied

(a) The goodness of fit must be less than 0.4

(b) The total number of photoelectrons in the ID must be less than 4,000

(c) $\cos(\theta) \geq -0.6$ where θ is the muon's zenith angle

(d) The entry point must be at least 2.5 m away from the nearest cable hole.

This reduction step reduces the event rate to ∼50 events per day and has an estimated efficiency of 99.8%.

6.1.4 FC4

The fourth reduction stage is designed to remove the flasher events which have survived the previous cuts. The light pattern of flasher events are quite similar and so they can be removed using a pattern recognition algorithm which divides the tank into a grid of 1,450 4 m^2 patches. For any two events, A and B, a parameter r is calculated:

$$r = \frac{1}{N} \sum_{i}^{N} \frac{(Q_i^A - \langle Q^A \rangle) \times (Q_i^B - \langle Q^B \rangle)}{\sigma^A \sigma^B} \tag{6.1}$$

where N is the number of patches, Q_i is the number of photoelectrons in patch i and σ is the standard deviation of Q_i. A second parameter is calculated, for these two events, which compares the time distribution of the hits using Kolmogorov-Smirnov[151] test. A third parameter finds out if the flashing tubes (tubes with the highest number of photoelectrons) in both events are closer than 75 cm. These three parameters are combined into a single likelihood function. Events which have a likelihood value above a tuned cut are rejected.

This reduction step reduces the event rate to ∼32 events per day. The efficiency for this step is estimated to be 99.6%.

6.1.5 FC5

The final fully contained reduction step aims to remove remaining muon backgrounds and flasher events. The first background is referred to as an invisible muon. These events contain a muon below the Cherenkov threshold which enters the tank and decays into an electron that is above Cherenkov threshold. Such decay electrons can appear as fully contained events. To remove this topology the following cut is applied:

15. One of the following conditions must be satisfied

    (a) The total number of photoelectrons must be larger than 1000 (500 for SK-II).

    (b) Less than 5 OD PMTs must be hit in a sliding 200 ns time window between -9000 ns and +200 ns.

    (c) When the distance between two OD clusters is less than 0.5 m, cut 15b plus the number of OD tubes hit between -200 ns and 300 ns must be less than 10.

For a muon to reach the fiducial volume it must be above the Cherenkov threshold in the OD so some light is expected. Cut 15 allows events where there is insignificant early OD activity or events where the electron is above the Michel electron energy.

The next cut targets the remaining coincidence muon events, which are removed by the following criteria:

16. One of the following conditions must be satisfied

    (a) Less than 20 OD PMTs must be hit in a sliding 200 ns time window between +300 ns and +2100 ns.

    (b) The total number of photoelectrons in the ID must be larger than 300 (150 for SK-II).

This cut scans over a longer time range and removes events with significant late OD activity if the event was triggered by the SLE trigger.

For SK-IV a new cut was introduced to remove muons which travel through the eight smaller cable holes not covered by a veto counter. In addition to cut 14 in FC3 the following criteria is also applied:

17. Less than 4 OD tubes hit in an 8 m radius from the reconstructed entry point in a 200 ns sliding time window between -500 ns and +300 ns.

Lastly some tighter cuts are applied to remove flasher events. The cuts applied are:

18. One of the following conditions must be satisfied
    (a) The time of flight goodness of fit must be less than 0.4.
    (b) The minimum number of photoelectrons in a sliding 100 ns time window between +200 ns and +700 ns must be less than 6.

For SK-II and SK-IV the following additional cuts are applied:

19. Both of the following conditions must be satisfied
    (a) The time of flight goodness of fit must be larger than 0.3.
    (b) The minimum number of photoelectrons in a sliding 100 ns time window between +200 ns and +700 ns must be ≥ 6.

This reduction step reduces the event rate to $\sim$20 events per day. The reduction efficiency for this step is estimated to be 99.9%.

6.1.6 FC Data Sample

Only events passing FC1 to FC5 are considered for further analysis. In order for the events to be used in the atmospheric neutrino analyses the following criteria must be satisfied:

20. All of the following conditions must be satisfied
    (a) The visible energy must be above 30 MeV.

(b) Less than 16 (10 for SK-II) hits in cluster of OD hit PMTs.

(c) The reconstructed neutrino vertex must be at least 2 m away from the tank walls.

These final criteria are expected to remove the majority of the remaining low energy background events. The final event rate after all of the selection criteria is around 8 events per day with a reduction efficiency of 98.5%.

The events in the FC data sample are then scanned by eye in order to tag any remaining cosmic muon or flasher backgrounds. These backgrounds are not removed from the data sample, they are only tagged to give an estimate of background contamination. Table 6.1 shows a summary of the FC reduction throughout the various SK phases.

Table 6.1 *The final event rates, reduction efficiencies and background contamination after the fully contained reduction steps. Shown for SK-I to SK-IV. SubGeV refers to events with a visible energy below 1.3 GeV and Multi GeV refers to events with a visible energy above 1.3 GeV.*

Phase	Event Rate [Day^{-1}]	Efficiency [%]	Background [%]			
			Flashers		Cosmics	
	Data		Sub GeV	Multi GeV	Sub GeV	Multi GeV
SK-I	8.26±0.07	99.25	0.1	0.5	0.2	0.3
SK-II	8.28±0.10	99.95	0.4	0.2	0.2	0.2
SK-III	8.41±0.13	99.62	0.1	0.2	0.3	0.3
SK-IV	8.14±0.09	99.19	0.1	0.1	0.1	0.1

6.2 Partially Contained Reduction

Just as with the FC reduction, the PC reduction is divided into five stages, PC1 to PC5. If an event passes the criteria for a reduction stage it then moves on to the next reduction stage. PC events, by definition, cause light in the OD and so the PC reduction steps are very different to the FC reduction.

6.2.1 PC1

The cuts in this reduction step are quite basic and aim to remove through-going muons and low energy backgrounds. Firstly, the total number of photoelectrons in the inner detector must be larger than 1000 (500 for SK-II).

Partially contained muons must travel at least 2 m through the ID in order to reach the OD, this corresponds to a momentum loss of around 500 MeV/c. The 1000 photoelectron cut corresponds to a muon momentum loss of 310 MeV/c.

The next cut aims to remove through-going muon events with multiple clusters in the OD by requiring

1. The RMS of OD hit times must be less than 260 ns (170 ns for SK-II).

For SK-I and SK-II a simple clustering algorithm is applied and the following cut is applied

2. The number of clusters in the OD must be 1.

Since SK-III the OD has been segmented and through-going muons became easier to remove by requiring that

3. There must be less than 10 hit OD tubes in either endcap.

4. One of the following conditions must be satisfied
   (a) The number of OD hit tubes in both of the endcaps must be less than 25.
   (b) The number of OD hit tubes in the barrel portion of the OD should be less than 70.

A variable, ODR_{mean}, the average distance between all hit pairs, is introduced. The value is defined as

$$ODR_{mean} = \frac{1}{N_{pair}} \sum_{i=1}^{N-1} |\vec{x_i} - \vec{x_j}|. \tag{6.2}$$

The following cut is then applied:

5. If the number of OD hits in a 500 ns time window is less than 20, then ODR_{mean} must be less than 2100 cm.

This reduction step reduces the event rate to 20,000 events per day.

6.2.2 PC2

The second stage of reduction aims to reduce some of the muon backgrounds. Firstly, events must pass the following criteria:

6. One of the following conditions must be satisfied
   (a) The number of OD hit tubes in the endcaps must be less than 20.
   (b) The number of OD hit tubes in the endcaps must be less than $\mathrm{MAX}(\mathrm{NA}_s)$

The parameter $\mathrm{MAX}(\mathrm{NA}_s)$ is defined as

$$MAX(NA_s) = e^{\alpha - \beta \times NA_s} \tag{6.3}$$

where $(\alpha, \beta) = (5.8, 0.023)$ for $NA_s < 75$ and (4.675, 0.008) otherwise.

A clustering algorithm is then used to apply the following cut

7. The second highest charge cluster in the OD must have 10 hit tubes or less.

This reduction step reduces the event rate to 8000 events per day.

6.2.3 PC3

Similarly to the FC3 cut, this reduction step is designed to remove flasher events using the broad timing distribution of these events. This cut requires that

8. One of the following conditions must be satisfied

(a) The minimum number of hit ID PMTs in a sliding 100 ns window from +300 ns to +800 ns must be less than 14.

(b) The number of hit ID PMTs in the same sliding time window is less than 9 if the overall number of hit ID PMTs is less 800.

6.2.4 PC4

This stage of the reduction makes use of an event reconstruction algorithm. Events are fitted and classified as: stopping muons, through-going muons, multiple muons or corner clipping muons. The following cuts are then applied

9. If the event is classified as a through-going muon then it must pass 4 out of the following 5 criteria. If it is classified as a stopping muon then it should pass 4 out of the 5 criteria, including cut 9b. For other event classifications only 2 of the following 5 criteria need to be passed.

   (a) The angle between the reconstructed muon direction and the vector between the vertex and the centre of the highest OD charge cluster must be less than 90°.

   (b) A similar cut to above is applied using the earliest saturated ID PMT instead of the centre of the highest charge OD cluster.

   (c) The reconstructed muon track length must be less than 1750 cm

   (d) The goodness-of-fit must be less than 0.52.A good fit indicates a cosmic muon.

   (e) The distance between the entry point and the corner of the tank must be at least 3 m

For stopping muons the following criteria is also applied

10. One of the following conditions must be satisfied:

    (a) The number of OD hits within 8 m of the entry point in a fixed 500 ns time window must be less than 10.

    (b) The goodness-of-fit must be less than 0.5.

Finally, low energy events are removed by requiring that

11. The total number of photoelectrons in the ID must be at least 2900.

This final cut corresponds to a muon momentum of roughly 500 MeV/c whereas a muon must have a momentum roughly 700 MeV/c in order to reach the OD.

6.2.5 PC5

The cuts in PC5 are more complex and aim to remove remaining muon backgrounds. In this reduction step there are two types of cuts: *hard cuts* and *soft cuts*. If an event fails a hard cut then it is rejected, however events are allowed to fail only one soft cut.

The hard cuts are:

12. All of the following conditions must be satisfied:
    (a) All of the following criteria must be satisfied:
        i. The distance between the highest and second highest charge OD clusters must be at most 20 m apart.
        ii. The number of photoelectrons in the second highest charge OD cluster must be less than 10.
        iii. There must be no more than one OD cluster with more than 9 hit OD tubes.
    (b) All of the following criteria must be satisfied:
        i. One of the endcaps must have less than 7 OD hit tubes.
        ii. One of the endcaps must have less than 10 photoelectrons.
        iii. The difference between the averaged hit time in each OD endcap is multiplied by the speed of light and divided by 40 m. This value must be less than 0.75 or larger than 1.5. This checks to see if the time difference is consistent with a vertical muon passing through the endcaps.
    (c) The angle between the Cherenkov ring direction and the vector between the vertex and the OD cluster should be less 90° for either of the two fitters used in this cut.
    (d) If there is a veto counter hit then the dot product between the muon direction and the vector between the vertex and the veto counter must be larger than -0.8.

(e) The distance between the reconstructed vertex and the edge of the ID must be larger than 1.5 m

Cut 12a removes through-going muons based on the clustering of OD hits. Through-going muons sometimes pass through the edge of the ID and travel vertically downwards. Such events are difficult to reconstruct so they may still appear in the sample, cut 12b removes such events. Stopping muons should be travelling in the opposite direction of the OD charge cluster whereas PC events should have a small angle between the muon direction and the vector between the vertex and the OD cluster. Cut 12c ensures that the angle is small and removes stopping muons. Unlike FC events, it is possible for a PC event to hit a veto counter, cut 12d requires that muon direction is not ant-parallel to the vector between the vertex and the veto counter. Cut 12e removes muons that clip the corner of the tank.

The soft cuts are:

13. All but one of the following conditions must be satisfied

    (a) Both of the following conditions must be satisfied:

        i. The number of OD hits within an 8 m radius of either the entry or exit points must be less than 5.

        ii. The difference between the averaged hit time in the entry and exit points is multiplied by the speed of light and divided by the muon track length. This value must be less than 0.75 or larger than 1.5. This checks to see if the time difference is consistent with a vertical muon passing through the entry and exit points.

    (b) The number of hit tubes in the highest charge cluster should be less than 10 or the number of hit tubes in the second largest cluster should be less than 17.

    (c) The number of OD hit PMTs within an 8 m radius of the entry point should be less than 10.

    (d) If the stopping muon goodness-of-fit is larger than 0 then both conditions must be satisfied:

        i. A 42° angle cone in the ID, facing the entry point, should contain less than 60% of the total number of photoelectrons in the ID.

ii. The total number of hit OD tubes within an 8 m radius of the entry point should be less than 7.

(e) If the reconstructed vertex of both fitters agree within 15 m then the number of OD hit tubes within an 8 m radius of the entry point should be less than 7.

(f) The angle between the reconstructed muon direction and the vector between the vertex and the centre of the highest OD charge cluster must be less than 90°. This cut was also used in PC4.

(g) If the track length is estimated to be larger than 15 m then another track length is calculated using the visible energy and a loss of 2 MeV/cm. This visible energy track length should be larger than the reconstructed track length minus 15 m.

(h) If the visible energy is above 25 GeV then there must be at least 1 decay electron.

The stopping muon fitter takes the earliest cluster in the ID as the estimated entry point. For PC events the fitting doesn't do so well (as the vertex is far from the wall) but if the goodness of fit is above 0, cut 13d is applied to remove stopping muons.

While most of the corner clipping muons have been removed in PC2 and PC3, some remain. These corner clipping muons leave a small cluster in the ID which can sometimes be reconstructed as an event originating in the tank. The reconstructed track length is often large so cut 13g is used to reject them. High energy neutrinos (above 25 GeV) mainly interact through DIS interactions and so hadrons (mainly pions) are produced which then decay to electrons. Cut 13h is applied to remove cosmic muons which don't satisfy this criteria.

6.2.6 PC Data Sample

After the reduction process, just as with the FC sample, further cuts are applied to create a final dataset.

14. The visible energy must be above 350 MeV.

15. More than 15 (9 for SK-II) hits in cluster of OD hit PMTs.

16. The reconstructed neutrino vertex must be at least 2 m away from the tank walls.

The final rate after these selection criteria is ∼1 event per day. The events in the PC data sample are scanned by eye in order to tag any remaining cosmic muon background. Table 6.2 shows a summary of the PC reduction throughout the various SK phases.

Table 6.2 *The final event rates, reduction efficiencies and background contamination after the partially contained reduction steps. Shown for SK-I to SK-IV.*

Phase	Event Rate [Day^{-1}] Data	Efficiency [%]	Background [%] Cosmics
SK-I	0.66±0.02	80.98	0.2
SK-II	0.65±0.04	74.80	0.7
SK-III	0.62±0.03	88.80	1.8
SK-IV	0.66±0.02	86.30	0.6

6.3 Upward-going Muon Reduction

6.3.1 Charge Cuts

The first cuts applied in the UPMU reduction are charge cuts. Low energy events are removed by requiring that the total number of photoelectrons in the inner detector is larger than 6000 (3000 for SK-II). This corresponds to a muon momentum of 1 GeV/c and a track length of 3.5 m. Extremely high energy events saturate the electronics to the point where the muon fitter does not work. Such events are removed by requiring that the total number of photoelectrons in the inner detector must be less than 1,750,000 (800,000 for SK-II).

6.3.2 Zenith Angle Cuts

The next set of cuts make use of seven different event fitters, each specialising in the fitting of stopping muons, through-going muons and very high energy muons with Bremsstrahlung.

Several muon fitting algorithms are applied sequentially to select upward-going events. For each algorithm, if the goodness of fit is above a threshold, the event is saved for a classification of upward-going or horizontal-going. If the event is classified as downward-going and satisfies the goodness of fit threshold, then the event is rejected. In the case where the goodness of fit threshold is not satisfied, the event is neither saved nor rejected and another muon fitting algorithm is applied.

This process continues until all of the fitting algorithms have been used. If none of the fitting algorithms gives a goodness-of-fit above the threshold then the event is rejected. If one of the fitting algorithms classifies an event as horizontal-going then the event is saved. To keep only the upward-going muons the events must pass the following zenith cut: $\cos\theta < 0$.

More information about the algorithms, fitters and thresholds used for this reduction step can be found in Reference [66].

6.3.3 Eye Scan

The final step of the UPMU reduction is to have two independent researchers use a visual display and reject background events that have been misclassified. The efficiency of this reduction step is estimated to be close to 100% with roughly half of the events reaching this stage being rejected.

6.3.4 UPMU Data Sample

Finally, the UPMU events are separated into stopping and through-going muons samples. The stopping muon samples must satisfy the following criteria to be used in the analysis:

1. Fitter must classify the event as a stopping muon.
2. The fitter momentum must be at least 1.6 GeV/c (7 m track length equivalent).
3. There must be less than 10 (16 for SK-II) hit OD tubes within 8 m of the fitter exit point.

Through-going muons must satisfy the following criteria in order to be used in the analysis:

4. All of the following criteria must be met
   (a) Fitter must classify the event as a through-going muon.
   (b) The distance between the ID entry and exit points must be at least 7 m.
   (c) At least 10 (16 for SK-II) OD PMTs must be hit within 8 m of the fitter exit point.

Table 6.3 shows a summary of event rates after the UPMU reduction.

Table 6.3 *The final event rates after the UPMU reduction steps. Shown for SK-I to SK-IV.*

Phase	Event Rate [Day^{-1}] Data
SK-I	1.41±0.03
SK-II	1.33±0.04
SK-III	1.49±0.05
SK-IV	1.45±0.03

6.3.5 Background Estimation for Upward-going Muons

Cosmic muons undergo multiple Coulomb scattering and can be reconstructed as upward-going muons (from neutrino interactions). The mis-classification of cosmic muons can also occur for horizontal muons which can also be reconstructed as upward-going. For this reason, most of the backgrounds are concentrated in the most horizontal zenith angle bin ($-0.1 < \cos\theta < 0$).

Background contamination is estimated by extrapolating to the downward-going region with $\cos\theta > 0$. Figure 6.3 shows the zenith and azimuth angles for stopping and through-going muon samples in SK-IV. Clusters can be seen in the downward-going ($\cos\theta \geq 0$) region at azimuth angles 120°, 180° and 270°. These clusters in azimuth angle correspond to regions of the surrounding rock which are relatively thin.

The muon samples are split into two distinct azimuthal regions. Region (1) is relatively thick mountain rock and region (2), where $60° < \phi < 310°$, represents

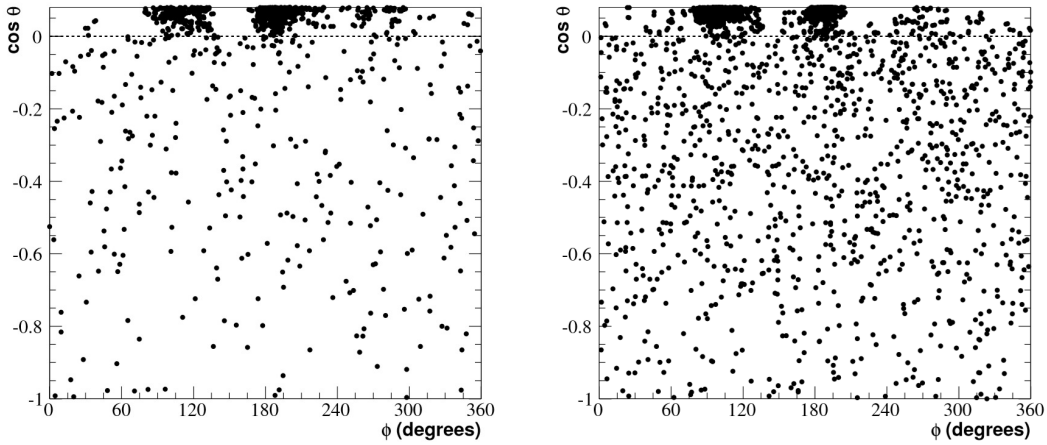

(a) *stopping muons* **(b)** *through-going muons*

Figure 6.3 *Distributions of the zenith angle vs azimuth angle for stopping muons and through-going muons. Taken from [143].*

the region with the relatively thin mountain rock. Figure 6.4 shows the azimuth distribution of stopping and through-going muon events.

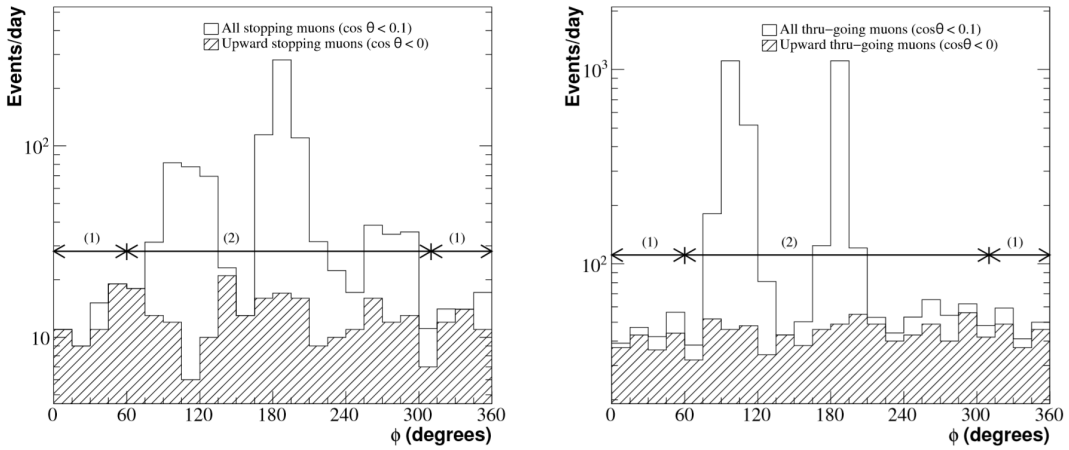

(a) *stopping muons* **(b)** *through-going muons*

Figure 6.4 *Azimuth angle distributions for stopping muons and through-going muons in SK-IV. Region (1) indicates a muon path through a thicker mountain region and region (2) indicates a muon path through a thinner mountain region. Taken from [143].*

Figure 6.5 shows the zenith angle distributions for the muon sample with regions (1) and (2) normalised by the coverage of the azimuth angle. It is clearly seen that the distribution is mostly flat for region (1) while for region (2) there is an exponential increase in the number of events as the zenith angle increases up to

downward-going events. A fit of the empirical function

$$f(\cos\theta) = p_0 + e^{p_1 + p_2 \times \cos\theta}, \tag{6.4}$$

to the zenith angle distribution shown in Figure 6.5, where p_0 is fixed to the average of the events in region (1). Background contamination is then estimated using

$$N_{background} = \int_{\cos\theta}^{0} e^{p_1 + p_2 \times \cos\theta}. \tag{6.5}$$

The uncertainties on the estimated number of background events are evaluated by modifying parameters p_0, p_1 and p_2 within their allowed regions. These background uncertainties are summarised in Table 6.4.

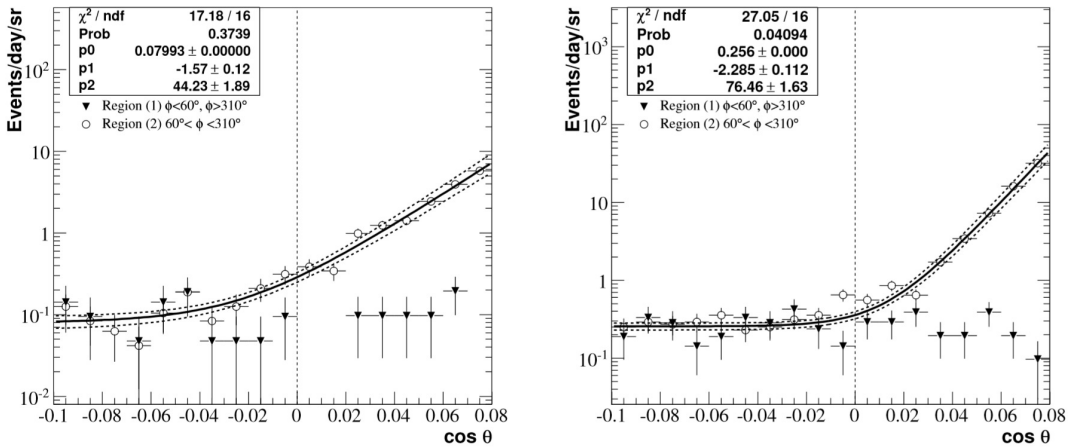

(a) *stopping muons* **(b)** *through-going muons*

Figure 6.5 *Background estimation for stopping (left) and through-going (right) muons in SK-IV. The plots show the zenith angle distributions for the muons. The black and white points show the data for regions (1) and (2) respectively. Region (1) indicates a muon path through a thicker mountain region and region (2) indicates a muon path through a thinner mountain region. A function is fitted (black solid line) to the data and used to estimate the background. Taken from [143].*

Table 6.4 *Summary of the uncertainties in the background contamination estimation for UPMU events between* $-0.1 < \cos\theta < 0$.

Event Type	SK-I	SK-II	SK-III	SK-IV
Stopping	16%	21%	20%	17%
Through-going Non-Showering	11%	15%	19%	14%
Through-going Showering	18%	14%	24%	20%

6.3.6 Through-going Showering Muons

Finally, the UPMU through-going sample is split into showering and non-showering samples. Muons at significantly high energies (above a few hundred GeV) lose energy through radiative processes such as Bremsstrahlung, electron-positron pair production as well as photo-nuclear interactions. It can be seen in Figure 6.6 that around 1 TeV, the radiative losses are roughly equal to the ionisation losses.

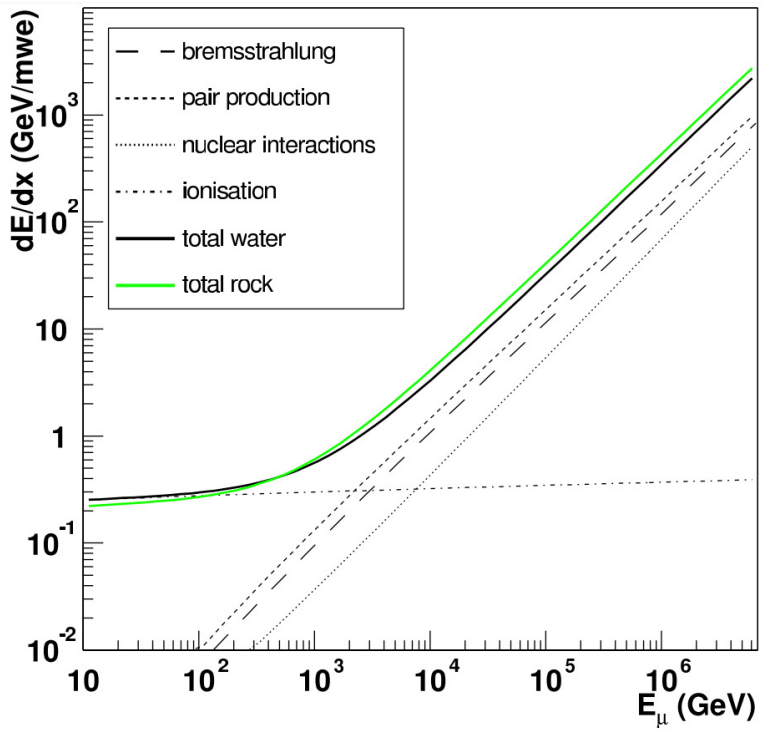

Figure 6.6 *The average energy loss per meter water equivalent for muons in rock (green) and sea water (black) as a function of muon energy. The contributions of the different processes are shown separately for water. This plot was generated using MUSIC,a muon propagation simulator. Taken from [98].*

Factors such as the water transparency and PMT acceptance affect the overall charge collected by PMTs. This introduces variations in the charge collected per unit track length for muons in the tank. Other considerations such as longer track lengths allowing for more light to be scattered into the projected Cherenkov cone also affect the non-uniformity.

These factors are used to correct the charge per unit track length for muons and to calculate the expected value of the corrected charge for a non-showering muon. Figure 6.7 shows that while a non-showering muon has a relatively uniform corrected energy loss per unit track length, showering muons have large deviations. The χ^2 from the fit is analysed and cuts applied to select showering events. The event is classified as a showering event if $\chi^2 \geq 50$ and $\Delta(Q)$, or if $\chi^2 < 50$ and $\Delta(Q) > 4.5 - 0.08\chi^2$; $\Delta(Q)$ is the difference between the corrected charge and the expected non-showering muon charge.

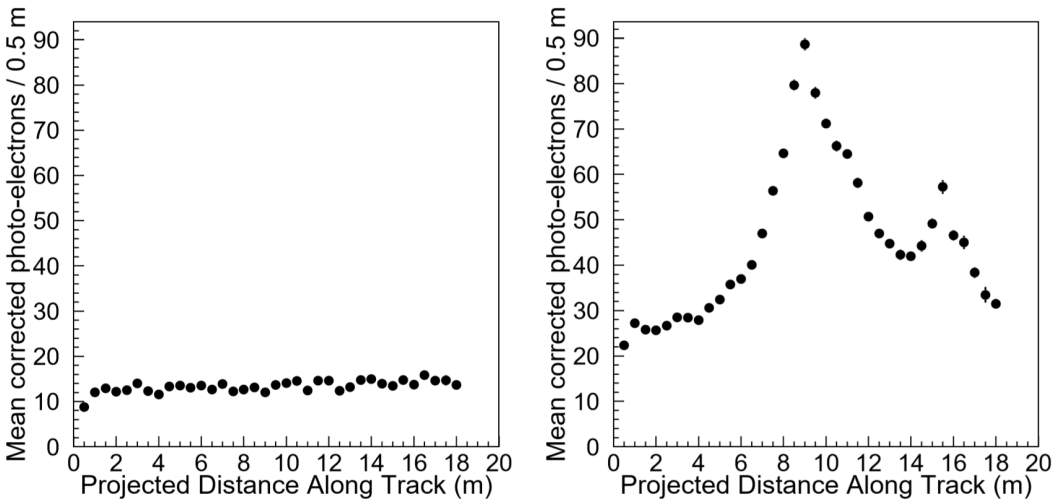

(a) *Non-showering muons* **(b)** *Showering muons*

Figure 6.7 *dE/dX distribution for an MC non-showering muon vs showering muon. Both muons have the same entry and exit point. Taken from [66].*

For more details on the χ^2 analysis, the charge correction and the overall UPMU reduction, the reader is referred to Reference [66].

6.4 ID OD Crosstalk Cuts

In addition to detection of photons or a PMT's dark rate, a PMT may sometimes register a charge if a nearby PMT registers a large enough charge; this is a process known as crosstalk. In Super-K this process occurs between nearby PMTs in the ID as well as between PMTs in the ID and OD. It is not clear whether this is due to the proximity of the PMTs themselves or if it is due to the proximity of the cables or other electronics.

Since the start of SK-IV it has been observed that FC events which deposit a large amount of charge in the ID were being mis-classified as PC events due to the large number of PMTs hit in the OD. These FC events have an OD hit pattern similar to that of the ID, an example of such an event can be seen in Figure 6.8. The crosstalk hits are all low charge hits which can be seen in the FC OD hit distributions in Figure 6.9.

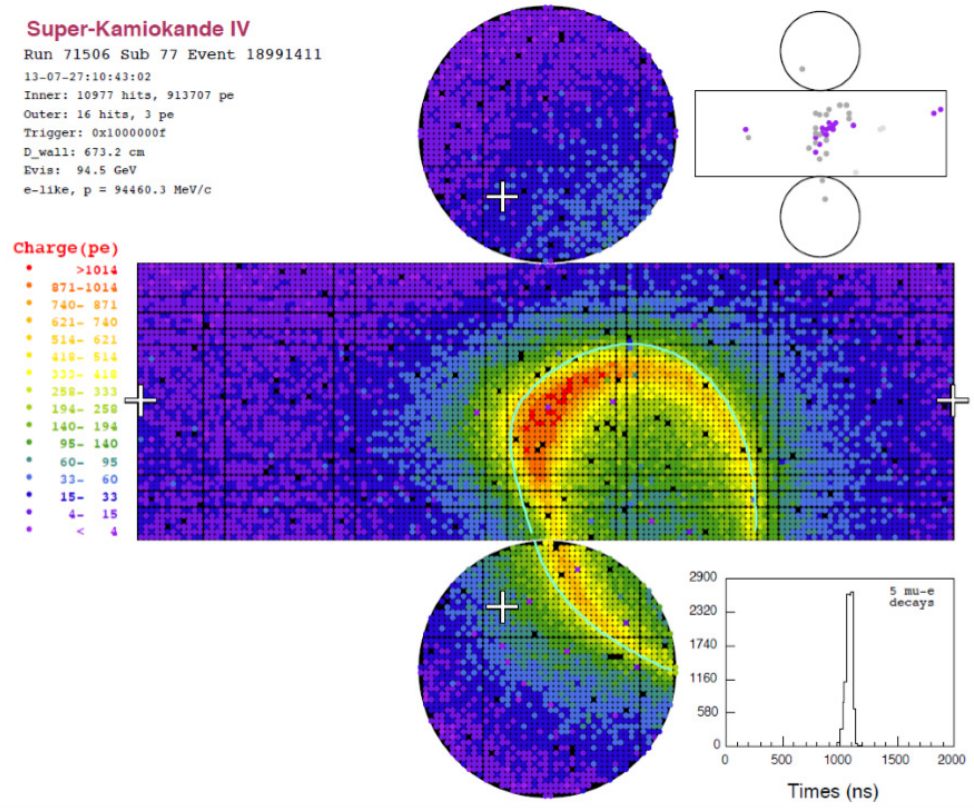

Figure 6.8 *A Super-K event display showing an FC e-like event with crosstalk between the ID and OD. The coloured circles represent hit PMTs, the large unfolded cylinder is the ID and the smaller unfolded cylinder in the upper right corner is the OD.*

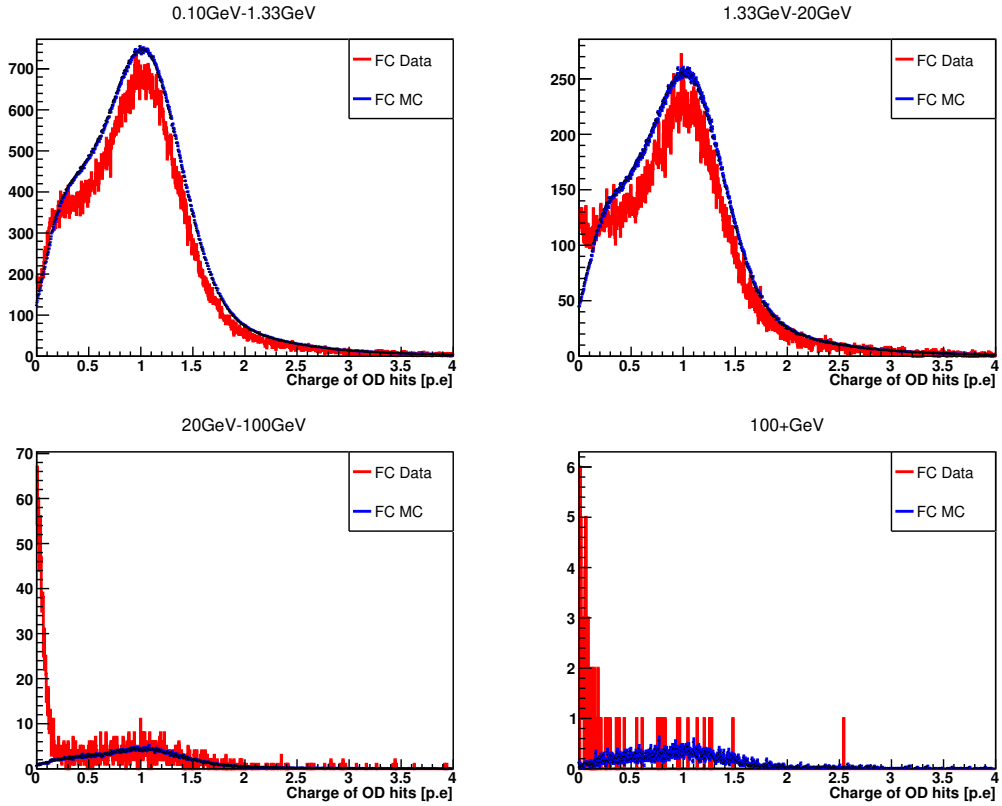

Figure 6.9 *Histograms showing the number of photoelectrons for each hit OD PMT in the FC data sample. Blue lines show the MC scaled by livetime to the data (red).*

6.4.1 Selecting a Cut

In order to deal with this issue the Super-K calibration laser data was taken using the setup mentioned in Section 4.1.2. The laser data is taken periodically with variable light intensity and should have little OD activity, making it ideal to study the crosstalk. Figure 6.10 shows an example laser event with many OD hits.

In order to differentiate the crosstalk hits from real OD hits, laser events were compared to PC events. The first step was to investigate the charge and time information of the OD hits. Charge distributions from the laser data as well as the charge information shown in Figure 6.9 show two key things. Firstly, assuming that there is enough charge to cause crosstalk, the crosstalk hit is always low in charge (< 0.5 photoelectrons) regardless of the amount of charge in the ID PMTs. Secondly, a higher ID charge increases the probability of crosstalk occurring.

The hit time distributions for the crosstalk events in Figure 6.11 show a delay

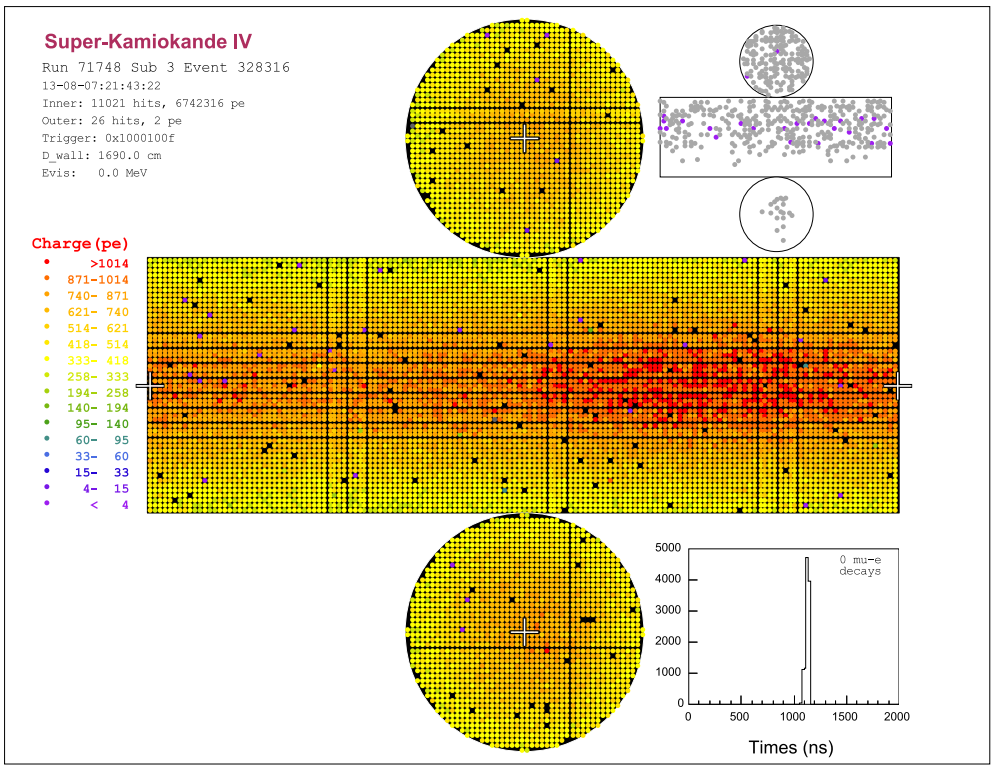

Figure 6.10 *A Super-K event display showing a laser event with crosstalk between the ID and OD. The coloured circles represent hit PMTs, the large unfolded cylinder is the ID and the smaller unfolded cylinder in the upper right corner is the OD.*

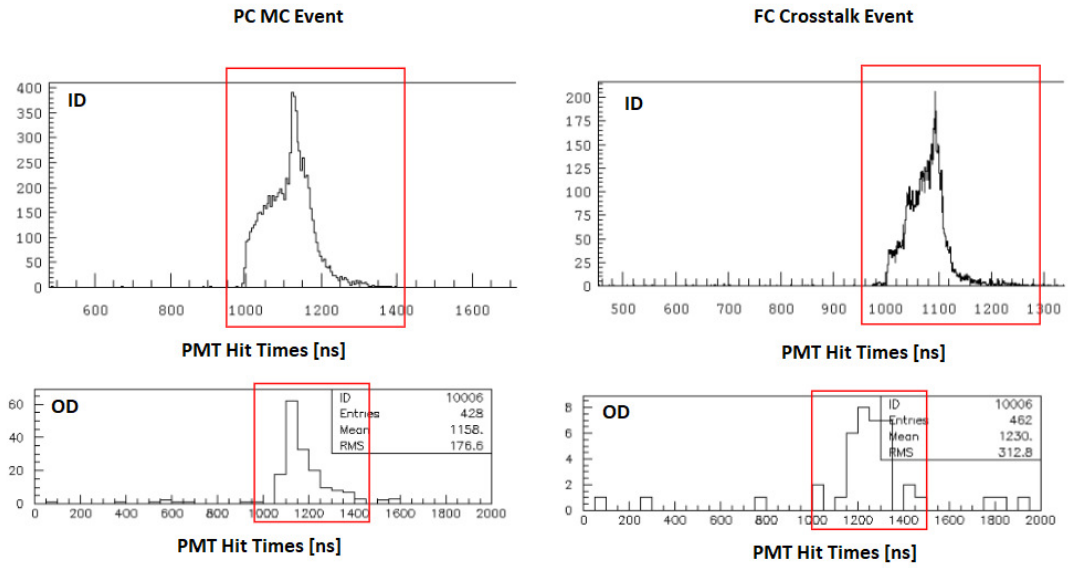

Figure 6.11 *The time distribution of PMT hits for a PC MC event on the left and an FC crosstalk event on the right. The top and bottom plots show ID and OD hits respectively.*

between ID hits and OD hits of roughly 100 ns which is not seen in PC events. To further investigate this time difference, OD hit times are compared to the hit times of nearby ID PMTs. This is defined as any ID PMT that is less than 90 cm away from the OD PMT. Nearly all of the OD PMTs are installed in the middle of four ID PMTs facing the opposite direction meaning they have four nearby ID PMTs. The time difference is defined as the time between an OD hit and its most recent nearby ID PMT hit. Nearby ID PMTs were chosen because the image in the OD is similar to that of the ID in these events, indicating that the phenomenon occurs close to the front end.

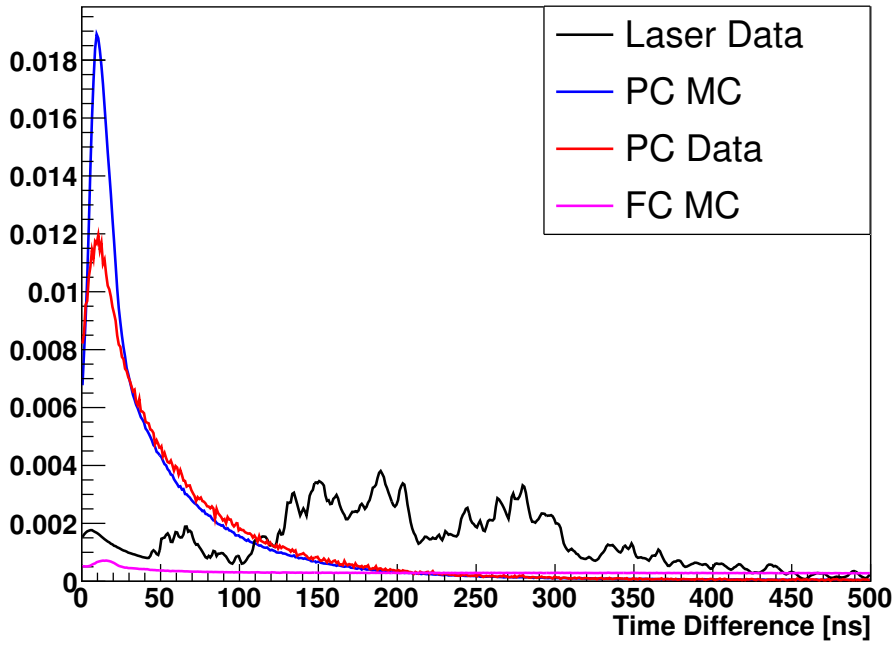

Figure 6.12 *A plot showing the time difference between OD hits and nearby ID hits for PC MC in blue, PC data in red and laser data in black. The histograms were normalised by area.*

Figure 6.12 shows a clear difference in the time difference variable between the crosstalk events and PC events, making it a good variable to use to discriminate between crosstalk and photons or dark noise. The final step was to look at distributions of the time difference versus charge so as to avoid removing real hits as much as possible. Figure 6.13 shows the distribution of the time difference versus the number of photoelectrons for each hit for laser data as well as PC MC.

The chosen cut removes any OD hit which is less than 0.2 photoelectrons and arrives more than 50 ns after its most recent nearby ID PMT hit. A criteria which is too loose would keep many crosstalk hits and a criteria which is too strict would

remove genuine hits left in the OD by PC events. This cut was chosen to reject as many crosstalk hits as possible while keeping the PC reduction efficiency at an acceptable level.

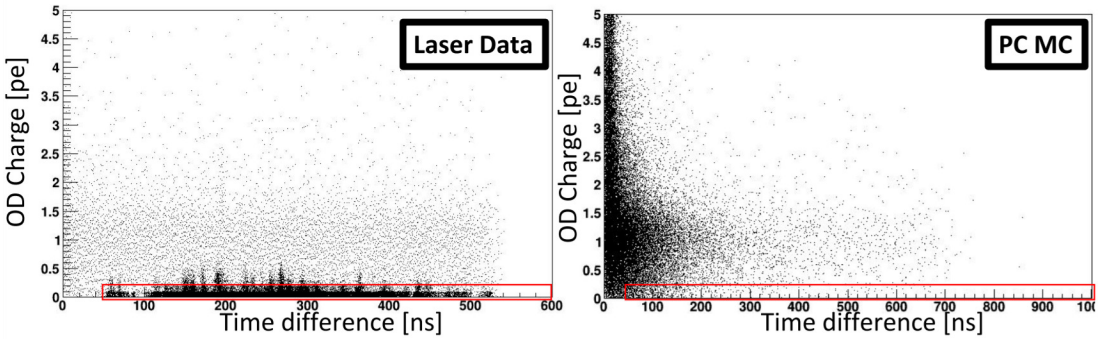

Figure 6.13 *Plots showing the number of photoelectrons for each OD hit vs the time difference between the hit OD tube and its nearby ID tubes. The left plot is for the laser data and the right plot is for PC MC.*

The rejection power of the cut was estimated by comparing the shape of the OD hit distributions for laser data (see Section 4.1.2) and FC MC, which can be seen in Figure 6.14. The difference between the integral of the two distributions was taken as the number of crosstalk hits. A comparison before and after the cut shows a reduction in the excess area by 97.3%.

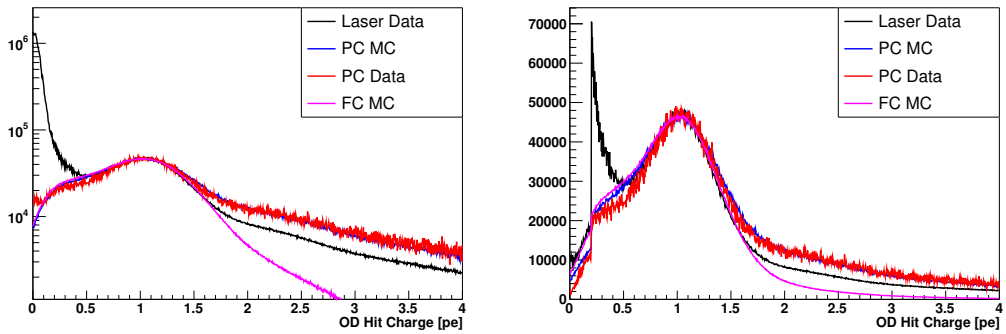

(a) *Before Cut* **(b)** *After Cut*

Figure 6.14 *OD hit distributions for FC MC (magenta), PC MC (blue), PC data (red) and laser data (black). The histograms have been scaled down to the laser data using the region 0.8→1.2 pe. The left plot shows the OD hit distributions before the crosstalk cut is applied, the right plot shows the distributions after the cut has been applied.*

The crosstalk cut is implemented before the reduction, to mask any hits satisfying the cut criteria. The PC reduction efficiency was then recalculated and a negligible drop in the reduction efficiency, by 0.03%, was found.

6.5 Event Reconstruction

The selected neutrino events are reconstructed in order to get the neutrino flavour, momentum, direction and interaction vertex. A brief discussion of the event reconstruction is given in this section, for a more detailed description the reader is referred to References [143, 156].

FC and PC events occur inside the tank and both can be reconstructed in the same way. To determine the event vertex, an initial simple point fit is used. All photons are assumed to come from a single point and the timing residual distribution of hit PMTs is constructed for each tested vertex. The position which gives the best goodness-of-fit, determined by a Gaussian fit to the data, is selected as the event vertex. The general direction is then estimated by taking the charge-weighted vector sum of directions from the vertex to each PMT.

With a preliminary vertex and direction, the next step is to find the brightest Cherenkov ring. The charge distribution is given as a function of Cherenkov angle, $n_{pe}(\theta)$. The edge of the ring θ_{edge} is taken as the angle where the second derivative equals zero after the peak of the distribution. A goodness-of-fit parameter is defined as:

$$\mathcal{Q}(\theta_{\text{edge}}) = \frac{\int_0^{\theta_{\text{edge}}} n_{pe}(\theta)d\theta}{\sin\theta_{\text{edge}}} \times ([\frac{dn_{pe}(\theta)}{d\theta}]_{\theta=\theta_{\text{edge}}})^2 \times exp(-\frac{(\theta_{\text{edge}} - \theta_{\text{exp}})^2}{2\sigma^2}), \quad (6.6)$$

where θ_{exp} is the expected Cherenkov angle calculated from the particle momentum, deduced from the total charge contained in the Cherenkov cone, and σ is the uncertainty of the angle determined from the solid angle of the ID PMT at the edge of the ring. The first, second and third terms in Equation 6.6 prefer Cherenkov rings with a large number of photoelectrons, sharp edges[2] and edges close to the expected value. The parameter $\mathcal{Q}(\theta_{\text{edge}})$ is maximised by varying θ_{edge} and the initial direction. A more precise vertex can now be found by recalculating the timing residual distribution. For PMTs inside the Cherenkov ring, photons are assumed to be emitted along the particle track, for PMTs outside of the ring photons are still assumed to be emitted from a single point. The goodness-of-fit test is carried out including these effects and a new vertex is found.

[2]This second term is removed for unphysical Cherenkov cones ($\theta_{\text{edge}} > 43^\circ$).

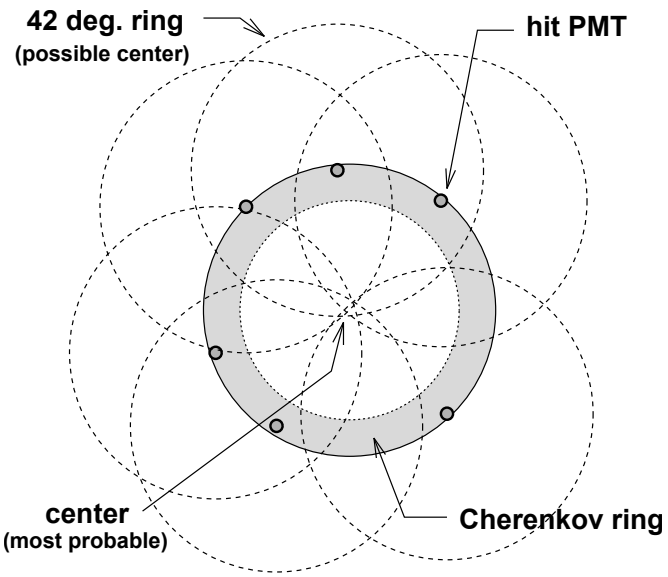

Figure 6.15 *An illustration of the basic principle of ring-finding. Taken from [143].*

The PMTs which were found to be in the Cherenkov ring are tagged and used to search for additional rings using the Hough transform method [63]. A spherical coordinate system, centred at the vertex position, is defined. Figure 6.15 shows the basic principle of the ring-finding technique. Virtual Cherenkov rings are centred at the position of each hit PMT. The point(s) where multiple virtual rings overlap indicates the direction of a potential Cherenkov cone. A likelihood method is used to determine if the newly found rings are consistent with Cherenkov rings. Each previously found Cherenkov ring is fixed and this step is run iteratively for up to five rings or until no new rings have been found.

The detected Cherenkov rings must then be classified as e-like or μ-like. The expected light distribution for electrons is diffuse due to Bremsstrahlung scattering (resulting in electromagnetic showers) allowed by its low mass. For typical muon energies in Super-K, muons do not cause electromagnetic showers and produce sharp rings. Also, the Cherenkov angle is smaller for muons which are not highly relativistic. These differences are used to compute a PID likelihood; a cut on the likelihood classifies rings as e-like and μ-like. The PID likelihood distribution is shown in Figure 6.16, approximately 1% of events are misclassified.

There is now a particle type associated with each ring and a momentum can be calculated for each particle. The momentum is largely dependent on the amount of charge collected by the PMTs within a 70° cone centred on the particle's direction. Corrections to the charge are calculated by considering PMT

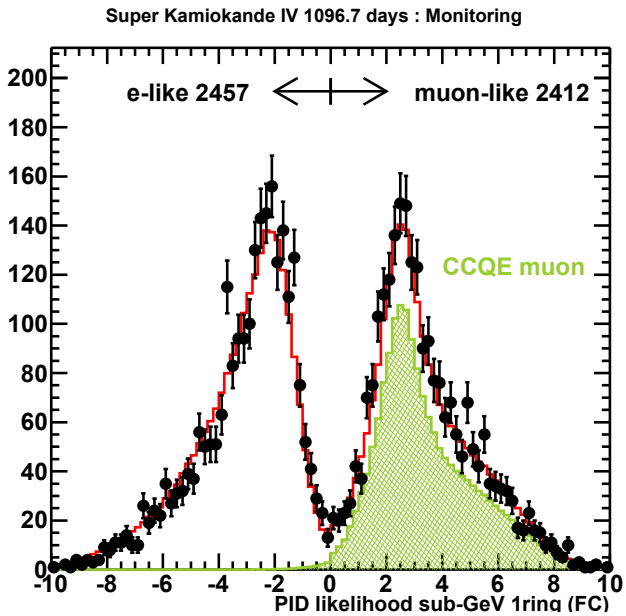

Figure 6.16 *PID likelihood distribution for single-ring FC events with visible energy less than 1.33 GeV. The black points are data from 1097 days of SK-IV, the red histogram is the MC and the shaded green region is the MC CCQE ν_μ events.*

acceptance and the attenuation of light in water. The final momentum is then estimated by combining the total corrected charge with the particle type.

Chapter 7

Neutrino Oscillation Analysis

The neutrino oscillation analysis described in Chapter 8 is carried out by weighting the SK MC on an event by event basis for different values of oscillation parameters. The MC is brought into agreement with the data by minimising the χ^2. This chapter describes the dataset, event classification and event binning used in the analysis. The formulation of the χ^2 is then shown followed by a description of the key systematic uncertainties in the analysis.

7.1 Dataset and Event Classification

In this section, the datasets used in this analysis are summarised. The analysis uses the FC, PC and UPMU data from SK-I up until SK-IV, totalling 5,326 days of live time. Simulation samples corresponding to an exposure of 500 years for each SK period are used to predict the unoscillated neutrino flux.

To increase the sensitivity to oscillation effects, the three event topologies: FC, PC and UPMU are further divided into sub-samples based on the reconstructed particle information. The sub-samples are then divided into bins of reconstructed momentum and zenith angle. There are a total of 520 bins.

All events are required to have a visible energy above 30 MeV (which removes low energy background events). The visible energy is the reconstructed kinetic energy above the Cherenkov threshold, for each observed ring, taking into account the type of particle emitting the light. Events are also required to have a

reconstructed vertex more than 2 m away from the closest point on the ID wall. Events are then further divided by the number of observed rings, the lepton flavour, the visible energy and the number of decay Michel electrons (electrons from muon decay as defined in Section 4.3.4).

The detected Cherenkov rings are all classified as e-like or μ-like by a particle identification (PID) likelihood algorithm. The PID algorithm takes into account the sharpness of the edges of the ring as well the angular distribution of light (see Section 6.5).

Fully contained events are divided into sub-GeV events if they have a visible energy below 1.33 GeV; events with a visible energy above this threshold are in the multi-GeV category. The main background in FC sub-GeV e-like sample is NC-π^0 events. Typically, the $\pi^0 \to \gamma\gamma$ decay results in a two-ring signal. However, if the decay is highly asymmetric, one photon may be undetected resulting in a single ring. Alternatively, the signals from the two photons can overlap resulting in a single ring. To reduce this type of background a specialised π^0 fitting algorithm is used [46]. The algorithm enforces the two photon hypothesis and reconstructs a second ring. A selection is then made based on the π^0 invariant mass, the fractional momentum of the second ring as well the difference between the π^0 likelihood and electron likelihood.

Once the π^0 events have been selected, the remaining e-like events are divided according to the number of decay electrons found. CCQE ν_e are not expected to have any decay electrons whereas CCQE ν_μ events are expected to have a single decay electron if the muon is not absorbed. Table 7.1 summarises the FC sub-GeV selection.

A likelihood function is used to select multi-GeV multi-ring e-like (MME) events. The MME likelihood function uses four variables: the PID likelihood, the fraction of momentum of the most energetic ring, the number of decay electrons and the distance between the neutrino interaction vertex and any decay electrons. The likelihood cut significantly increases the purity of CC ν_e and $\bar{\nu}_e$ events while reducing the background from CC ν_μ and $\bar{\nu}_\mu$.

In order to increase the sensitivity to the mass hierarchy, multi-GeV e-like events are further separated into neutrino and antineutrino samples. For single-ring events this is done by considering CC single pion (CC1$\pi^\pm$) events, where the

Table 7.1 *A summary of the FC sub-GeV event sample criteria.*

Sample	Number of rings	Momentum MeV/c (invariant mass MeV/c^2)	Number of decay electrons
Single-ring e-like 0-decay	1	> 100	0
Single-ring e-like 1-decay	1	> 100	≥ 1
Single-ring μ-like 0-decay	1	> 100	0
Single-ring μ-like 1-decay	1	> 100	1
Single-ring μ-like 2-decay		> 100	≥ 2
π^0 0-decay	2	$(85 - 215)$	0

pion is below the Cherenkov threshold. The CC1$\pi^{\pm}$ interaction is:

$$\nu_\alpha + N \rightarrow l_\alpha^- + N' + \pi^+ \tag{7.1}$$

$$\bar{\nu}_\alpha + N \rightarrow l_\alpha^+ + N' + \pi^-. \tag{7.2}$$

For neutrino interactions, the produced π^+ decays into a μ^+ which then decays into a positron, which can be detected. The detection efficiency for decay electrons is 88% (68%) for Sub-GeV (Multi-GeV) stopping muons. For antineutrinos, the produced π^- mesons mostly get absorbed by oxygen nuclei and no decay electron is detected. For multi-ring e-like events, the neutrino/antineutrino separation is carried out by applying a likelihood cut. The likelihood uses the number of rings, the number of decay electrons and the transverse momentum. Table 7.2 summarises the FC multi-GeV selection.

PC events are separated into OD stopping and OD through-going. All PC events are classified as OD through-going unless in a 500 ns sliding time window the amount of photoelectrons in the OD is less than two thirds of the expected value given the potential track length. UPMU events are divided into stopping and through-going where through-going is further subdivided into showering and non-showering muons. The criteria for the UPMU classification is detailed in Section 6.3. The samples are then binned into bins of momentum/visible energy and zenith angle separately for each SK running phase. Table 7.4 shows the

Table 7.2 *A summary of the FC multi-GeV event sample criteria.*

Sample	Number of rings	Cuts
Single-ring e-like ν_e	1	One or more decay electrons.
Single-ring e-like $\bar{\nu}_e$	1	No decay electrons
Single-ring μ-like	1	
Multi-ring e-like ν_e	$\geq$2	Highest momentum ring e-like. Pass MME likelihood. Pass ν_e likelihood.
Multi-ring e-like $\bar{\nu}_e$	$\geq$2	Highest momentum ring e-like. Pass MME likelihood. Pass $\bar{\nu}_e$ likelihood.
Multi-ring μ-like	$\geq$2	Most energetic ring has visible energy above 600 MeV. Momentum above 600 MeV/c
Multi-ring e-like other	$\geq$2	Most energetic ring e-like. Fails MME likelihood.

sample purity broken down by neutrino flavour and Table 7.5 shows the detailed binning information for each sample. After the selection process, there are 13 FC samples, 2 PC samples and 3 UPMU samples. Table 7.3 shows the number of events in each sample for both data and normalised MC.

7.2 Analysis Method

The atmospheric neutrino MC is reweighted with different oscillation parameter assumptions and the data is then fitted to the weighted MC. The data is binned into energy and zenith angle bins which are detailed further in Section 7.1. The fit uses a binned χ^2 method assuming Poisson statistics.

7.2.1 Definition of χ^2

For n bins of data, the likelihood can be defined as [132]:

$$\mathcal{L}(E, O) = \prod_{i=1}^{n} \frac{e^{-E_i} E_i^{O_i}}{O_i!}, \tag{7.3}$$

Sample	Data	MC
FC Sub-GeV		
***e*-like, Single-ring**		
0 decay-e	10294	10266.1
1 decay-e	1174	1150.7
***μ*-like, Single-ring**		
0 decay-e	2843	2824.3
1 decay-e	8011	8008.7
2 decay-e	687	687.0
***π^0*-like**		
Single-ring	578	571.8
Two-ring	1720	1728.4
Multi-ring	1682	1624.2
FC Multi-GeV		
Single-ring		
ν_e-like	705	671.3
$\bar{\nu}_e$-like	2142	2193.7
μ-like	2565	2573.8
Multi-ring		
ν_e-like	907	915.5
$\bar{\nu}_e$-like	745	773.8
μ-like	2310	2294.0
Other	1808	1772.6
PC		
Stopping	566	570.0
Through-going	2801	2889.9
UPMU		
Stopping	1456.4	1448.9
Through-going		
Non-showering	5035.3	4900.4
Showering	1231.0	1305.0

Table 7.3 *The number of observed and expected events for each event classification. The MC events has been normalised by the data live time assuming neutrino oscillations with* $\Delta m^2_{32} = 2.4 \times 10^{-3} eV^2$ *and* $\sin^2\theta_{23} = 0.5$. *Sub-GeV multi-ring interactions are not used in the present analysis.*

where E_i is the expected number of events in each bin and O_i is the observed

Sample	Sample Purity [%]				
	CC ν_e	CC $\bar{\nu}_e$	CC $\nu_\mu + \bar{\nu}_\mu$	CC ν_τ	NC
FC Sub-GeV					
e-like, Single-ring					
0 decay-e	71.7	24.8	0.2	0.0	3.3
1 decay-e	80.5	1.9	10.8	0.1	6.7
μ-like, Single-ring					
0 decay-e	4.1	1.3	75.9	0.1	18.6
1 decay-e	0.1	0.0	97.2	0.0	2.7
2 decay-e	0.0	0.0	97.9	0.1	2.0
π^0-like					
Single-ring	9.6	3.3	1.5	0.0	85.6
Two-ring	6.7	2.5	1.1	0.0	89.7
Multi-ring	29.4	4.7	34.2	0.0	31.8
FC Multi-GeV					
Single-ring					
ν_e-like	62.1	9.0	10.0	3.3	15.6
$\bar{\nu}_e$-like	54.6	37.2	0.9	1.0	6.3
μ-like	0.3	0.1	99.2	0.2	0.2
Multi-ring					
ν_e-like	55.7	10.2	11.7	4.0	18.4
$\bar{\nu}_e$-like	53.1	27.0	4.1	2.2	13.6
μ-like	2.7	0.4	91.3	0.5	5.1
Other	27.5	2.9	34.8	4.9	29.9
PC					
Stopping	8.4	3.2	82.9	1.0	4.5
Through-going	0.6	0.3	97.8	0.7	0.6
UPMU					
Stopping	0.8	0.3	98.6	0.0	0.3
Through-going					
Non-showering	0.2	0.1	99.6	0.0	0.1
Showering	0.1	0.0	99.8	0.0	0.1

Table 7.4 *Sample purity broken down by neutrino flavour assuming neutrino oscillations with* $\Delta m^2_{32} = 2.4 \times 10^{-3} eV^2$ *and* $\sin^2\theta_{23} = 0.5$. *Sub-GeV multi-ring interactions are not used in the present analysis.*

number of events in each bin. The χ^2 is then given by the log likelihood ratio:

$$\chi^2 \equiv -2log\frac{\mathcal{L}(E,O)}{\mathcal{L}(O,E)} = 2\sum_{i=1}^{n}(E_i - O_i + O_i log\frac{O_i}{E_i}). \quad (7.4)$$

Sample	Energy bins	$\cos\theta_z$ bins
FC Sub-GeV		
e-like, Single-ring		
0 decay-e	5 $e^{\pm}$ momentum	10 in $[-1, 1]$
1 decay-e	5 $e^{\pm}$ momentum	
μ-like, Single-ring		
0 decay-e	5 $\mu^{\pm}$ momentum	10 in $[-1, 1]$
1 decay-e	5 $\mu^{\pm}$ momentum	10 in $[-1, 1]$
2 decay-e	5 $\mu^{\pm}$ momentum	
π^0-like		
Single-ring	5 $e^{\pm}$ momentum	
Two-ring	5 π^0 momentum	
Multi-ring		
FC Multi-GeV		
Single-ring		
ν_e-like	4 $e^{\pm}$ momentum	10 in $[-1, 1]$
$\bar{\nu}_e$-like	4 $e^{\pm}$ momentum	10 in $[-1, 1]$
μ-like	2 $\mu^{\pm}$ momentum	10 in $[-1, 1]$
Multi-ring		
ν_e-like	3 visible energy	10 in $[-1, 1]$
$\bar{\nu}_e$-like	3 visible energy	10 in $[-1, 1]$
μ-like	4 visible energy	10 in $[-1, 1]$
Other	4 visible energy	10 in $[-1, 1]$
PC		
Stopping	2 visible energy	10 in $[-1, 1]$
Through-going	4 visible energy	10 in $[-1, 1]$
UPMU		
Stopping	3 visible energy	10 in $[-1, 0]$
Through-going		
Non-showering		10 in $[-1, 0]$
Showering		10 in $[-1, 0]$

Table 7.5 *The energy/momentum and zenith binning for each event type.*

The uncertainties are assumed to be uncorrelated and are included in each bin using the "pull approach" [74]. For example, if the true value of the CCQE cross section is larger than the nominal value, the number of expected events in a CCQE bin would increase. Including the effect of systematic uncertainties, the number of expected events in each bin E_i becomes:

$$E_i \rightarrow E_i(1 + \sum_{j}^{m} f_j^i \epsilon_j), \tag{7.5}$$

where m is the total number of systematic uncertainties, ϵ_j is the variation of the j-th systematic uncertainty and f_j^i is the fractional change of the event rate in the i-th bin due to a 1σ variation in the j-th systematic uncertainty. For each systematic error, the data and MC are brought into best agreement by fitting ϵ_j, requiring that $\partial\chi^2/\partial\epsilon_j = 0$. In order to constrain the range of ϵ_j, a quadratic penalty term

$$\sum_{j}^{m} (\frac{\epsilon_j}{\sigma_j^{sys}})^2, \tag{7.6}$$

is added to Equation 7.4. This term prevents the systematic uncertainty from straying too far from its prior range, allowing it to vary reasonably to come into agreement with the data. Including the penalty term, the resulting χ^2 definition is:

$$\chi^2 = 2\sum_{i=1}^{n}(E_i - O_i + O_i log\frac{O_i}{E_i}) + \sum_{j}^{m}(\frac{\epsilon_j}{\sigma_j^{sys}})^2. \tag{7.7}$$

As the fit is performed, the expected number of events in each bin varies with different parameter assumptions. The variation is not a uniform scaling across all bins, rather each bin is affected differently. This means that the best fit values are determined by the shape of the distributions rather than total number of events.

7.3 Systematic Uncertainties

The analyses in this thesis use 162 systematic uncertainty parameters. The systematic errors are related to the neutrino flux model, neutrino interactions, event reduction and reconstruction. This sections details the key systematic

errors. A detailed description of other errors and their estimation can be found in References [132, 143].

7.3.1 Atmospheric Neutrino Flux

The uncertainty in the absolute atmospheric neutrino flux is estimated by Honda *et al.* [104] by considering the uncertainties in the primary cosmic ray flux, the hadronic interaction model (δ_σ), pion production (δ_π), kaon production (δ_K) and air density (δ_{air}). The contributions of δ_π and δ_σ are taken as the absolute normalisation error while δ_K and δ_{air} are considered as separate systematics because of their relationship with the incoming neutrino's direction. Figure 7.1 shows the systematic uncertainty on the flux normalisation as a function of neutrino energy. An additional independent systematic is estimated using the difference between the Honda flux [103–106], the Fluka flux [47] and the Bartol flux [45], in order to account for the differences in the flux models above 10 GeV.

Atmospheric neutrinos mainly come from pions produced in the atmosphere for neutrino energies up to 10 GeV. Above a few tens of GeV, kaons contribute significantly to the neutrino flux, for neutrino energies above 100 GeV the flux is mainly produced from kaons. The uncertainty on the neutrino flux, caused by K/π production ratio, is estimated to be 5% for neutrino energies below 100 GeV and 20% above 1 TeV, with a linear increase in the uncertainty for neutrino energies between 100 GeV and 1 TeV. This uncertainty is deduced from the K/π ratio measurement, with 3% accuracy, by the SPY experiment [40].

The neutrino path length depends on the production height in the atmosphere, which in turn depends on the density of the atmosphere. The uncertainty in the density is estimated to be 10%, by comparing US-standard 76 [44] and MSISE-90 [97] models for the atmosphere. The resulting variation in production height is propagated through the oscillation probability calculation. This uncertainty is less important for upward-going neutrinos which have a very long path length (compared to the atmospheric production height) but becomes more important for downward-going and horizontal neutrinos.

In addition to the absolute flux, an uncertainty is estimated for the $\bar{\nu}/\nu$ ratio. The antineutrino to neutrino ratio depends on the ratios of positive to negative charged pions/kaons produced in the atmosphere. This uncertainty is estimated by comparing $\bar{\nu}/\nu$ ratios between the Honda [106], Fluka [47] and Bartol [45] flux

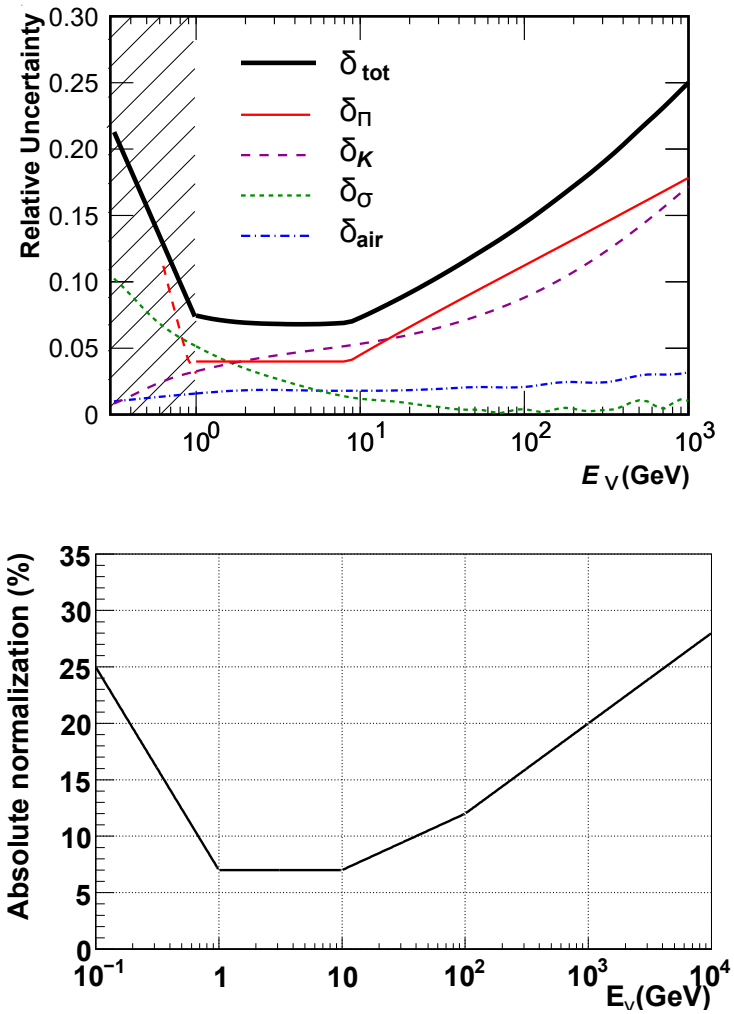

Figure 7.1 *The calculated uncertainty of the neutrino flux normalisation including contributions from the hadronic interaction cross section (δ_σ), pion production (δ_π), kaon production (δ_K) and air density (δ_{air}) (top). The uncertainty on the flux normalisation as a function of energy taking only contributions from the hadronic interaction model and pion production (bottom), taken from Ref [143].*

models.

The Sun's activity affects the primary cosmic ray flux. Solar activity has an 11 year cycle [79]. The uncertainty in the neutrino flux is estimated by taking the variation in the neutrino flux caused by a ± 1 year variation in the solar cycle. This estimated uncertainty of solar activity is 20%, 50%, 20%, 10% for SK-I to SK-IV respectively.

The neutrino oscillation probability is dependent on the amount of matter traversed. The atmospheric neutrino analyses make use of density data from

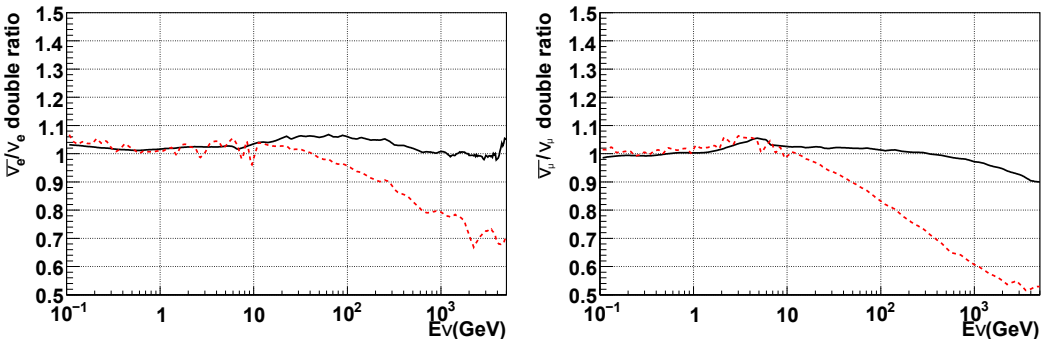

Figure 7.2 *The anti-neutrino/neutrino double ratio for $\bar{\nu}_e/\nu_e$ (left) and $\bar{\nu}_\mu/\nu_\mu$ (right). The solid black line shows the ratio between the Honda and Fluka ratios while the dashed red line shows the ratio between the Honda and Bartol ratios. Taken from Ref [143].*

the Preliminary Earth Reference Model (PREM) [69]. However, the chemical composition of the Earth's core affects the electron density. The Core is assumed to be made of iron and nickel, these elements have an electron density lower than lighter elements. The difference in electron density is used as an uncertainty on the Core's electron density.

7.3.2 Neutrino Interaction

The uncertainties related to neutrino interactions are the same for each of the SK running periods. This section highlights key systematic uncertainties related to the different types of neutrino interactions.

There are three key uncertainties estimated for the CCQE interaction. In addition to the absolute CCQE interaction cross section, uncertainties are estimated for the cross section ratios $\bar{\nu}/\nu$ and $(\nu_\mu + \bar{\nu}_\mu)/(\nu_e + \bar{\nu}_e)$. These uncertainties are estimated by taking the difference between the Fermi-gas model [152] and the Nieves model [134]. The difference between the models is taken as a 1σ uncertainty.

Quasi-elastic scattering and single meson production depend on the axial vector mass M_A which appears in the cross section as $-1.3/(1 - Q^2/M_A^2)^2$ [89]. The axial vector mass is set to 1.21 GeV/c and has a 10% uncertainty [89] so the uncertainty is estimated by taking the ratio of the Q^2 spectrum with M_A set to 1.21 GeV and 1.1 GeV.

DIS cross section calculations agree with experimental measurements within 5% for neutrino energies above 10 GeV [143], so a 5% uncertainty is used for the total cross section. Below 10 GeV, there is a larger additional uncertainty which is estimated by comparing the default model (GRV98 [87] with corrections by Bodek and Yang [51]) and the CKMT [55] model.

The uncertainty on the NC/CC ratio is estimated to be 20% [18].

7.3.3 Event Selection and Reconstruction

The uncertainties related to the event selection and reconstruction are independent for each of the SK running periods due to differences in the detector configuration. This section highlights key systematic uncertainties related to the event selection.

The first set of key systematic uncertainties arise from the data reduction. The data reduction, detailed in Chapter 6, uses several cuts to remove backgrounds and classify events into FC, PC and UPMU topologies. The distributions of each cut variable used for the event selection process are compared for data and MC, the difference is taken into account as a systematic uncertainty in the reduction efficiency. These uncertainties are summarised in Table 7.6. The uncertainties for stopping and through-going muons are considered to be correlated.

Table 7.6 *Summary of the systematic uncertainties associated with data reduction for different event topologies.*

Event Classification	Systematic Uncertainty [%]			
	SK-I	SK-II	SK-III	SK-IV
FC	0.2	0.2	0.8	0.3
PC	2.5	4.8	0.5	1.0
UPMU Stopping	0.7	0.7	0.7	0.5
UPMU Through-going	0.5	0.5	0.5	0.3

In addition to the reduction uncertainty, systematic uncertainties also arise from the separation of event topologies.Events are separated into fully and partially contained samples by the number of hit PMTs in an OD cluster. The systematic uncertainty associated with the FC/PC separation is estimated by comparing the observed and MC distributions of the number of PMTs in an OD cluster. The uncertainty is estimated to be 0.6%, 0.5%, 0.9% and 0.38% for SK-I to SK-IV respectively.

Partially contained events are separated into stopping and through-going samples by the energy deposit in the outer detector. This uncertainty is estimated by comparing the number of photoelectrons in the OD for data and MC. This estimation is also carried out separately for different OD regions (top, bottom and barrel) as the regions are calibrated separately.

Very high energy upwards through-going muons accompanied by radiative emission are classified as showering samples. They are identified by checking the deviation of energy deposit from the expected constant energy loss. The rest of the through-going muon sample is classified as non-showering. This uncertainty is estimated by comparing the $\Delta(Q)$ distributions, mentioned in Chapter 6, for data and MC. The estimated uncertainty is 3.4%, 4.4%, 2.4% and 3.0% for SK-I to SK-IV respectively.

The next set of systematic uncertainties arise from the event reconstruction which includes particle identification, identification of rings and the detection of decay electrons. The particle identification process involves cuts on a likelihood ratio, the uncertainties are estimated by comparing the distributions of the likelihood ratio e/π^+ for the FC data and MC. Uncertainties range from 0.1% to 0.4%, depending on the event category, and are estimated for single-ring and multi-ring events separately. Multiple rings are iteratively searched for and a likelihood cut is applied in order to select rings. The likelihood distribution is compared between FC data and MC in order to estimate the uncertainty. The uncertainty is different for each event category and ranges from 0.3% to 2.8%. The uncertainty of the decay electron tagging efficiency is estimated by comparing the detection efficiency in stopping cosmic muon data and MC. The uncertainty is estimated to be 0.8% across all energies.

Lastly there is an uncertainty associated with the energy calibration. As discussed in Section 4.3.5, several calibration sources are used to estimate the uncertainty on the energy scale, differences in the detector configuration result in different uncertainties for each SK period. The estimated uncertainty of the absolute energy scale is 1.1%, 1.7%, 2.7% and 2.3% for SK-I to SK-IV respectively.

Chapter 8

NSI in Atmospheric Neutrinos

As discussed in Chapter 2, the effective Hamiltonian for neutrino propagation through matter is:

$$H_{eff} = \frac{1}{2E} U \begin{pmatrix} 0 & 0 & 0 \\ 0 & \Delta m^2_{21} & 0 \\ 0 & 0 & \Delta m^2_{31} \end{pmatrix} U^\dagger \pm \sqrt{2} G_F N_e \begin{pmatrix} 1+\varepsilon_{ee} & \varepsilon_{e\mu} & \varepsilon_{e\tau} \\ \varepsilon_{\mu e} & \varepsilon_{\mu\mu} & \varepsilon_{\mu\tau} \\ \varepsilon_{\tau e} & \varepsilon_{\tau\mu} & \varepsilon_{\tau\tau} \end{pmatrix}, \quad (8.1)$$

where U is the PMNS mixing matrix, N_e is the electron number density along the neutrino's path length and the plus (minus) sign is for neutrinos (antineutrinos). The first term in Equation 8.1 is the vacuum term and is energy dependent, the second term includes standard and non-standard matter effects and depends only on the fermion density. In the $\mu - \tau$ sector there are two quantities of interest: the flavour-changing NC parameter $\varepsilon_{\mu\tau}$ which allows matter induced $\nu_\mu \rightarrow \nu_\tau$ transitions and the non-universal $\varepsilon_{\tau\tau} - \varepsilon_{\mu\mu}$ parameter which allows for different NC scattering amplitudes for the two neutrino flavours. In the $e - \tau$ sector, contributions from $\varepsilon_{\mu\alpha}$ can be ignored and matter induced flavour transitions are allowed via $\varepsilon_{e\tau}$. Different NC scattering amplitudes are then considered by simultaneously considering ε_{ee} and $\varepsilon_{\tau\tau}$. In this chapter, a measurement of these quantities is made using 5,326 days of Super-K data, 2,519 of which are from SK-IV.

While the analyses in this thesis use the full numerical calculation for oscillation probabilities, insight can be gained for individual parameters using approximate

formulae. Assuming Δm^2_{21}, θ_{12} and θ_{13} are zero, the ν_μ survival probability in constant matter density can be expressed as [130]:

$$P(\nu_\mu \to \nu_\mu) = 1 - P(\nu_\mu \to \nu_\tau) = 1 - \sin^2 2\theta_{eff} \sin^2[\zeta \frac{\Delta_{31} L}{2}], \tag{8.2}$$

where

$$\sin^2 2\theta_{eff} \equiv \frac{|\sin 2\theta_{23} \pm 2\eta_{\mu\tau}|^2}{\zeta^2}, \tag{8.3}$$

$$\zeta \equiv \sqrt{|\sin 2\theta_{23} \pm 2\eta_{\mu\tau}|^2 + [\cos 2\theta_{23} + (\eta_{\mu\mu} - \eta_{\tau\tau})]^2}, \tag{8.4}$$

$$\eta_{\alpha\beta} \equiv \frac{\varepsilon_{\alpha\beta} V_e}{\Delta_{ij}}, \tag{8.5}$$

$$V_e \equiv \sqrt{2} G_F N_e, \tag{8.6}$$

$$\Delta_{ij} \equiv \Delta m^2_{ij}/2E \tag{8.7}$$

and the plus (minus) sign is for normal (inverted) hierarchy. For antineutrinos the sign of V_e changes. It can be seen in the above equations that the NSI $\varepsilon_{\alpha\beta}$ term only appears in terms with the mass splitting which means that the oscillation probability is invariant under the simultaneous transformation $\varepsilon_{\alpha\beta} \to -\varepsilon_{\alpha\beta}$ and $\Delta m^2_{31} \to -\Delta m^2_{31}$. For maximal mixing ($\theta_{23} = 45°$) the oscillation probability is no longer dependent on the sign of the difference between $\varepsilon_{\tau\tau}$ and $\varepsilon_{\mu\mu}$, but only its absolute value.

Equations 8.2 and 8.3 show how the effective mixing angle and mass splitting vary. A larger fermion density, larger NSI parameter strength or a high neutrino energy all result in an increase in the effective mass splitting and a reduced effective mixing angle as $\zeta > 1$.

In this analysis neutrinos oscillation probabilities are calculated for MC events on an event-by-event basis as they propagate through the Earth. Atmospheric neutrinos pass through various densities of matter before reaching the detector. The Earth is modelled as a sphere of radius 6371 km with a simplified version of the preliminary reference Earth model (PREM) [69]. Figure 8.1 shows the difference in Earth layer densities for the simple and full model. Table 8.1 shows the density layers used; the atmosphere is modelled as a vacuum. No change in

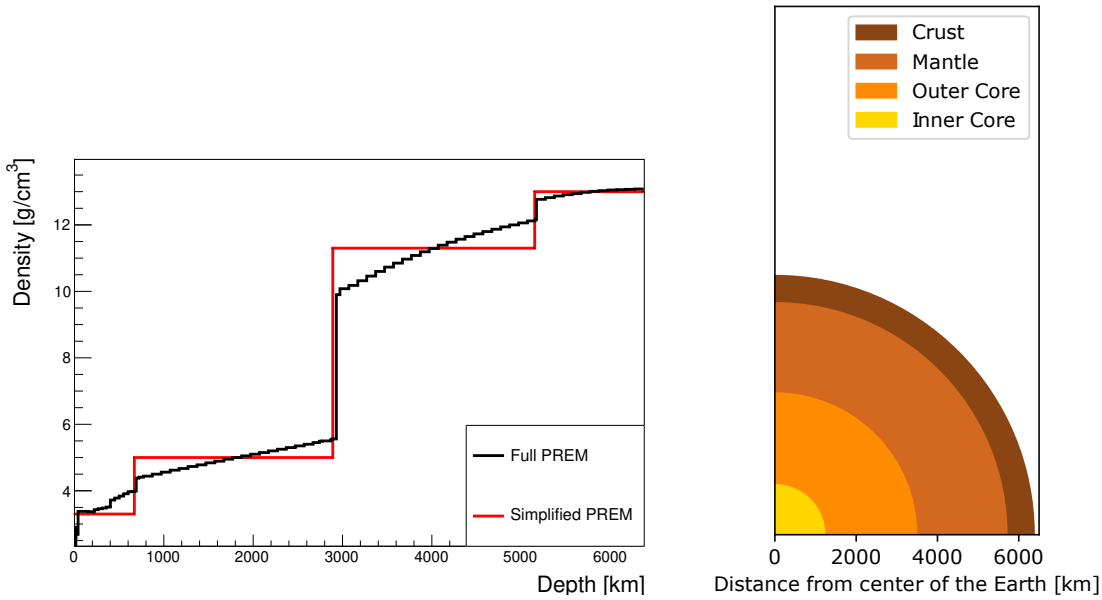

Figure 8.1 *The density of the Earth versus the depth (left). The black line shows the full measured values of the PREM model and the red line shows the values used in the analysis. The right plot shows the different density layers of the Earth.*

the analysis sensitivity was found with the full model but the computation time increased dramatically. Hence, the simplified model is used for the results here.

Table 8.1 *Model of the Earth used in the analysis.*

Region	R_{min} [km]	R_{max} [km]	density [g/cm^3]
Inner core	0	1220	13.0
Outer core	1220	3480	11.3
Mantle	3480	5701	5.0
Crust	5701	6371	3.3

8.1 NSI in the $\mu - \tau$ Sector

8.1.1 Oscillation Effect

Figure 8.2 shows the calculated ν_μ survival probability contours as a function of zenith angle and neutrino energy for different values of the $\mu - \tau$ NSI parameters. The discontinuities, in the lower zenith regions, in the plots show neutrinos

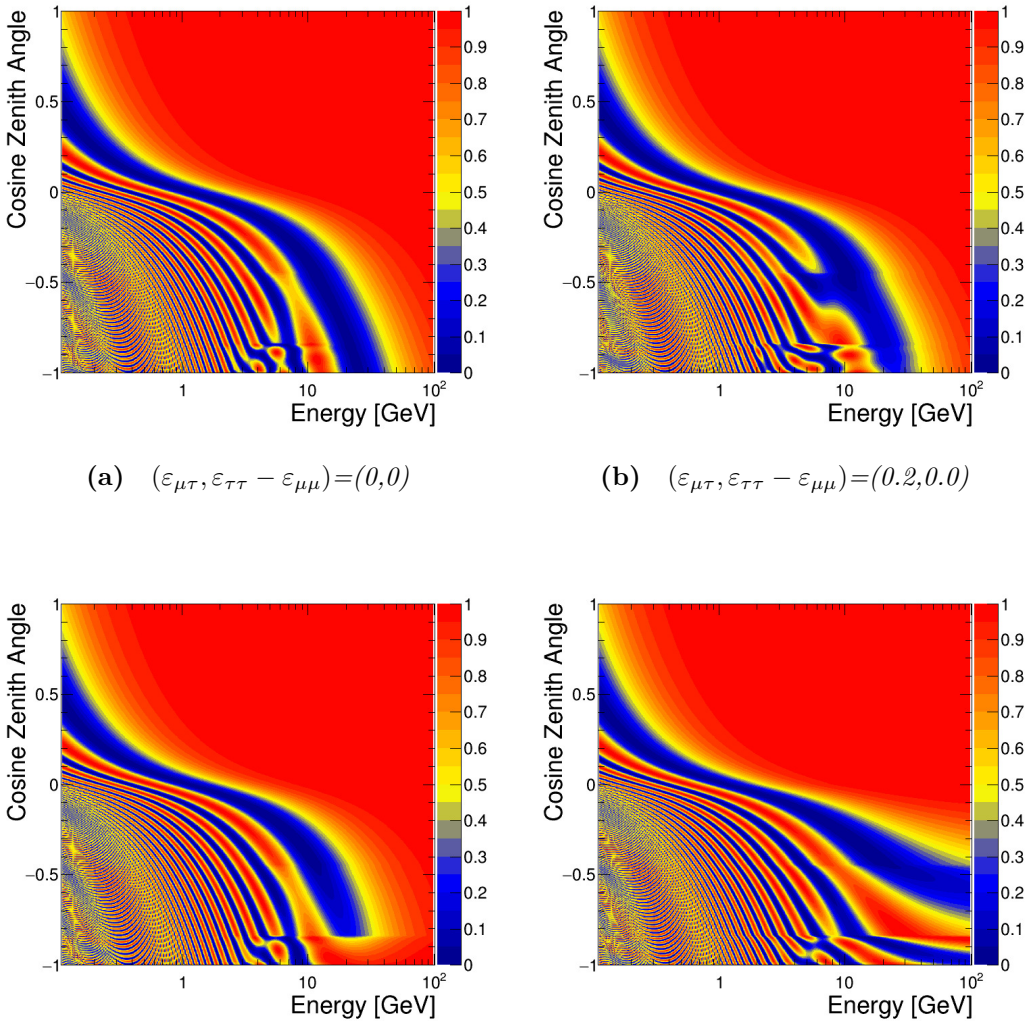

(a) $(\varepsilon_{\mu\tau}, \varepsilon_{\tau\tau} - \varepsilon_{\mu\mu})$=(0,0)

(b) $(\varepsilon_{\mu\tau}, \varepsilon_{\tau\tau} - \varepsilon_{\mu\mu})$=(0.2,0.0)

(c) $(\varepsilon_{\mu\tau}, \varepsilon_{\tau\tau} - \varepsilon_{\mu\mu})$=(0.0,0.2)

(d) $(\varepsilon_{\mu\tau}, \varepsilon_{\tau\tau} - \varepsilon_{\mu\mu})$=(0.2,0.2)

Figure 8.2 *Oscillation contours showing the ν_μ survival probability for different values of $\mu - \tau$ NSI parameters. Oscillation probabilities calculated using full three-flavour equations with all other NSI set to zero. The horizontal axis shows the energy and the vertical axis shows the zenith angle. The top left plot shows standard oscillation only, top right shows standard plus flavour-changing neutral currents. The bottom left plot shows standard plus lepton non-universality and the bottom right plot includes flavour-changing neutral currents and lepton non-universality.*

passing through the core of the Earth. The strength of NSI depends on the amount of matter traversed and is energy independent. However, the standard oscillation term in Equation 8.1 is energy dependent so the relative strength of NSI is expected to depend on the neutrino energy. The effects of NSI can be

divided into three energy regions: low, medium, high. The boundaries of these regions depend on the matter density and the value of ε. A conservative $\varepsilon \sim \mathcal{O}(1)$ results in a matter term $\sqrt{2}G_F N_f \varepsilon \sim 1\times10^{-13}$ eV which is used to give the energy ranges below.

At low energies ($E_\nu < 1$ GeV), the eigenvalue of the vacuum term $\Delta m^2_{32}/2E_\nu$ is much larger than matter eigenvalue $\sqrt{2}G_F N_f \varepsilon$ so oscillations between $\nu_\mu \rightarrow \nu_\tau$ are mostly governed by two flavour vacuum oscillations. In this region the contribution from NSI is not significant. The neutrinos in this energy region are in the FC Sub-GeV sample, which is expected to show no change when NSI is considered.

The middle energy region ($1 < E_\nu < 30$ GeV) is where the decreasing vacuum term becomes comparable to the matter term. In this energy region vacuum oscillations no longer dominate and are altered by matter oscillations. Non-zero $\varepsilon_{\mu\tau}$ increases the effective mass splitting which increases the oscillation frequency; for the larger effective mass splitting the oscillation maximum is expected at higher neutrino energies or shorter path lengths, compared to vacuum oscillations. The neutrinos in this energy region are in the FC Multi-GeV, PC and UPMU-stopping samples, which are expected to show an excess of ν_μ for significant path lengths when NSI is considered.

At high energies ($E_\nu > 30$ GeV) the vacuum term significantly suppresses $\nu_\mu \rightarrow \nu_\tau$ transitions while $\varepsilon_{\mu\tau}$ increases the effective mass splitting. In this energy region $\nu_\mu \rightarrow \nu_\tau$ transitions will be driven by $\varepsilon_{\mu\tau}$ if the neutrino's path length, through the Earth, is sufficiently long. The non-universal term is also expected to have an effect in this energy region. When $\varepsilon_{\tau\tau} - \varepsilon_{\mu\mu}$ is non-zero, the effective mixing angle decreases, suppressing transitions even further. The neutrinos in this energy region are in the UPMU through-going sample.

8.1.2 Analysis

The analysis is carried out in two parts. First, fits are performed with the standard three-flavour oscillation formalism extended to allow for a non-zero value of $\varepsilon_{\mu\tau}$. A scan is made in steps of $\varepsilon_{\mu\tau}$. For each point the value of the χ^2 is calculated (see Chapter 7). In the second step $\varepsilon_{\mu\tau}$ is considered along with the diagonal NSI elements $\varepsilon_{\mu\mu}$ and $\varepsilon_{\tau\tau}$ along with two-flavour standard oscillations. For this, a value of χ^2 is determined for each grid point in the two dimensional

space $\varepsilon_{\mu\tau}$ and $\varepsilon_{\tau\tau} - \varepsilon_{\mu\mu}$.

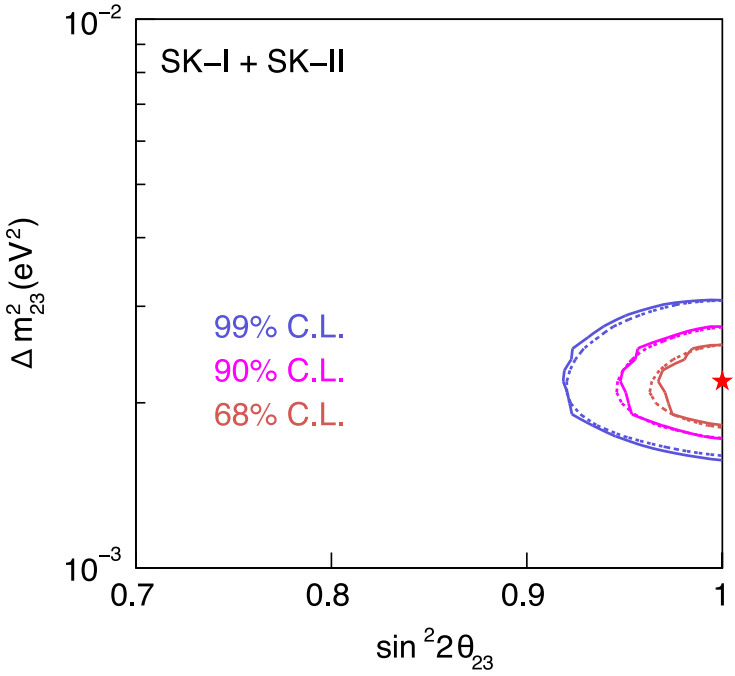

Figure 8.3 *The allowed standard oscillation parameter regions. Solid lines show allowed regions when including NSI and the dotted lines show the regions without NSI. Taken from [133].*

The previous Super-K atmospheric neutrino NSI analysis [132, 133] showed that the allowed regions for the standard oscillation parameters do not change significantly when NSI are considered (see Figure 8.3). For this reason, the values of the standard oscillation parameters are fixed to those in the latest published results from Super-K [18], shown in Table 8.2. The uncertainty on the standard oscillation parameters is propagated to the systematic errors.

Table 8.2 *The values of the fixed standard oscillation parameters in the NSI analyses and their uncertainties.*

Parameter	Value	
	Normal Hierarchy	Inverted Hierarchy
Δm^2_{32} [$\times 10^{-3}$ eV^2]	$2.5^{+0.13}_{-0.20}$	$2.5^{+0.13}_{-0.20}$
Δm^2_{21} [$\times 10^{-5}$ eV^2]	7.65±0.18	7.65±0.18
$\sin^2\theta_{23}$	$0.5875^{+0.031}_{-0.064}$	$0.575^{+0.036}_{-0.073}$
$\sin^2\theta_{12}$	0.309±0.014	0.309±0.014
$\sin^2\theta_{13}$	0.0219±0.0012	0.0219±0.0012
δ_{CP} [rad]	4.19	4.19

Prior to carrying out the analysis in this chapter, a sensitivity study was performed. Rather than fitting data to MC, the study compares MC to MC.

The study confirmed that when there is zero NSI, the fitting algorithm gives a best fit point with zero NSI to a good precision. Such a test is necessary to confirm that there is no bias in the fitting algorithm as well as to ascertain what level of NSI would be detectable in Super-K.

8.1.3 Limit on $\varepsilon_{\mu\tau}$ from three-flavour fit

For the three-flavour fit all standard oscillation parameters are set to their best fit from the latest Super-K results shown in Table 8.2. The values of Δm^2_{32} and θ_{23} are set to the most recent best fit Super-K results, normal hierarchy is assumed. The scanned parameter space in $\varepsilon_{\mu\tau}$ is from -0.06 to 0.06 in steps of 0.01 (121 points). The best calculated χ^2 versus $\varepsilon_{\mu\tau}$ is shown in Figure 8.4. The minimum χ^2 is found for $\varepsilon_{\mu\tau} = -0.023$. The minimum χ^2 is 568 for 519 degrees of freedom. The 90% C.L. limit is:

$$-0.033 < \varepsilon_{\mu\tau} < -0.003\,. \tag{8.8}$$

The systematic uncertainties and their ϵ_j values at the best fit point are summarised in Tables A.1 to A.4 in Appendix A.

The zenith angle distributions for the best fit point do not differ largely from the best fit with the standard oscillation formalism for most of the sub-samples. The only samples which shows a difference is the most upward-going zenith angle bins in the UPMU showering sample.

8.1.4 Limit on $\mu - \tau$ NSI parameters from two-flavour fit

For the two-flavour fit Δm^2_{21}, θ_{12} and θ_{13} are all set to zero. The values of Δm^2_{32} and θ_{23} are set to the most recent best fit Super-K results, normal hierarchy is assumed. The scanned parameter space in $\varepsilon_{\mu\tau}$ is from -0.06 to 0.06 in steps of 0.01 (121 steps) and in $\varepsilon_{\tau\tau} - \varepsilon_{\mu\mu}$ from -0.5 to 0.5 in steps of 0.0125 (81 steps). The minimum χ^2 is found for $(\varepsilon_{\mu\tau}, \varepsilon_{\tau\tau} - \varepsilon_{\mu\mu})$ = (-0.029, 0.075). The minimum χ^2 is 571.352 for 518 degrees of freedom.

The 90% C.L. limits are:

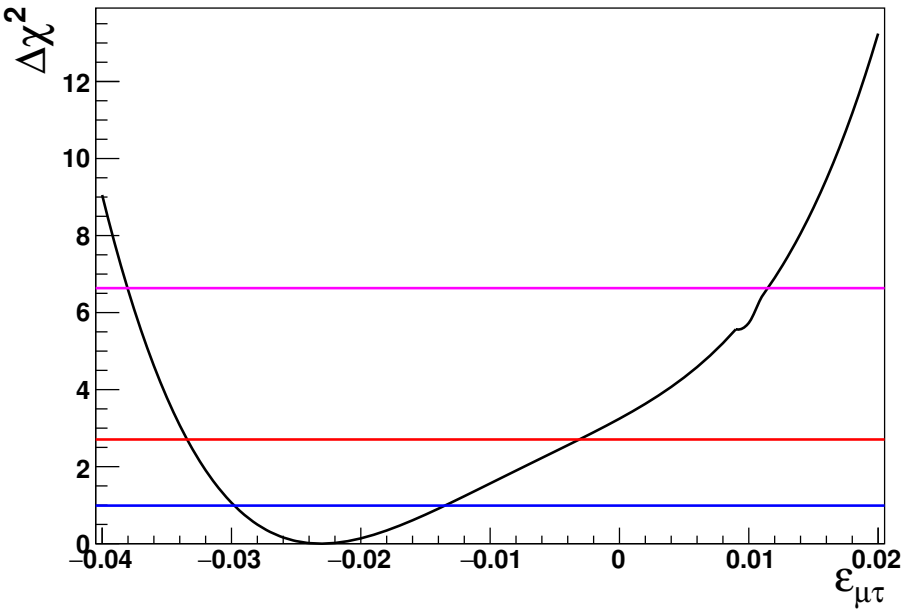

Figure 8.4 *$\Delta\chi^2$ distribution as a function of $\varepsilon_{\mu\tau}$. The three flavour standard oscillation parameters are fixed and all other NSI parameters are set to zero. The three horizontal lines correspond to the 68%, 90% and 99% C.L. defined by $\Delta\chi^2$ = 0.99, 2.71, 6.63 respectively.*

$$-0.046 < \varepsilon_{\mu\tau} < 0.019 \tag{8.9}$$

$$-0.050 < \varepsilon_{\tau\tau} - \varepsilon_{\mu\mu} < 0.138 \tag{8.10}$$

The systematic uncertainties and their ϵ_j values at the best fit point are summarised in Tables A.5 to A.8 in Appendix A.

The zenith angle distributions for the best fit point do not differ largely from the best fit with the standard oscillations formalism for most of the sub-samples. The samples which show the most difference are the most upward-going zenith angle bins in the UPMU and PC sub samples. Figure 8.5 shows the zenith angle distribution for the best fit point and standard oscillation (no NSI) for the UPMU stopping and showering samples.

Figure 8.6 shows the allowed regions of the NSI parameters ($\varepsilon_{\mu\tau}$, $\varepsilon_{\tau\tau} - \varepsilon_{\mu\mu}$). The three contours correspond to the 68%, 90% and 99% confidence level regions defined by $\chi^2 = \chi^2_{min}$+ 2.30, 4.61 and 9.21 respectively. Figures 8.7 and 8.8 show the $\chi^2 = \chi^2_{min}$ distributions for $\varepsilon_{\mu\tau}$ and $\varepsilon_{\tau\tau} - \varepsilon_{\mu\mu}$ respectively.

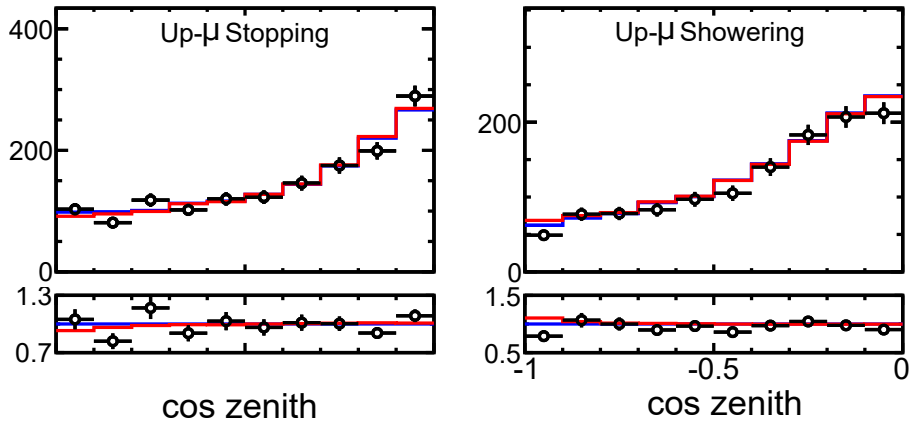

Figure 8.5 *The zenith angle distribution for the UPMU stopping sample (left) and the UPMU showering sample (right). The black points show the data, the red line shows the best fit standard oscillation parameters from [18] and the blue case shows the best fit NSI result from the two flavour fit.*

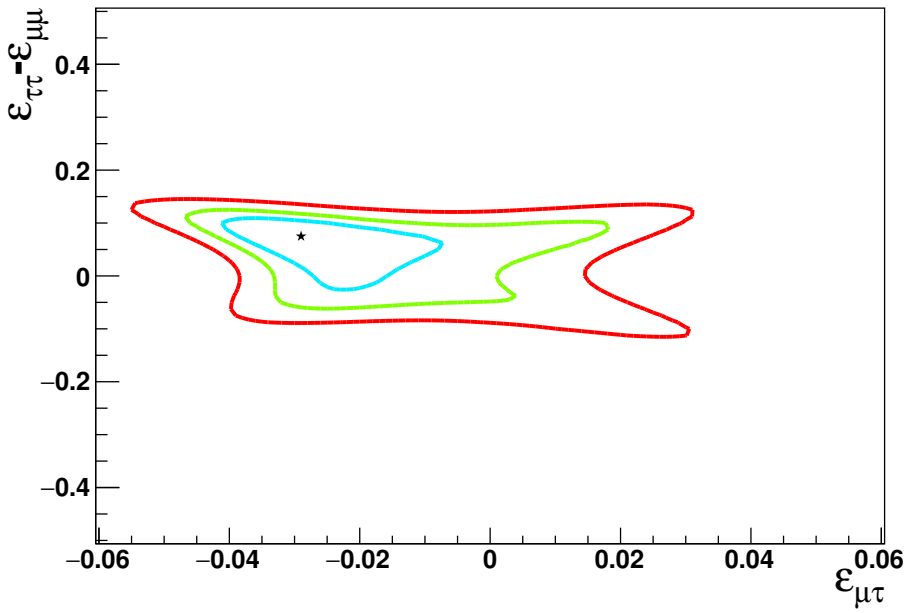

Figure 8.6 *Allowed NSI parameter region assuming two-flavour standard oscillations with NSI in the $\mu - \tau$ sector. The horizontal axis shows $\varepsilon_{\mu\tau}$ and the vertical axis shows ($\varepsilon_{\tau\tau}$ - $\varepsilon_{\mu\mu}$). Δm^2_{32} and θ_{23} are fixed while Δm^2_{21}, θ_{12} and θ_{13} are set to zero. The three contours correspond to the 68%, 90% and 99% C.L. defined by $\Delta\chi^2$ = 2.30, 4.61 and 9.21 respectively. The star represents the best-fit point for the NSI parameters.*

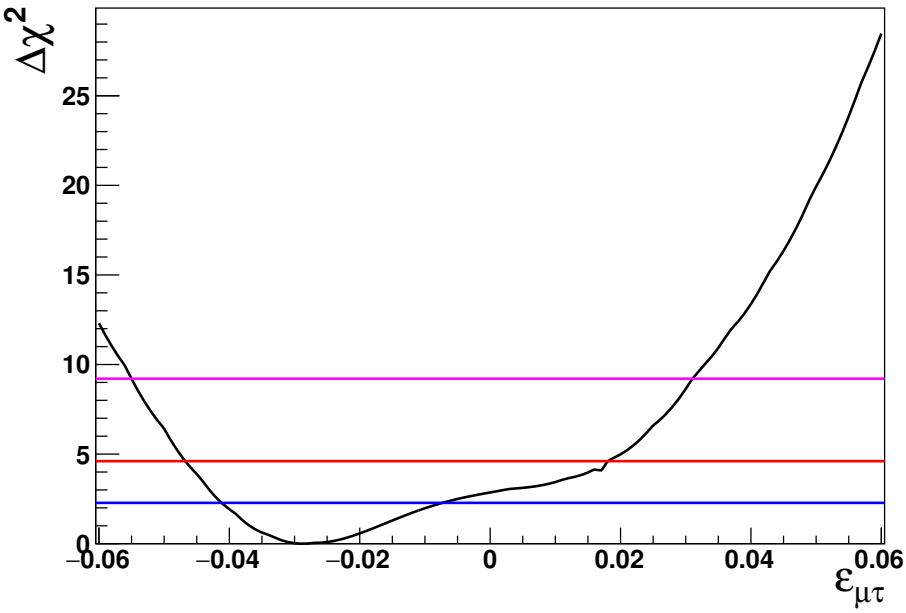

Figure 8.7 *$\Delta\chi^2$ distribution as a function of $\varepsilon_{\mu\tau}$. Δm^2_{32} and θ_{23} are fixed while Δm^2_{21}, θ_{12} and θ_{13} are set to zero. ($\varepsilon_{\tau\tau}$ - $\varepsilon_{\mu\mu}$) is integrated out. The three horizontal lines correspond to the 68%, 90% and 99% C.L. defined by $\Delta\chi^2$ = 2.30, 4.61 and 9.21 respectively.*

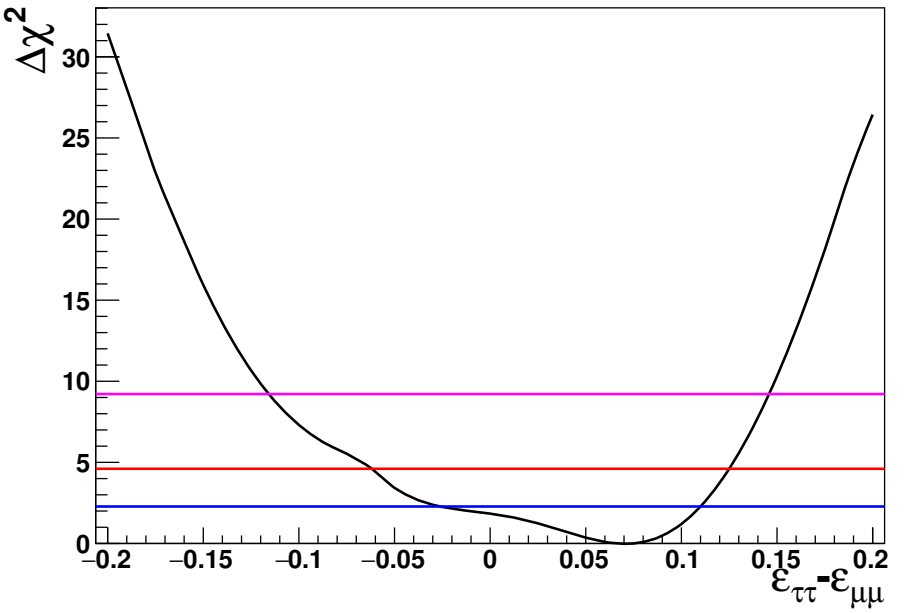

Figure 8.8 *$\Delta\chi^2$ distribution as a function of ($\varepsilon_{\tau\tau}$ - $\varepsilon_{\mu\mu}$). Δm^2_{32} and θ_{23} are fixed while Δm^2_{21}, θ_{12} and θ_{13} are set to zero. $\varepsilon_{\mu\tau}$ is integrated out. The three horizontal lines correspond to the 68%, 90% and 99% C.L. defined by $\Delta\chi^2$ = 2.30, 4.61 and 9.21 respectively.*

8.1.5 Discussion

The best fit value of $\varepsilon_{\mu\tau}$ is negative and the 90% C.L. obtained from the three-flavour fit is entirely in the negative region. This result is driven by the most upward-going bin in the UPMU showering sample where there is a slight deficit in the number of events. This can be understood by considering that the effective neutrino oscillation frequency increases. For neutrinos of a fixed energy, this manifests as a shorter oscillation length. Above 30 GeV, the oscillation length is greater than the diameter of the Earth and $\varepsilon_{\mu\tau}$ shortens the oscillation length enough to allow oscillations for the most upward-going neutrinos. Below this energy the oscillation length is short enough that standard and NSI terms can cause oscillations which makes it difficult to discriminate between standard and NSI oscillations in the lower energy samples.

The lower energy UPMU stopping and PC samples constrain the value of $\varepsilon_{\tau\tau} - \varepsilon_{\mu\mu}$ and the best fit point is positive. Negative values of $\varepsilon_{\tau\tau} - \varepsilon_{\mu\mu}$ result in a larger excess which causes an asymmetry in the constraints. The three-flavour $\varepsilon_{\mu\tau}$ analysis results in a tight constraint which is relaxed when $\varepsilon_{\tau\tau} - \varepsilon_{\mu\mu}$ is included.

The result of the three-flavour fit can be directly compared to IceCube's NSI result [6] in which all NSI parameters were set to zero except for $\varepsilon_{\mu\tau}$. IceCube studied neutrinos with energies in the range 6 - 56.2 GeV. IceCube, as well as other experiments, use a convention which assumes all NSI comes from interaction with d quarks so as to easily compare with neutrino scattering experiments. In order to compare results the NSI parameters in this analysis have to be divided by 3 (neutral earth matter has 3 times as many d quarks as electrons). The IceCube limit on $\varepsilon_{\mu\tau}$ at 90% C.L. (using d quark normalisation) is:

$$-6.7 \times 10^{-3} < \varepsilon_{\mu\tau} < 8.1 \times 10^{-3}, \tag{8.11}$$

while the limit from this study at 90% C.L. (using d quark normalisation) is:

$$-1.1 \times 10^{-2} < \varepsilon_{\mu\tau} < -1 \times 10^{-3}. \tag{8.12}$$

The three flavour fit neglects any non-universal diagonal NSI couplings and the introduction of this coupling relaxes the constraint. The two flavour analysis including flavour-changing neutral currents and non-universal parameters can be compared to a previous Super-K study carried out more than a decade ago. The

analysis presented here uses a dataset 2.5 times the size of the last atmospheric neutrino NSI zenith angle study which was carried out in 2009 with 2288 days of data [133]. In addition to the larger dataset, this analysis includes positive and negative values of $\varepsilon_{\mu\tau}$, whereas the past study included only positive values. The two flavour fit results from this study are consistent with the past result albeit with slightly tighter constraints. Furthermore the analysis binning, MC and systematic uncertainties have all changed since the last analysis was carried out. The constraints on the $\mu - \tau$ NSI parameters at 90% C.L. are:

$$|\varepsilon_{\mu\tau}| < 3.3 \times 10^{-2} \tag{8.13}$$

$$|\varepsilon_{\tau\tau} - \varepsilon_{\mu\mu}| < 1.5 \times 10^{-1} \tag{8.14}$$

for the previous analysis while the results from this analysis are:

$$-4.5 \times 10^{-2} < \varepsilon_{\mu\tau} < 1.9 \times 10^{-2} \tag{8.15}$$

$$-5.1 \times 10^{-2} < \varepsilon_{\tau\tau} - \varepsilon_{\mu\mu} < 1.4 \times 10^{-1}. \tag{8.16}$$

The first difference between the past and current analysis is the asymmetric bounds. The past results were symmetric in $\varepsilon_{\mu\tau}$ due to the analytical expression used to calculate the oscillation probabilities, resulting in symmetric bounds about zero. This analysis uses a full numerical calculation which shows the difference between positive and negative values of $\varepsilon_{\mu\tau}$. Additionally, the mixing angle was maximal, in the past analysis, which results in positive-negative symmetry in $\varepsilon_{\tau\tau} - \varepsilon_{\mu\mu}$. NSIs affect the effective mixing angle and mass splitting so the key difference between the new and past result comes from the difference in standard oscillation parameters. Although shifted, the current bounds are tighter than previous bounds. Sensitivity is still limited by a lack of statistics. The slight improvement expected from the statistical update is confirmed by carrying out the two-flavour analysis on SK-I and SK-II data. The 90% C.L. regions using only SK-I and II data are:

$$-5.7 \times 10^{-2} < \varepsilon_{\mu\tau} < 2.6 \times 10^{-2} \tag{8.17}$$

$$-1.1 \times 10^{-1} < \varepsilon_{\tau\tau} - \varepsilon_{\mu\mu} < 1.7 \times 10^{-1}. \tag{8.18}$$

The SK atmospheric data is already described very well by the standard

oscillation formalism and this tightly constrains the allowed NSI regions. The constraints obtained from this analysis are consistent with past results and no significant signal of non-standard neutrino interactions was found.

8.2 NSI in the $e - \tau$ Sector

8.2.1 Oscillation Effect

Similarly to the $\nu_\mu - \nu_\tau$ sector, the effects of NSI in the $\nu_e - \nu_\tau$ sector can be divided into three energy regions: low, medium, high.

At low energies ($E_\nu < 1$ GeV), the eigenvalue of the vacuum term $\Delta m^2_{32}/2E_\nu$ is much larger than matter eigenvalue $\sqrt{2}G_F N_f \varepsilon$ so oscillations between $\nu_\mu \rightarrow \nu_\tau$ are mostly governed by two flavour vacuum oscillations. In this region the contribution from NSI is not significant. The neutrinos in this energy region are in the FC Sub-GeV sample, which is expected to show no change when NSI is considered.

In the middle energy region ($1 < E_\nu < 15$ GeV), $\nu_\mu \rightarrow \nu_\tau$ transitions can be affected by $\varepsilon_{\tau\tau}$ as discussed in Section 8.1.1. A non-zero $\varepsilon_{e\tau}$ can affect transitions between ν_e and ν_τ. Effects from $\varepsilon_{e\tau}$ are expected to manifest as an upward-going excess in ν_e resulting from $\nu_\tau \rightarrow \nu_e$ transitions. In principle, ν_e could oscillate to ν_μ or ν_τ. However this contribution is negligable due to the lack of high energy ν_e flux (see Figure 5.2); the ν_μ/ν_e flavour ratio increases with neutrino energy, especially so for steeper zenith angles.

The effect of $\varepsilon_{e\tau}$ overlaps with the effect of non-zero θ_{13} as both are expected to induce $\nu_\tau \rightarrow \nu_e$ transitions, this will be discussed further in Section 8.2.3.

At high energies ($E_\nu > 15$ GeV) the ν_e atmospheric neutrino flux is significantly reduced so transitions from ν_e to other neutrinos, which would manifest as a deficit, can be neglected. However, transitions from $\nu_\tau \rightarrow \nu_e$ driven by $\varepsilon_{e\tau}$ would result in an excess of ν_e. The effects of $\varepsilon_{\tau\tau}$ discussed in Section 8.1.1 also apply here.

In summary, the $\nu_e - \nu_\tau$ NSI parameters can be constrained by higher energy ($E_\nu > 1$ GeV) neutrinos. The ν_μ samples constrain the $\varepsilon_{\tau\tau}$ parameter and ν_e samples constrain the $\varepsilon_{e\tau}$ parameter.

8.2.2 Limits On $\varepsilon_{e\tau}$ and $\varepsilon_{\tau\tau}$

All standard oscillation parameters are set to their best fit from the latest Super-K results shown in Table 8.2. Normal hierarchy is assumed. The scanned parameter space in $\varepsilon_{e\tau}$ is from -1.5 to 1.5 in steps of 0.025 (121 steps), in $\varepsilon_{\tau\tau}$ is from -1.0 to 1.0 in steps of 0.025 (81 steps), and in ε_{ee} from -4 to 4 in steps of 0.5 (17 steps). The minimum χ^2 is found for $(\varepsilon_{ee}, \varepsilon_{e\tau}, \varepsilon_{\tau\tau})$ = (0.0, -0.025, 0.075). The minimum χ^2 is 568 for 517 degrees of freedom.

The parameters $\varepsilon_{e\tau}$, $\varepsilon_{\tau\tau}$ and ε_{ee} are highly correlated so the limits on $\varepsilon_{e\tau}$ and $\varepsilon_{\tau\tau}$ are shown for fixed values of ε_{ee}; the nature of the correlation is discussed in Section 8.2.3. The NSI allowed contour regions are shown in Figure 8.9.

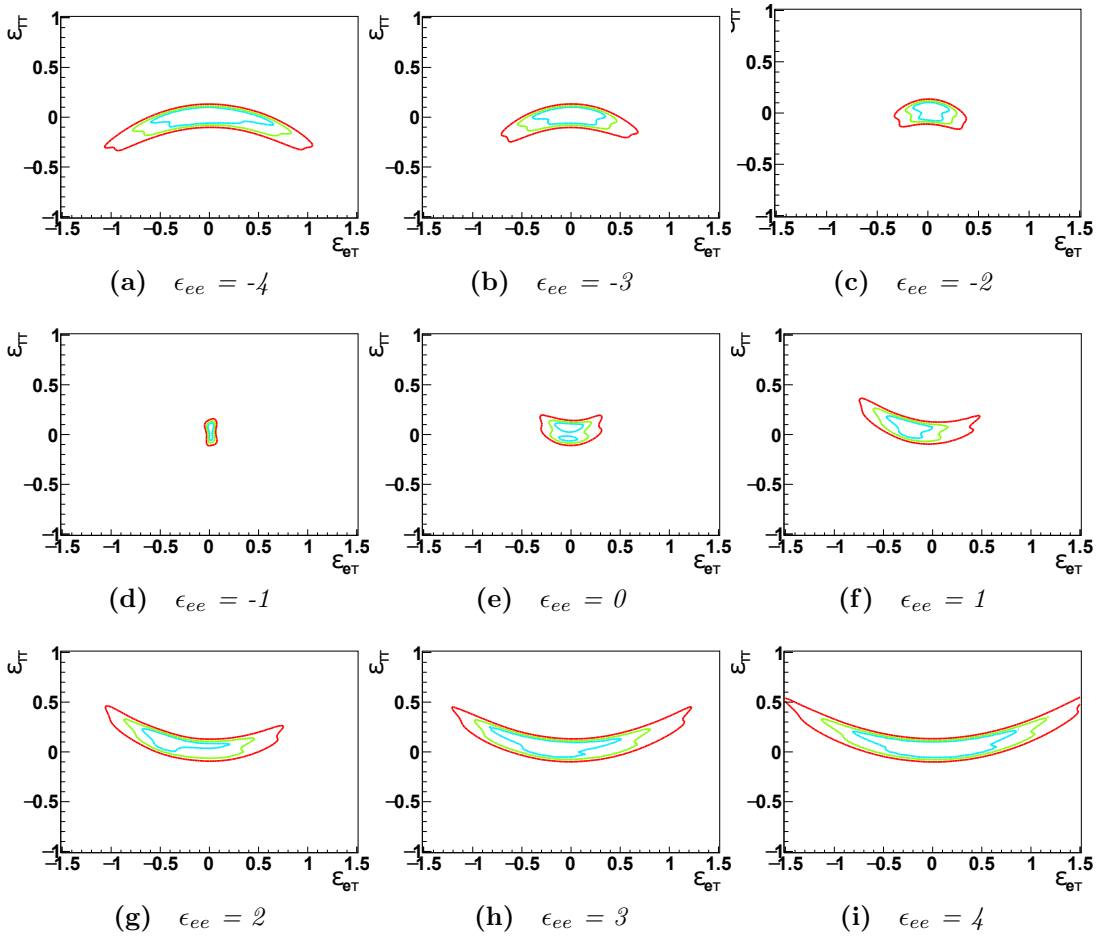

Figure 8.9 *Allowed NSI parameter regions in $\varepsilon_{e\tau} - \varepsilon_{\tau\tau}$ plane for fixed values of ε_{ee}. The contours represent the 68%, 90% and 99% C.L. defined by $\Delta\chi^2$ = 2.30, 4.61, 9.21 respectively.*

The systematic uncertainties and their ϵ_j values at the best fit point are summarised in Tables A.9 to A.12 in Appendix A.

The zenith angle distributions for the best fit point do not differ largely from the best fit standard oscillations for most of the sub-samples. The only samples which shows a difference is the most upward-going zenith angle bins in the UPMU showering sample.

8.2.3 Discussion

The results are presented as contours in the $\varepsilon_{e\tau} - \varepsilon_{\tau\tau}$ plane for fixed values of ε_{ee}. The shape of the contours is explained as follows. If $\varepsilon_{\mu\alpha} = 0$, an approximation justified by experimental constraints, then the matter component of the neutrino propagation Hamiltonian is:

$$H_{matter} = \sqrt{2} G_F N_e \begin{pmatrix} 1+\varepsilon_{ee} & 0 & \varepsilon_{e\tau} \\ 0 & 0 & 0 \\ \varepsilon_{\tau e} & 0 & \varepsilon_{\tau\tau} \end{pmatrix}. \tag{8.19}$$

Following Reference [76], the diagonalisation of Equation 8.19 results in

$$H_{matter} = \mathcal{O}\mathrm{diag}(\lambda_{e'}, 0, \lambda_{\tau'})\mathcal{O}^{\dagger}, \tag{8.20}$$

where

$$\mathcal{O} = \begin{pmatrix} \cos\beta & 0 & e^{-i\phi_{e\tau}}\sin\beta \\ 0 & 1 & 0 \\ -e^{i\phi_{e\tau}}\sin\beta & 0 & \cos\beta \end{pmatrix}. \tag{8.21}$$

In this new basis,

$$\nu'_{\mu} = \nu_{\mu}, \tag{8.22}$$

$$\nu'_{e} = \cos\beta\nu_e + e^{-i\phi_{e\tau}}\sin\beta\nu_{\tau}, \tag{8.23}$$

$$\nu'_{\tau} = -e^{i\phi_{e\tau}}\sin\beta\nu_e + \cos\beta\nu_{\tau}. \tag{8.24}$$

The eigenvalues from the diagonalisation are:

$$\lambda_{e'} = \sqrt{2}G_F N_e(\frac{1+\varepsilon_{ee}+\varepsilon_{\tau\tau}}{2} + \sqrt{(\frac{1+\varepsilon_{ee}-\varepsilon_{\tau\tau}}{2})^2 + |\varepsilon_{e\tau}|^2}, \tag{8.25}$$

$$\lambda_{\tau'} = \sqrt{2}G_F N_e(\frac{1+\varepsilon_{ee}+\varepsilon_{\tau\tau}}{2} - \sqrt{(\frac{1+\varepsilon_{ee}-\varepsilon_{\tau\tau}}{2})^2 + |\varepsilon_{e\tau}|^2}, \tag{8.26}$$

and the matter angles are:

$$\tan 2\beta = \frac{2|\varepsilon_{e\tau}|}{1+\varepsilon_{ee}-\varepsilon_{e\tau}}, \tag{8.27}$$

$$\phi_{e\tau} = arg(\varepsilon_{e\tau})/2. \tag{8.28}$$

In the case that $\lambda_{e'}$ and $\lambda_{\tau'}$ dominate over the vacuum terms, ν_μ oscillation would be suppressed in matter in clear conflict with the data. A hierarchical structure where one of the matter eigenvalues is comparable to the vacuum mass splitting and the other eigenvalue much larger decouples one state and allows vacuum oscillations to occur between the remaining two states. In the case that $\lambda_{e'} >> \Delta m^2_{32}/2E \sim \lambda_{\tau'}$, ν'_e decouples from the system and the vacuum term drives $\nu_\mu \to \nu'_\tau$ oscillations.

The size of $\lambda_{\tau'}$ is strongly constrained by atmospheric neutrinos and it can be assumed that $\lambda_{\tau'} << \Delta m^2_{32}/2E$ otherwise the ν_μ disappearance probability would not exhibit the characteristic energy dependence observed in atmospheric neutrinos. In the limit $\lambda_{\tau'} = 0$ the three NSI parameters satisfy a parabolic relationship:

$$\varepsilon_{\tau\tau} = \frac{|\varepsilon_{e\tau}|^2}{1+\varepsilon_{ee}}. \tag{8.29}$$

The parabolic curve presents itself in the χ^2 distributions in Figure 8.9 with $\varepsilon_{\tau\tau}$ extending to negative values when $1+\varepsilon_{ee}$ is negative and positive values when $1+\varepsilon_{ee}$ is positive. The low energy ($E_\nu < 1$ GeV) data sample has negligable matter effects and would be best fit by vacuum oscillation parameters, however the effective mixing angle and mass splitting in matter are constrained by high energy datasets. The need to keep the preferred vacuum parameters consistent between the high and low energy data, constrains the effective mixing angle and mass splitting which translates to a constraint on the NSI ϵ parameters; this is the reason for the cut-offs in the parabolic shape.

There is a positive-negative symmetry in $\varepsilon_{e\tau}$ which is broken in the case of a non-zero θ_{13}. $\varepsilon_{e\tau}$ can cause an excess of upward-going ν_e which oscillate from ν_τ, a similar effect is caused by θ_{13} and the standard matter effect. The energy and zenith angle regions of the expected excess coincide for θ_{13} and $\varepsilon_{e\tau}$, shown in Figure 8.10. An expansion of the Hamiltonian equation with NSI shows that θ_{13} terms appear with terms depending on $\arg(\varepsilon_{e\tau})$ breaking the positive-negative symmetry [76].

The standard matter effect is dependent on the sign of the matter term and the sign of the mass splitting: an excess of ν_e is observed for neutrinos and normal hierarchy, or $\bar{\nu}_e$ for antineutrinos and inverted hierarchy. A larger atmospheric neutrino flux and interaction cross section, compared to antineutrinos, results in asymmetric constraints on $\varepsilon_{e\tau}$.

Table 8.3 *Constraints on $\varepsilon_{e\tau}$ for the current analysis and the previous SK result.*

ε_{ee}	SK NSI 2011	New Result
1.5	$\lvert\varepsilon_{e\tau}\rvert < 0.54$	$-0.75 < \varepsilon_{e\tau} < 0.325$
0.0	$\lvert\varepsilon_{e\tau}\rvert < 0.39$	$-0.225 < \varepsilon_{e\tau} < 0.225$
-1.5	$\lvert\varepsilon_{e\tau}\rvert < 0.24$	$-0.1 < \varepsilon_{e\tau} < 0.125$

Table 8.4 *Constraints on $\varepsilon_{\tau\tau}$ for the current analysis and the previous SK result.*

ε_{ee}	SK NSI 2011	New Result
1.5	$-0.09 < \varepsilon_{\tau\tau} < 0.15$	$-0.05 < \varepsilon_{\tau\tau} < 0.35$
0.0	$-0.09 < \varepsilon_{\tau\tau} < 0.21$	$-0.075 < \varepsilon_{\tau\tau} < 0.15$
-1.5	$-0.15 < \varepsilon_{\tau\tau} < 0.09$	$-0.075 < \varepsilon_{\tau\tau} < 0.125$

These results can be compared to the previous Super-K NSI zenith angle analysis [132, 133]. This analysis uses the full three-flavour standard oscillations extended to include NSI, whereas the past result was achieved using two-flavour standard oscillations. This limitation resulted in symmetric constraints on the NSI parameters. The three-flavour standard oscillation, including standard matter effects, have imposed tighter constraints on positive values of $\varepsilon_{e\tau}$. Another key difference is the scanned range of ε_{ee}. In the former analysis, the range was determined by considering the allowed range of ε^d_{ee} given by CHARM data [62]. The range was extended in this analysis to include (large) values of ε_{ee} consistent with global oscillation data discussed in Section 2.3.2.

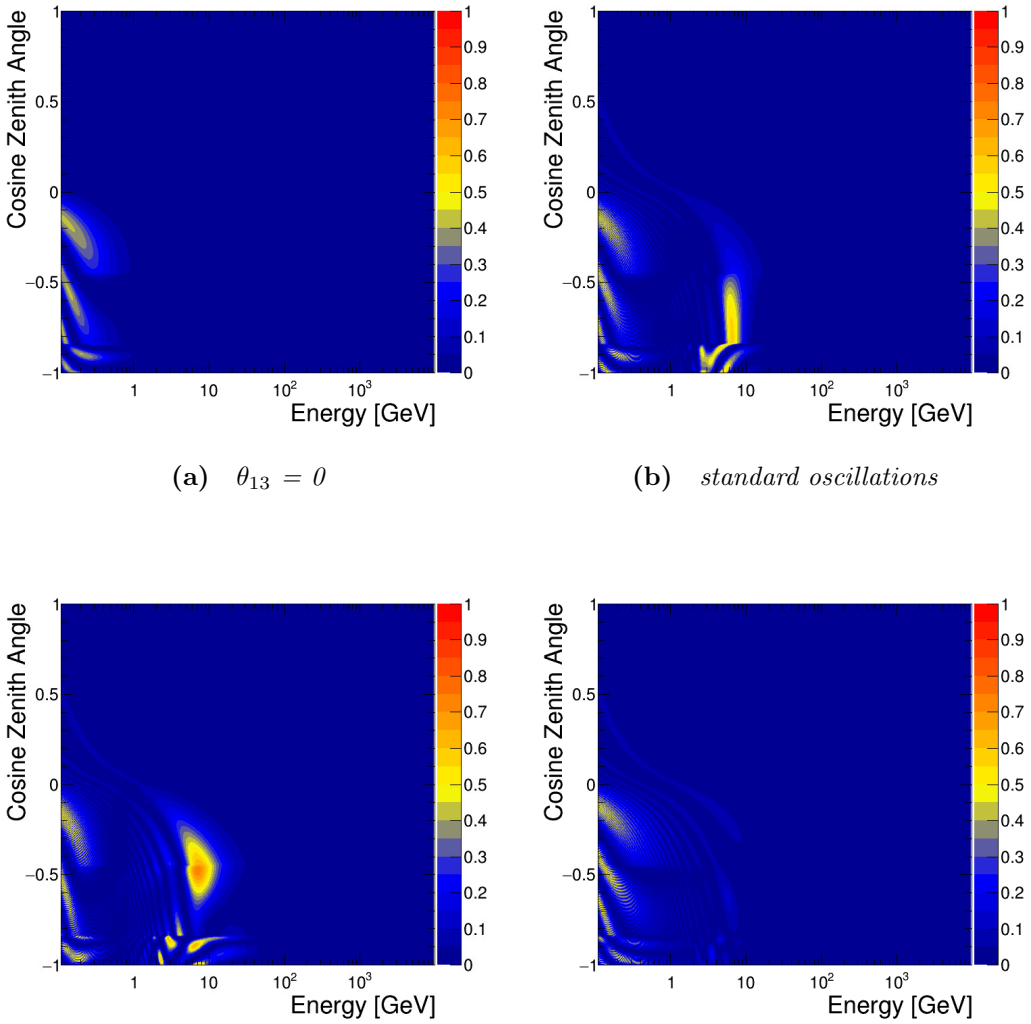

(a) $\theta_{13} = 0$ **(b)** *standard oscillations*

(c) $\varepsilon_{e\tau} = 0.2$ **(d)** $\varepsilon_{e\tau}$ = -0.2

Figure 8.10 *Oscillation contours showing the $\nu_\mu \rightarrow \nu_e$ oscillation probability for different values parameters. Oscillation probabilities calculated using full three-flavour equations with all other NSI set to zero. The horizontal axis shows the energy and the vertical axis shows the zenith angle. The top left plot shows standard oscillation only, top right shows standard plus flavour-changing neutral currents. The bottom left plot shows standard plus lepton non-universality and the bottom right plot includes flavour-changing neutral currents and lepton non-universality. Normal hierarchy has been assumed.*

Comparisons of the new and past results are shown in Tables 8.3 and 8.4. The new constraints on $\varepsilon_{e\tau}$ and $\varepsilon_{\tau\tau}$ are somewhat looser than the past result, which is expected due to the assumed standard oscillation parameters. The past analysis fixed $(\Delta m^2_{32}, \sin^2\theta_{32})$ to $(2.1 \times 10^{-3}\ \text{eV}^2, 0.5)$ which was the best fit point for

SK atmospheric neutrino data at the time. It should be noted that while the standard oscillation parameter assumptions affect the allowed ranges of the NSI parameters, the minimum χ^2 values for different standard oscillation parameter assumptions are larger than those for the best fit point so the allowed region for the NSI parameters is not expected to significantly differ if the standard oscillation parameters are allowed to vary.

This is the first attempt at searching for NSI in the $e - \tau$ sector in atmospheric neutrinos, accounting for three-flavour standard oscillations. Although no signal of NSI was found, constraints have been obtained for $\varepsilon_{e\tau}$ and $\varepsilon_{\tau\tau}$ for various values of ε_{ee}. The atmospheric neutrino data is explained well by standard $\nu_\mu \to \nu_\tau$ oscillation so $\varepsilon_{\tau\tau}$ is constrained tightly. However, large values of $\varepsilon_{e\tau}$ and ε_{ee} are still compatible with the data.

Chapter 9

Hyper-Kamiokande

Hyper-Kamiokande is a next-generation large water Cherenkov detector which will succeed Super-K. The physics program includes precise measurement of neutrino oscillation parameters, measurement of CP violation in the lepton sector, neutrino cross section measurements, searches for exotic oscillation scenarios, solar neutrino day/night asymmetry measurements and spectrum upturn, supernovae detection and diffuse supernova background measurements as well as nucleon decay searches.

The Hyper-Kamiokande detector will be located in the Tochibora mine of the Kamioka Mining and Smelting Company in Gifu, Japan under Nijuugo mountain. This gives an overburden of 650 m of rock or 1,750 meters-water-equivalent (m.w.e). The site is located 8 km south of the Super-Kamiokande site and the J-PARC [78] neutrino beamline is directed such that both of the detectors will have the same 2.5° off-axis angle.

This chapter is intended to give the reader a brief summary of the key components of the Hyper-Kamiokande detector relevant to this thesis. For a more detailed description, see Reference [17].

9.1 Physics Goals

In the next sections, the physics program of Hyper-K is outlined. For more details refer to the Hyper-K design report [17].

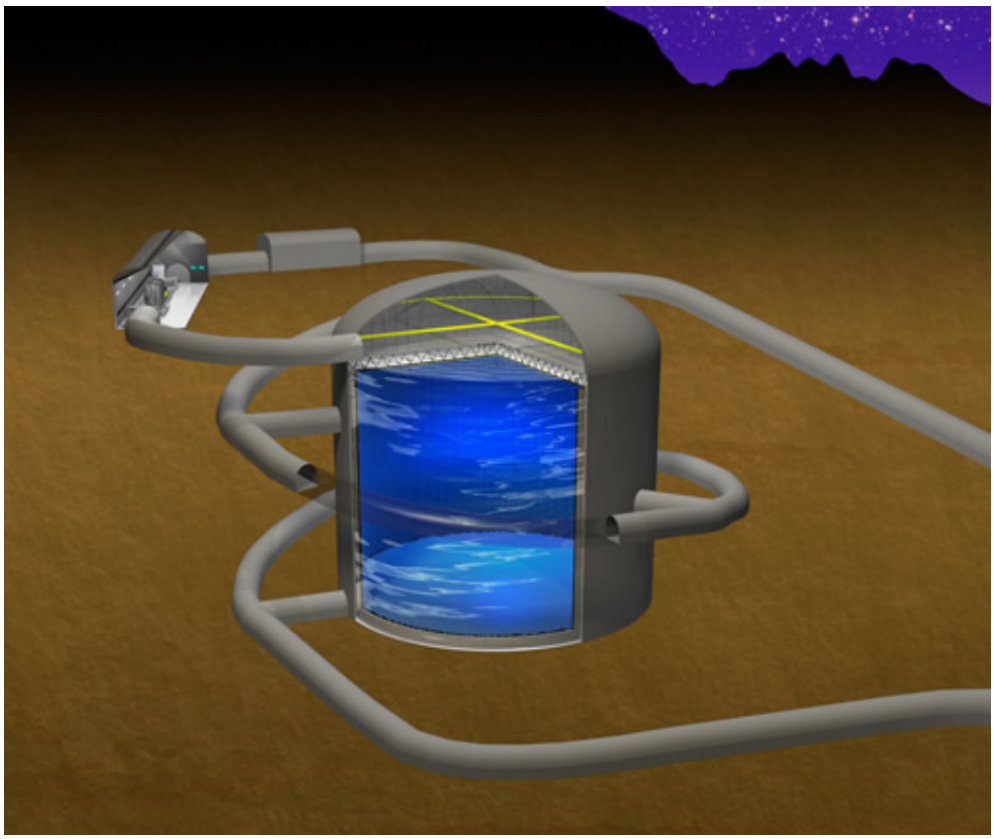

Figure 9.1 *An illustration of a Hyper-Kamiokande cylindrical tank. Taken from [17].*

9.1.1 Long Baseline and Atmospheric Neutrinos

In a similar way to T2K [11], Hyper-K will use a beam of neutrinos produced at the J-PARC [108] facility in Tokai, Japan. The neutrinos are produced by accelerating protons and colliding them on a graphite target. The collisions typically produce pions which then decay to give muon neutrinos. The far detector will be 295 km away from the beam production point, at an off-axis angle of 2.5°. This gives Hyper-K the same baseline and off-axis angle as Super-K. The energy spectrum of the neutrino beam varies with off-axis angle At an angle of 2.5° the energy spectrum peaks at roughly 600 MeV which corresponds to the oscillation maximum for a baseline of 295 km.

The near detector is used to measure the flux and direction of the neutrino beam, together with the contamination from electron neutrinos or wrong sign neutrinos. Another key purpose of the near detector is to make measurements of neutrino interaction cross sections. Figure 9.2 shows the ND280 near detector complex [13] currently used for the T2K experiment; this near detector suite will be upgraded

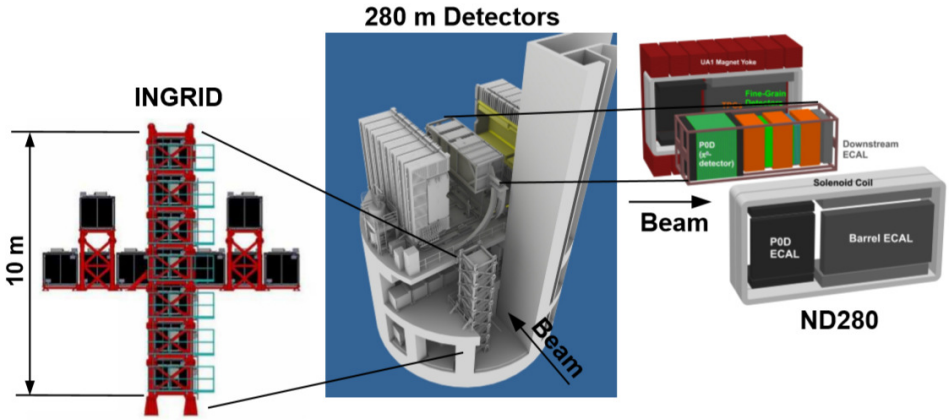

Figure 9.2 *The ND280 near detector complex with the INGRID on-axis detector (left) and the ND280 off-axis detectors (right). Taken from [17].*

in preparation for T2K-II [8, 19] and will then be used for Hyper-K. A model of the planned ND280 upgrade is shown in Figure 9.3.

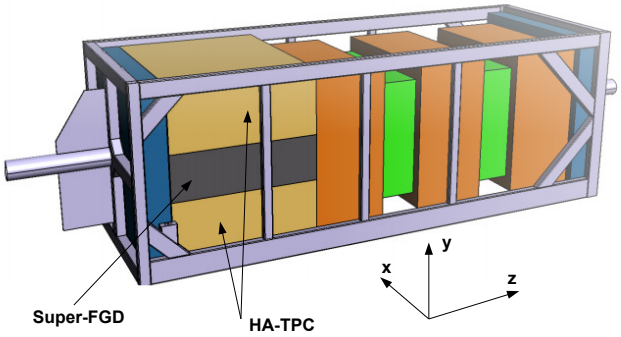

Figure 9.3 *A diagram of the upgraded ND280 detector where the TOF detectors have not been drawn. Two High-Angle TPCs (yellow) with a scintillator detector "Super-FGD" (grey) will be installed in the most upstream portion of the detector (left). The three (orange) TPCs and two (green) FGDs make up the tracker system in the downstream portion in the current ND280 detector and will remain after the upgrade. Taken from [19].*

Planned upgrades to the J-PARC main ring will see the beam power increase from 500 kW to 1.3 MW in time for Hyper-K data-taking [78]. Hyper-K will collect many events and have smaller statistical uncertainties, compared to T2K.

Near detector systematics need to be lowered to around 1-2% for Hyper-K physics measurements. Current uncertainties on the estimated neutrino flux at Super-K are roughly 6%, with half of this coming from flux and cross section uncertainties [16]. One of the key limitations comes from the difference in target material; T2K uses two scintillator targets, one of which is made up of 40% water. ND280 compares the interaction rate on the two targets and uses a subtraction analysis to constrain the neutrino interaction cross section in water and so additional uncertainties arise (from the subtraction), compared to measurements taken on pure water. A further limitation comes from differences in the acceptance of the near and far detectors. Upgrades to ND280 will increase the fiducial mass and angular acceptance of the detector, the addition of a time-of-flight (ToF) detector will also improve the reconstruction of backward-going events.

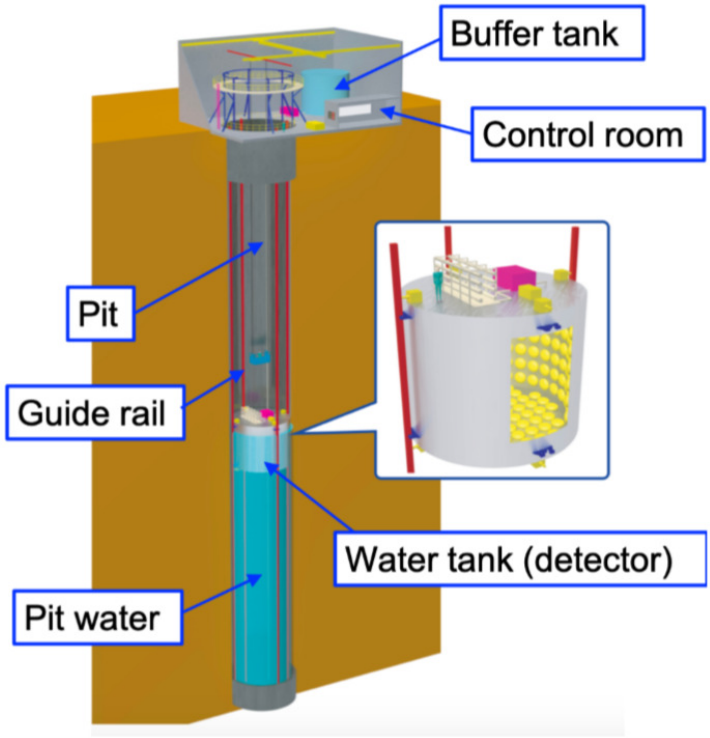

Figure 9.4 *A conceptual design of the IWCD detector facility [164].*

These limitations will be addressed by the implementation of a complementary additional "near" detector called the intermediate water Cherenkov detector (IWCD) [17]. Figure 9.4 shows a conceptual design of IWCD. IWCD can measure interactions in water with the same angular acceptance as the far detector, this removes the need for extrapolation. A key feature of IWCD will be its off-axis

spanning technique. The detector will be able to span various off-axis angles from 1-4°, taking advantage of the angle dependent energy spectrum properties of the beam. The detector will also be loaded with gadolinium which will enable separation of neutrino and antineutrino events and improve event classification by tagging neutrons.

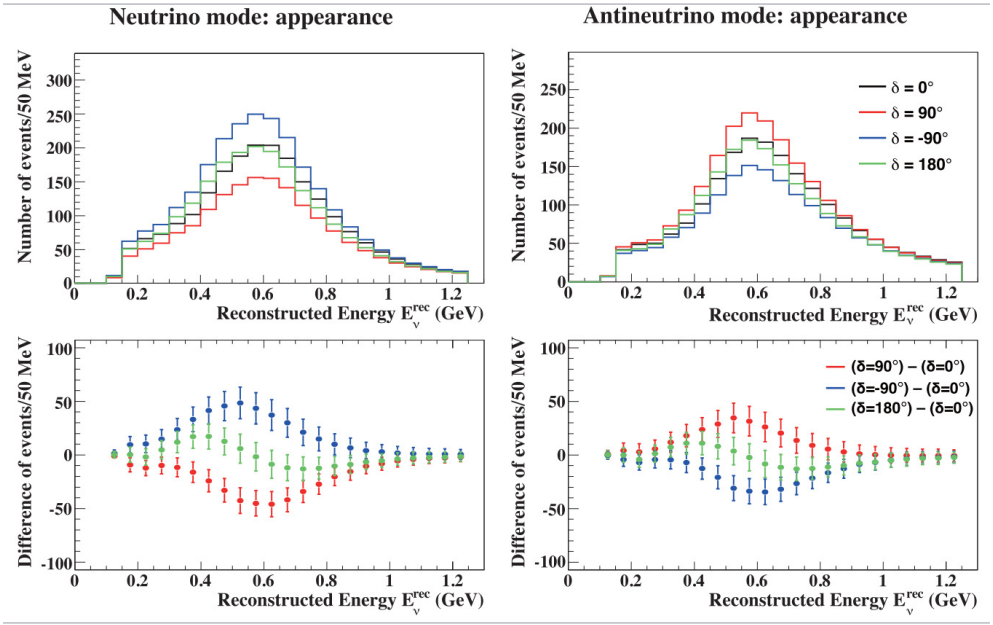

Figure 9.5 *Reconstructed neutrino energy distribution for several values of δ_{CP} (top) and the difference in reconstructed neutrino energy distribution from the case of δ_{CP}. The plots are for the ν_e appearance mode for neutrinos (left) and antineutrinos (right). Normal hierarchy is assumed and* $\sin^2\theta_{13} = 0.1$. *Taken from [17].*

The main goal of the long baseline program is the measurement of CP violation in the lepton sector. The CP violating phase δ_{CP}, is measured by comparing the oscillation probabilities of neutrinos ($\nu_\mu \to \nu_e$) and antineutrinos ($\bar{\nu}_\mu \to \bar{\nu}_e$). The J-PARC neutrino beam can be run in neutrino or antineutrino mode, allowing for separation of neutrino and antineutrino events, which makes the measurement of δ_{CP} possible. Figure 9.5 shows how the reconstructed ν_e energy spectrum varies with different values of δ_{CP}. The long baseline program will also make precise measurements of the neutrino oscillation parameters θ_{13}, θ_{23} and Δm^2_{32}. Figure 9.6 shows that after 10 years, Hyper-K is expected to exclude CP conservation with a significance of 3σ (5σ) for 76% (57%) of the phase space.

Due to the relatively short path length, the sensitivity of the long baseline program alone to the mass hierarchy is limited. Atmospheric neutrinos however, traverse the earth and the contribution from the matter effect results in an surplus

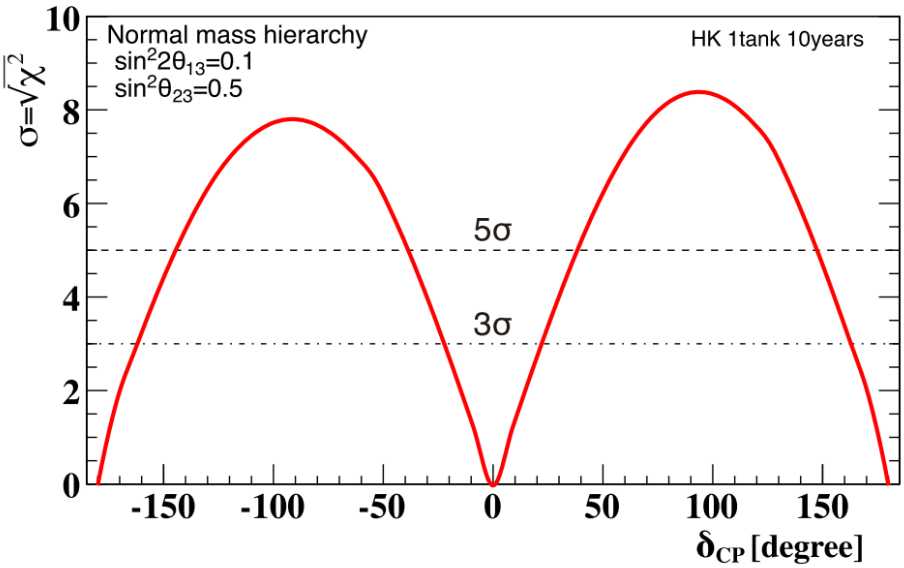

Figure 9.6 *Expected significance, for a single Hyper-K tank running for 10 years, to exclude CP conservation ($\delta_{CP} = 0$). Normal hierarchy is assumed with* $\sin^2\theta_{13} = 0.1$ *and* $\sin^2\theta_{23} = 0.5$. *Taken from [17].*

of ν_e appearance for the normal hierarchy whereas the increase is seen in $\bar{\nu}_e$ for the inverted hierarchy. Figure 9.7 shows how the oscillated flux differs from the unoscillated flux for different values for θ_{13} and δ_{CP}.

The strong matter effects in the atmospheric neutrino data will be complemented by the precise knowledge of baseline and narrow energy region that enables T2HK to precisely measure θ_{23}. Thus, combining the beam and atmospheric neutrinos increases Hyper-K's sensitivity to the oscillation parameters.

9.1.2 Solar Neutrinos

Measurements of solar neutrinos enable determination of the neutrino oscillation parameters between mass eigenstates ν_1 and ν_2. The allowed region for the $\nu_1 - \nu_2$ neutrino oscillation parameter space can be seen in Figure 2.6. The mixing angle measured by solar and reactor neutrino experiments are in agreement, however there exists a 2σ tension in the mass squared splitting Δm^2_{21} between Super-K and KamLAND [118]. Super-K measured a day-night asymmetry in the number of observed solar neutrinos [148]. This results in a value of Δm^2_{21} lower than the global best fit (which is dominated by KamLAND [20]). Hyper-K is expected to measure the day-night asymmetry to more than 5σ significance. Due to a

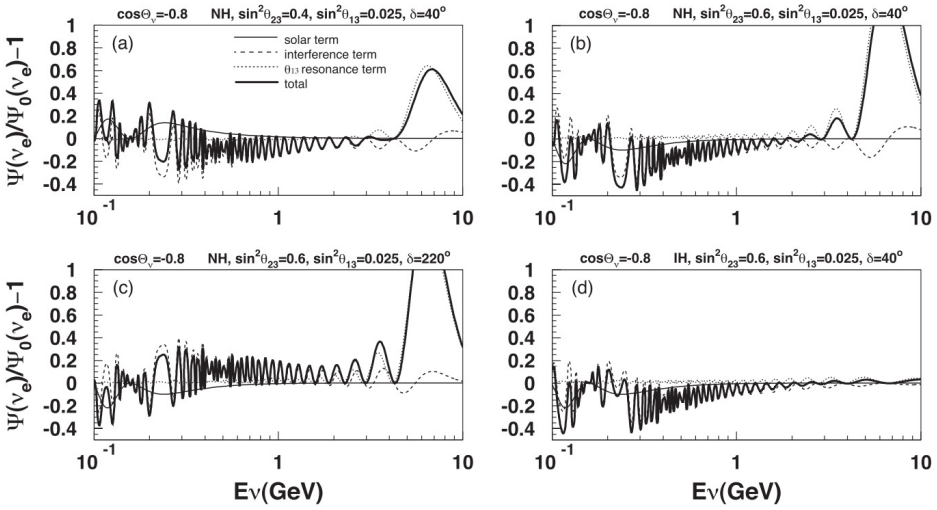

Figure 9.7 *Upward-going oscillated ν_e flux relative to the non-oscillated flux as a function of neutrino energy. Thick solid lines indicate the total flux whereas the thin line, dashed line and dotted line indicate the contribution from the solar term, interference term and the θ_13 resonance term respectively. The top two plots show the effect of the θ_{23} octant. The top right plot and bottom left plot show the effect of δ_{CP}. The bottom right plot is for inverted hierarchy the resonance is not seen in this sample but is seen in $\bar{\nu}_e$ instead. Taken from [17].*

transition from vacuum oscillations below 2 MeV to matter effects in the Sun above 5 MeV, lower energy solar neutrinos are expected to show an increase in ν_e survival probability which is called solar spectrum upturn. The shape of this upturn spectrum can distinguish between regular matter oscillations and more exotic models [127]. Hyper-K will be able to measure the spectrum upturn, with respect to a flat survival probability, to 3σ (5σ) significance with a low energy threshold of 4.5 MeV (3.5 MeV).

9.1.3 Supernova Neutrinos

A core collapse supernova is the ultimate fate of massive stars between 8 and 50 solar masses. The star fuses elements until it reaches nickel and iron, after which no energy can be released from fusion. Once the core passes the Chandrasekhar limit of 1.4 $M_\odot$ the electron degeneracy pressure can no longer sustain the gravitational pressure and the core begins to collapse [57]. The supernova begins with a prompt neutronisation burst phase in which a burst of electron captures ($p + e^- \rightarrow n + \nu_e$) emit ν_e with very high luminosity. The following accretion and cooling phases produce neutrinos and antineutrinos of all three types. Neutrinos

interact weakly with matter so the majority (99%) of the energy released from the supernova is carried away by neutrinos.

In 1987, 25 neutrinos from supernova SN1987a, were detected by Kamiokande [101], IMB [91] and Baksan [36]. The supernova occurred in the Large Magellanic Cloud (LMC) galaxy roughly 50 kpcs away. The neutrino observations confirmed the basic model of core collapse supernovae and the detection of more supernova neutrinos will provide further inputs to improve supernova models.

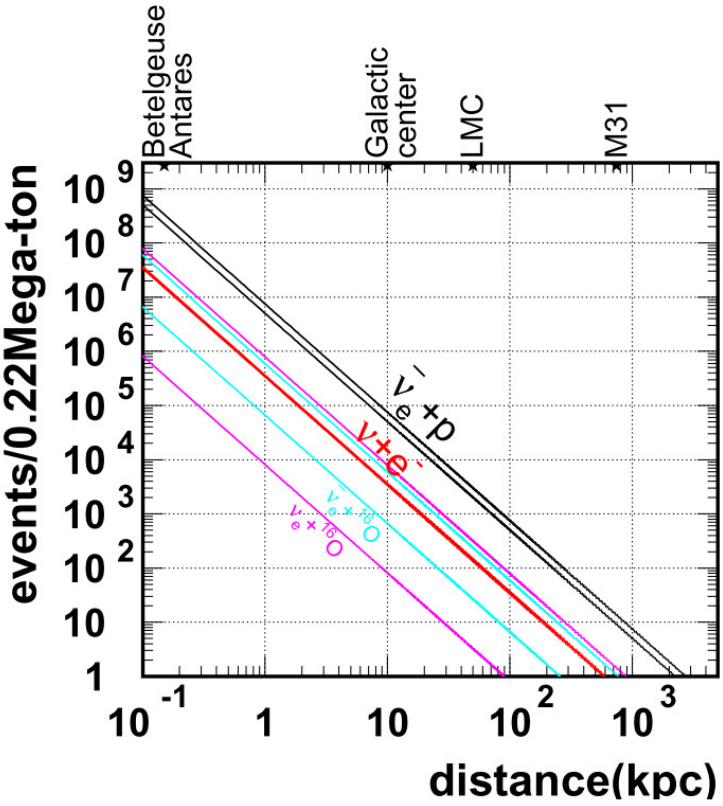

Figure 9.8 *The expected number of supernova neutrino events, for each neutrino interaction, as a function of the distance to the supernova. The figure is for a single Hyper-K tank and the bands for each line indicate the variation based on the assumption of neutrino oscillation parameters. Taken from [17].*

Supernova neutrinos undergo different interactions in water, the main interaction in Hyper-K will be the detection of electron antineutrinos undergoing inverse beta decay ($\bar{\nu}_e + p \rightarrow e^+ + n$). The advantage of Hyper-K as a supernova detector comes from the very large detector volume, Figure 9.8 shows the expected event rate as a function of the distance to the supernova. For a supernova occurring at a distance of 50 kpcs, in the LMC, 2,200 to 3,600 neutrino events are expected.

Neutrinos and antineutrinos from all of the past core collapse supernovae are

expected to be present throughout the universe. These neutrinos are called supernova relic neutrinos (SRN) or diffuse supernova background (DSNB) [48]. The detection of DSNB will give a better insight into the history of the universe as well as the rate of core collapse supernovae and heavy element synthesis. Hyper-K will look for the DSNB in an energy range of 16-30 MeV. The shape of the DSNB energy spectrum can provide important information about the history of star formation.

9.1.4 Proton decay

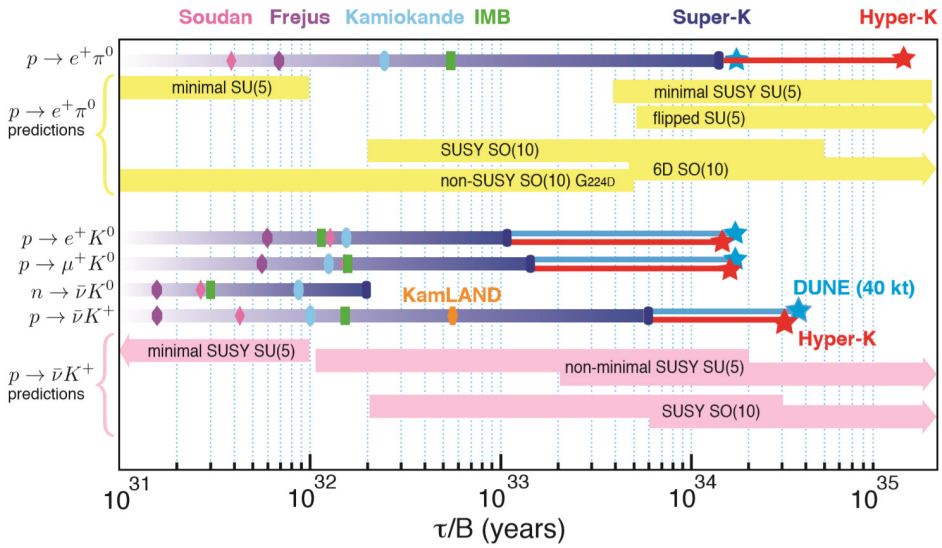

Figure 9.9 *A comparison of the experimental limits on the rates of nucleon decay and projected limits for Hyper-K (10 years, single tank) and DUNE. Ranges of theoretical predictions also shown. Taken from [17].*

The goal of the original Kamiokande experiment, the predecessor of Super-K, was to search for proton decay, this was also a major goal of the Super-K experiment and now Hyper-K. Proton decay is a key prediction of many grand unified theories (GUTs) [67, 121] with predictions of the proton lifetime being longer than 10^{30} years. Due to the large detector mass, Hyper-K will be able to probe proton lifetimes up to $\sim 10^{35}$ years. Figure 9.9 shows the 90% C.L. limits set by Super-K and various other experiments as well as the expected lifetime sensitivity of Hyper-K and DUNE [22].

The $p \to e^+\pi^0$ is the golden channel for water Cherenkov detectors as there is no invisible energy and the two body decay should result in a very small total

momentum. The decay would cause three Cherenkov cones, one from the positron and the other two from the pion decay to two photons. Hyper-K will select the proton decay events by looking for 2 or 3 e-like rings (the 2 photons from pion decay may produce rings close enough to be reconstructed as a single ring). For 3-ring events, two of the rings with the invariant mass closest to the mass of π^0 will be selected as the π^0 candidate and a further cut on the π^0 mass is applied. Finally, the invariant mass of the three rings is required to be consistent with the proton mass and the total momentum is less than 100 MeV/c for a free proton enriched sample; for a bound proton enriched sample the total momentum should be between 100 and 250 MeV/c. Figure 9.10 shows the expected number of events and backgrounds for this search.

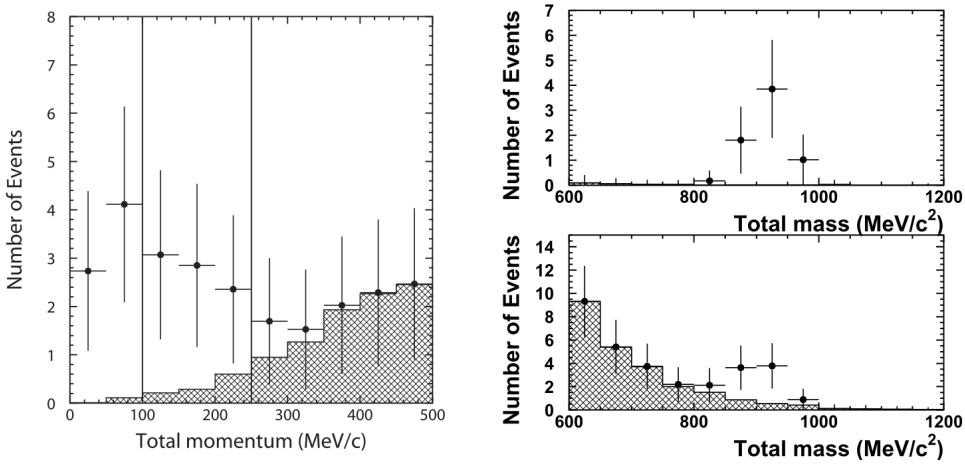

Figure 9.10 *The total momentum of events passing the $p \rightarrow e^+\pi^0$ event selection criteria except the momentum cut (left) with solid vertical lines indicating the momentum cuts. The reconstructed invariant mass of events passing the $p \rightarrow e^+\pi^0$ event selection criteria except the invariant mass cut (right), for free (top) and bound (bottom) protons. The hatched regions in the plots indicate the atmospheric neutrino background whereas the black dots represent the sum of proton decays and background. All plots are for a 10 year exposure of a single Hyper-K tank with an assumed proton lifetime of 1.7x10^{34} years. Taken from [17].*

9.2 Detector Design

The Hyper-Kamiokande tank will have a height of 73 m and a diameter of 69 m making it 273 ktons. It is divided into two optically separated volumes, an inner cylinder will form the ID, and a larger cylinder which encapsulates the ID will

serve as the veto region (OD). The tank will be filled with ultrapure water.

The OD will have a lateral depth (along the cave barrel walls) of 1 m and a 2 m depth from the top and bottom cave walls. Similar to Super-K, Hyper-K will mount PMTs on either side of a PMT support frame which is roughly 60 cm wide. Accounting for the deadspace in the PMT support frame, the total volume of the ID is 230 ktons. If we assume only events with a reconstructed vertex 2 away from the ID walls are used, this would mean a total fiducial volume of 191 ktons which is eight times larger than Super-K (22.5 kton).

Up to 40% of the ID surface will be instrumented with 50 cm Hamamatsu R12860-HQE PMTs (see Table 9.1) while the OD will be instrumented with up to 0.28% photocoverage 8 cm PMTs coupled to wavelength shifting plates, which will be discussed in Chapter 10. PMTs will be tested to ensure that they have a suitable pressure tolerance and acrylic covers will be placed on top of the ID PMTs to prevent a chain implosion event.

In order to increase physics sensitivities, there is an option to build a second Hyper-K tank in South Korea six years after the first tank [145].

9.3 Photosensors

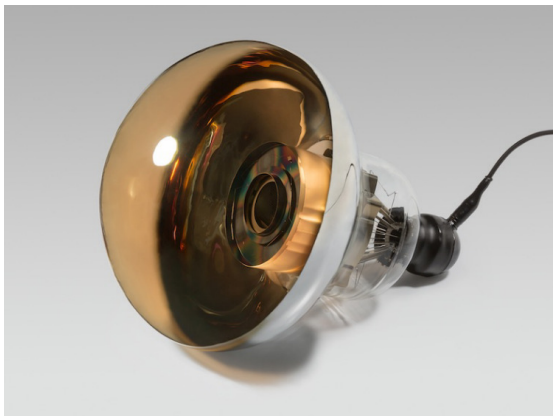

Figure 9.11 *A picture of the 50 cm Hamamatsu R12860-HQE box-and-line PMT. Taken from [17].*

The Hyper-Kamiokande inner detector will have up to 40% of its surface covered with 50 cm Hamamatsu R12860-HQE PMTs (see Figure 9.11). These PMTs have been newly developed for Hyper-K with several improvements over the existing 50 cm R3600 PMTs used in Super-K. The PMTs' properties and their

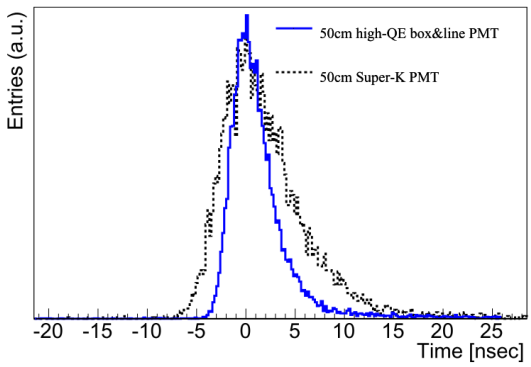

Figure 9.12 *The single photoelectron transit time distribution of the Hyper-K PMT (blue) and Super-K PMT (black). Taken from [17].*

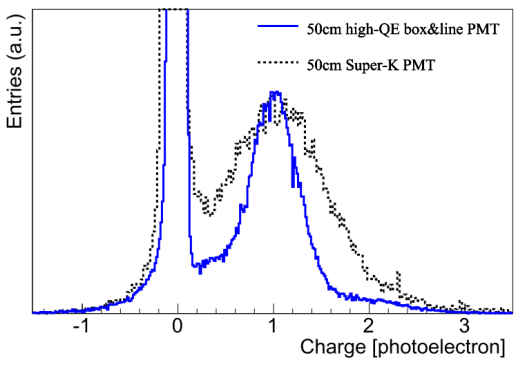

Figure 9.13 *The single photoelectron charge distribution of the Hyper-K PMT (blue) and Super-K PMT (black). Taken from [17].*

improvements are discussed in detail in Reference [17].

The improvements include:

- **Higher quantum efficiency:** Improvements to the photocathode have resulted in a QE of 30% at 390 nm for the Hyper-K PMTs, compared to a peak QE of 22% for the Super-K PMTs.
- **Higher collection efficiency:** In the area covered by a 46 cm diameter, Super-K PMTs have a CE of 73%, Hyper-K PMTs have a CE of 95%. Outside of the 46 cm region the CE of Super-K PMTs drops below 50% while for the Hyper-K PMTs it is 87%. This increase in collection efficiency is achieved by optimising the glass curvature and focusing electrode as well as changing the dynode structure. Photoelectrons could sometimes miss the first dynode in the Venetian Blind dynode structure used in the Super-K PMTs. The Box-and-Line dynode used in the Hyper-K PMTs makes use of a wide box as the first dynode which collects nearly all of the emitted photoelectrons (see Figure 9.14).
- **Better time resolution:** Figure 9.12 shows the transit time spread for the Super-K and Hyper-K PMTs and a clear improvement, by a factor of two, can be seen. The time resolution for single photoelectron signals is 4.1 ns (FWHM). The left region of the transit time distribution has a resolution of 1.1 ns (σ) .

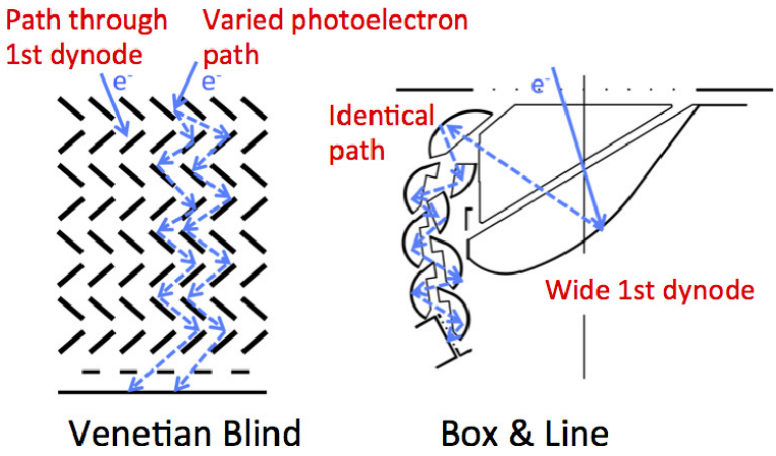

Figure 9.14 *A sketch of the Venetian Blind dynode structure used in Super-K PMTs (left) and the Box-and-Line dynode structure used in Hyper-K PMTs (right). Taken from [138].*

The improvements to the photosensor have resulted in a single photon detection efficiency two times better than that of the Super-K PMTs. A figure showing the relative single photon detection efficiency as a function of position angle on the PMT is shown in Figure 9.15. It is worth noting that the increase in sensitivity has also increased the PMT's dark rate. The dark noise hits, resulting from thermionic emission from the photocathode, vary with temperature and PMT voltage. The dark noise for the Hyper-K PMTs have been measured, in air, to be 8.3 kHz at 15° C this is double the rate of Super-K PMTs which have a dark noise rate of 4.2 kHz. Efforts are being made to reduce the dark noise in order to increase the sensitivity of low energy physics analyses. Another concern for low energy studies is the radioactive contaminants in PMT glass. Radioactive contamination in the glass has been measured and the concentration of ^{40}K has been reduced by an order of magnitude compared to the glass used in Super-K PMTs. A summary of the PMT's properties are shown in Table 9.1.

Some portion of the ID may be instrumented with other types of PMT which may increase the physics capabilities of Hyper-K. One of the designs for alternative PMTs is the Multi-PMT (mPMT). The mPMT, shown in Figure 9.16, consists of 19 7.7 cm PMTs housed in an acrylic 50 cm dome. The dome acts as a pressure-tolerant vessel and contains all of the readout electronics inside. There are several advantages to this design. The increased number of PMTs will improve the granularity and the smaller PMTs have a much lower dark rate so the overall module will have less noise than a typical 50 cm PMT. Another advantage comes from the fact that the PMTs are angled such that they are perpendicular to the tangent of the surface of the dome, this increases directionality information which

Table 9.1 *Specifications of the 50cm Hamamatsu R12860-HQE PMT. Values taken from [17].*

Property	
Shape	Hemispherical
Photocathode area	50 cm (20 inch) diameter
Bulb material	Borosilicate glass (3 mm thickness)
Photocathode material	Bialkali (Sb-K-Cs)
Quantum efficiency	30% at $\lambda = 390$ nm typical
Collection efficiency	95% at 10^7 gain
Dynode structure	10-stage box-and-line
Gain	10^7 at 2000 V
Dark pulse rate	8 kHz at 10^7 gain at 13° C (after stabilising)
Weight	9 kg (without cable)
Volume	61,000 cm^3
Pressure tolerance	1.25 MPa waterproof

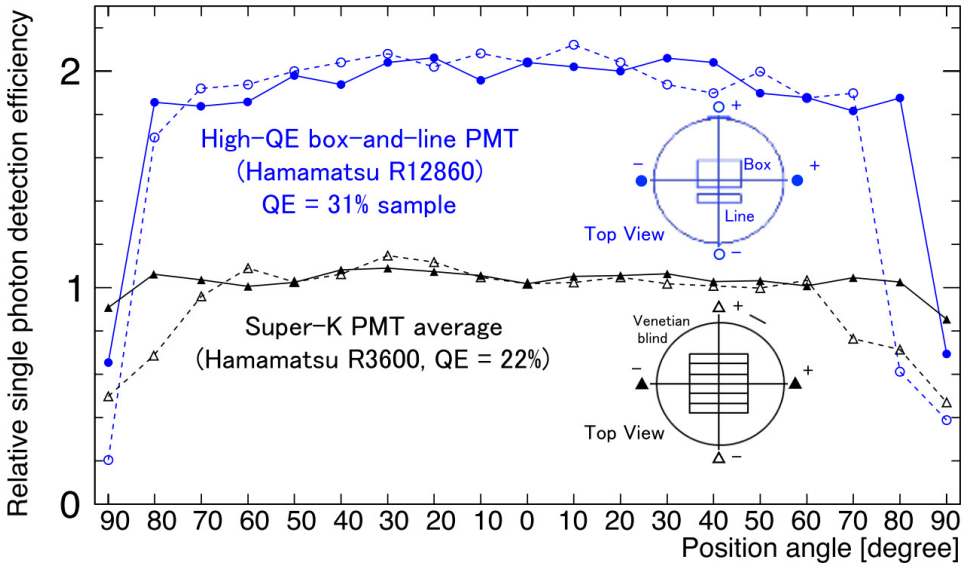

Figure 9.15 *Relative single photon detection efficiency as a function of the position on the photocathode. The PMT centre is at a position angle of 0° and the PMT edges are at ±90°. The black lines show the average measured values for of four Super-K PMTs whereas the blue lines show the measured value of a Hyper-K PMT. Scans were taken along perpendicular lines and the results are shown in the dashed and solid lines. Taken from [17].*

may be useful in reconstructing event vertices and directions.

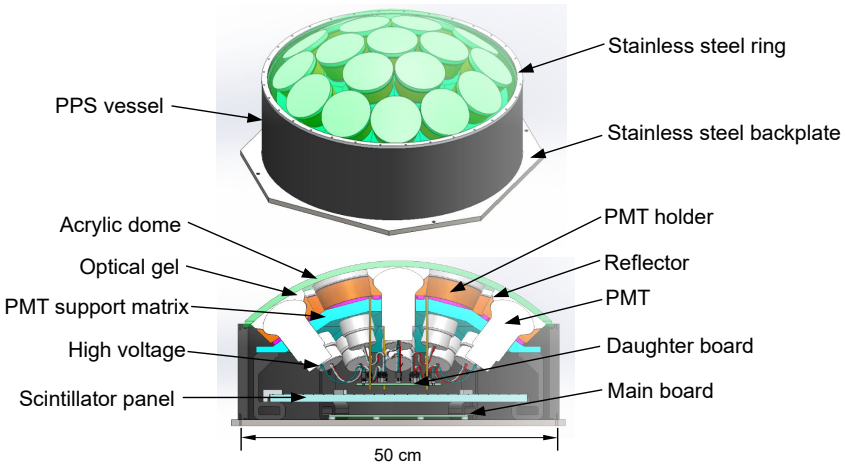

Figure 9.16 *A conceptual drawing of a multi-PMT with 19 7.7 cm PMTs outward-facing PMTs, on each side, for the ID and OD. The PMTs are enclosed in a 50 cm acrylic vessel and readout electronics are embedded inside. Taken from [17].*

9.3.1 Electronics

The dark noise and time resolution requirements for Hyper-K are stricter than Super-K because the B&L PMTs have twice the performance of the Super-K PMTs. The charge and timing information for any PMT signal above 0.25 photoelectrons will be read out and stored, a software trigger then goes over the stored hit information to select events. The current design uses the same electronics system for both the ID and OD.

One of the key changes in the Hyper-K electronics system is that the frontend electronics module will be housed in a water-tight, pressure-tolerant housing and placed in the PMT support structure in the water. The reason for this comes from the size of Hyper-K. Hyper-K will have up to 60,000 PMTs (ID + OD) and if the frontend electronics modules are located on the roof of the tank, as is the case for Super-K, then the structure would need to be designed to support the weight of the cables which is expected to be roughly 1 kton. The cables must also be longer than those in Super-K which reduces the signal amplitude and reduces the signal quality. Placing the frontend modules in the water allows for shorter cable lengths and significantly reduces the weight that must be supported by the PMT support structure.

9.4 Detector Simulation

The Hyper-Kamiokande detector is simulated using an open source[1] Geant4 [27] simulation called WCSim (Water Cherenkov Simulation). This simulates the geometry, physics and electronics response of user-defined water Cherenkov detector configurations.

The Hyper-Kamiokande inner detector volume along with the HQE B&L PMTs are simulated. The PMT simulation includes the dark noise rate, timing resolution as well as an overall photon detection efficiency. The outer detector is not currently included in the official WCSim release. Development efforts for the outer detector implementation in WCSim are outlined in Chapter 10.

Geant4 is used to propagate particles through the detector volume, calculating any energy loss due to physics interactions. Any particles resulting from interactions of the initial particle are also tracked. Photons which reach the sensitive regions of our simulated detector have quantum efficiency and collection efficiency cuts applied in order to register a hit. The code then uses the SK-I (or a user defined) electronics scheme to digitise the hits.

The output of WCSim stores the vertex and energy information of the initial particles as well as the true and digitised hits (in a window) for all hits in each event. The hit information can then be used to inform design efforts or tune and test the event reconstruction algorithms used for Hyper-K: fitQun [156] and BONSAI [153]. Both of these event reconstruction algorithms are used in Super-K and SKDETSIM but have been adapted to work with Hyper-K and WCSim.

[1] The WCSim package is available at `https://github.com/WCSim/WCSim`.

Chapter 10

Hyper-Kamiokande Outer Detector

The Hyper-K outer detector will use outward-facing PMTs to veto incoming charged particles. Super-K's OD has a 1% photocoverage of 20 cm PMTs, the same photocoverage for Hyper-K would scale up to 6,700 20 cm PMTs. The Hyper-K OD has a thickness of 1 m around the barrel and 2 m from the top and bottom caps, while the Super-K OD has a 2 m depth in the barrel and endcap regions. This means that, compared to Super-K, incoming charged particles (in the barrel regions) produce less light and the light is less spread out; for this reason, an OD design with a finer granularity than that of Super-K is preferred. Increasing the number of 20 cm PMTs greatly increases the cost of the OD but the finer granularity can be achieved in a cost effective manner by using smaller PMTs. As well as reduced costs, the 8 cm PMTs being considered have a dark count rate of 100 Hz, much lower than the 2 kHz rate of the 20 cm PMTs. Keeping the same photocoverage with 8 cm PMTs would mean nearly 50,000 PMTs in the OD. To reduce this number, a detailed optimisation of the reflective materials on the OD walls together with additional wavelength shifting plates has been proposed [17]. This will increase the effective photocoverage in the OD, allowing us to reduce the 1% photocoverage (of PMTs) while maintaining high light collection. So the OD will have 0.28% coverage of 8 cm PMTs which equates to 13,300 PMTs.

Another possible method to increase the light collection is the use of a Winston Cone [159]. This is a reflective parabolic surface which can be coupled to a PMT to collect light and reflect it towards the PMT surface. Winston cones have been used in the spherical detectors SNO [52] and Borexino [37]. The major flaw with

this method of light collection is that photons which travel parallel to the PMT surface would be blocked by the reflector, reducing the light collected by these PMTs. Hyper-K is not a spherically symmetric detector, and the shadowing of light would complicate the reconstruction of events, for this reason they were deemed unsuitable for use in the OD.

Each PMT will be coupled to a wavelength shifting (WLS) plate in order to increase the light collection. The wavelength shifting plates absorb photons between 280 and 400 nm where the majority of Cherenkov light is produced, and emit photons at longer wavelengths. The emitted photons have a random direction and wavelengths between 410 and 460 nm which closely matches the QE of the PMTs. Roughly one photon is emitted for each photon absorbed by the wavelength shifter [162]. The light emitted in the plate is trapped by total internal reflection if the angle of incidence, with respect to the plate surface, is large enough.

This chapter covers the R&D work that has been undertaken in order to understand and optimise the wavelength shifting plate design and the effect of reflective materials on the OD walls. Comparisons are made between three different WLS plates: EJ-286 made by Eljen [155], a plate made by Kuraray [119] and a plate which is used in Super-K. Simulations of the OD and improvements to the reflectors are also discussed.

10.1 Simulating Plate Response

A 2D analytical simulation was developed in order to model the response of a WLS plate. The simulation creates a square with a circle cut out of the middle. The square represents the plate while the circle in the middle represents the PMT. Photons are generated randomly and uniformly across the plate. Each photon has a randomly generated direction sampled uniformly from 0 to 2π in the plane of the plate. The photons are then propagated through the plate until they reach the plate edge, at which point they are either reflected or killed. When a photon reaches the PMT it is stored as a detected hit.

The simulation is run in two different modes. The first mode assumes no reflectors around the edge of the plate. In this case, a photon reaching the edge is reflected with an angle of reflection equal to its angle of incidence if the angle of incidence

is larger than the critical angle. The second mode assumes that a reflector, such as aluminised Mylar tape, is used around the plate edges. In this case photons reaching the edge are reflected.

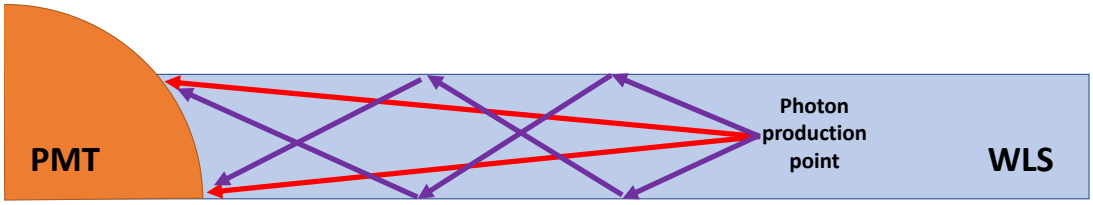

Figure 10.1 *A diagram showing a side view of a PMT+WLS setup. the red lines show photons reaching the PMT directly while the purple lines show light reaching after being internally reflected from the top and bottom of the plate.*

There are several key simplifications in this simulation. The first is that the thickness of the plate is ignored. The angle range at which a photon can be totally internally reflected from the top and bottom of the plate is larger than the angles that would result in a photon reaching the PMT directly (without reflecting off of the top and bottom). This is shown in Figure 10.1. While no major effect is expected to result from this simplification, a full 3D Geant4 simulation of the plates is being developed.

The second simplification is to limit the maximum number of reflections. In the case of reflective edges, given enough reflections, the simulation will eventually detect every simulated photon. In a realistic situation, photons will be attenuated. Hence, we do not expect photons to survive a large number of reflections. Figure 10.2 shows the expected number of reflections for various attenuation lengths. Nominally the maximum number of reflections is set to two. Table 10.1 shows the percentage of detected hits which arrive in two or fewer reflections, for various attenuation lengths. The simulation uses the refractive indices of the plate and surrounding medium only to calculate attenuation losses, not the overall light capture factor. The refractive indices used are 1.58 for the Eljen sample which is made of PVT and 1.49 for the Kuraray and Super-K samples which are made of PMMA.

Figure 10.3 shows the expected efficiency of a simulated plate with the contribution of 0, 1 and 2 reflections. Figures 10.4 and 10.5 show heatmaps of the plate efficiency without and with reflective edges. The simulation predicts a large increase in the light collection with the addition of reflective material around the edges of the plate. The contribution of the reflective edges increases as the

Table 10.1 *The percentage of detected hits with 2 or fewer reflections for various attenuation lengths. Values are also shown for different values of edge reflectivity.*

Attenuation Length [m]	Detected Hits With 2 or Fewer Reflections [%]		
	Edge Reflectivity: 1	0.9	0.8
1	100	100	100
2	96	97	98
3	91	93	95
4	86	89	92

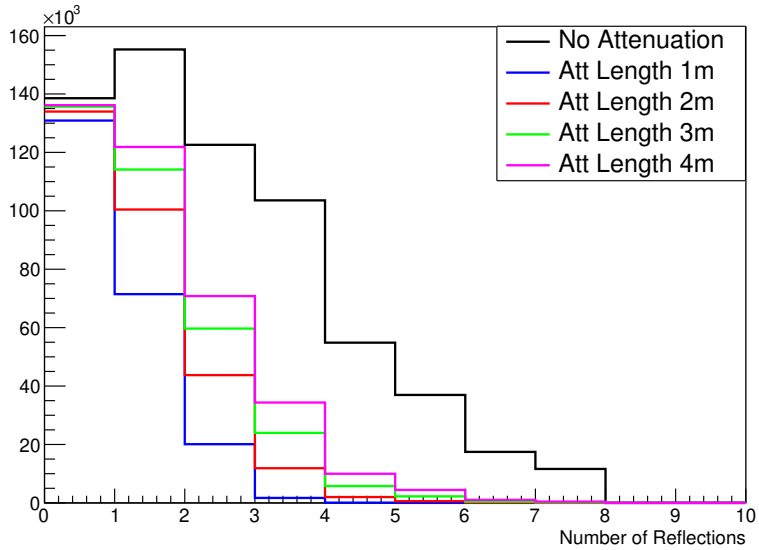

Figure 10.2 *A distribution showing the number of reflections it took before a photon was detected in the simulation. The simulation is for a 23 cm square plate with 90% reflective edges and a refractive index of 1.58. The plate was simulated in air. The different coloured lines show various attenuation lengths.*

distance between the light source and the PMT increases, flattening out the efficiency curve.

The simulation allows us to understand the plate response at any point using only geometric arguments, essentially giving an acceptance at any point in the plate.

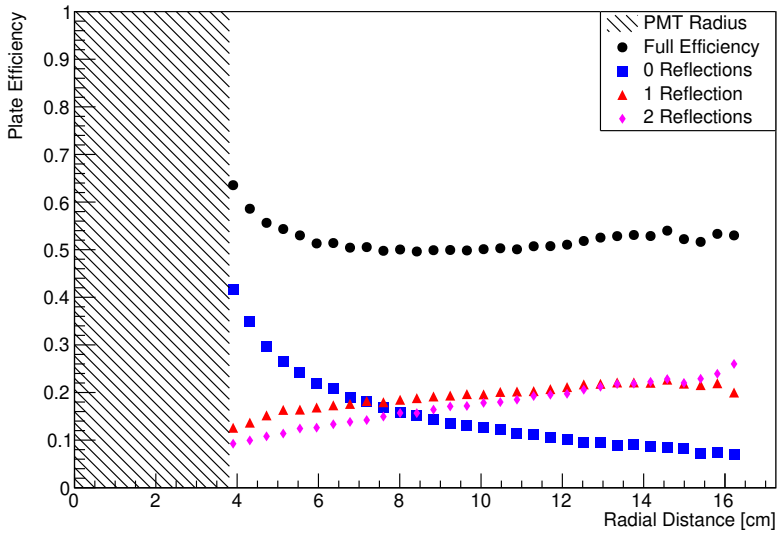

Figure 10.3 *Distribution showing the efficiency of a simulated WLS plate. The simulation is for a 23 cm square plate with reflective edges and no attenuation. The black circles show the overall efficiency while the blue squares, red triangles and magenta rhombuses show the contribution from 0, 1 and 2 reflections respectively. 100% edge reflectivity and perfect coupling between the PMT and plate are assumed.*

10.2 Plate Shapes

The size of the WLS plate determines the overall detection efficiency. A plate that is too large will not increase light collection as light will be attenuated in the plate before reaching the PMT. Similarly, the shape of the WLS plate may have an effect on the overall light collection. In order to investigate the possible effects, the simulation was run for square, rectangle and circle plates.

All plates have the same zero reflection contribution, which is given by:

$$\sin^{-1}(R_{PMT}/x)/\pi, \tag{10.1}$$

where R_{PMT} is the PMT radius and x is the distance of the photon from the PMT centre. The reflected contributions vary between the different plate shapes. Figure 10.7 shows the expected efficiency for a 23×46 cm rectangular WLS plate. The rectangular plate shows a similar behaviour to the square plate, the 1 and 2 reflection contributions increase with radial distance. The circle plate, shown in

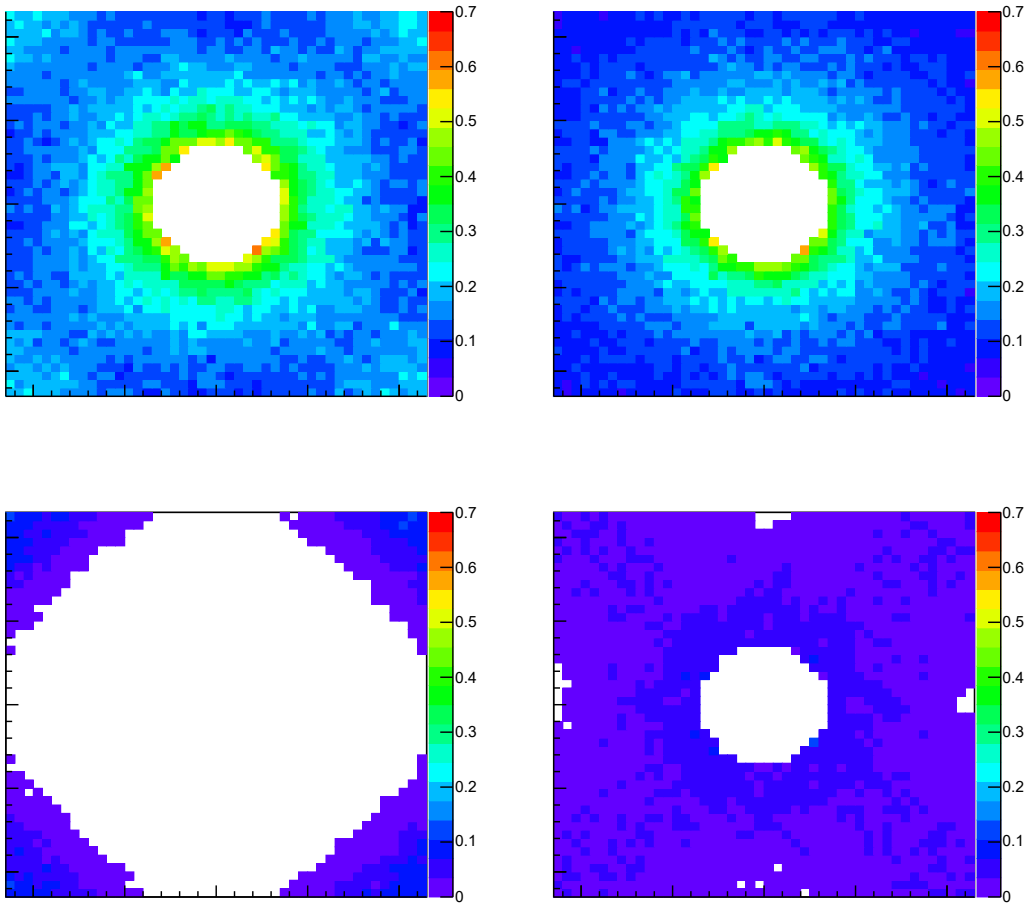

Figure 10.4 *Heatmaps showing the efficiency of a simulated WLS plate. The simulation is for a 23 cm square plate without reflective edges and no attenuation. The top left plot shows the overall efficiency and the top right plot shows the contribution from 0 reflections. The bottom left and right plots show the contribution 1 and 2 reflections respectively.*

Figure 10.6, is different as the one reflection contribution decreases with increasing radial distance and there is no contribution from 2 or more reflections. This is because the light is reflected at large enough angles such that it is not collected by the PMT.

The poor reflection of the circle plate naturally leads to the idea of a plate shape that focuses the reflected light onto the PMT without allowing it to "miss" the PMT. The simplest version of this idea is to have square or rectangular plates constraining the path of the light and ensuring that it heads for the PMT. Another possibility is a triangular plate, this plate design will be referred to as a petal design. Diagrams of the petal designs are shown in Figures 10.8 and 10.9. The

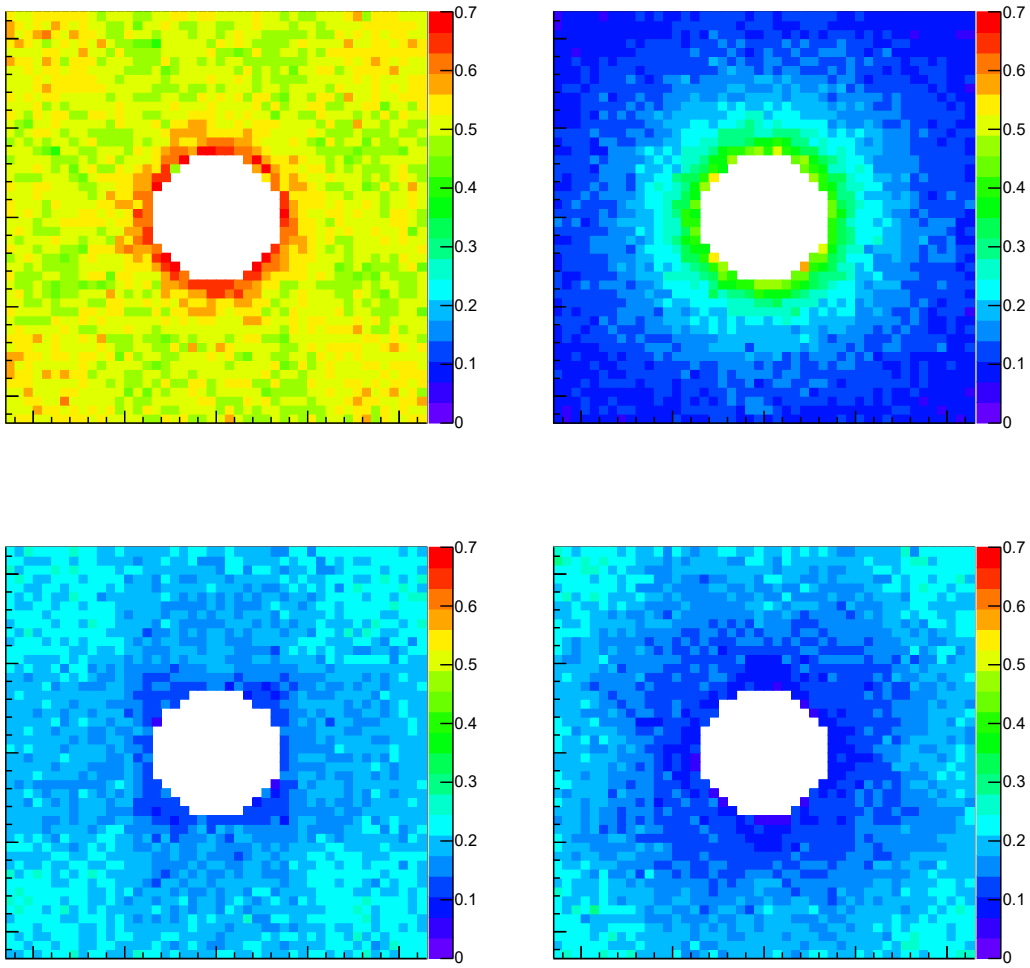

Figure 10.5 *Heatmaps showing the efficiency of a simulated WLS plate. The simulation is for a 23 cm square plate with reflective edges and no attenuation. The top left plot shows the overall efficiency and the top right plot shows the contribution from 0 reflections. The bottom left and right plots show the contribution 1 and 2 reflections respectively.*

petal designs are being investigated further.

10.3 Absorption and Emission Spectra

There are two key properties of wavelength shifters which are used to characterise them: absorption and emission. Wavelength shifters absorb light over a range of wavelengths with the absorption length depending on the wavelength of the

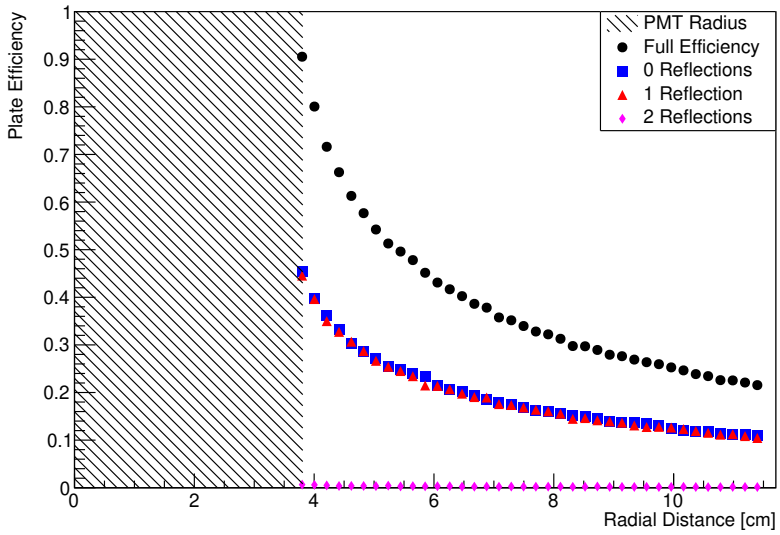

Figure 10.6 *Distribution showing the efficiency of a simulated WLS plate. The simulation is for a 23 cm circle plate with reflective edges and no attenuation. The black circles show the overall efficiency while blue squares, red triangles and magenta rhombuses show the contribution from 0, 1 and 2 reflections respectively.*

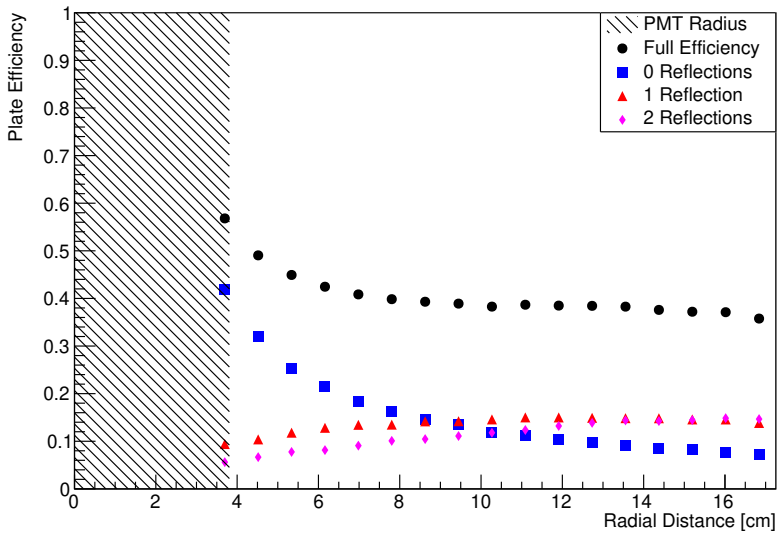

Figure 10.7 *Distribution showing the efficiency of a simulated WLS plate. The simulation is for a 23x46 cm rectangle plate with reflective edges and no attenuation. The black circles show the overall efficiency while blue squares, red triangles and magenta rhombuses show the contribution from 0, 1 and 2 reflections respectively.*

absorbed photon. This absorption spectrum varies between wavelength shifting dopants so it must be understood in order to compare various wavelength shifting

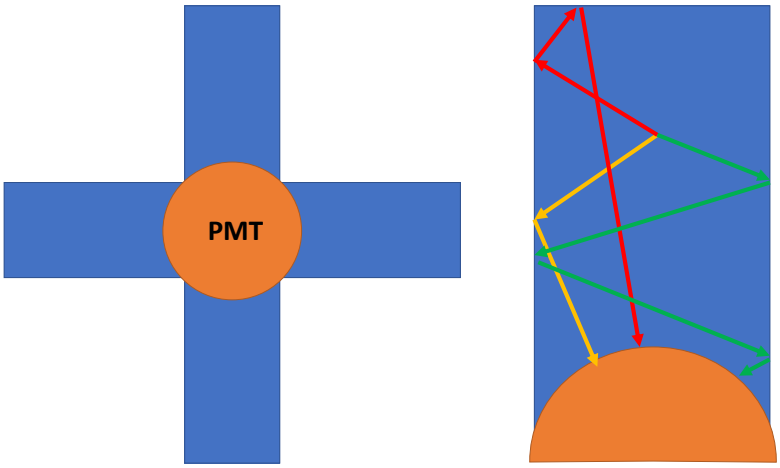

Figure 10.8 *A diagram showing an example rectangle petal design, the image on the right shows possible light reflections.*

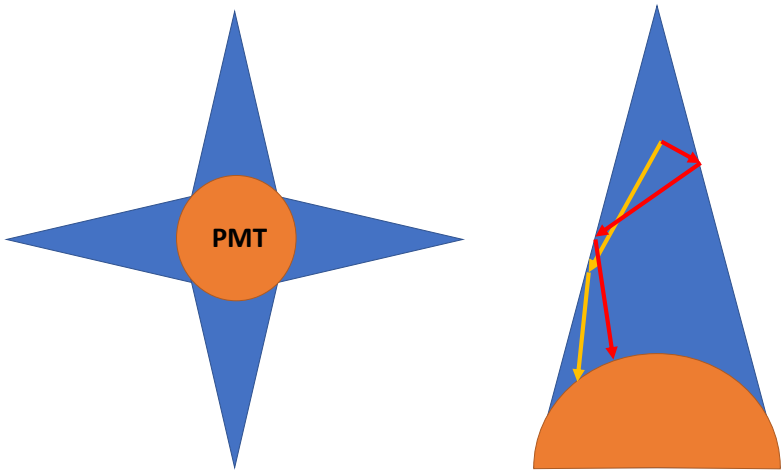

Figure 10.9 *A diagram showing an example triangle petal design, the image on the right shows possible light reflections.*

samples. The ideal wavelength shifter (for use in Hyper-K) will be one that has high absorption in the Cherenkov wavelength range. The Cherenkov spectrum decreases as $(1/\lambda^2)$ and below 300 nm there is significant absorption in the water so the ideal range of plate absorption is 300 to 400 nm.

Once a photon has been absorbed, light is emitted in a range of wavelengths. Typically, the emitted light has a higher wavelength and is independent of the energy of the absorbed light. To maximise the light detection capabilities, the emission spectrum of the WLS plate should match the quantum efficiency range of the PMTs.

This section describes the spectra measurements for each candidate sample.

Table 10.2 *The dimensions of the four WLS samples which had their absorption and emission spectra measured.*

Sample	Height [cm]	Width [cm]	Depth [cm]
Eljen	1.0	1.2	1.3
Super-K	1.0	1.0	1.3
Kuraray	1.0	1.0	1.3
Sheffield	1.0	1.0	0.5

In addition to the three commercial samples Eljen, Kuraray and Super-K, the absorption and emission spectra was measured for a non-commercial sample. This was made for Sheffield University and does not come in the form of a WLS plate. The Sheffield sample was measured in order to determine its suitability of as a wavelength shifter. Table 10.2 summarises the dimensions of each sample measured.

10.3.1 Measuring Emission

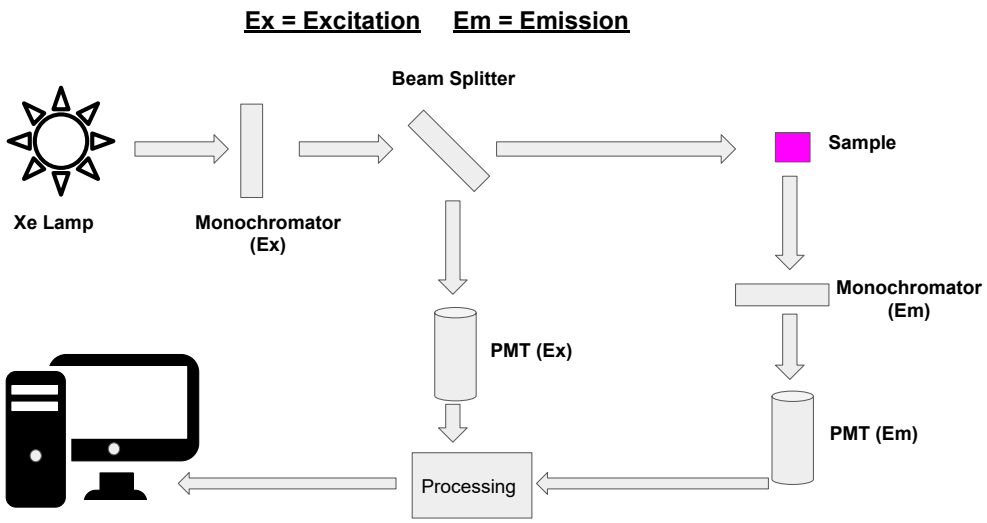

Figure 10.10 *A diagram of the emission spectrum measurement setup.*

The emission spectrum measurement is made using a JASCO FP-6500 spectrofluorometer [59] which has the ability to emit and to measure light of precise wavelengths. Figure 10.10 shows a diagram of the setup. Light emitted from a xenon lamp is passed through a monochromator for wavelength selection. The light is then split by a beam splitter so the intensity of the incident light can be measured. The light then passes through the wavelength shifting sample where

it is absorbed and fluorescent light is emitted. The emitted light passes through a monochromator and its intensity is measured by a PMT. This setup allows us to determine the emission spectrum for different wavelengths of incident light.

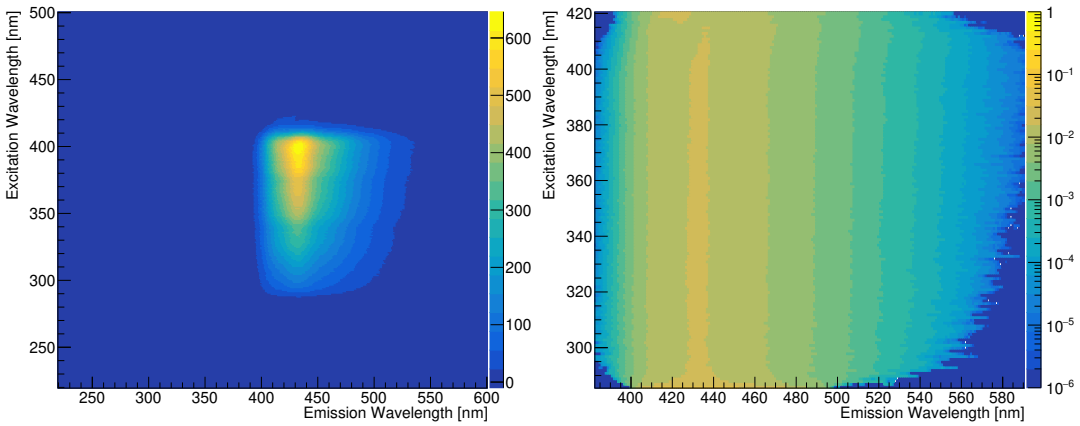

(a) *Measured Intensity* **(b)** *Normalised Intensity*

Figure 10.11 *2D emission spectrum for the SK WLS sample. Left plot shows the emission intensity for different excitation wavelengths and the right plot shows the intensity normalised for each excitation wavelength.*

For each sample, the measured excitation wavelengths spanned 220 nm to 500 nm and the emission wavelengths from 220 nm to 600 nm. Figure 10.11 shows the 2D emission spectrum for the Super-K WLS Sample. The intensity of the excitation light is stable but is not uniform over the entire wavelength range so what matters is the relative intensity of the emitted wavelengths for each specific excitation wavelength. Figure 10.11b shows that when the emission spectrum is normalised by the area for each excitation wavelength bin, the emission spectrum is consistent over any wavelength that can excite the WLS.

The emission spectrum is obtained by selecting an excitation wavelength and checking the normalised intensity of emitted wavelengths. An excitation wavelength of 350 nm is chosen as this results in maximal absorption for all of the WLS samples tested. Figure 10.12 shows the emission spectrum for the four WLS samples.

The emission spectra for the Eljen and Sheffield samples have a peak which is closer to the PMT QE peak compared to SK and Kuraray samples. The width of the emission spectrum of Eljen and Sheffield samples is also preferred as they do not emit much light at longer wavelengths.

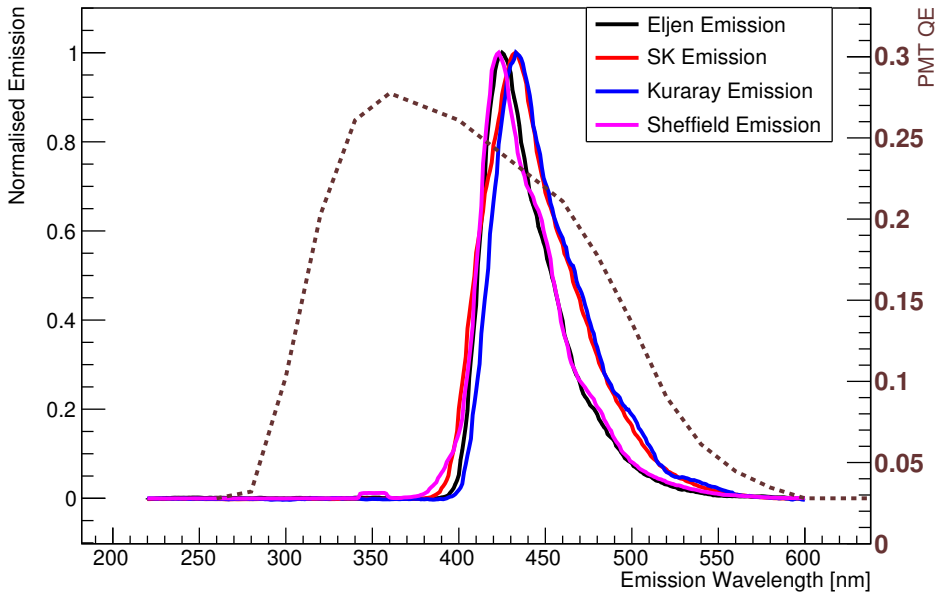

Figure 10.12 *The measured emission spectrum for four WLS samples. The excitation wavelength for these measured values is 350 nm. The dotted brown line shows the QE of the ETEL PMT which is taken from Reference [70].*

10.3.2 Measuring Absorption

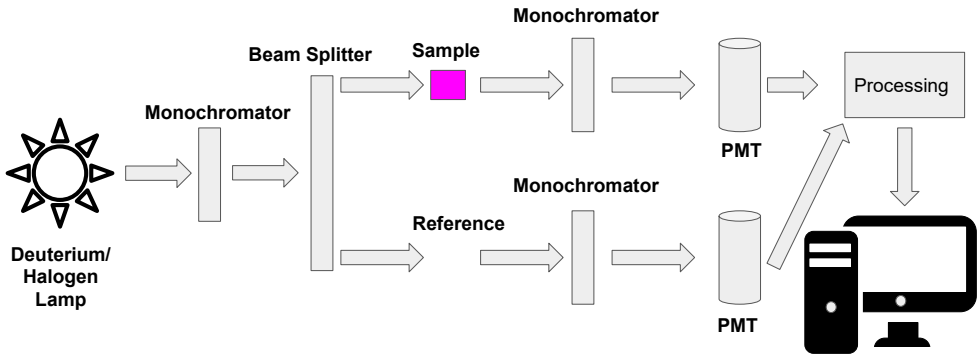

Figure 10.13 *A diagram of the absorption spectrum measurement setup.*

The absorption measurements are taken using a JASCO V-550 spectrophotometer [60]. The spectrophotometer emits light which is split using a beam splitter and directed towards two optically separated PMTs. There is a space for materials to be placed between the light and the PMT. One of the paths has no sample in the path, the detected light for this PMT serves as a reference. The WLS samples are then placed, one at a time, in the second holder. The difference between the

signals of the two PMTs gives an overall absorbance for the sample. A diagram of the setup is shown in Figure 10.13

The absorbance, A, is given by:

$$A = log_{10}(\frac{\Phi_t}{\Phi_i}), \tag{10.2}$$

where Φ_t is the intensity of light transmitted by the sample and Φ_i is the intensity of light incident on that sample. The absorbance of a material is related to the transmittance, T, by the equation:

$$A = -log_{10}T. \tag{10.3}$$

The transmittance tells us the fraction of light that has been transmitted through the sample, this can be used along with the sample thickness to calculate the attenuation length. The attenuation length is given by

$$\lambda = \frac{-L}{log(T)}, \tag{10.4}$$

where L is the thickness of the sample.

The candidate 8 cm PMTs have different expose heights and curvatures, a higher expose height allows for thicker plates without covering up too much of the PMTs active area. Depending on the PMT used, the final WLS plates in Hyper-K could be either 0.6 or 1.3 cm thick. For this reason, the attenuation length was used to calculate the probability of absorption for each thickness. Figures 10.14 and 10.15 show the absorption probabilities for the four WLS samples for the full and half thickness plates respectively.

All of the samples tested have good absorption in the between 200 and 400 nm, this is ideal for Cherenkov detectors as the majority of the photons produced have a wavelength in this region. The Kuraray sample has a slight dip in absorption around 300 nm and the SK sample absorbs less than all other samples above 300 nm. After ∼400 nm the ideal WLS sample should have a low probability of absorption. This is because these are the wavelengths at which light is emitted. The better transmittance will result in better propagation throughout the plate. The transmittance of the SK sample is not as good as the Eljen or Kuraray

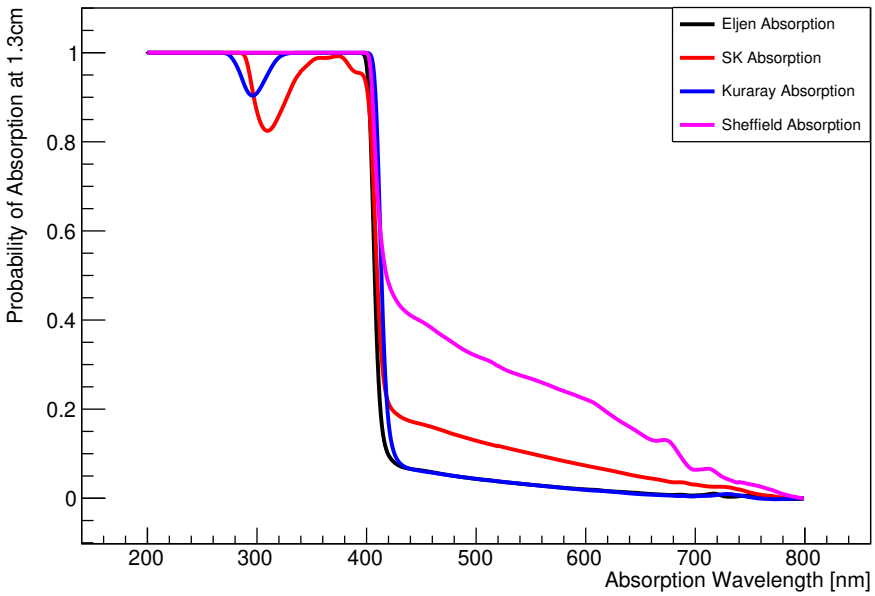

Figure 10.14 *The measured absorption spectrum for four WLS samples. The vertical axis shows the probability of absorption at 1.3 cm.*

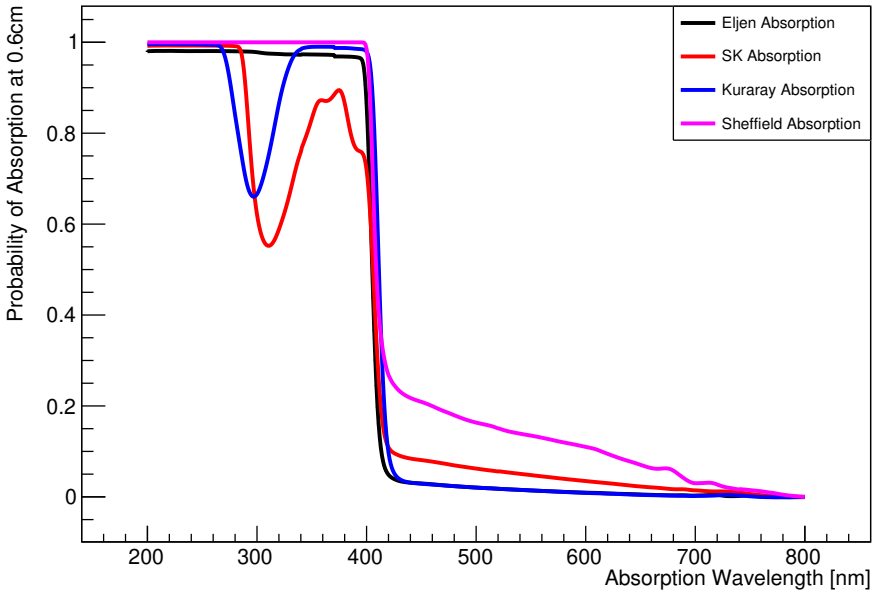

Figure 10.15 *The measured absorption spectrum for four WLS samples. The vertical axis shows the probability of absorption at 0.6 cm.*

sample. The poor transmittance of the Sheffield sample is because of the plastic used. The Eljen plate is made from PVT, the Kuraray and Super-K plates use PMMA and the Sheffield sample is made with Polystyrene.

10.4 Plate Efficiency Measurement

In these measurements, a PMT is coupled to a WLS plate and measurements are taken at several points across the plate along one axis. The detected light is then compared to that of the PMT alone. Each wavelength shifter has a curved circular hole cut out of the centre so they can be mounted onto a PMT with the base of the plate sitting close to the measured edge of the photocathode (see Figure 10.16). The hole is curved such that it follows the shape of the PMT bulb (see Figure 10.1). The efficiency measurements were carried out using a 3 inch ETEL 9320KFLB [70] domed PMT with an active diameter of 78 mm (3") with a blue-green sensitive bialkali photocathode.

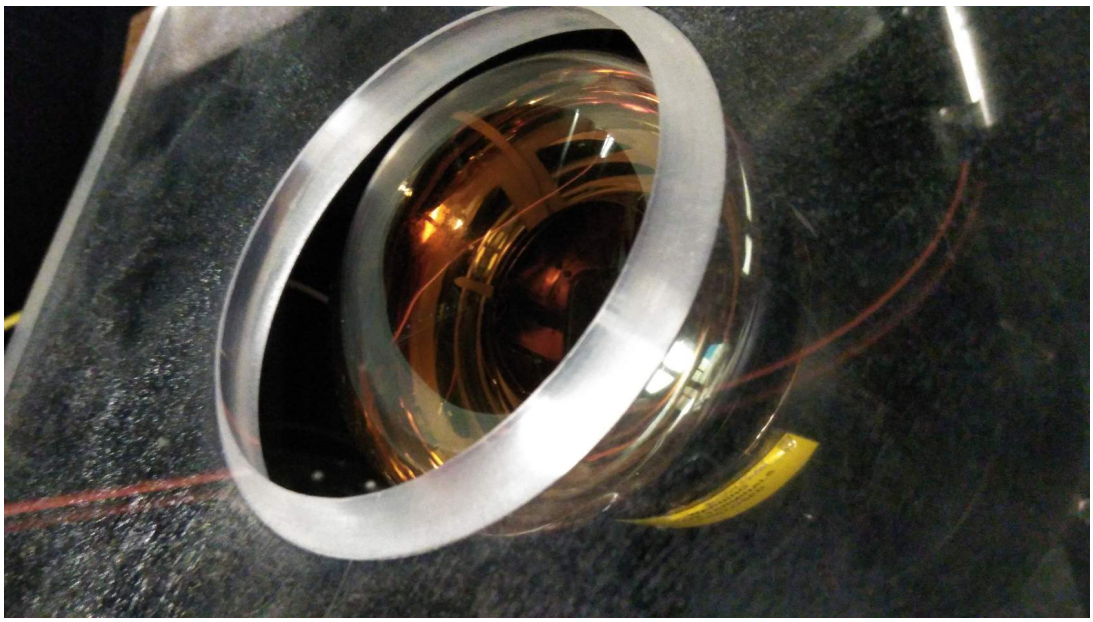

Figure 10.16 *A closeup picture of the curved WLS hole before the plate is mounted onto a PMT.*

Various plate sizes and shapes were measured, the dimensions of each plate are summarised in Table 10.3. Two measurement setups were used. Initially, measurements were taken using the two Eljen plates using relatively slow shaping electronics which led to a relatively large background from dark counts that needed to be subtracted. Subsequently, the setup was improved by making use of faster amplifiers and DAQ electronics, allowing faster data taking with less

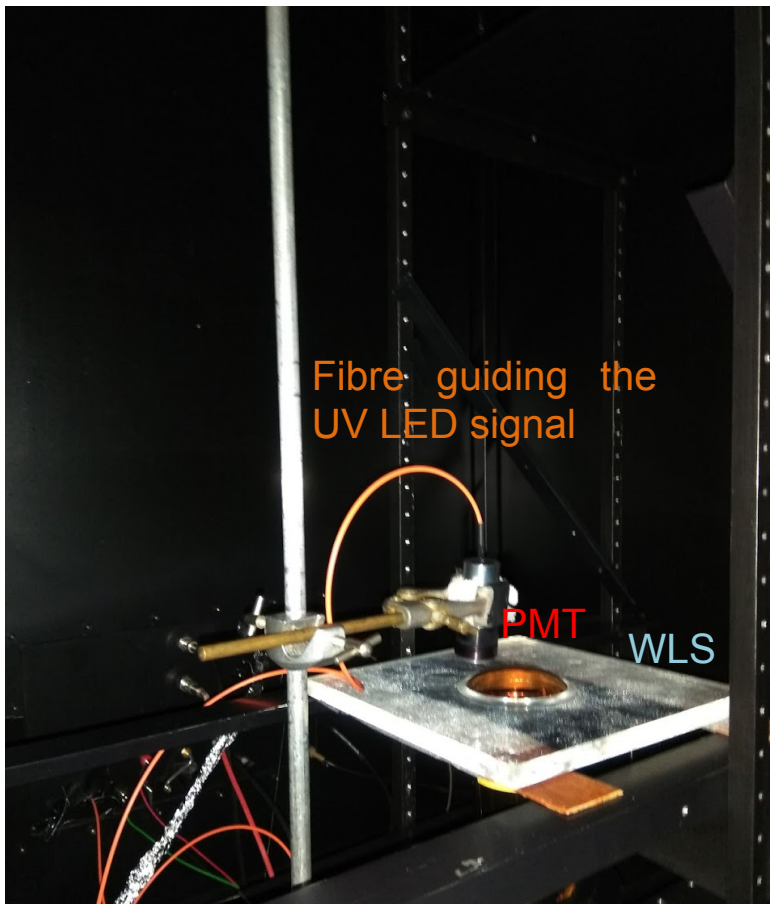

Figure 10.17 *A picture of the efficiency measurement setup.*

background. All plates were retested with this setup.

Table 10.3 *The dimensions of the WLS plates used for the efficiency measurements.*

Plate	Height [cm]	Width [cm]	Depth [cm]
Eljen Small	23	23	1.3
Eljen Large	30	50	1.3
Kuraray	25	25	1.3
SK Square	21	21	1.3
SK Circle	21	21	1.3
SK Rectangle Petal	5	18	1.3

10.4.1 First Setup

Light from a 370 nm ultraviolet LED is guided, via an optical fibre, into a large light-tight dark box where the measurements are taken. The end of the fibre is

fed into a collimator which results in a spot size of ±0.5 cm. A pulse generator generates a 10 kHz signal which triggers the LED. The LED is pulsed in such a way that the majority of signals are single photoelectron signals. The signal from the PMT is then amplified by an ORTEC 4890 preamplifier and then an ORTEC 570 amplifier [141] giving an amplification factor of 100. The amplified signal is then read by an ORTEC EASY-MCA [140] multi-channel analyser (MCA) connected to a computer. The measurement of each individual point was taken for 20 minutes, which corresponds to 10^7 triggers. The MCA is triggered by a delayed copy of the signal that generates the LED pulse. On receipt of a trigger the MCA generates a gate that extends at least 0.5 μs beyond the start of the pulse. In addition to this, the amplifier shaping time is $\sim$1 μs. This means that the gate is quite wide and stray light in the dark box must be accounted for in the analysis. Measurements showed that one hour after opening the box, the background rate reduced by an order of magnitude so there was a one hour wait between the measurements of each point.

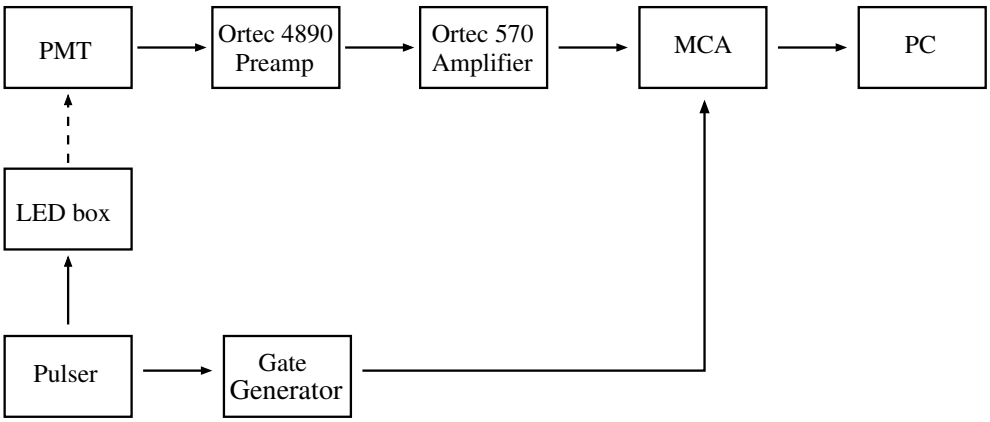

Figure 10.18 *A Block diagram of the electronic readout chain.*

The procedure for measuring a plate is to first take a measurement at the centre of the PMT and gradually move the fibre towards the edge of the plate. For each point two runs were taken, one with the LED off followed by a run with the LED on. The LED off measurement is used to subtract the background. Once all of the points on all of the plates are measured, the measurements are repeated with Mylar wrapped around the edges. After the WLS and reflector measurements were taken, the measurements were repeated with Tyvek® underneath the plates in addition to the aluminised edges. It was found that placing Tyvek beneath the plate did not increase the efficiency. This suggests all of the initial light is absorbed in the plate, see Figure 10.14.

The signal region is defined as all of hits above the valley (55 counts), see

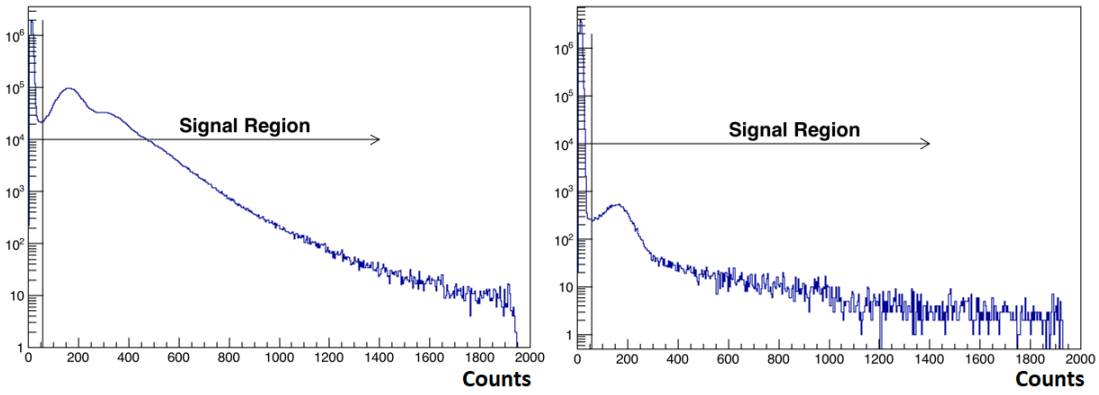

(a) *LED ON* **(b)** *LED OFF*

Figure 10.19 *The MCA spectra when the LED is turned on (left) and turned off (right). The measurement was taken with the LED positioned at the centre of the PMT.*

Figure 10.19. For each point, the number of counts is converted to a hit rate and the dark count (background) measurement is subtracted from the LED on measurement. All rates are then divided by the measured rate at the centre of the PMT to give a relative efficiency.

10.4.2 Second Setup

For the second setup the same LED, collimator, optical fibre and PMT are used. A pulse generator generates a 10 kHz signal which triggers the LED, the LED is pulsed in such a way that the majority of signals are single photoelectron signals. The signal from the PMT is amplified (and inverted) by a custom built fast amplifier with a gain of 20 and a shaping time of $\mathcal{O}(1$ ns). The amplified signal is then read by a CAEN DT5742 [54] waveform digitiser, with a sampling rate of 5 GHz, connected to a computer. The waveform for each trigger (gate and signal) is saved.

The procedure for measuring a plate is largely the same as the first setup with two exceptions. The background rate after opening the box was found to be negligible (as the timing window is less than 100 ns) so LED off measurements did not need to be taken for each point. This also means that it was not necessary to wait before taking a subsequent measurement. Instead, several LED off measurements were taken, opening and closing the box after each measurement. The average of the LED off measurements was used as the background rate. Once all of the points on all of the plates are measured, the measurements are repeated with

reflective edges around each plate. The reflective edges used in this setup are different from that used in the first setup. The first setup used a removable aluminised jacket where the WLS plate could easily be placed in and taken out of. For the second setup, reflective foil tape was stuck to the edges of the plates.

The whole waveform was saved for this setup so the signal selection was done on a trigger by trigger basis in analysis scripts. For each trigger, a hit was registered if the registered voltage exceeded 10 mV for 4 ns. These values correspond to a typical signal observed for measurements taken at the PMT centre, see Figure 10.20. The signal selection criteria results in 0.1% of triggers registering a hit when the LED is off.

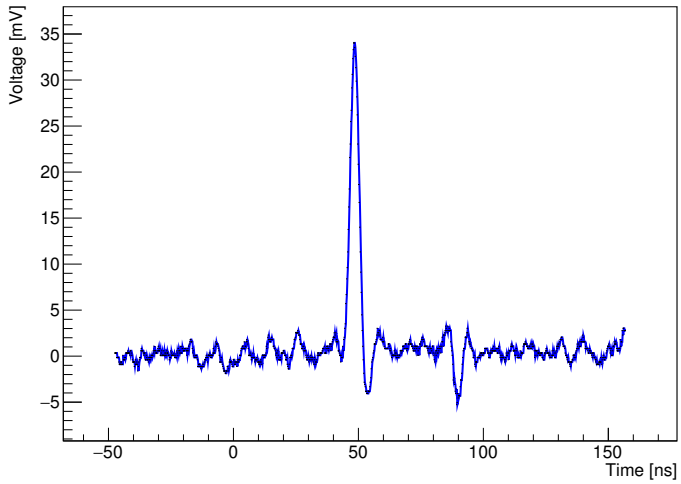

Figure 10.20 *A typical waveform for the amplified PMT signal in the second setup.*

10.5 Fit To Data

The simulation assumes that all of the photons that arrive in fewer than 2 reflections are detected when in reality there are several factors affecting the overall efficiency of the plate. Two key factors affecting the efficiency of the plate are the losses through the top and bottom as well as the coupling of the plate to the PMT. In order to address this, an overall scaling factor η will be used to scale the simulation down to the measured result. The reflective edges in the simulation reflect all of the photons received, so another parameter ρ will be used to model the lower reflectivity of the edges by scaling down reflected contributions. The

Table 10.4 *The refractive indices for the WLS plates along with the fraction of light captured in air and in water.*

Plate	Refractive Index	Capture Air	Capture Water
Eljen	1.58	0.77	0.54
Kuraray	1.49	0.74	0.45

simulation results are used to model the WLS plate using the equation

$$\eta \times (\sum_i \rho^i \times M_i), \tag{10.5}$$

where η is the inherent efficiency of the plate, ρ is the reflectivity of the edges and M_i is the model contribution for i number of reflections.

Several factors are contained in the η parameter. The most obvious contribution comes from the losses through the top and bottom of the plate. The loss through the top and bottom can be calculated by first working out the solid angle:

$$\Omega = 2\pi(1 - \cos\theta_C), \tag{10.6}$$

where θ_C is the critical angle. From this we calculate the fraction of a hemisphere covered by the solid angle giving the percentage of light lost. The fraction of light captured by the plate is

$$1 - \Omega/2\pi = 1 - (2\pi(1 - \cos\theta_C))/2\pi = \cos\theta_C. \tag{10.7}$$

The critical angle is dependent on the refractive index of the material used as well as the refractive index of the surrounding medium. Table 10.4 shows the expected fraction of captured light for the Eljen and Kuraray plates. It can be seen that from the effect of refractive index alone, the capture difference between the Eljen and Kuraray plates is roughly 4% for measurements in air, whereas for measurements in water it is 20%.

The other main contribution to the η parameter comes from the difference in the PMT QE at 370 nm and the average QE over the WLS emission wavelengths. A small contribution may be present if the quantum yield of the WLS plate is different from 1. The uniformity of the PMT's angular response may also effect the result, however the efficiency at the centre of the PMT and the sides has been

measured to be 95%.

10.5.1 Results

For the measurements taken with the setup mentioned in Section 10.4.1 only two plates were measured. The model was fit to the small square Eljen plate as well as the larger rectangular Eljen plate. Figures 10.21 and 10.22 show the efficiency plots for the small and large plates respectively. It can be seen that the addition of reflective material around the edges clearly improves the plate response and increases the efficiency. The best fit η parameter is 46% for the small plate while the large plate has a lower value of 32%, Table 10.5 shows the best fit values for each plate. The lower efficiency of the large plate may be because the larger plate can better constrain the reflectivity (ρ) parameter as the data points are taken at further distances where reflection contributions are significant. However, the two Eljen plates are visually different and it is also possible that there is some variation in production quality. In order to check the validity of the model, the best fit parameters for the large plate were used to model the small plate and the model is in reasonable agreement with the data, see Figure 10.23.

Table 10.5 *The best fit η and ρ parameters for each plate.*

Plate	Reflector?	η [%]	ρ [%]
Eljen Square	No	31±2	28±3
Eljen Square	Yes	46±2	44±3
Eljen Square (with constraint on η)	Yes	32	70±1
Eljen Rectangle	No	32±1	96±6
Eljen Rectangle	Yes	32±1	70±3

For the setup mentioned in Section 10.4.2 the efficiency plots show a similar shape to the previous measurements however the efficiency relative to the PMT centre is much lower. Figure 10.24 shows the measured efficiency for the Eljen and Kuraray plates without reflective edges. The Eljen plate has a higher efficiency than the Kuraray plate which is expected, considering that the spectra shown in Section 10.3 more closely match the PMT's QE range. However when reflective material is added to the edges, the Kuraray plate performs better than the Eljen plate, this can be seen in Figure 10.25. Interpretation of this result is limited as measurement data of the Eljen plate with aluminised edges is not good quality and must be retaken.

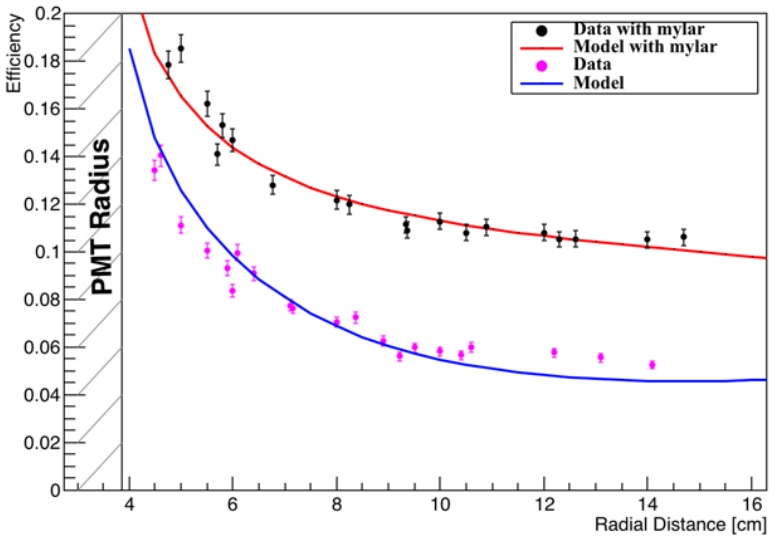

Figure 10.21 *The efficiency vs radial distance from the centre of the PMT. Black dots represent the measurements for WLS plate with reflective edges and the pink dots represent measurements on the WLS plate without reflective edges. The red and blue lines show the fitted model for the reflective and non reflective edges respectively. This plate is the Eljen 23×23×1.3 cm plate.*

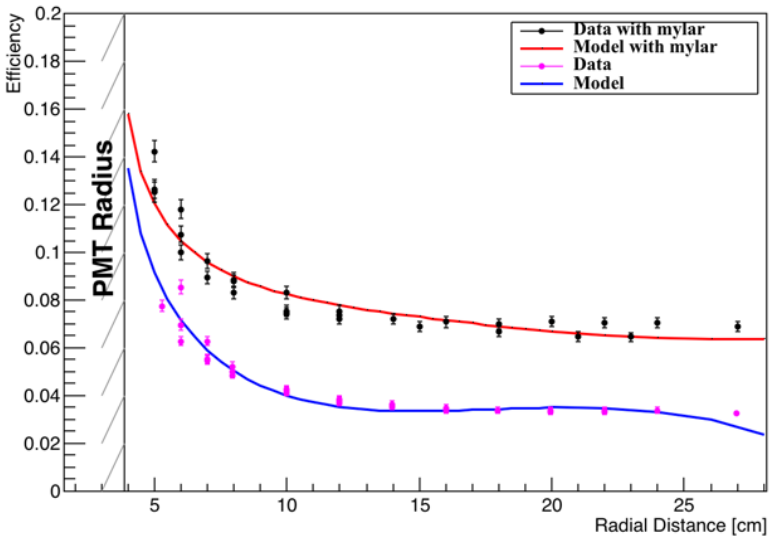

Figure 10.22 *The efficiency vs radial distance from the centre of the PMT. Black dots represent the measurements for WLS plate with reflective edges and the pink dots represent measurements on the WLS plate without reflective edges. The red and blue lines show the fitted model for the reflective and non reflective edges respectively. This plate is the Eljen 30×50×1.3 cm plate.*

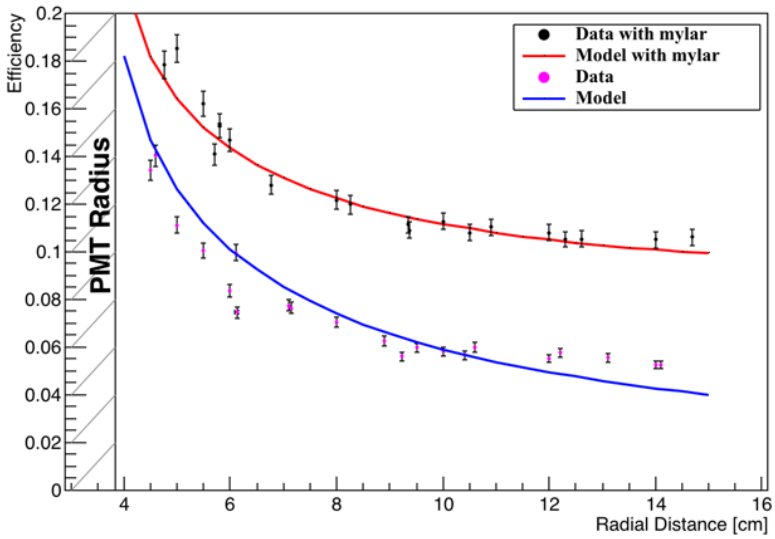

Figure 10.23 *The efficiency vs radial distance from the centre of the PMT. Black dots represent the measurements for WLS plate with reflective edges and the pink dots represent measurements on the WLS plate without reflective edges. The red and blue lines show the fitted model for the reflective and non reflective edges respectively. This plate is the Eljen 23×23×1.3 cm plate but the model uses the best fit point of the larger 30×50×1.3 cm plate.*

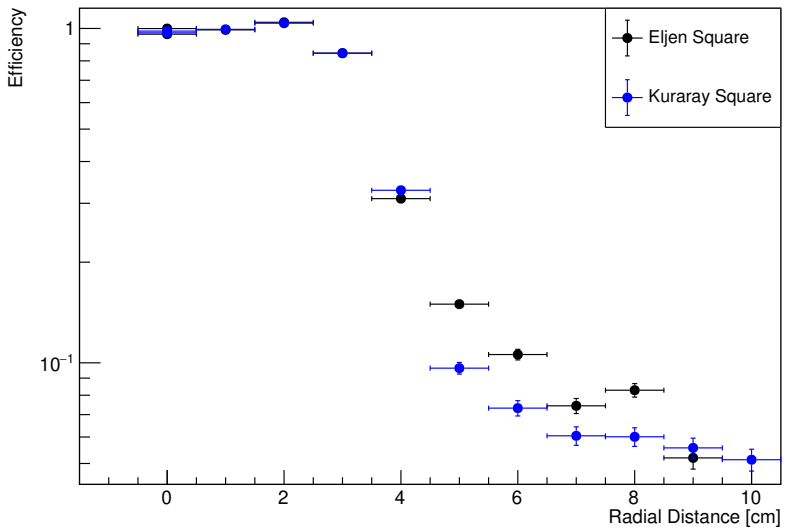

Figure 10.24 *The efficiency vs radial distance from the centre of the PMT. Black dots represent the measurements for the Eljen square and the blue dots represent measurements on the Kuraray plate. The plates do not have reflective material around the edges.*

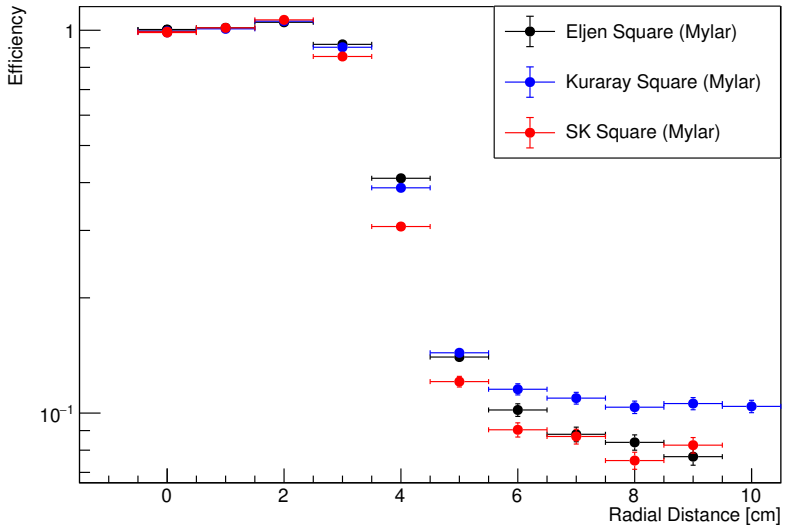

Figure 10.25 *The efficiency vs radial distance from the centre of the PMT. Black dots represent the measurements for the Eljen square and the blue dots represent measurements on the Kuraray plate and the red dots represent the SK plate. The plates have reflective material around the edges.*

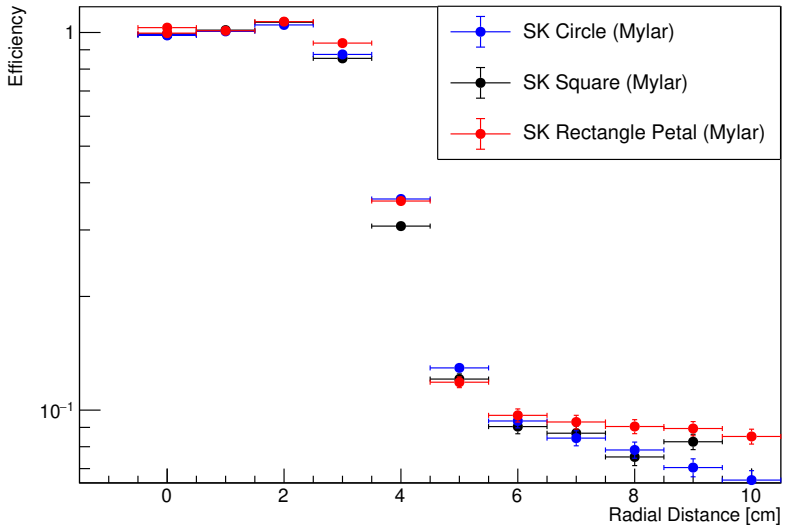

Figure 10.26 *The efficiency vs radial distance from the centre of the PMT. Black dots represent the measurements for a square, the blue dots for a circle and the red dots for a rectangular petal. All shapes are made from the SK WLS plate. The plates have reflective material around the edges.*

Circle and petal shapes were cut out of a Super-K OD plate and measurements were carried out at several radial distances. As can be seen in Figure 10.26, the

expectations from the simulation agree with the measured data. The efficiency of the circle shape drops off with increasing distance as the edges of the plate reflect light around the PMT. The efficiency of the petal shape is higher than the square or circle shapes as light is directed towards the PMT.

10.6 WCSim Simulation

In order to study the performance of the OD, the WCSim simulation software was extended to include an outer detector region. This is still an ongoing effort and the latest version is available at `https://github.com/mahditaani/WCSim/tree/prod/ODWithWLS`. The key additions to WCSim are outward-facing sensitive PMTs, WLS plates, an extended water volume and Tyvek walls. The photocoverage, OD thickness and Tyvek reflectivity are user-defined. Figure 10.27 shows a visualisation of the Hyper-K detector in WCSim including the OD.

The simulation is improved by inputting measured values for the properties of the OD materials. All measurements described in the chapter are used in WCSim.

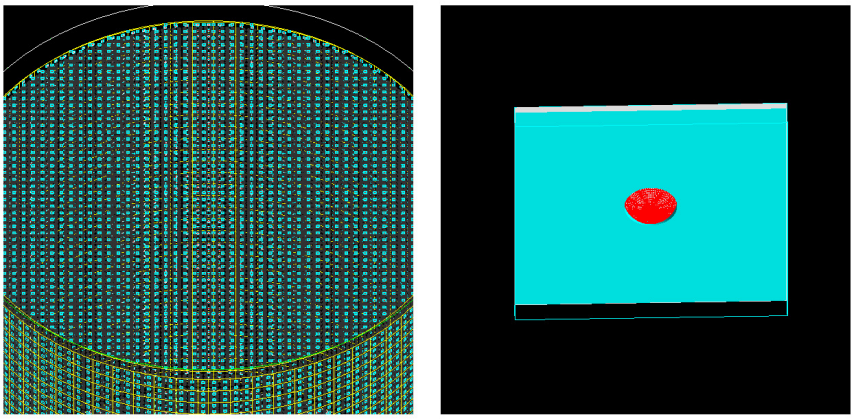

Figure 10.27 *Visualisation of the Hyper-K OD. The figure on the left shows a zoomed out image of the outer detector, blue squares show the WLS plates and red circles show the OD PMTs. ID PMTs have been turned off to easily see the OD. The image on the right shows a zoomed in image of a single WLS plate.*

10.7 Tyvek

Tyvek is used as a reflector in the Super-K OD as it is cheap, durable and very reflective. A significant contribution to the light collection comes from the reflections allowed by Tyvek so it must be well understood in order to optimise the OD design. To study the effects of Tyvek, the WCSim simulation software (see Section 9.4) is used. Measurements of various Tyvek samples are also described in this section.

10.7.1 Simulations

To understand the effects of Tyvek in the OD, WCSim was used to simulate the OD with various configurations. The Tyvek on the outermost wall of the OD (cave) is treated separately from the innermost wall (structure) in order to understand the importance of the reflectors on either side.

One thousand 1 GeV muons are simulated, each particle is generated outside of the OD and enters the OD with a direction perpendicular to the cave wall (directed towards the centre of the tank). The OD has a thickness of one metre and a PMT photocoverage of 0.42% (20,000 3 inch PMTs). Each PMT is coupled to a 50×50 cm WLS plate. To remove any differences expected from various WLS plates, the attenuation length in the plates is set to 1 mm for all wavelengths. This means that the plates absorb photons but the emitted photons do not reach the PMT, so the numbers shown here are very conservative.

There are several Geant4 parameters which can be tuned for reflective surfaces. Constants for specular spike (R_{SS}), specular lobe (R_{SL}), backscatter (R_{BS}) and Lambertian (R_L) can be set. The sum of these constants equals one and they indicate the fraction of reflected light which will be reflected with their respective angular distributions.

To see the effect of the reflectivity, simulations were carried out fixing the values of $R_{SL} = 0.75$ and $R_L = 0.25$. Figure 10.28 shows the averaged light collection as a function of Tyvek reflectivity. Large increase in light collection are observed with increasing reflectivity. It can be clearly seen that reflectors are required on both sides of the OD as light collection is greatly increased with multiple reflections.

To see the effect of specular versus diffuse reflection, the absolute reflectivity

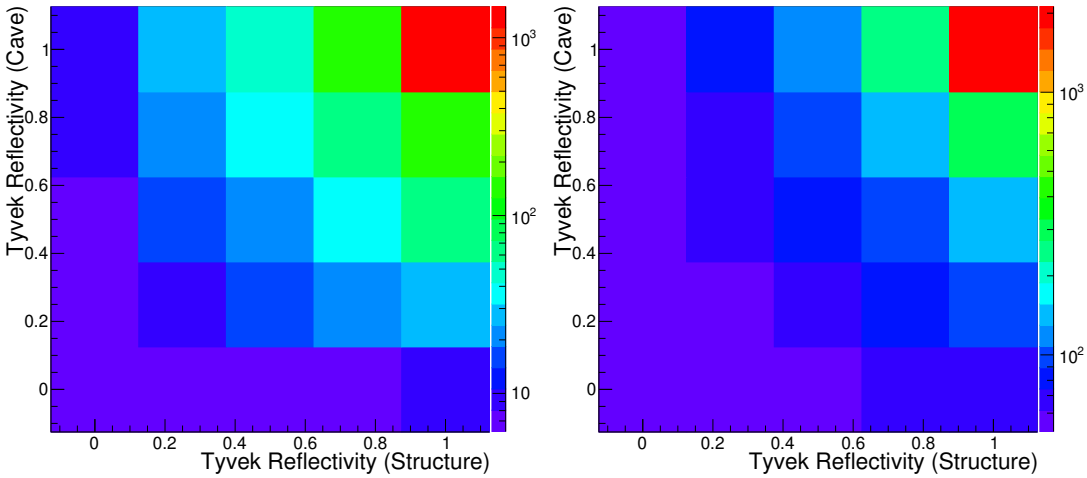

(a) *Number Of PMTs Hit* **(b)** *Number of Photoelectrons*

Figure 10.28 *The average number of photoelectrons detected (right) and the average number of hit PMTs (left) per event, for a 1 GeV incoming muon with various Tyvek reflectivity.*

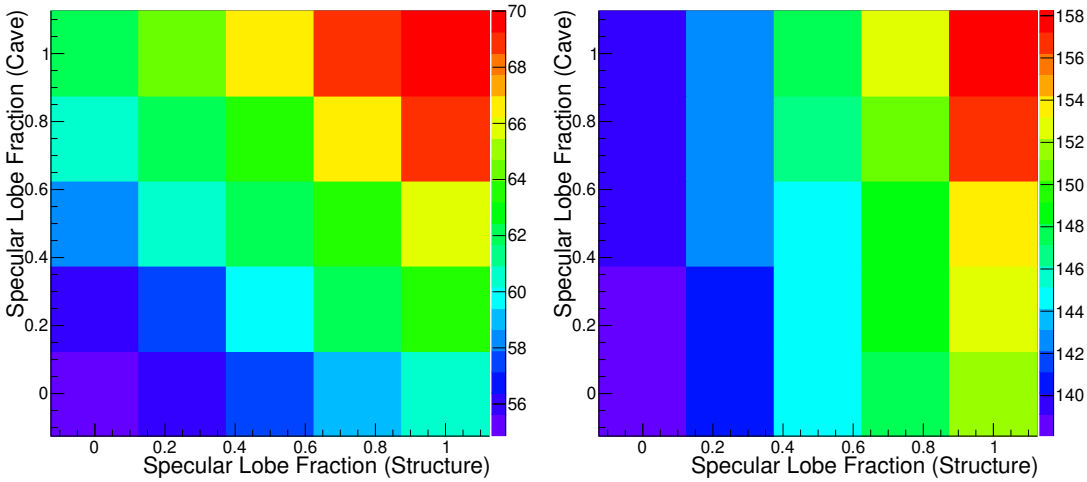

(a) *Number Of PMTs Hit* **(b)** *Number of Photoelectrons*

Figure 10.29 *The average number of photoelectrons detected (right) and the average number of hit PMTs (left) per event, for a 1 GeV incoming muon with various Tyvek specular lobe contributions.*

was fixed to 75%. Figure 10.29 shows the light collection for varying degrees of specular reflection with the remainder of the reflection being diffuse. A modest increase in light collection is expected for more specular reflections though this is much smaller than the effect of the reflectivity. Materials more reflective than Tyvek do exist, however for the 50,000 m^2 required for Hyper-K such options are

prohibitively expensive.

10.7.2 Measurements

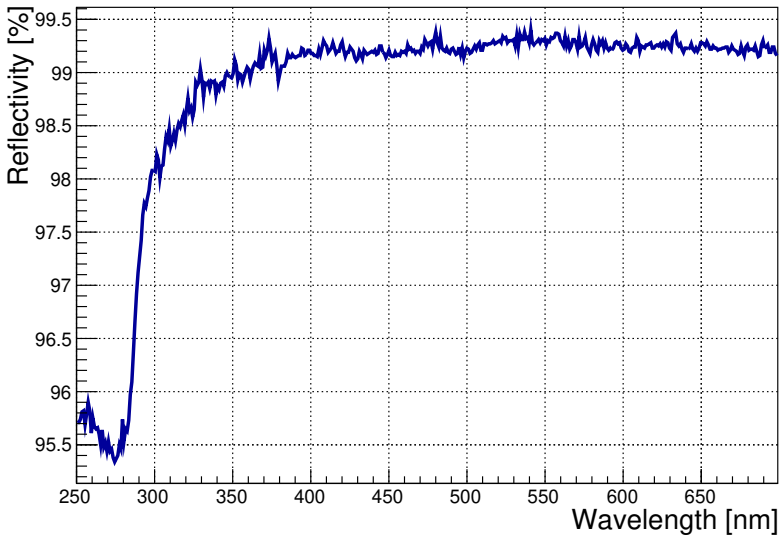

Figure 10.30 *The absolute reflectivity of the Spectralon reference sample.*

Considering the large difference in the expected light collection caused by Tyvek reflectivity, precise measurements of the reflectivity are required. This is measured using a JASCO V-650 spectrophotometer [61] with an integrating sphere attachment. The use of an integrating sphere removes the need to model the Tyvek reflection angles as it receives light for all reflected angles (not including backscatter). Measurements of the Tyvek reflectivity can be compared to a reference sample with a known absolute reflectivity. The reference sample used in these measurements is Spectralon [120], a highly reflective diffuse material with reflectivity values provided by Labsphere. The reflectivity of the reference sample is shown in Figure 10.30.

Several samples have been measured. In Super-K there are two different forms of Tyvek used, the Tyvek used on the innermost wall of the OD has a layer of black polyethylene to aid optical separation of the ID and OD. The Tyvek used on the outermost wall does not have this black layer, the two samples will be referred to as SK Black Tyvek and SK Tyvek respectively. Note that the actual Tyvek layer is of the same type for both of these materials. In addition to the two SK samples, 1073B and 1082D Tyvek have also been measured. Figure 10.32 shows the reflectivity as a function of wavelength for each of the measured samples.

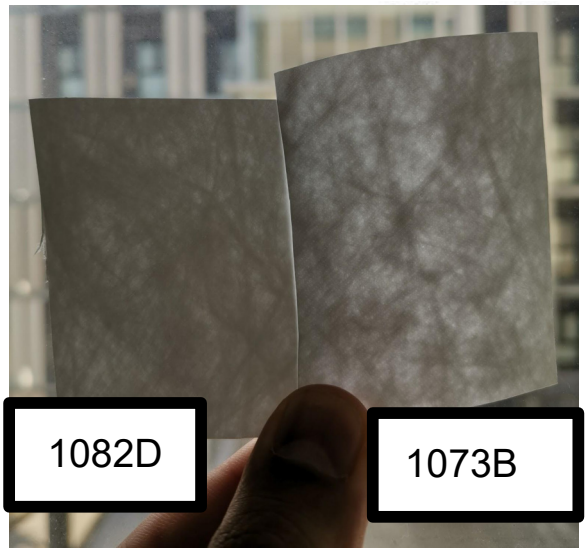

Figure 10.31 *A picture of two Tyvek samples, 1082D on the left and 1073B on the right.*

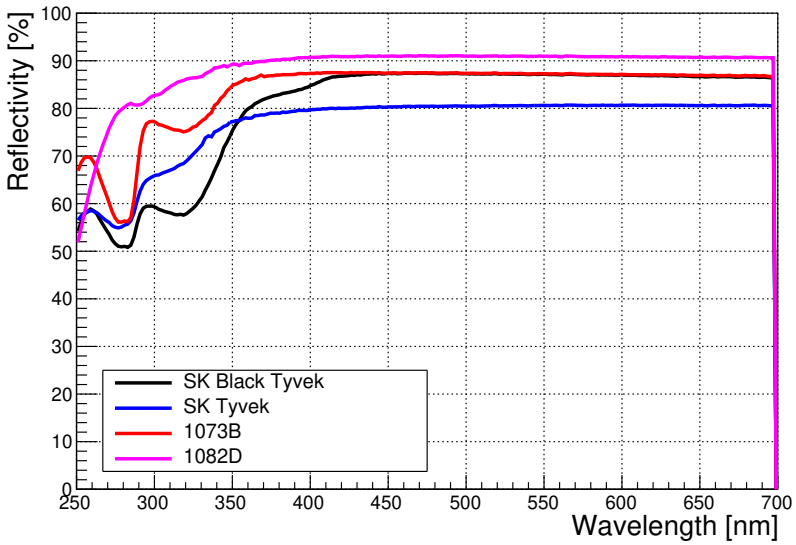

Figure 10.32 *The absolute reflectivity of several Tyvek samples.*

Tyvek is made of randomly layered polyethylene fibres and measurements show that the reflectivity increases for thicker samples, as Tyvek is not completely opaque. Table 10.6 shows the thickness and opacity for different versions of Tyvek. Figure 10.31 shows a photo of two samples, and the thinner sample (1073B) is visibly more translucent. 1082D Tyvek is currently the thickest available Tyvek and is clearly preferred to the other tested samples. Figure 10.33 shows the reflectivity for 1082D Tyvek and the Tyvek used in Super-K. The fibre structure of Tyvek also causes a slight positional dependence so measurements were taken

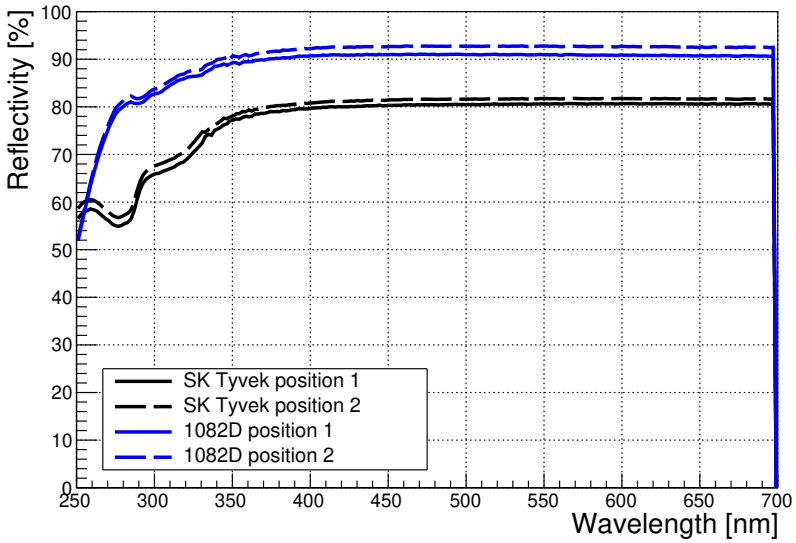

Figure 10.33 *The absolute reflectivity of Super-K Tyvek (without black PE layer) in black and 1082D in blue. The solid and dashed lines represent measurements taken at slightly different positions.*

at various positions to give an idea of the variation.

Table 10.6 *Thickness and opacity of different Tyvek samples, values taken from Dupont datasheets. Values are given as averages and numbers vary slightly depending on the standard used to measure the properties.*

Tyvek Version	Thickness [μm]	Opacity [%]
1073B	178	91
1073D	211	96
1085D	267	96
1082D	275	97

The clear dependence on the thickness of Tyvek indicates a potential benefit to joining together layers of Tyvek. The bonding of Tyvek must be carefully considered; a simple lamination using heat would ruin the structure of Tyvek possibly reducing its reflective performance. Daya Bay [41] uses a form of multi-layered Tyvek bonded together with a layer of polyethylene in the middle, however samples of this Tyvek are currently unavailable. As a proof of concept, the Tyvek samples were bonded together using two basic methods: ultrasonic welding and glue. For the first method, samples were clamped together before being ultrasonic welded at the edges. For the second method, HT-Seal F119 sealant [99] was applied between layers and clamps held the sample together for one day, to cure.

Figure 10.34 shows the reflectivity as a function of wavelength for the multi-layer

ultrasonic samples. Increasing the number of layers clearly shows an increase in reflectivity, especially in the most important 300-350 nm region. Figure 10.35 shows the same plots for the glued samples. Figure 10.36 shows a glued multi-layer sample and a spot where the glue seeps through, the region where the glue seeps through will be referred to as a dark spot. Using the glue, the increase was not as large and was worse when measured on a dark spot.

The 1082D Tyvek was not available when multi-layered samples were being made so the sample was simply folded in half to give an idea of what to expect with multi-layered 1082D. Figure 10.37 shows the absolute reflectivity for the folded 1082D sample. A clear increase in reflectivity can be seen, though this increase is not as large for shorter wavelengths.

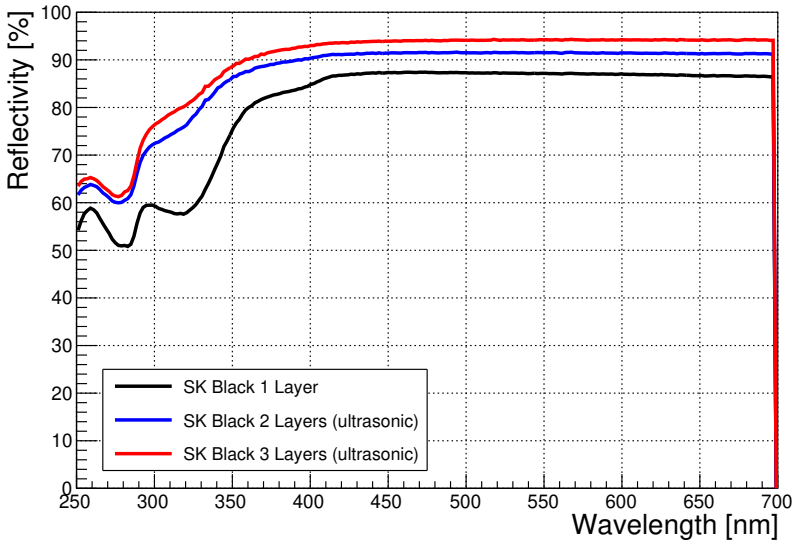

Figure 10.34 *The absolute reflectivity of Super-K Tyvek with multiple layers. The first layer has black PE backing and the remaining layers are bonded around the edges via ultrasonic welding.*

10.8 Discussion

The study shows that a 2D simulation can reasonably model the performance of a WLS plate. The performance of three commercial WLS plates has been measured as well as different plate shapes. The absorption spectra for the Kuraray, Eljen and Sheffield samples as well as the emission spectra for the Eljen and Sheffield samples are improvements over the plates used in SK.

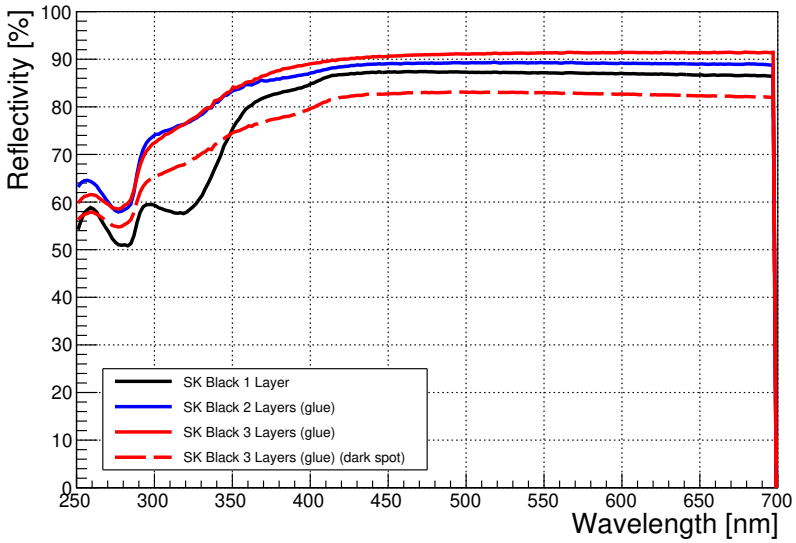

Figure 10.35 *The absolute reflectivity of Super-K Tyvek with multiple layers. The first layer has black PE backing and the remaining layers are bonded together using glue.*

Figure 10.36 *A picture of a multi-layer Tyvek sample, joined using glue. The spotted region in the middle is referred to as the "dark spot".*

While the measurements showed that the Kuraray plate outperforms the Eljen plate, the measured Eljen properties are more suited for use in a water-Cherenkov detector. The refractive index of the Eljen plastic is 1.58 compared to Kuraray's 1.49. This means that a larger fraction of the light will be trapped in the Eljen plate, increasing its efficiency. The measured absorption and emission spectra

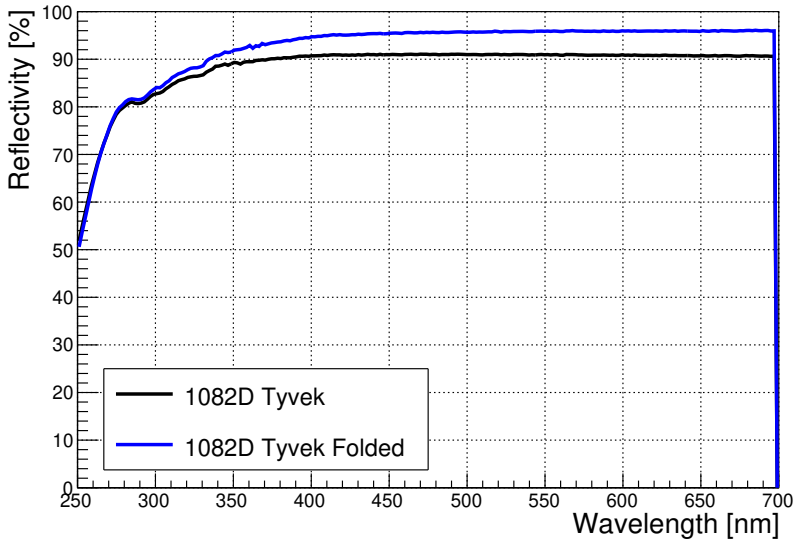

Figure 10.37 *The absolute reflectivity of 1082D Tyvek. The black line shows the values for a single layer of 1082D and the blue lines shows the reflectivity for the same sample folded in half (two layers).*

also show a preference for the Eljen plate as the emission for the Eljen plate more closely matches the PMT's QE and the absorption spectrum in the Kuraray plate has a dip around 300 nm, which is not seen in the Eljen plate. It should be noted that the absorption is maximal for 370 nm which is the wavelength of light used in this study so no effect from the worse absorption is expected. To see the effect of the absorption a future study can be done with the Cherenkov photons emitted by cosmic muons. Another key factor is the refractive index which may result in a 20% difference in light collection even if all other factors were the same.

The difference in the expected and measured efficiencies may be caused by a number of factors. The coupling of the plate to the PMT may be different between the two plates, although we did take efforts to make sure that the holes were the same. Also the setup was changed and so the measurements need to be retaken and verified.

The effect of plate shapes has been studied and the simulations and measurements favour a petal design. These shapes have a higher efficiency because they directly guide light to the PMT. While petal shapes prove to be more efficient than other shapes, it should be noted that the petal shapes have a lower overall area so they may result in less light being captured compared to a square with more area. A study should be carried out to see what sized petals would compare to a square of a particular size.

While reflective material beneath the plate did not make a difference in these studies it may make a difference if the WLS plates were thinner. Halving the thickness of the plates and adding reflective material below may reflect photons which haven't been absorbed giving them twice the travel distance. A future study can be done with thinner plates and reflective materials below.

This study did not include the effect of the attenuation length, for large plates the attenuation length becomes very important. In a future study the attenuation length of each sample should be measured and the simulations should be rerun to get a better calculation of the acceptance angles across the plate. This would remove the need to limit reflections in the simulation as well as directly relating the fitted ρ parameter to the reflectivity of the edges of the plate.

10.8.1 Combined WLS Results

The measurements of the WLS plate properties can be combined to give an overall effective photocoverage. The efficiency measurements in Section 10.4 are taken with a 370 nm wavelength LED light source, in air. The final setup will use Cherenkov photons and will be in water. Several steps are taken to convert the lab measurements to the expected values for Cherenkov photons in water.

First, the quantum efficiency of the PMT is convolved with the measured emission spectrum. The quantum efficiency of the PMT at 370 nm is maximal (30%), the averaged quantum efficiency for the whole plate is $\sim$22% . This means that even if every emitted photon reaches the PMT, the amount of detected light from a point on the plate should be roughly two thirds of the value obtained from measurements at the centre of the PMT. Also, the absorption in the plates is maximal at 370 nm, however the light in the OD will be Cherenkov light which follows a spectrum. In order to account for this, the measured absorption spectrum is convoluted with the Cherenkov spectrum to get an idea of the amount of light absorbed by the plate. Combining these factors gives the expected efficiency for Cherenkov photons hitting the plate. A separate convolution of the PMT quantum efficiency with the Cherenkov spectrum is used to estimate the response of the PMT to Cherenkov light.

These numbers assume that every photon emitted by the plate reaches the PMT; including the efficiency measurements gives a more realistic response accounting for propagation in the plate. Lastly a factor is used to account for the difference

expected from going from air to water. The difference in medium alters the amount of emitted photons which are trapped in the plate by total internal reflection so this factor can be included as an overall scaling factor. The air→water scaling factor is given by $\cos(\theta_{\text{water}})/\cos(\theta_{\text{air}})$ where θ is the critical angle for plates in the respective medium. This factor is 70% for Eljen and 60% for Kuraray/Super-K, as the higher refractive index of the Eljen plate traps more light than the other two plates.

Table 10.7 *The expected effective photocoverage for various WLS plates. Assuming (η ,ρ) = (0.32, 0.7). All plates have reflective edges and a PMT photocoverage of 0.28% is assumed.*

Plate	Size (L×L cm)	Photocoverage [%]	Light increase [(WLS+PMT)/PMT]
Eljen	50	0.73	2.6
Kuraray	50	0.67	2.4
SK	50	0.67	2.4
Eljen	40	0.59	2.1
Kuraray	40	0.62	2.2
SK	40	0.56	2.0

Plates are simulated in various sizes and the best fit values of η and ρ are applied in order to estimate the expected efficiency. Table 10.7 shows the effective photocoverage for different WLS plates. The lowest expected increase, from a 40×40 cm Super-K plate would result in a doubled effective photocoverage with larger plates producing further increases in light collection.

10.8.2 Tyvek

The Tyvek simulation studies show that it is important to have reflectors on both sides of the OD and the type of reflection is much less important than the overall reflectivity. The reflectivity of Tyvek is related to its thickness, with thicker samples showing a higher reflectivity. Simple bonding methods have shown an increase in Tyvek reflectivity though further tests need to be carried out in order to determine the stability of such methods in ultrapure water. Tests would also need to be carried out with the bonded samples in water to get a more realistic value for the reflectivity. Ultimately, when tested under the same conditions, Tyvek 1082D [68] has a higher reflectivity than the Tyvek used in Super-K and bonding two layers shows a further increase.

10.8.3 Next Steps

The light collection has been studied independently for WLS plates and Tyvek. In the final OD design, there will be some interplay between the two components. High reflectivity Tyvek allows multiple reflections in the OD but this effect will be dampened by the WLS plates. Future studies will include both components in order to optimise the size of the plates. The optimisations to individual components of the OD has been achieved but the overall performance of the OD must be tested with cosmic muons and low energy background sources. A detector veto efficiency must be obtained and final changes to the OD design should maximise it. There may be some physics capability in the OD if the increased light collection can give a good enough estimate of the deposited energy. Events which stop in the OD may be selected and treated as contained events. Also, various forms of OD segmentation can be studied. It is seen in Chapter 6 that the cosmic muon veto efficiency is increased by segmenting the barrel and endcap regions, this study has yet to be carried out for Hyper-K.

Chapter 11

Conclusions and Outlook

In this thesis two searches for non-standard interactions were carried out using atmospheric neutrinos. The large range of neutrino energies and a significant pathlength through matter make atmospheric neutrinos a good source to search for matter effects. This study includes a statistical update of more than twice the data since the last SK NSI zenith analysis; further improvements come from more precise measurements of standard neutrino oscillation parameters and improvements to the simulation and event reconstruction.

The search in the $\mu - \tau$ sector looked for flavour-changing neutral current interactions between ν_μ and ν_τ driven by $\varepsilon_{\mu\tau}$ and lepton non-universality driven by $(\varepsilon_{\tau\tau} - \varepsilon_{\mu\mu})$. The search was carried out with a two-flavour analysis, decoupling from ν_e and the following constraints were obtained at 90% C.L.:

$$-0.046 < \varepsilon_{\mu\tau} < 0.019 \tag{11.1}$$

$$-0.050 < \varepsilon_{\tau\tau} - \varepsilon_{\mu\mu} < 0.138 \tag{11.2}$$

These constraints slightly improve over past SK results and are consistent with results from IceCube [4]. No evidence of NSI was found.

The search in the $e - \tau$ sector looked for flavour-changing neutral current interactions between ν_e and ν_τ driven by $\varepsilon_{e\tau}$ and lepton non-universality driven by $\varepsilon_{\tau\tau}$. This analysis improves over the past SK NSI analysis by including full three-flavour standard neutrino oscillations with more precise standard oscillation

parameter assumptions. The parameters $\varepsilon_{e\tau}$ and $\varepsilon_{\tau\tau}$ are highly correlated to ε_{ee} so constraints are obtained for several values of ε_{ee}. While the new constraints are somewhat looser than the past result, this is expected from the difference in assumed standard oscillation paramaters. Asymmetric bounds result from the inclusion of three-flavour standard oscillations and standard matter effects. No evidence of NSI is found.

Non-standard interactions affect the oscillation probabilities of neutrinos and anti-neutrinos separately and improvements to the NSI allowed region can be expected from improvements in neutrino/antineutrino separation. Currently the atmospheric neutrino analyses statistically separate neutrinos and antineutrinos for electron-like samples; a statistical separation of muon-like samples has been developed though it has not yet been included in the atmospheric analysis framework. Implementation of the $\nu_\mu/\bar{\nu}_\mu$ separation may not improve NSI constraints for Super-K as the contained events have a relatively low energy, however the selection could be implemented in Hyper-K to improve NSI constraints. Additional separation power will come from SK-Gd. Gadolinium will be added to the ultrapure water and antineutrino interactions will be individually tagged from the final state particles. This method of tagging requires that the neutrino interaction takes place inside the tank which excludes the highest energy samples, thus improved constraints can be expected only for the non-universality NSI parameter.

The NSI analyses were carried out using binned datasets which results in some loss of information. A significant portion of the dataset lies in a region where slightly varying the energy or zenith angle drastically alters the survival probability. A future maximum likelihood analysis could use the unbinned data to extract more information and perhaps increase the precision of the oscillation parameter measurements.

Future improvement in the analysis could come from the treatment of the systematic uncertainties. In the current analysis, the systematic uncertainties are assumed to be uncorrelated. This simplifies the fitting procedure, but a more complete treatment of the uncertainties would require adding correlation terms to the χ^2 calculation [74].

Further improvements to NSI measurements can be expected from the Hyper-K experiment. In addition to the increased statistics, the larger Hyper-K tank(s) will be able to contain higher energy neutrino events $E_\nu > 10$ GeV; the high

energy neutrinos are potentially subject to matter NSI effects and, in Super-K, muons created from these neutrinos leave the tank resulting in the inability to accurately reconstruct the incoming neutrino energy. At the time of writing this thesis, no dedicated Hyper-K atmospheric neutrino MC exists. The expected detector performance is evaluated using Super-K atmospheric neutrino MC scaled up to account for the extra detector volume. This approach does not account for the higher energy muon events which would be fully contained in Hyper-K but are partially contained in Super-K. In order to determine a reasonable Hyper-K sensitivity to NSI parameters, a full Hyper-K atmospheric neutrino MC must be developed.

Another improvement can be expected from the combination of long baseline and atmospheric neutrino data in Hyper-K. The long baseline measurements can be taken as "vacuum" parameters as matter effects are negligible for such short pathlengths. The atmospheric neutrinos will be subject to standard and non-standard matter effects and tensions between the two datasets could indicate new physics. Assuming the same systematic errors as SK-IV and scaling up the SK-IV MC to the exposure expected for a single Hyper-K tank running for 10 years, the constraint on $\varepsilon_{\mu\tau}$ and $\varepsilon_{\tau\tau} - \varepsilon_{\mu\mu}$ could improve by a factor of two. This does not include improvements to neutron tagging or the higher energy contained events.

Hyper-K is expected to start taking data in 2028 and this thesis covers the overall Hyper-K design and the development of the Hyper-K outer detector. The key components used to maximise the light collection in the outer detector are wavelength shifting plates, to increase the effective photocoverage and Tyvek, to allow for more light to be reflected onto the photosensors.

Wavelength shifting plates from multiple manufacturers have been tested, characterised and compared. The efficiency of the plates has been studied for various plate shapes. Designs which optimise the plate performance per unit area have been found. The studies in this thesis show the improved efficiency at fixed distances from the PMT, further studies are required in order to compare efficiencies of entire plates rather than the efficiencies at fixed radial distances. Clear improvements can be seen when plate edges are aluminised and square plates are preferred over circular ones.

Simulation studies of the Hyper-K outer detector have found that reflective edges on both sides of the OD are necessary to maximise light collection and the

reflectivity of the materials is much more important than the type of reflection (specular, diffuse etc.). Different versions of Tyvek have been compared and their reflectivity has been measured. Improvements have been found when joining together layers of Tyvek via ultrasonic bonding at the seams. Further studies are required to test the stability of bonded materials in ultrapure water (and gadolinium-loaded water) and effects on the water transparency should be carried out. Measurements of reflective materials should also be carried out in water to see a realistic measurement of reflectivity.

Appendix A

Systematic Uncertainties

Table A.1 *The best fit systematic errors for the best fit point in the three-flavour $\varepsilon_{\mu\tau}$ fit. The systematic errors shown here are related to the neutrino flux. The final column shows the estimated 1σ uncertainty and the penultimate column shows the best fit ϵ_j.*

Sample			Fit Value [%]	σ [%]
Flux normalisation	$E_\nu < 1$		13.33	25
	$E_\nu > 1$		6.81	15
$(\nu_\mu + \bar{\nu}_\mu)/(\nu_e + \bar{\nu}_e)$			0.09	2
			-1.12	3
			1.68	5
$\bar{\nu}_e/\nu_e$			1.59	5
			3.36	5
			-1.39	8
$\bar{\nu}_\mu/\nu_\mu$			0.23	2
			2.94	6
			-1.96	15
Up/down ratio	$< 400\ MeV$	e-like	-0.03	0.1
	$< 400\ MeV$	μ-like	-0.08	0.3
	$< 400\ MeV$	0-decay μ-like	-0.28	1.1
	$> 400\ MeV$	e-like	-0.20	0.8
	$> 400\ MeV$	μ-like	-0.13	0.5
	$> 400\ MeV$	0-decay μ-like	-0.43	1.7
	Multi-GeV	e-like	-0.18	0.7
	Multi-GeV	μ-like	-0.05	0.2
	Multi-ring Sub-GeV	e-like	-0.10	0.4
	Multi-ring Sub-GeV	μ-like	-0.05	0.2
	Multi-ring Multi-GeV	e-like	-0.08	0.3
	Multi-ring Multi-GeV	μ-like	-0.05	0.2
	PC		-0.05	0.2
Horizontal/vertical ratio	$< 400\ MeV$	e-like	0.02	0.1
	$< 400\ MeV$	μ-like	0.02	0.1
	$< 400\ MeV$	0-decay μ-like	0.06	0.3
	$> 400\ MeV$	e-like	0.29	1.4
	$> 400\ MeV$	μ-like	0.39	1.9
	$> 400\ MeV$	0-decay μ-like	0.29	1.4
	Multi-GeV	e-like	0.67	3.2
	Multi-GeV	μ-like	0.48	2.3
	Multi-ring Sub-GeV	e-like	0.29	1.4
	Multi-ring Sub-GeV	μ-like	0.27	1.3
	Multi-ring Multi-GeV	e-like	0.58	2.8
	Multi-ring Multi-GeV	μ-like	0.31	1.5
	PC		0.35	1.7
K/π ratio in flux calculation			-7.89	10
Neutrino path length			-0.97	5
Sample-by-sample	FC Multi-GeV		-6.39	5
	PC + Stopping UP-μ		-0.50	5
Matter Effects			0.49	6.8

Table A.2 *The best fit systematic errors for the best fit point in the three-flavour $\varepsilon_{\mu\tau}$ fit. The systematic errors shown here are related to the neutrino interaction. The final column shows the estimated 1σ uncertainty and the penultimate column shows the best fit ϵ_j.*

Sample		Fit Value [%]	σ [%]
M_A in QE		-0.46	10
Single π production; Axial coupling		-4.50	10
Single π production; C_{A5}		-3.08	10
Single π production; Background		-8.75	10
CCQE cross section		6.44	10
CCQE $\bar{\nu}/\nu$ ratio		9.29	10
CCQE μ/e ratio		0.72	10
DIS cross section		-2.13	5
DIS model comparisons		3.01	10
DIS Q^2 distribution (high W)		7.78	10
DIS Q^2 distribution (low W)		-5.92	10
Coherent π production		-9.34	100
NC/CC		12.88	20
CC ν_τ cross section		-10.59	25
Single π production; $\pi^0/\pi^\pm$ ratio		-20.98	40
Single π production; $\bar{\nu}_i/\nu_i$ $(i = e; \mu)$		-11.22	10
NC fraction from hadron simulation		-0.69	10
$\pi^\pm$ decay uncertainty	e-like 0-decay	-0.19	0.6
	μ-like 0-decay	-0.26	0.8
	e-like 1-decay	-1.31	4.1
	μ-like 1-decay	-0.29	0.9
	μ-like 2-decay	-1.82	5.7
Meson exchange current		-1.66	10
Δm^2_{21} [139]		0.02	2.4
$\sin^2(\theta_{12})$ [139]		0.33	4.6
$\sin^2(\theta_{13})$ [139]		0.19	5.4

Table A.3 *The best fit systematic errors for the best fit point in the three-flavour $\varepsilon_{\mu\tau}$ fit. The systematic errors shown here are related to the detector performance, event selection and reconstruction. The "σ" column shows the estimated 1σ uncertainty and the "Fit" column shows the best fit ϵ_j. Uncertainties are shown for SK-I and SK-II.*

Sample			SK-I		SK-II	
			Fit	σ	Fit	σ
FC reduction			-0.01	0.2	0.01	0.2
PC reduction			0.03	2.4	-3.43	4.8
FC/PC separation			-0.11	0.6	0.08	0.5
PC stopping/through-going separation (barrel)			3.54	7	-5.90	9.4
PC stopping/through-going separation (bottom)			-16.34	23	-2.51	13
PC stopping/through-going separation (top)			6.52	46	-3.37	19
Non-ν background $\mu-like$	Sub-GeV		0.01	0.1	0.07	0.4
	Multi-GeV		0.04	0.4	0.07	0.4
	Sub-GeV 1-ring 0-decay		0.01	0.1	0.05	0.3
	PC		0.02	0.2	0.12	0.7
Non-ν background e$-like$	Sub-GeV		0.07	0.5	-0.00	0.2
	Multi-GeV		0.01	0.1	-0.00	0.3
	Multi-GeV 1-ring e-like		3.59	13	-5.16	38
	Multi-GeV Multi-ring e-like		3.79	12	3.75	11
Fiducial Volume			-0.82	2	-0.08	2
Ring separation	$< 400\ MeV$	e-like	0.43	2.3	-1.09	1.3
	$< 400\ MeV$	μ-like	0.13	0.7	-1.92	2.3
	$> 400\ MeV$	e-like	0.07	0.4	-1.42	1.7
	$> 400\ MeV$	μ-like	0.13	0.7	-0.59	0.7
	Multi-GeV	e-like	0.69	3.7	-2.17	2.6
	Multi-GeV	μ-like	0.32	1.7	-1.42	1.7
	Multi-ring Sub-GeV	e-like	0.65	3.5	-3.18	3.8
	Multi-ring Sub-GeV	μ-like	0.84	4.5	-6.86	8.2
	Multi-ring Multi-GeV	e-like	0.58	3.1	-1.59	1.9
	Multi-ring Multi-GeV	μ-like	0.76	4.1	-0.67	0.8
PID 1-ring	Sub-GeV	e-like	-0.04	0.23	0.23	0.66
	Sub-GeV	μ-like	-0.03	0.18	0.18	0.5
	Multi-GeV	e-like	-0.03	0.19	0.08	0.24
	Multi-GeV	μ-like	-0.03	0.19	0.09	0.26
PID Multi-ring	Sub-GeV	e-like	0.22	3.1	3.47	6
	Sub-GeV	μ-like	0.05	0.66	1.44	2.5
	Multi-GeV	e-like	0.46	6.5	5.60	9.7
	Multi-GeV	μ-like	0.21	2.9	2.25	3.9
Multi-ring likelihood selection	e-like		-6.46	6	-1.23	3.8
Energy calibration			1.39	3.3	1.11	2.8
Up/down asymmetry energy calibration			0.25	0.6	0.24	0.6
Up-μ reduction	Stopping		-0.10	0.7	-0.09	0.7
	Through-going		-0.07	0.5	-0.07	0.5
Up-μ stopping/through-going separation			-0.00	0.4	-0.01	0.6
Up-μ stopping energy cut			0.06	0.9	0.14	1.3
Up-μ through-going path cut			0.40	1.5	0.82	2.3
Up-μ Through-going showering separation			7.37	3.4	-4.79	4.4
Up-μ stopping BG subtraction			10.75	16	-2.86	21
Up-μ non-showering BG subtraction			-3.48	18	-3.52	14
Up-μ showering BG subtraction			-12.46	18	-15.83	14
$\nu_e/\bar{\nu}_e$ separation			0.99	7.2	6.99	7.9
Sub-GeV 1-ring π^0 selection	$100 < P_e < 250$ MeV/c		1.66	9	6.90	10
	$250 < P_e < 400$ MeV/c		1.69	9.2	9.65	14
	$400 < P_e < 630$ MeV/c		2.94	16	7.59	11
	$630 < P_e < 1000$ MeV/c		2.58	14	11.03	16
	$1000 < P_e < 1330$ MeV/c		2.21	12	6.76	9.8
Sub-GeV 2-ring π^0			1.28	5.6	-2.69	4.4
Decay-e tagging			-3.27	10	-0.91	10
Solar activity			-1.78	20	20.23	50

Table A.4 *The best fit systematic errors for the best fit point in the three-flavour $\varepsilon_{\mu\tau}$ fit. The systematic errors shown here are related to the detector performance, event selection and reconstruction. The "σ" column shows the estimated 1σ uncertainty and the "Fit" column shows the best fit ϵ_j. Uncertainties are shown for SK-III and SK-IV.*

Sample			SK-III		SK-IV	
			Fit	σ	Fit	σ
FC reduction			0.07	0.8	0.70	1.3
PC reduction			-0.01	0.5	-0.78	1
FC/PC separation			-0.14	0.9	0.00	0.02
PC stopping/through-going separation (barrel)			-14.48	29	-0.73	8.5
PC stopping/through-going separation (bottom)			-0.35	12	-1.61	6.8
PC stopping/through-going separation (top)			-15.66	87	-26.65	40
Non-ν background $\mu-like$	Sub-GeV		0.12	0.5	-0.01	0.02
	Multi-GeV		0.12	0.5	-0.01	0.02
	Sub-GeV 1-ring 0-decay		0.09	0.4	-0.05	0.09
	PC		0.42	1.8	-0.27	0.49
Non-ν background e$-like$	Sub-GeV		-0.00	0.2	-0.00	0.02
	Multi-GeV		-0.01	0.7	-0.00	0.08
	Multi-GeV 1-ring e-like		-0.98	27	2.62	18
	Multi-GeV Multi-ring e-like		0.77	11	0.49	12
Fiducial Volume			0.23	2	-1.46	2
Ring separation	$< 400\ MeV$	e-like	0.81	2.3	-0.95	1.6
	$< 400\ MeV$	μ-like	1.05	3	-1.79	3
	$> 400\ MeV$	e-like	0.46	1.3	-0.60	1
	$> 400\ MeV$	μ-like	0.21	0.6	-0.36	0.6
	Multi-GeV	e-like	0.46	1.3	-0.60	1
	Multi-GeV	μ-like	0.35	1	-0.71	1.2
	Multi-ring Sub-GeV	e-like	0.46	1.3	-1.13	1.9
	Multi-ring Sub-GeV	μ-like	0.91	2.6	-1.37	2.3
	Multi-ring Multi-GeV	e-like	0.39	1.1	-0.54	0.9
	Multi-ring Multi-GeV	μ-like	0.74	2.1	-1.43	2.4
PID 1-ring	Sub-GeV	e-like	-0.05	0.26	0.12	0.28
	Sub-GeV	μ-like	-0.04	0.19	0.10	0.22
	Multi-GeV	e-like	-0.06	0.31	0.16	0.35
	Multi-GeV	μ-like	-0.06	0.3	0.16	0.35
PID Multi-ring	Sub-GeV	e-like	3.48	9.5	-2.26	4.2
	Sub-GeV	μ-like	1.91	5.2	-0.86	1.6
	Multi-GeV	e-like	1.80	4.9	-1.78	3.3
	Multi-GeV	μ-like	0.99	2.7	-0.86	1.6
Multi-ring likelihood selection	e-like		-4.98	5.3	-2.30	3
Energy calibration			1.36	2.4	-0.74	2.1
Up/down asymmetry energy calibration			0.74	1.3	-0.14	0.4
Up-μ reduction	Stopping		0.16	0.7	0.08	0.5
	Through-going		0.11	0.5	0.05	0.3
Up-μ stopping/through-going separation			0.03	0.4	-0.11	0.6
Up-μ stopping energy cut			0.95	2	-0.17	1.7
Up-μ through-going path cut			-0.99	2.8	-1.48	1.5
Up-μ Through-going showering separation			2.84	2.4	3.21	3
Up-μ stopping BG subtraction			-4.38	20	-9.77	17
Up-μ non-showering BG subtraction			1.47	24	2.12	17
Up-μ showering BG subtraction			0.03	24	-1.10	24
$\nu_e/\bar{\nu}_e$ separation			0.40	7.7	2.47	6.8
Sub-GeV 1-ring π^0 selection	$100 < P_e < 250$ MeV/c		0.95	6.3	5.21	4.6
	$250 < P_e < 400$ MeV/c		0.74	4.9	3.40	3
	$400 < P_e < 630$ MeV/c		3.62	24	14.71	13
	$630 < P_e < 1000$ MeV/c		1.24	8.2	19.24	17
	$1000 < P_e < 1330$ MeV/c		1.66	11	27.16	24
Sub-GeV 2-ring π^0			1.62	5.9	-0.74	5.6
Decay-e tagging			0.86	10	1.39	10
Solar activity			2.70	20	0.63	10

Table A.5 *The best fit systematic errors for the best fit point in the two-flavour $\varepsilon_{\mu\tau} - \varepsilon_{\tau\tau}$ fit. The systematic errors shown here are related to the neutrino flux. The final column shows the estimated 1σ uncertainty and the penultimate column shows the best fit ϵ_j.*

Sample			Fit Value [%]	σ [%]
Flux normalisation	$E_\nu < 1$		14.36	25
	$E_\nu > 1$		6.22	15
$(\nu_\mu + \bar{\nu}_\mu)/(\nu_e + \bar{\nu}_e)$			-0.46	2
			-2.02	3
			2.35	5
$\bar{\nu}_e/\nu_e$			2.57	5
			3.69	5
			-1.24	8
$\bar{\nu}_\mu/\nu_\mu$			0.07	2
			2.42	6
			-2.18	15
Up/down ratio	$< 400\ MeV$	e-like	-0.01	0.1
	$< 400\ MeV$	μ-like	-0.03	0.3
	$< 400\ MeV$	0-decay μ-like	-0.10	1.1
	$> 400\ MeV$	e-like	-0.07	0.8
	$> 400\ MeV$	μ-like	-0.05	0.5
	$> 400\ MeV$	0-decay μ-like	-0.16	1.7
	Multi-GeV	e-like	-0.06	0.7
	Multi-GeV	μ-like	-0.02	0.2
	Multi-ring Sub-GeV	e-like	-0.04	0.4
	Multi-ring Sub-GeV	μ-like	-0.02	0.2
	Multi-ring Multi-GeV	e-like	-0.03	0.3
	Multi-ring Multi-GeV	μ-like	-0.02	0.2
	PC		-0.02	0.2
Horizontal/vertical ratio	$< 400\ MeV$	e-like	0.00	0.1
	$< 400\ MeV$	μ-like	0.00	0.1
	$< 400\ MeV$	0-decay μ-like	0.00	0.3
	$> 400\ MeV$	e-like	0.01	1.4
	$> 400\ MeV$	μ-like	0.01	1.9
	$> 400\ MeV$	0-decay μ-like	0.01	1.4
	Multi-GeV	e-like	0.01	3.2
	Multi-GeV	μ-like	0.01	2.3
	Multi-ring Sub-GeV	e-like	0.01	1.4
	Multi-ring Sub-GeV	μ-like	0.01	1.3
	Multi-ring Multi-GeV	e-like	0.01	2.8
	Multi-ring Multi-GeV	μ-like	0.01	1.5
	PC		0.01	1.7
K/π ratio in flux calculation			-8.61	10
Neutrino path length			-0.16	5
Sample-by-sample	FC Multi-GeV		-5.80	5
	PC + Stopping UP-μ		-1.57	5
Matter Effects			-0.71	6.8

Table A.6 *The best fit systematic errors for the best fit point in the two-flavour $\varepsilon_{\mu\tau} - \varepsilon_{\tau\tau}$ fit. The systematic errors shown here are related to the neutrino interaction. The final column shows the estimated 1σ uncertainty and the penultimate column shows the best fit ϵ_j.*

Sample		Fit Value [%]	σ [%]
M_A in QE		-1.45	10
Single π production; Axial coupling		-4.60	10
Single π production; C_{A5}		-3.14	10
Single π production; Background		-9.34	10
CCQE cross section		6.36	10
CCQE $\bar{\nu}/\nu$ ratio		8.61	10
CCQE μ/e ratio		2.75	10
DIS cross section		-1.74	5
DIS model comparisons		2.92	10
DIS Q^2 distribution (high W)		6.94	10
DIS Q^2 distribution (low W)		-5.94	10
Coherent π production		-11.91	100
NC/CC		14.50	20
CC ν_τ cross section		3.11	25
Single π production; $\pi^0/\pi^\pm$ ratio		-23.68	40
Single π production; $\bar{\nu}_i/\nu_i$ $(i = e; \mu)$		-11.19	10
NC fraction from hadron simulation		-2.28	10
$\pi^\pm$ decay uncertainty	e-like 0-decay	-0.18	0.6
	μ-like 0-decay	-0.25	0.8
	e-like 1-decay	-1.26	4.1
	μ-like 1-decay	-0.28	0.9
	μ-like 2-decay	-1.75	5.7
Meson exchange current		-1.01	10
Δm^2_{21} [139]		-0.00	2.4
$\sin^2(\theta_{12})$ [139]		0.29	4.6
$\sin^2(\theta_{13})$ [139]		0.68	5.4

Table A.7 *The best fit systematic errors for the best fit point in the two-flavour $\varepsilon_{\mu\tau} - \varepsilon_{\tau\tau}$ fit. The systematic errors shown here are related to the detector performance, event selection and reconstruction. The "σ" column shows the estimated 1σ uncertainty and the "Fit" column shows the best fit ϵ_j. Uncertainties are shown for SK-I and SK-II.*

Sample			SK-I		SK-II	
			Fit	σ	Fit	σ
FC reduction			-0.01	0.2	0.01	0.2
PC reduction			0.03	2.4	-3.45	4.8
FC/PC separation			-0.12	0.6	0.07	0.5
PC stopping/through-going separation (barrel)			3.28	7	-6.37	9.4
PC stopping/through-going separation (bottom)			-17.11	23	-2.73	13
PC stopping/through-going separation (top)			2.15	46	-4.64	19
Non-ν background $\mu - like$	Sub-GeV		0.01	0.1	0.09	0.4
	Multi-GeV		0.06	0.4	0.09	0.4
	Sub-GeV 1-ring 0-decay		0.01	0.1	0.07	0.3
	PC		0.03	0.2	0.15	0.7
Non-ν background e$-like$	Sub-GeV		0.08	0.5	0.00	0.2
	Multi-GeV		0.02	0.1	0.00	0.3
	Multi-GeV 1-ring e-like		3.54	13	-4.15	38
	Multi-GeV Multi-ring e-like		3.75	12	3.53	11
Fiducial Volume			-0.77	2	-0.03	2
Ring separation	$< 400\ MeV$	e-like	0.54	2.3	-1.06	1.3
	$< 400\ MeV$	μ-like	0.16	0.7	-1.88	2.3
	$> 400\ MeV$	e-like	0.09	0.4	-1.39	1.7
	$> 400\ MeV$	μ-like	0.16	0.7	-0.57	0.7
	Multi-GeV	e-like	0.87	3.7	-2.13	2.6
	Multi-GeV	μ-like	0.40	1.7	-1.39	1.7
	Multi-ring Sub-GeV	e-like	0.82	3.5	-3.11	3.8
	Multi-ring Sub-GeV	μ-like	1.06	4.5	-6.70	8.2
	Multi-ring Multi-GeV	e-like	0.73	3.1	-1.55	1.9
	Multi-ring Multi-GeV	μ-like	0.96	4.1	-0.65	0.8
PID 1-ring	Sub-GeV	e-like	-0.05	0.23	0.25	0.66
	Sub-GeV	μ-like	-0.04	0.18	0.19	0.5
	Multi-GeV	e-like	-0.04	0.19	0.09	0.24
	Multi-GeV	μ-like	-0.04	0.19	0.10	0.26
PID Multi-ring	Sub-GeV	e-like	0.39	3.1	3.78	6
	Sub-GeV	μ-like	0.08	0.66	1.57	2.5
	Multi-GeV	e-like	0.82	6.5	6.11	9.7
	Multi-GeV	μ-like	0.36	2.9	2.46	3.9
Multi-ring likelihood selection	e-like		-5.93	6	-0.99	3.8
Energy calibration			1.44	3.3	1.14	2.8
Up/down asymmetry energy calibration			0.26	0.6	0.24	0.6
Up-μ reduction	Stopping		-0.10	0.7	-0.10	0.7
	Through-going		-0.07	0.5	-0.07	0.5
Up-μ stopping/through-going separation			-0.01	0.4	-0.01	0.6
Up-μ stopping energy cut			0.08	0.9	0.16	1.3
Up-μ through-going path cut			0.36	1.5	0.78	2.3
Up-μ Through-going showering separation			7.27	3.4	-4.84	4.4
Up-μ stopping BG subtraction			12.02	16	-2.47	21
Up-μ non-showering BG subtraction			-3.41	18	-3.45	14
Up-μ showering BG subtraction			-12.47	18	-15.85	14
$\nu_e/\bar{\nu}_e$ separation			1.09	7.2	6.86	7.9
Sub-GeV 1-ring π^0 selection	$100 < P_e < 250$ MeV/c		1.51	9	6.75	10
	$250 < P_e < 400$ MeV/c		1.55	9.2	9.46	14
	$400 < P_e < 630$ MeV/c		2.69	16	7.43	11
	$630 < P_e < 1000$ MeV/c		2.35	14	10.81	16
	$1000 < P_e < 1330$ MeV/c		2.02	12	6.62	9.8
Sub-GeV 2-ring π^0			1.26	5.6	-2.71	4.4
Decay-e tagging			-3.41	10	-0.99	10
Solar activity			-1.95	20	20.41	50

Table A.8 *The best fit systematic errors for the best fit point in the two-flavour $\varepsilon_{\mu\tau} - \varepsilon_{\tau\tau}$ fit. The systematic errors shown here are related to the detector performance, event selection and reconstruction. The "σ" column shows the estimated 1σ uncertainty and the "Fit" column shows the best fit ϵ_j. Uncertainties are shown for SK-III and SK-IV.*

Sample			SK-III		SK-IV	
			Fit	σ	Fit	σ
FC reduction			0.08	0.8	0.73	1.3
PC reduction			-0.01	0.5	-0.78	1
FC/PC separation			-0.14	0.9	0.00	0.02
PC stopping/through-going separation (barrel)			-15.03	29	-1.24	8.5
PC stopping/through-going separation (bottom)			-0.44	12	-1.84	6.8
PC stopping/through-going separation (top)			-24.27	87	-32.57	40
Non-ν background $\mu - like$	Sub-GeV		0.14	0.5	-0.01	0.02
	Multi-GeV		0.14	0.5	-0.01	0.02
	Sub-GeV 1-ring 0-decay		0.11	0.4	-0.04	0.09
	PC		0.51	1.8	-0.24	0.49
Non-ν background e$-like$	Sub-GeV		-0.00	0.2	-0.00	0.02
	Multi-GeV		-0.00	0.7	-0.00	0.08
	Multi-GeV 1-ring e-like		-0.86	27	2.65	18
	Multi-GeV Multi-ring e-like		0.71	11	0.23	12
Fiducial Volume			0.25	2	-1.39	2
Ring separation	$< 400\ MeV$	e-like	0.82	2.3	-0.87	1.6
	$< 400\ MeV$	μ-like	1.08	3	-1.62	3
	$> 400\ MeV$	e-like	0.47	1.3	-0.54	1
	$> 400\ MeV$	μ-like	0.22	0.6	-0.32	0.6
	Multi-GeV	e-like	0.47	1.3	-0.54	1
	Multi-GeV	μ-like	0.36	1	-0.65	1.2
	Multi-ring Sub-GeV	e-like	0.47	1.3	-1.03	1.9
	Multi-ring Sub-GeV	μ-like	0.93	2.6	-1.25	2.3
	Multi-ring Multi-GeV	e-like	0.39	1.1	-0.49	0.9
	Multi-ring Multi-GeV	μ-like	0.75	2.1	-1.30	2.4
PID 1-ring	Sub-GeV	e-like	-0.06	0.26	0.11	0.28
	Sub-GeV	μ-like	-0.04	0.19	0.08	0.22
	Multi-GeV	e-like	-0.07	0.31	0.13	0.35
	Multi-GeV	μ-like	-0.07	0.3	0.13	0.35
PID Multi-ring	Sub-GeV	e-like	3.32	9.5	-1.90	4.2
	Sub-GeV	μ-like	1.82	5.2	-0.72	1.6
	Multi-GeV	e-like	1.71	4.9	-1.49	3.3
	Multi-GeV	μ-like	0.94	2.7	-0.72	1.6
Multi-ring likelihood selection	e-like		-4.75	5.3	-1.94	3
Energy calibration			1.37	2.4	-0.70	2.1
Up/down asymmetry energy calibration			0.74	1.3	-0.13	0.4
Up-μ reduction	Stopping		0.16	0.7	0.08	0.5
	Through-going		0.11	0.5	0.05	0.3
Up-μ stopping/through-going separation			0.03	0.4	-0.12	0.6
Up-μ stopping energy cut			0.93	2	-0.25	1.7
Up-μ through-going path cut			-1.02	2.8	-1.52	1.5
Up-μ Through-going showering separation			2.80	2.4	3.17	3
Up-μ stopping BG subtraction			-3.42	20	-8.46	17
Up-μ non-showering BG subtraction			1.51	24	2.15	17
Up-μ showering BG subtraction			0.06	24	-1.14	24
$\nu_e/\bar{\nu}_e$ separation			0.48	7.7	2.58	6.8
Sub-GeV 1-ring π^0 selection	$100 < P_e < 250$ MeV/c		0.86	6.3	5.08	4.6
	$250 < P_e < 400$ MeV/c		0.67	4.9	3.32	3
	$400 < P_e < 630$ MeV/c		3.28	24	14.37	13
	$630 < P_e < 1000$ MeV/c		1.12	8.2	18.79	17
	$1000 < P_e < 1330$ MeV/c		1.50	11	26.53	24
Sub-GeV 2-ring π^0			1.56	5.9	-0.83	5.6
Decay-e tagging			0.75	10	1.14	10
Solar activity			2.76	20	0.76	10

Table A.9 *The best fit systematic errors for the best fit point in the $\varepsilon_{ee}-\varepsilon_{e\tau}-\varepsilon_{\tau\tau}$ fit. The systematic errors shown here are related to the neutrino flux. The final column shows the estimated 1σ uncertainty and the penultimate column shows the best fit ϵ_j.*

Sample			Fit Value [%]	σ [%]
Flux normalisation	$E_\nu < 1$		13.55	25
	$E_\nu > 1$		6.83	15
$(\nu_\mu + \bar{\nu}_\mu)/(\nu_e + \bar{\nu}_e)$			0.04	2
			-1.11	3
			1.96	5
$\bar{\nu}_e/\nu_e$			1.68	5
			3.39	5
			-1.61	8
$\bar{\nu}_\mu/\nu_\mu$			0.22	2
			3.01	6
			-3.57	15
Up/down ratio	$< 400\ MeV$	e-like	-0.02	0.1
	$< 400\ MeV$	μ-like	-0.07	0.3
	$< 400\ MeV$	0-decay μ-like	-0.26	1.1
	$> 400\ MeV$	e-like	-0.19	0.8
	$> 400\ MeV$	μ-like	-0.12	0.5
	$> 400\ MeV$	0-decay μ-like	-0.40	1.7
	Multi-GeV	e-like	-0.17	0.7
	Multi-GeV	μ-like	-0.05	0.2
	Multi-ring Sub-GeV	e-like	-0.10	0.4
	Multi-ring Sub-GeV	μ-like	-0.05	0.2
	Multi-ring Multi-GeV	e-like	-0.07	0.3
	Multi-ring Multi-GeV	μ-like	-0.05	0.2
	PC		-0.05	0.2
Horizontal/vertical ratio	$< 400\ MeV$	e-like	0.02	0.1
	$< 400\ MeV$	μ-like	0.02	0.1
	$< 400\ MeV$	0-decay μ-like	0.05	0.3
	$> 400\ MeV$	e-like	0.24	1.4
	$> 400\ MeV$	μ-like	0.32	1.9
	$> 400\ MeV$	0-decay μ-like	0.24	1.4
	Multi-GeV	e-like	0.54	3.2
	Multi-GeV	μ-like	0.39	2.3
	Multi-ring Sub-GeV	e-like	0.24	1.4
	Multi-ring Sub-GeV	μ-like	0.22	1.3
	Multi-ring Multi-GeV	e-like	0.48	2.8
	Multi-ring Multi-GeV	μ-like	0.25	1.5
	PC		0.29	1.7
K/π ratio in flux calculation			-11.16	10
Neutrino path length			-0.82	5
Sample-by-sample	FC Multi-GeV		-6.37	5
	PC + Stopping UP-μ		-0.25	5
Matter Effects			0.24	6.8

Table A.10 *The best fit systematic errors for the best fit point in the $\varepsilon_{ee} - \varepsilon_{e\tau} - \varepsilon_{\tau\tau}$ fit. The systematic errors shown here are related to the neutrino interaction. The final column shows the estimated 1σ uncertainty and the penultimate column shows the best fit ϵ_j.*

Sample		Fit Value [%]	σ [%]
M_A in QE		-0.56	10
Single π production; Axial coupling		-4.42	10
Single π production; C_{A5}		-3.04	10
Single π production; Background		-8.73	10
CCQE cross section		6.41	10
CCQE $\bar{\nu}/\nu$ ratio		9.10	10
CCQE μ/e ratio		0.64	10
DIS cross section		-2.06	5
DIS model comparisons		3.00	10
DIS Q^2 distribution (high W)		8.46	10
DIS Q^2 distribution (low W)		-5.79	10
Coherent π production		-8.09	100
NC/CC		12.60	20
CC ν_τ cross section		-12.22	25
Single π production; $\pi^0/\pi^\pm$ ratio		-20.88	40
Single π production; $\bar{\nu}_i/\nu_i$ $(i = e; \mu)$		-11.22	10
NC fraction from hadron simulation		-0.79	10
$\pi^\pm$ decay uncertainty	e-like 0-decay	-0.18	0.6
	μ-like 0-decay	-0.24	0.8
	e-like 1-decay	-1.25	4.1
	μ-like 1-decay	-0.27	0.9
	μ-like 2-decay	-1.73	5.7
Meson exchange current		-1.61	10
Δm^2_{21} [139]		0.02	2.4
$\sin^2(\theta_{12})$ [139]		0.32	4.6
$\sin^2(\theta_{13})$ [139]		0.16	5.4

Table A.11 *The best fit systematic errors for the best fit point in the $\varepsilon_{ee} - \varepsilon_{e\tau} - \varepsilon_{\tau\tau}$ fit. The systematic errors shown here are related to the detector performance, event selection and reconstruction. The "σ" column shows the estimated 1σ uncertainty and the "Fit" column shows the best fit ϵ_j. Uncertainties are shown for SK-I and SK-II.*

Sample			SK-I		SK-II	
			Fit	σ	Fit	σ
FC reduction			-0.01	0.2	0.01	0.2
PC reduction			0.01	2.4	-3.46	4.8
FC/PC separation			-0.10	0.6	0.08	0.5
PC stopping/through-going separation (barrel)			3.67	7	-5.80	9.4
PC stopping/through-going separation (bottom)			-16.27	23	-2.47	13
PC stopping/through-going separation (top)			6.17	46	-3.43	19
Non-ν background $\mu - like$	Sub-GeV		0.01	0.1	0.07	0.4
	Multi-GeV		0.04	0.4	0.07	0.4
	Sub-GeV 1-ring 0-decay		0.01	0.1	0.05	0.3
	PC		0.02	0.2	0.12	0.7
Non-ν background e$-like$	Sub-GeV		0.07	0.5	-0.00	0.2
	Multi-GeV		0.01	0.1	-0.00	0.3
	Multi-GeV 1-ring e-like		3.58	13	-5.06	38
	Multi-GeV Multi-ring e-like		3.78	12	3.72	11
Fiducial Volume			-0.83	2	-0.10	2
Ring separation	$< 400\ MeV$	e-like	0.44	2.3	-1.09	1.3
	$< 400\ MeV$	μ-like	0.14	0.7	-1.93	2.3
	$> 400\ MeV$	e-like	0.08	0.4	-1.42	1.7
	$> 400\ MeV$	μ-like	0.14	0.7	-0.59	0.7
	Multi-GeV	e-like	0.72	3.7	-2.18	2.6
	Multi-GeV	μ-like	0.33	1.7	-1.42	1.7
	Multi-ring Sub-GeV	e-like	0.68	3.5	-3.18	3.8
	Multi-ring Sub-GeV	μ-like	0.87	4.5	-6.87	8.2
	Multi-ring Multi-GeV	e-like	0.60	3.1	-1.59	1.9
	Multi-ring Multi-GeV	μ-like	0.79	4.1	-0.67	0.8
PID 1-ring	Sub-GeV	e-like	-0.04	0.23	0.23	0.66
	Sub-GeV	μ-like	-0.03	0.18	0.17	0.5
	Multi-GeV	e-like	-0.03	0.19	0.08	0.24
	Multi-GeV	μ-like	-0.03	0.19	0.09	0.26
PID Multi-ring	Sub-GeV	e-like	0.23	3.1	3.46	6
	Sub-GeV	μ-like	0.05	0.66	1.44	2.5
	Multi-GeV	e-like	0.48	6.5	5.60	9.7
	Multi-GeV	μ-like	0.22	2.9	2.25	3.9
Multi-ring likelihood selection	e-like		-6.52	6	-1.25	3.8
Energy calibration			1.39	3.3	1.11	2.8
Up/down asymmetry energy calibration			0.25	0.6	0.24	0.6
Up-μ reduction	Stopping		-0.09	0.7	-0.09	0.7
	Through-going		-0.07	0.5	-0.07	0.5
Up-μ stopping/through-going separation			0.00	0.4	-0.01	0.6
Up-μ stopping energy cut			0.05	0.9	0.13	1.3
Up-μ through-going path cut			0.41	1.5	0.80	2.3
Up-μ Through-going showering separation			7.45	3.4	-4.76	4.4
Up-μ stopping BG subtraction			10.52	16	-2.97	21
Up-μ non-showering BG subtraction			-3.50	18	-3.54	14
Up-μ showering BG subtraction			-12.14	18	-15.55	14
$\nu_e/\bar{\nu}_e$ separation			0.97	7.2	6.99	7.9
Sub-GeV 1-ring π^0 selection	$100 < P_e < 250$ MeV/c		1.71	9	6.93	10
	$250 < P_e < 400$ MeV/c		1.75	9.2	9.71	14
	$400 < P_e < 630$ MeV/c		3.04	16	7.63	11
	$630 < P_e < 1000$ MeV/c		2.66	14	11.10	16
	$1000 < P_e < 1330$ MeV/c		2.28	12	6.80	9.8
Sub-GeV 2-ring π^0			1.30	5.6	-2.68	4.4
Decay-e tagging			-3.29	10	-0.93	10
Solar activity			-1.78	20	20.24	50

Table A.12 *The best fit systematic errors for the best fit point in the $\varepsilon_{ee} - \varepsilon_{e\tau} - \varepsilon_{\tau\tau}$ fit. The systematic errors shown here are related to the detector performance, event selection and reconstruction. The "σ" column shows the estimated 1σ uncertainty and the "Fit" column shows the best fit ϵ_j. Uncertainties are shown for SK-III and SK-IV.*

Sample			SK-III		SK-IV	
			Fit	σ	Fit	σ
FC reduction			0.07	0.8	0.70	1.3
PC reduction			-0.01	0.5	-0.78	1
FC/PC separation			-0.13	0.9	0.00	0.02
PC stopping/through-going separation (barrel)			-14.21	29	-0.53	8.5
PC stopping/through-going separation (bottom)			-0.34	12	-1.59	6.8
PC stopping/through-going separation (top)			-16.64	87	-27.05	40
Non-ν background $\mu - like$	Sub-GeV		0.11	0.5	-0.01	0.02
	Multi-GeV		0.11	0.5	-0.01	0.02
	Sub-GeV 1-ring 0-decay		0.09	0.4	-0.05	0.09
	PC		0.41	1.8	-0.27	0.49
Non-ν background e$-like$	Sub-GeV		-0.00	0.2	-0.00	0.02
	Multi-GeV		-0.01	0.7	-0.00	0.08
	Multi-GeV 1-ring e-like		-0.98	27	2.57	18
	Multi-GeV Multi-ring e-like		0.73	11	0.42	12
Fiducial Volume			0.22	2	-1.48	2
Ring separation	$< 400\ MeV$	e-like	0.80	2.3	-0.95	1.6
	$< 400\ MeV$	μ-like	1.05	3	-1.78	3
	$> 400\ MeV$	e-like	0.45	1.3	-0.59	1
	$> 400\ MeV$	μ-like	0.21	0.6	-0.36	0.6
	Multi-GeV	e-like	0.45	1.3	-0.59	1
	Multi-GeV	μ-like	0.35	1	-0.71	1.2
	Multi-ring Sub-GeV	e-like	0.45	1.3	-1.13	1.9
	Multi-ring Sub-GeV	μ-like	0.91	2.6	-1.37	2.3
	Multi-ring Multi-GeV	e-like	0.38	1.1	-0.53	0.9
	Multi-ring Multi-GeV	μ-like	0.73	2.1	-1.42	2.4
PID 1-ring	Sub-GeV	e-like	-0.05	0.26	0.12	0.28
	Sub-GeV	μ-like	-0.04	0.19	0.10	0.22
	Multi-GeV	e-like	-0.06	0.31	0.16	0.35
	Multi-GeV	μ-like	-0.06	0.3	0.16	0.35
PID Multi-ring	Sub-GeV	e-like	3.47	9.5	-2.25	4.2
	Sub-GeV	μ-like	1.90	5.2	-0.86	1.6
	Multi-GeV	e-like	1.79	4.9	-1.77	3.3
	Multi-GeV	μ-like	0.99	2.7	-0.86	1.6
Multi-ring likelihood selection	e-like		-5.03	5.3	-2.35	3
Energy calibration			1.36	2.4	-0.74	2.1
Up/down asymmetry energy calibration			0.74	1.3	-0.14	0.4
Up-μ reduction	Stopping		0.16	0.7	0.09	0.5
	Through-going		0.11	0.5	0.05	0.3
Up-μ stopping/through-going separation			0.03	0.4	-0.11	0.6
Up-μ stopping energy cut			0.95	2	-0.15	1.7
Up-μ through-going path cut			-0.99	2.8	-1.49	1.5
Up-μ Through-going showering separation			2.87	2.4	3.20	3
Up-μ stopping BG subtraction			-4.56	20	-9.96	17
Up-μ non-showering BG subtraction			1.45	24	2.11	17
Up-μ showering BG subtraction			0.26	24	-0.85	24
$\nu_e/\bar{\nu}_e$ separation			0.41	7.7	2.46	6.8
Sub-GeV 1-ring π^0 selection	$100 < P_e < 250$ MeV/c		0.97	6.3	5.24	4.6
	$250 < P_e < 400$ MeV/c		0.76	4.9	3.42	3
	$400 < P_e < 630$ MeV/c		3.70	24	14.82	13
	$630 < P_e < 1000$ MeV/c		1.26	8.2	19.38	17
	$1000 < P_e < 1330$ MeV/c		1.69	11	27.36	24
Sub-GeV 2-ring π^0			1.62	5.9	-0.73	5.6
Decay-e tagging			0.86	10	1.35	10
Solar activity			2.70	20	0.65	10

Bibliography

[1] *Standard Model of Elementary Particles*, 2019 (accessed May 12, 2020). URL https://en.wikipedia.org/wiki/Standard_Model#/media/File:Standard_Model_of_Elementary_Particles.svg.

[2] International Association of Geomagnetism and Aeronomy, Working Group V-MOD. Participating members . International Geomagnetic Reference Field: the eleventh generation. *Geophysical Journal International*, 183(3):1216–1230, 2010. doi: 10.1111/j.1365-246X.2010.04804.x. URL https://onlinelibrary.wiley.com/doi/abs/10.1111/j.1365-246X.2010.04804.x.

[3] M. G. Aartsen *et al.* Neutrino oscillation studies with IceCube-DeepCore. *Nuclear Physics B*, 908:161 – 177, 2016. ISSN 0550-3213. doi: https://doi.org/10.1016/j.nuclphysb.2016.03.028. URL http://www.sciencedirect.com/science/article/pii/S0550321316300141. Neutrino Oscillations: Celebrating the Nobel Prize in Physics 2015.

[4] M. G. Aartsen *et al.* Search for nonstandard neutrino interactions with IceCube DeepCore. *Physical Review D*, 97(7):072009, 2018.

[5] M. G. Aartsen *et al.* Measurement of Atmospheric Neutrino Oscillations at 6–56 GeV with IceCube DeepCore. *Physical Review Letters*, 120:071801, Feb 2018. doi: 10.1103/PhysRevLett.120.071801. URL https://link.aps.org/doi/10.1103/PhysRevLett.120.071801.

[6] M. G. Aartsen *et al.* Search for nonstandard neutrino interactions with IceCube DeepCore. *Physical Review D*, 97:072009, Apr 2018. doi: 10.1103/PhysRevD.97.072009. URL https://link.aps.org/doi/10.1103/PhysRevD.97.072009.

[7] J. N. Abdurashitov *et al.* Measurement of the solar neutrino capture rate with gallium metal. *Physical Review C*, 60(5):055801, 1999.

[8] K. Abe *et al.* Proposal for an Extended Run of T2K to 20× $10^2$1 POT. *arXiv preprint arXiv:1609.04111*, 242.

[9] K. Abe *et al.* The T2K experiment. *Nuclear Instruments and Methods in Physics Research Section A: Accelerators, Spectrometers, Detectors and Associated Equipment*, 659(1):106–135, 2011.

[10] K. Abe *et al.* Solar neutrino results in Super-Kamiokande-III. *Physical Review D*, 83:052010, Mar 2011. doi: 10.1103/PhysRevD.83.052010. URL https://link.aps.org/doi/10.1103/PhysRevD.83.052010.

[11] K. Abe *et al.* The T2K experiment. *Nuclear Instruments and Methods in Physics Research Section A: Accelerators, Spectrometers, Detectors and Associated Equipment*, 659(1):106–135, 2011.

[12] K. Abe *et al.* Calibration of the Super-Kamiokande detector. *Nuclear Instruments and Methods in Physics Research, Section A: Accelerators, Spectrometers, Detectors and Associated Equipment*, 737:253–272, 2014. ISSN 01689002. doi: 10.1016/j.nima.2013.11.081.

[13] K. Abe *et al.* Measurement of the intrinsic electron neutrino component in the T2K neutrino beam with the ND280 detector. *Physical Review D*, 89:092003, May 2014. doi: 10.1103/PhysRevD.89.092003. URL https://link.aps.org/doi/10.1103/PhysRevD.89.092003.

[14] K. Abe *et al.* Observation of electron neutrino appearance in a muon neutrino beam. *Physical Review Letters*, 112:061802, Feb 2014. doi: 10.1103/PhysRevLett.112.061802. URL https://link.aps.org/doi/10.1103/PhysRevLett.112.061802.

[15] K. Abe *et al.* Solar neutrino measurements in Super-Kamiokande-IV. *Physical Review D*, 94:052010, Sep 2016. doi: 10.1103/PhysRevD.94.052010. URL https://link.aps.org/doi/10.1103/PhysRevD.94.052010.

[16] K. Abe *et al.* Combined Analysis of Neutrino and Antineutrino Oscillations at T2K. *Physical Review Letters*, 118:151801, Apr 2017. doi: 10.1103/PhysRevLett.118.151801. URL https://link.aps.org/doi/10.1103/PhysRevLett.118.151801.

[17] K. Abe *et al.* Hyper-Kamiokande Design Report. 2018. URL https://arxiv.org/abs/1805.04163.

[18] K. Abe *et al.* Atmospheric neutrino oscillation analysis with external constraints in Super-Kamiokande I-IV. *Physical Review D*, 97(7):72001, 2018. ISSN 24700029. doi: 10.1103/PhysRevD.97.072001. URL https://doi.org/10.1103/PhysRevD.97.072001.

[19] K. Abe *et al.* T2K ND280 Upgrade-Technical Design Report. Technical report, 2019.

[20] S. Abe *et al.* Precision Measurement of Neutrino Oscillation Parameters with KamLAND. *Physical Review Letters*, 100:221803, Jun 2008. doi: 10.1103/PhysRevLett.100.221803. URL https://link.aps.org/doi/10.1103/PhysRevLett.100.221803.

[21] Y. Abe *et al.* Indication of Reactor $\vec{\nu}_e$ Disappearance in the Double Chooz Experiment. *Physical Review Letters*, 108:131801, Mar 2012. doi: 10.1103/PhysRevLett.108.131801. URL https://link.aps.org/doi/10.1103/PhysRevLett.108.131801.

[22] R. Acciarri *et al.* Long-baseline neutrino facility (LBNF) and deep underground neutrino experiment (DUNE) conceptual design report, volume 4 the DUNE detectors at LBNF. *arXiv preprint arXiv:1601.02984*, 2016.

[23] M. A. Acero *et al.* First measurement of neutrino oscillation parameters using neutrinos and antineutrinos by NOvA. *Physical Review Letters*, 123: 151803, Oct 2019. doi: 10.1103/PhysRevLett.123.151803. URL https://link.aps.org/doi/10.1103/PhysRevLett.123.151803.

[24] P. Adamson *et al.* Measurement of the Neutrino Mass Splitting and Flavor Mixing by MINOS. *Physical Review Letters*, 106:181801, May 2011. doi: 10.1103/PhysRevLett.106.181801. URL https://link.aps.org/doi/10.1103/PhysRevLett.106.181801.

[25] P. Adamson *et al.* Search for flavor-changing non-standard neutrino interactions by MINOS. *Physical Review D*, 88(7):072011, 2013.

[26] P. Adamson *et al.* First measurement of muon-neutrino disappearance in NOvA. *Physical Review D*, 93:051104, Mar 2016. doi: 10.1103/PhysRevD.93.051104. URL https://link.aps.org/doi/10.1103/PhysRevD.93.051104.

[27] S. Agostinelli *et al.* GEANT4: A Simulation toolkit. *Nucl. Instrum. Meth.*, A506:250–303, 2003. doi: 10.1016/S0168-9002(03)01368-8.

[28] A. A. Aguilar-Arevalo *et al.* First measurement of the muon neutrino charged current quasielastic double differential cross section. *Physical Review D*, 81:092005, May 2010. doi: 10.1103/PhysRevD.81.092005.

[29] Q. R. Ahmad *et al.* Measurement of the Rate of $\nu_e + d \rightarrow p + p + e^-$ Interactions Produced by ^8B Solar Neutrinos at the Sudbury Neutrino Observatory. *Physical Review Letters*, 87:071301, Jul 2001. doi: 10.1103/PhysRevLett.87.071301. URL https://link.aps.org/doi/10.1103/PhysRevLett.87.071301.

[30] Q. R. Ahmad *et al.* Direct evidence for neutrino flavor transformation from neutral-current interactions in the Sudbury Neutrino Observatory. *Physical review letters*, 89(1):011301, 2002.

[31] Q. R. Ahmad *et al.* Direct Evidence for Neutrino Flavor Transformation from Neutral-Current Interactions in the Sudbury Neutrino Observatory. *Physical Review Letters*, 89:011301, Jun 2002. doi: 10.1103/PhysRevLett.89.011301. URL https://link.aps.org/doi/10.1103/PhysRevLett.89.011301.

[32] J. K. Ahn *et al.* Observation of Reactor Electron Antineutrinos Disappearance in the RENO Experiment. *Physical Review Letters*, 108: 191802, May 2012. doi: 10.1103/PhysRevLett.108.191802. URL `https://link.aps.org/doi/10.1103/PhysRevLett.108.191802`.

[33] E. K. Akhmedov, M. A. Tórtola, and J. W. F. Valle. A simple analytic three-flavour description of the day-night effect in the solar neutrino flux. *Journal of High Energy Physics*, 2004(05):057, 2004.

[34] J. Alcaraz *et al.* Cosmic protons. *Physics Letters, Section B: Nuclear, Elementary Particle and High-Energy Physics*, 490(1-2):27–35, sep 2000. ISSN 03702693. doi: 10.1016/S0370-2693(00)00970-9.

[35] J. Alcaraz *et al.* Helium in near earth orbit. *Physics Letters, Section B: Nuclear, Elementary Particle and High-Energy Physics*, 494(3-4):193–202, nov 2000. ISSN 03702693. doi: 10.1016/S0370-2693(00)01193-X.

[36] E. N. Alexeyev, , *et al.* Detection of the neutrino signal from SN 1987A in the LMC using the INR Baksan underground scintillation telescope. *Physics Letters B*, 205(2-3):209–214, 1988.

[37] G Alimonti *et al.* The borexino detector at the laboratori nazionali del gran sasso. *Nuclear Instruments and Methods in Physics Research Section A: Accelerators, Spectrometers, Detectors and Associated Equipment*, 600 (3):568–593, 2009.

[38] B. W. Allardyce *et al.* Pion reaction cross sections and nuclear sizes. *Nuclear Physics A*, 209(1):1 – 51, 1973. ISSN 0375-9474. doi: https://doi.org/10.1016/0375-9474(73)90049-3.

[39] W. W. M. Allison *et al.* The atmospheric neutrino flavor ratio from a 3.9 fiducial kiloton-year exposure of Soudan 2. *Physics Letters B*, 449(1-2): 137–144, 1999.

[40] G. Ambrosini *et al.* K/π production ratios from 450 GeV/c protons on beryllium. *Physics Letters B*, 420(1-2):225–232, 1998.

[41] F. P. An *et al.* Observation of Electron-Antineutrino Disappearance at Daya Bay. *Physical Review Letters*, 108:171803, Apr 2012. doi: 10.1103/PhysRevLett.108.171803. URL `https://link.aps.org/doi/10.1103/PhysRevLett.108.171803`.

[42] M. Apollonio *et al.* Search for neutrino oscillations on a long base-line at the CHOOZ nuclear power station. *The European Physical Journal C-Particles and Fields*, 27(3):331–374, 2003.

[43] D. Ashery *et al.* True absorption and scattering of pions on nuclei. *Physical Review C*, 23:2173–2185, May 1981. doi: 10.1103/PhysRevC.23.2173.

[44] US Standard Atmosphere. *US standard atmosphere*. National Oceanic and Atmospheric Administration, 1976.

[45] G. D. Barr *et al.* Three-dimensional calculation of atmospheric neutrinos. *Physical Review D - Particles, Fields, Gravitation and Cosmology*, 70(2): 13, 2004. ISSN 15502368. doi: 10.1103/PhysRevD.70.023006.

[46] T. Barszczak. The Efficient discrimination of electron and pi-zero events in a water Cherenkov detector and the applicati on to neutrino oscillation experiments. Technical report, 2005.

[47] G. Battistoni *et al.* The FLUKA atmospheric neutrino flux calculation. *Astroparticle Physics*, 19(2):269–290, 2003. ISSN 09276505. doi: 10.1016/S0927-6505(02)00246-3.

[48] J. F. Beacom. The diffuse supernova neutrino background. *Annual Review of Nuclear and Particle Science*, 60:439–462, 2010.

[49] R. Becker-Szendy *et al.* Electron-and muon-neutrino content of the atmospheric flux. *Physical Review D*, 46(9):3720, 1992.

[50] R Becker-Szendy *et al.* IMB-3 : a large water Cherenkov detector for nucleon decay and neutrino interactions. Technical report, 1993.

[51] A. Bodek and U. K. Yang. Modeling Neutrino and Electron Scattering Inelastic Cross Sections, 2003.

[52] J. Boger *et al.* The sudbury neutrino observatory. *Nuclear Instruments and Methods in Physics Research Section A: Accelerators, Spectrometers, Detectors and Associated Equipment*, 449(1-2):172–207, 2000.

[53] R. Brun *et al.* GEANT3. 1987.

[54] CAEN. The specification for the CAEN DT5742 waveform digitiser. URL `https://www.caen.it/products/dt5742/`.

[55] A. Capella *et al.* Structure functions and low x physics. *Physics Letters B*, 337(3-4):358–366, 1994.

[56] P. A. Čerenkov. Visible Radiation Produced by Electrons Moving in a Medium with Velocities Exceeding that of Light. *Physical Review*, 52(4): 378–379, aug 1937. ISSN 0031-899X. doi: 10.1103/PhysRev.52.378.

[57] S. Chandrasekhar. *An introduction to the study of stellar structure*, volume 2. Courier Corporation, 1957.

[58] R. Claus *et al.* A Wavelength Light Collector For A Water Cherenkov Detector. *Nuclear Instruments and Methods in Physics Research*, 6:540, 1955.

[59] JASCO Corporation. JASCO FP-6500 is a spectrofluorometer produced by JASCO Inc., . URL `http://www.jascoinc.com/docs/product-spec-sheets/FP6500_072.pdf`.

[60] JASCO Corporation. JASCO V-550 is a spectrophotometer produced by JASCO Inc., . URL http://www.jascoinc.com/.

[61] JASCO Corporation. JASCO V-650 is a spectrophotometer produced by JASCO Inc., . URL http://www.jascoinc.com/.

[62] S. Davidson *et al.* Present and future bounds on non-standard neutrino interactions. *Journal of High Energy Physics*, 2003(03):011, 2003.

[63] E. R. Davies. *Machine vision: theory, algorithms, practicalities*. Elsevier, 2004.

[64] R. Davis *et al.* Search for neutrinos from the sun. *Physical Review Letters*, 20:1205–1209, May 1968. doi: 10.1103/PhysRevLett.20.1205. URL https://link.aps.org/doi/10.1103/PhysRevLett.20.1205.

[65] P. de Perio. Neut pion fsi. *AIP Conference Proceedings*, 1405(1):223–228, 2011. doi: 10.1063/1.3661590.

[66] S. Desai. *High Energy Neutrino Astrophysics with Super-Kamiokande*. PhD thesis, Boston University, 2004.

[67] S. Dimopoulos, S. Raby, and F. Wilczek. Proton decay in supersymmetric models. *Physics Letters B*, 112(2):133–136, 1982.

[68] Dupont. Tyvek is a Dupont registered trademark. URL http://www.dupont.com.

[69] A. M. Dziewonski and D. L. Anderson. Preliminary reference earth model. *Physics of the earth and planetary interiors*, 25(4):297–356, 1981.

[70] ET Enterprices. The datasheet for the ETEL 9320KFLB PMT. URL http://et-enterprises.com/images/data_sheets/9320KFLB.pdf.

[71] I. Esteban *et al.* Global analysis of three-flavour neutrino oscillations: synergies and tensions in the determination of θ 23, δ CP, and the mass ordering. *Journal of High Energy Physics*, 2019(1):106, 2019. NuFIT 4.1 (2019), http://www.nu-fit.org/.

[72] Y. Farzan and M. Tórtola. Neutrino oscillations and non-standard interactions. *Frontiers in Physics*, 6:10, 2018.

[73] P. Fernandez Menendez. *Neutrino Physics in Present and Future Kamioka Water- Cerenkov Detectors with Neutron Tagging Abstract (English)*. Phd, University Autonomous of Madrid, 2017.

[74] G. L. Fogli *et al.* Getting the most from the statistical analysis of solar neutrino oscillations. *Physical Review D*, 66:053010, Sep 2002. doi: 10.1103/PhysRevD.66.053010. URL https://link.aps.org/doi/10.1103/PhysRevD.66.053010.

[75] J. A. Formaggio and G. P. Zeller. From eV to EeV: Neutrino cross sections across energy scales. *Rev. Mod. Phys.*, 84:1307–1341, Sep 2012. doi: 10.1103/RevModPhys.84.1307.

[76] A. Friedland and C. Lunardini. Test of tau neutrino interactions with atmospheric neutrinos and K2K data. *Physical Review D*, 72(5):053009, 2005.

[77] A. Friedland, C. Lunardini, and C. Pena-Garay. Solar neutrinos as probes of neutrino–matter interactions. *Physics Letters B*, 594(3-4):347–354, 2004.

[78] M. Friend. J-PARC accelerator and neutrino beamline upgrade programme. In *Journal of Physics: Conference Series*, volume 888, page 012042. IOP Publishing, 2017.

[79] C. Fröhlich and J. Lean. The Sun's total irradiance: Cycles, trends and related climate change uncertainties since 1976. *Geophysical Research Letters*, 25(23):4377–4380, 1998.

[80] Y. Fujii *et al.* Quasielastic π^--nucleus scattering at 950MeV/c. *Physical Review C*, 64:034608, Aug 2001. doi: 10.1103/PhysRevC.64.034608.

[81] S. Fukuda *et al.* Solar B 8 and hep Neutrino Measurements from 1258 Days of Super-Kamiokande Data. *Physical Review Letters*, 86(25):5651, 2001.

[82] S Fukuda *et al.* The Super-Kamiokande detector. *Physics Research A*, 501:419, 2003. doi: 10.1016/S0168-9002(03)00425-X.

[83] Y. Fukuda *et al.* Atmospheric muon-neutrino / electron-neutrino ratio in the multigev energy range. *Physics Letters B*, 335(NGTHEP-94-1):237–245, 1994.

[84] Y. Fukuda *et al.* Solar neutrino data covering solar cycle 22. *Physical Review Letters*, 77(9):1683, 1996.

[85] Y. Fukuda *et al.* Evidence for oscillation of atmospheric neutrinos. *Physical Review Letters*, 81:1562–1567, Aug 1998. doi: 10.1103/PhysRevLett.81.1562. URL `https://link.aps.org/doi/10.1103/PhysRevLett.81.1562`.

[86] T. A. Gabriel, J. D. Amburgey, and B. L. Bishop. CALOR: A Monte Carlo Program Package for the Design and Analysis of Calorimeter Systems. 1977.

[87] M. Glück, E. Reya, and A. Vogt. Dynamical parton distributions revisited. *The European Physical Journal C - Particles and Fields*, 5(3):461–470, Sep 1998. ISSN 1434-6052. doi: 10.1007/s100529800978.

[88] M. C. Gonzalez-Garcia and M. Maltoni. Determination of matter potential from global analysis of neutrino oscillation data. *Journal of High Energy Physics*, 2013(9):152, 2013.

[89] R. Gran *et al.* Measurement of the quasielastic axial vector mass in neutrino interactions on oxygen. *Physical Review D*, 74:052002, Sep 2006. doi: 10.1103/PhysRevD.74.052002. URL `https://link.aps.org/doi/10.1103/PhysRevD.74.052002`.

[90] L. Haegel. The latest T2K neutrino oscillation results. *arXiv preprint arXiv:1709.04180*, 2017.

[91] T. Haines. Neutrinos from SN1987a in the IMB detector. 1988.

[92] S. Haino *et al.* Measurements of primary and atmospheric cosmic-ray spectra with the BESS-TeV spectrometer. *Physics Letters, Section B: Nuclear, Elementary Particle and High-Energy Physics*, 594(1-2):35–46, jul 2004. ISSN 03702693. doi: 10.1016/j.physletb.2004.05.019.

[93] Hamamatsu. H2431-50 is a pmt manufactured by hamamatsu., . URL `https://www.hamamatsu.com`.

[94] Hamamatsu. R1408 is a PMT manufactured by Hamamatsu., . URL `https://www.hamamatsu.com`.

[95] Hamamatsu. R3600 is a PMT manufactured by Hamamatsu., . URL `https://www.hamamatsu.com`.

[96] Y. Hayato. A neutrino interaction simulation program library NEUT. *Acta Phys. Polon.*, B40:2477–2489, 2009.

[97] A. E. Hedin. Extension of the MSIS thermosphere model into the middle and lower atmosphere. *Journal of Geophysical Research: Space Physics*, 96 (A2):1159–1172, 1991.

[98] A. J. Heijboer. *Track Reconstruction and Point Source Searches with ANTARES*. PhD thesis, Universiteit van Amsterdam, 2004.

[99] Hermetic. HT-Seal F-119 is a sealant produced by Hermetic. URL `https://www.hermetic.co.jp/item/pipe-sealant/182`.

[100] P. W. Higgs. Broken symmetries and the masses of gauge bosons. *Physical Review Letters*, 13(16):508, 1964.

[101] K. S. Hirata *et al.* Observation in the Kamiokande-II detector of the neutrino burst from supernova SN1987A. *Physical Review D*, 38(2):448, 1988.

[102] M. Honda *et al.* Calculation of the flux of atmospheric neutrinos. *Physical Review D*, 52:4985–5005, Nov 1995. doi: 10.1103/PhysRevD.52.4985.

[103] M. Honda *et al.* Comparison of 3-dimensional and 1-dimensional schemes in the calculation of atmospheric neutrinos. *Physical Review D - Particles, Fields, Gravitation and Cosmology*, 64(5):12, 2001. ISSN 15502368. doi: 10.1103/PhysRevD.64.053011.

[104] M. Honda *et al.* New calculation of the atmospheric neutrino flux in a three-dimensional scheme. *Physical Review D - Particles, Fields, Gravitation and Cosmology*, 70(4), 2004. ISSN 15502368. doi: 10.1103/PhysRevD.70.043008.

[105] M. Honda *et al.* Calculation of atmospheric neutrino flux using the interaction model calibrated with atmospheric muon data. *Physical Review D - Particles, Fields, Gravitation and Cosmology*, 75(4), 2007. ISSN 15507998. doi: 10.1103/PhysRevD.75.043006.

[106] M. Honda *et al.* Improvement of low energy atmospheric neutrino flux calculation using the JAM nuclear interaction model. *Physical Review D - Particles, Fields, Gravitation and Cosmology*, 83(12), 2011. ISSN 15507998. doi: 10.1103/PhysRevD.83.123001.

[107] H. Ikeda *et al.* Front-end hybrid circuit for super-KAMIOKANDE. *Nuclear Instruments and Methods in Physics Research Section A: Accelerators, Spectrometers, Detectors and Associated Equipment*, 320(1-2):310–316, aug 1992. ISSN 0168-9002. doi: 10.1016/0168-9002(92)90791-2.

[108] Y. Ikeda. J-PARC status update. *Nuclear Instruments and Methods in Physics Research Section A: Accelerators, Spectrometers, Detectors and Associated Equipment*, 600(1):1–4, 2009.

[109] A. F. M. Ishaq *et al.* Thermal neutron capture in isotopes of nickel. *Zeitschrift für Physik A Atoms and Nuclei*, 281(4):365–372, dec 1977. ISSN 0340-2193. doi: 10.1007/BF01408184. URL `http://link.springer.com/10.1007/BF01408184`.

[110] C. Ishihara. *Full three flavor oscillation analysis of atmospheric neutrino data observed in Super-Kamiokande*. PhD thesis, 2010.

[111] T. James Irvine. *Development of Neutron-Tagging Techniques and Application to Atmospheric Neutrino Oscillation Analysis in Super-Kamiokande*. Phd, University of Tokyo, 2014.

[112] J. V. Jelley. Cerenkov radiation and its applications. *British Journal of Applied Physics*, 6:227, 1955.

[113] M. Jiang *et al.* Atmospheric neutrino oscillation analysis with improved event reconstruction in Super-Kamiokande IV. *Progress of Theoretical and Experimental Physics*, 2019(5):053F01, 2019.

[114] M. K. Jones *et al.* Pion absorption above the $\Delta(1232)$ resonance. *Physical Review C*, 48:2800–2817, Dec 1993. doi: 10.1103/PhysRevC.48.2800.

[115] T. Kajita. Discovery of neutrino oscillations. *Reports on Progress in Physics*, 69(6):1607–1635, may 2006. doi: 10.1088/0034-4885/69/6/r01. URL `https://doi.org/10.1088%2F0034-4885%2F69%2F6%2Fr01`.

[116] R. R. Kinsey *et al.* The NUDAT/PCNUDAT program for nuclear data. 10 1996. URL https://www.nndc.bnl.gov/nudat2/reCenter.jsp?z=98&n=154. Data extracted from the NUDAT database, 27 June 2019.

[117] H. W. Koch and J. W. Motz. Bremsstrahlung cross-section formulas and related data. *Reviews of modern physics*, 31(4):920, 1959.

[118] Y. Koshio. Solar results from Super-Kamiokande. In *AIP Conference Proceedings*, volume 1666, page 090001. AIP Publishing LLC, 2015.

[119] Kuraray. Prototype WLS plate manufactured by Kuraray. URL https://www.kuraray.com/.

[120] Labsphere. Spectralon is diffuse highly reflective target produced by Labsphere. URL https://www.labsphere.com/labsphere-products-solutions/materials-coatings-2/coatings-materials/spectralon/.

[121] P. Langacker. Grand unified theories and proton decay. *Physics Reports*, 72(4):185–385, 1981.

[122] T. S. H. Lee and R. P. Redwine. Pion-nucleus interactions. *Annual Review of Nuclear and Particle Science*, 52(1):23–63, 2002. doi: 10.1146/annurev.nucl.52.050102.090713.

[123] J. Liao, D. Marfatia, and K. Whisnant. Nonstandard interactions in solar neutrino oscillations with Hyper-Kamiokande and JUNO. *Physics Letters B*, 771:247–253, 2017.

[124] P. Lipari. The east–west effect for atmospheric neutrinos. *Astroparticle Physics*, 14(3):171–188, 2000.

[125] C. H. Llewellyn-Smith. Neutrino Reactions at Accelerator Energies. *Phys. Rept.*, 3:261–379, 1972. doi: 10.1016/0370-1573(72)90010-5.

[126] Z. Maki, M. Nakagawa, and S. Sakata. Remarks on the Unified Model of Elementary Particles. *Progress of Theoretical Physics*, 28(5):870–880, 11 1962. ISSN 0033-068X. doi: 10.1143/PTP.28.870. URL https://doi.org/10.1143/PTP.28.870.

[127] M. Maltoni and A. Y. Smirnov. Solar neutrinos and neutrino physics. *The European Physical Journal A*, 52(4):87, 2016.

[128] G. Mie. Beiträge zur Optik trüber Medien, speziell kolloidaler Metallösungen. *Annalen der Physik*, 330(3):377–445, jan 1908. ISSN 00033804. doi: 10.1002/andp.19083300302. URL http://doi.wiley.com/10.1002/andp.19083300302.

[129] S.P. Mikheev and A.Y. Smirnov. Resonance enhancement of oscillations in matter and solar neutrino spectroscopy. *Sov. J. Nucl. Phys. (Engl. Transl.); (United States)*, 42:6, 12 1985.

[130] O. G. Miranda and H. Nunokawa. Non standard neutrino interactions: Current status and future prospects. *New Journal of Physics*, 17(9), 2015. ISSN 13672630. doi: 10.1088/1367-2630/17/9/095002.

[131] O. G. Miranda, M. A. Tórtola, and J. W. F. Valle. Are solar neutrino oscillations robust? *Journal of High Energy Physics*, 2006(10):008, 2006.

[132] G. Mitsuka. *Study of Non-Standard Neutrino Interactions with Atmospheric Neutrino Data in Super-Kamiokande*. Phd, University Of Tokyo, 2009. URL `http://www-sk.icrr.u-tokyo.ac.jp/sk/{_}pdf/articles/dthesis{_}feb9-mitsuka.pdf`.

[133] G. Mitsuka *et al.* Study of nonstandard neutrino interactions with atmospheric neutrino data in Super-Kamiokande I and II. *Physical Review D*, 84(11):113008, dec 2011. ISSN 1550-7998. doi: 10.1103/PhysRevD.84.113008. URL `https://journals.aps.org/prd/pdf/10.1103/PhysRevD.84.113008https://link.aps.org/doi/10.1103/PhysRevD.84.113008`.

[134] J. Nieves, J. E. Amaro, and M. Valverde. Inclusive quasielastic charged-current neutrino-nucleus reactions. *Physical Review C*, 70:055503, Nov 2004. doi: 10.1103/PhysRevC.70.055503. URL `https://link.aps.org/doi/10.1103/PhysRevC.70.055503`.

[135] J. Nieves *et al.* Inclusive charged-current neutrino-nucleus reactions. *Physical Review C*, 83:045501, Apr 2011. doi: 10.1103/PhysRevC.83.045501.

[136] H. Nishino. *Search for Nucleon Decay into Charged Antilepton plus Meson in Super-Kamiokande*. Phd, University of Tokyo, 2009.

[137] T. Ohlsson. Status of non-standard neutrino interactions. sep 2012. doi: 10.1088/0034-4885/76/4/044201. URL `http://arxiv.org/abs/1209.2710http://dx.doi.org/10.1088/0034-4885/76/4/044201`.

[138] Y. Okajima *et al.* Detailed performance evaluation of a new 20-inch photomultiplier tube with a Box and Line dynode. In *International Conference on New Photo-detectors*, volume 252, page 015. SISSA Medialab, 2016.

[139] K. A. Olive. Review of particle physics. *Chinese physics C*, 38(9):090001–090001, 2014.

[140] ORTEC. The specification for the ORTEC EASY-MCA., . URL `https://www.ortec-online.com/products/electronics/multichannel-analyzers-mca/basic-analog/easy-mca-2k-or-8k`.

[141] ORTEC. The specification for the ORTEC 570 amplifier., . URL `https://www.ortec-online.com/products/electronics/amplifiers/570`.

[142] A. Palazzo. Hint of nonstandard Mikheyev-Smirnov-Wolfenstein dynamics in solar neutrino conversion. *Physical Review D*, 83:101701, May 2011. doi: 10.1103/PhysRevD.83.101701. URL `https://link.aps.org/doi/10.1103/PhysRevD.83.101701`.

[143] L. Pik. *Study of the neutrino mass hierarchy with the atmospheric neutrino data observed in Super-Kamiokande*. PhD thesis, 2012.

[144] B. Pontecorvo. Inverse beta processes and nonconservation of lepton charge. *Sov. Phys. JETP*, 7:172–173, 1958. [Zh. Eksp. Teor. Fiz.34,247(1957)].

[145] The Hyper-Kamiokande Proto-Collaboration. Physics potentials with the second Hyper-Kamiokande detector in Korea. *Progress of Theoretical and Experimental Physics*, 2018(6), 06 2018. ISSN 2050-3911. doi: 10.1093/ptep/pty044. URL `https://doi.org/10.1093/ptep/pty044`. 063C01.

[146] D. Rein and L. M. Sehgal. Neutrino-excitation of baryon resonances and single pion production. *Annals of Physics*, 133(1):79 – 153, 1981. ISSN 0003-4916. doi: https://doi.org/10.1016/0003-4916(81)90242-6.

[147] D Rein and L. M. Sehgal. Coherent $\pi 0$ production in neutrino reactions. *Nuclear Physics B*, 223(1):29 – 44, 1983. ISSN 0550-3213. doi: https://doi.org/10.1016/0550-3213(83)90090-1.

[148] A. Renshaw *et al.* First Indication of Terrestrial Matter Effects on Solar Neutrino Oscillation. *Physical Review Letters*, 112:091805, Mar 2014. doi: 10.1103/PhysRevLett.112.091805.

[149] E. Richard. *Studies Of The Energy, Azimuthal, and Time Specta of the Atmospheric Neutrino Flux at Super-Kamiokande*. PhD thesis, 2015.

[150] T. Sanuki *et al.* Precise Measurement of Cosmic-Ray Proton and Helium Spectra with the BESS Spectrometer. *The Astrophysical Journal*, 545(2): 1135–1142, dec 2000. ISSN 0004-637X. doi: 10.1086/317873.

[151] N. V. Smirnov. Estimate of deviation between empirical distribution functions in two independent samples. *Bulletin Moscow University*, 2(2): 3–16, 1939.

[152] R. A. Smith and E. J. Moniz. NEUTRINO REACTIONS ON NUCLEAR TARGETS. *Nucl. Phys.*, B43:605, 1972. doi: 10.1016/0550-3213(75)90612-4,10.1016/0550-3213(72)90040-5. [Erratum: Nucl. Phys.B101,547(1975)].

[153] M. Smy. Low energy event reconstruction and selection in Super-Kamiokande-III. *Proceedings of 30th International Cosmic Ray Conference*, 2007.

[154] A Suzuki *et al.* Improvement of 20 in. diameter photomultiplier tubes. Technical report, 1993.

[155] Eljen Technology. EJ-286 is a wavelength shifting plate produced by Eljen Technology. URL https://eljentechnology.com/products/wavelength-shifting-plastics/ej-280-ej-282-ej-284-ej-286.

[156] S. Tobayama. *An analysis of the oscillation of atmospheric neutrinos*. PhD thesis, University of British Columbia, 2016.

[157] L. V. Volkova. Energy Spectra and Angular Distributions of Atmospheric Neutrinos. *Sov. J. Nucl. Phys.*, 31:784–790, 1980. [Yad. Fiz.31,1510(1980)].

[158] R. Wendell. Atmospheric Neutrino Oscillations at Super-Kamiokande. *PoS*, ICRC2015:1062, 2016. doi: 10.22323/1.236.1062.

[159] R. Winston. Light collection within the framework of geometrical optics. *Josa*, 60(2):245–247, 1970.

[160] L. Wolfenstein. Neutrino oscillations in matter. *Physical Review D*, 17: 2369–2374, May 1978. doi: 10.1103/PhysRevD.17.2369. URL https://link.aps.org/doi/10.1103/PhysRevD.17.2369.

[161] L. Wolfenstein. Neutrino oscillations and stellar collapse. *Physical Review D*, 20:2634–2635, Nov 1979. doi: 10.1103/PhysRevD.20.2634. URL https://link.aps.org/doi/10.1103/PhysRevD.20.2634.

[162] D. Xue-Feng *et al.* Measurement of the fluorescence quantum yield of bis-MSB. *Chinese Physics C*, 39(12):126001, 2015.

[163] S. Yamada *et al.* Commissioning of the New Electronics and Online System for the Super-Kamiokande Experiment. *IEEE Transactions on Nuclear Science*, 57(2):428–432, apr 2010. ISSN 0018-9499. doi: 10.1109/TNS.2009.2034854.

[164] K. Yury. Hyper-kamiokande. *arXiv preprint arXiv:2005.13641*, 2020.

[165] Q. Zhao. Flasher Identification at Daya Bay. Poster presented at ACAT2013, Beijing, China.